Piezoresistance and Electrical Conduction in Solution-Processed 2D Nanosheet Networks

EOIN CAFFREY

A THESIS SUBMITTED TO
THE UNIVERSITY OF DUBLIN

IN PART-FULFILLMENT OF THE REQUIREMENTS FOR THE DEGREE OF
DOCTOR OF PHILOSOPHY

IN THE SUBJECT OF
PHYSICS

UNDER THE SUPERVISION OF
PROFESSOR JONATHAN N. COLEMAN

SCHOOL OF PHYSICS,
TRINITY COLLEGE DUBLIN
February 2025

Declaration

I declare that this thesis has not been submitted as an exercise for a degree at this or any other university and it is entirely my own work.

I agree to deposit this thesis in the University's open access institutional repository or allow the library to do so on my behalf, subject to Irish Copyright Legislation and Trinity College Library conditions of use and acknowledgement.

Elements of this work that have been carried out jointly with others or by collaborators have been duly acknowledged in the text wherever included.

_____

Eoin Caffrey

Abstract

Nanosheet networks are attracting much interest as printed electronic devices, utilising the physical properties of 2D nanosheets. Electrical conduction and the impact of strain on conduction in the networks is of particular interest when considering applications as wearable devices, for measuring strain or as flexible electronics and interconnects.

As nanosheet networks become thinner, they enter a percolation regime, where the electrical conductivity is no longer an intrinsic material property. In this study, networks of liquid phase exfoliated (LPE) graphene nanosheets were spray coated onto flexible polymer substrates. The unstrained electrical conductivity of the networks was measured, and the networks were strained linearly and with cyclic profiles. Both conductivity and piezoresistance show percolative behaviours for thinner networks. They transition to bulk-like behaviour when the network thickness is greater than ~100 nm. This data yielded a bulk conductivity of ~260 S/m. Using percolation theory, an equation for the gauge factor as a function of network thickness and network conductivity in the percolation region was derived. These models describe the experimental data very well, including the divergence in the gauge factor as the percolation threshold is approached from above. They also show that the dominant factor contributing to the piezoresistive response in the percolation regime is the effect of strain on the network structure. These networks have a maximum gauge factor of ~350, close to the percolation threshold, while having stable cyclic responses, with minimal electrical hysteresis and a minimal frequency dependence on the piezoresistive response.

As network resistivity has been shown to depend on nanosheet dimensions, it was hypothesised that a similar effect may apply to the piezoresistive response. LPE graphene nanosheets were size selected using liquid cascade centrifugation to produce inks with six distinct nanosheet thickness distributions ranging from ~20 nm to ~3 nm. These were

spray coated onto flexible substrates and tested electrically, and the piezoresistive response of each was extracted from cyclic strain measurements. The network resistivity decreased with decreasing nanosheet thickness, in line with existing models, however the gauge factor increased with increasing nanosheet thickness. Using an existing model, the nanosheet resistivity and junction resistances were determined to be $(2.9 \pm 1.3) \times 10^{-5}$ Ωm and 8.9 ± 1.0 kΩ respectively. To understand the change in gauge factor, this model was used as a starting point to derive a new model relating gauge factor to nanosheet thickness. Fitting the model enabled the effect of strain on the nanosheets and the inter-nanosheet junctions to be differentiated. In this system, the fitting suggests that the graphene nanosheets have a negative piezoresistive response.

Changing the nanosheet aspect ratio can have a significant impact on the electrical performance of devices made from nanosheet networks. Inks of LPE and electrochemically exfoliated (EE) nanosheets were prepared and spray coated to form films. The network structure of both materials was characterised using nanotomography, which illustrated the increased conformality and reduced porosity of EE networks. The bulk electrical conductivity of the networks differed by an order of magnitude, with the EE network being more conductive. Both networks displayed percolation behaviour in the conductivity as a function of network thickness. Fitting these with a percolation model yielded scaling exponents in line with the 2D and 3D exponents for EE and LPE networks respectively. The piezoresistive response of the LPE networks was higher in the bulk regime, however both materials showed an increase in piezoresistance as the percolation threshold thickness was approached from above. These changes can be understood with respect to the network structure and the nanosheet sizes.

Novel impedance spectroscopy techniques are enabling the direct measurement of nanosheet resistance and junction resistance in 2D nanosheet networks, offering a

potential avenue to further mechanistic understanding of the piezoresistive effect in nanomaterial systems. Networks of EE MoS_2 were characterised electromechanically using both DC resistance and AC impedance spectroscopic techniques. DC piezoresistance showed a relatively low gauge factor of ~3, with a linear response which withstood cyclic deformation. The AC impedance measurements showed that the junction resistance increased linearly with strain while the nanosheet resistance remained constant. These observations are consistent with highly aligned nanosheets sliding past one another under the application of strain, without transferring strain to the nanosheets themselves. This technique may enable further mechanistic insight into a range of piezoresistive nanomaterial systems.

List of publications

1. **E. Caffrey**, J.R. Garcia, D. O'Suilleabhain, C. Gabbett, T. Carey, J.N. Coleman, Quantifying the Piezoresistive Mechanism in High-Performance Printed Graphene Strain Sensors, ACS Applied Materials & Interfaces, 14 (2022) 7141-7151.
   [Basis for Chapter 5]
2. T. Carey, A. Alhourani, R. Tian, S. Seyedin, A. Arbab, J. Maughan, L. Šiller, D. Horvath, A. Kelly, H. Kaur, **E. Caffrey**, J.M. Kim, H.R. Hagland, J.N. Coleman, Cyclic production of biocompatible few-layer graphene ink with in-line shear-mixing for inkjet-printed electrodes and Li-ion energy storage, npj 2D Materials and Applications, 6 (2022)
3. T. Carey, O. Cassidy, K. Synnatschke, **E. Caffrey**, J. Garcia, S. Liu, H. Kaur, A.G. Kelly, J. Munuera, C. Gabbett, D. O'Suilleabhain, J.N. Coleman, High-Mobility Flexible Transistors with Low-Temperature Solution-Processed Tungsten Dichalcogenides, ACS Nano, 17 (2023) 2912-2922.
4. A.G. Kelly, S. Sheil, D.A. Douglas-Henry, **E. Caffrey**, C. Gabbett, L. Doolan, V. Nicolosi, J.N. Coleman, Transparent Conductors Printed from Grids of Highly Conductive Silver Nanosheets, ACS Applied Materials & Interfaces, 15 (2023) 39864-39871.
5. F.C. Donnelly, F. Purcell-Milton, **E. Caffrey**, L. Branzi, S. Stafford, F.A. Alhammad, O. Cleary, M. Ghariani, V. Kuznetsova, Y.K. Gun'ko, Chiroptically Active Multi-Modal Calcium Carbonate-Based Nanocomposites, Nanomaterials, 2024.
6. C. Gabbett, L. Doolan, K. Synnatschke, L. Gambini, E. Coleman, A.G. Kelly, S. Liu, **E. Caffrey**, J. Munuera, C. Murphy, S. Sanvito, L. Jones, J.N. Coleman, Quantitative analysis of printed nanostructured networks using high-resolution 3D FIB-SEM nanotomography, Nature Communications, 15 (2024) 278.
7. J. Garcia, **E. Caffrey**, L. Doolan, D.V. Horvath, T. Carey, C. Gabbett, J.N. Coleman, Near Room Temperature Production of Segregated Network Composites of Carbon Nanotubes and Regolith as Multifunctional, Extra-Terrestrial Building Materials, Small, n/a (2024) 2310954.
8. T. Carey, J. Maughan, L. Doolan, **E. Caffrey**, J. Garcia, S. Liu, H. Kaur, C. Ilhan, S. Seyedin, J.N. Coleman, Knot Architecture for Biocompatible and Semiconducting 2D Electronic Fiber Transistors, Small Methods, n/a (2024) 2301654.
9. C. Gabbett, A.G. Kelly, E. Coleman, L. Doolan, T. Carey, K. Synnatschke, S. Liu, A. Dawson, D. O'Suilleabhain, J. Munuera, **E. Caffrey**, J.B. Boland, Z. Sofer, G. Ghosh, S. Kinge, L.D.A. Siebbeles, N. Yadav, J.K. Vij, M.A. Aslam, A. Matkovic, J.N. Coleman, Understanding how junction resistances impact the conduction mechanism in nano-networks, Nature Communications, 15 (2024) 4517.

10. **E. Caffrey**, J.M. Munuera, T. Carey, J.N. Coleman, Quantifying the effect of nanosheet dimensions on the piezoresistive response of printed graphene nanosheet networks, Nanoscale Horizons, (2024). DOI 10.1039/D4NH00224E
    [Basis for Chapter 6]
11. K. Synnatschke, A. Müller, C. Gabbett, M.J. Mohn, A.G. Kelly, K. Mosina, B. Wu**, E. Caffrey**, O. Cassidy, C. Backes, Z. Sofer, U. Kaiser, J.N. Coleman, Inert Liquid Exfoliation and Langmuir-Type Thin Film Deposition of Semimetallic Metal Diborides, ACS Nano, 18 (2024) 28596-28608.
12. J. Neilson, **E. Caffrey**, O. Cassidy, C. Gabbett, K. Synnatschke, E. Schneider, J.M. Munuera, T. Carey, M. Rimmer, Z. Sofer, J. Maultzsch, S.J. Haigh, J.N. Coleman, Production of Ultrathin and High-Quality Nanosheet Networks via Layer-by-Layer Assembly at Liquid–Liquid Interfaces, ACS Nano, 18 (2024) 32589-32601.
13. **E. Caffrey**, T. Carey, L. Doolan, A. Dawson, E. Coleman, Z. Sofer, O. Cassidy, C. Gabbett, J.N. Coleman, Using Electrical Impedance Spectroscopy to Separately Quantify the Effect of Strain on Nanosheet and Junction Resistance in Printed Nanosheet Networks, Small, n/a (2024) 2406864.
    [Basis for Chapter 8]
14. O. Cassidy, K. Synnatschke, J.M. Munuera, C. Gabbett, T. Carey, L. Doolan, **E. Caffrey**, J.N. Coleman, Layer-by-layer assembly yields thin graphene films with near theoretical conductivity, npj 2D Materials and Applications, 9 (2025) 2.
15. S. Masoumi, R. Xiong, **E. Caffrey**, R. Gatensby, C. Ilhan, J.N. Coleman, A. Pakdel, Flexible thermoelectric generators from spray-printed PEDOT:PSS/Bi0.5Sb1.5Te3 composites, RSC Advances, 15 (2025) 6574-6584.

Acknowledgements

First and foremost, I would like to thank Johnny for his continuous support, encouragement, and positivity over the last four years. Even when times looked bleak, meetings always concluded with some positive spin. Your depth of knowledge, enthusiasm, and ability to think of new ways of fitting data saved the day more times than I would like to admit.

Luke, you have played many roles throughout the PhD, friend, housemate, scientific sounding board, killer of many of my wilder project ideas and supporter of a few more. Thanks for always being there to bring me back to earth.

James, you welcomed and trained me in the ways of the Coleman group in the depths of COVID and kept me on the right path, even if it did lead to Honolulu! Jose, your steadying hand guided me through some rough months with very little data, but now I know that "It'll be grand" sounds best with a slight Spanish accent, and that the line will eventually go up. Tian, thanks for showing me how science should really be done and for sharing some fantastic, purely scientific trips with me. I'll never forget my scarf when going to a warm climate again. Kev, Cian, and Adam it seems only fitting to thank the three of you together, as you always find a way to end up together, often at the heart of where the craic is happening. You guys are some of the most brilliant scientific minds I know while also knowing how to have a great time doing it. Erxiong, your dedication, drive and commitment to projects was inspiring.

Thanks to Joe, Rebekah, and Anthony, the crew of Rascals! Dom, Shixin, Jack, Borja thanks for sharing your different 2D materials perspectives with me. And to the rest of the Coleman group, Yash, Domhnall, Mark, Emmet, Alina, Vincent, Oran C, Oran B, Harneet, Barathi, Yufan, Yumei, and Laila. Thank you. Kate, Seán, my incredible students, thank you for all of your hard work.

Beyond the realms of the Coleman lab, thanks to Oisín, Andrew, Phelo, Ray, and Elle, thanks for tagging along on this journey, the world would be nothing without good friends to share it with.

Thank you to Martin, Yurii and Harry for welcoming me into your labs as an undergrad, and all of my teachers who have inspired me throughout my time in education.

Thanks Mom and Dad, for always being there to support me in everything I do and for your constant encouragement to take risks and follow my dreams. Nana and Granda, thank you for great cups of tea and chats when I'm home in Limerick.

Finally, Laoise, thank you for sharing my love of travel, putting up with my love of new cookware, for always listening to my complaints, celebrating even the smallest achievements and for coming along with me on this journey.

Table of Contents

List of Figures

6.4	Network Imaging
6.5	Electrical Characterisation
6.6	Piezoresistive Characterisation
6.7	Modelling Piezoresistance
7.1	Ink Characterisation
7.2	Nanosheet Characterisation
7.3	Film Characterisation
7.4	Nanosheet and Pore 3D Reconstruction
7.5	Network Imaging
7.6	Electrical Percolation
7.7	Piezoresistive Responses
8.1	Ink Characterisation
8.2	Film Characterisation
8.3	DC Piezoresistance
8.4	AC Characterisation
8.5	Extracted Electrical Parameters

To my family

"Don't fear difficult moments. The best comes from them."

Rita Levi-Montalcini

Chapter 1
Introduction & Outline

1.1 Introduction

Nanomaterials have been proposed as the materials of the future, offering new ways to tackle existing problems.[1] Many people see this relatively new class of materials as the holy grail due to the wide-ranging areas where they can deliver improvements to material properties or device performance.[2] It has now risen to the same degree of 'buzz-word' recognition as artificial intelligence and quantum computing. However, the term 'nanomaterials' covers an incredibly broad range of materials of different dimensionalities, produced in many distinct ways with vastly different quality requirements depending on the eventual application.[3] As a result, researchers must establish whether they are interested in the fundamental behaviours of singular nanoparticles or nanosheets, seeking to develop industrially scalable synthetic routes to high quality materials, or looking to utilise nanomaterials to develop the next cutting-edge technologies.

Many of the advantages of nanomaterials arise from their unique properties, which are attributed to their reduced size compared to conventional materials. These unique properties can also lead to novel phenomena and mechanisms that must be investigated

and understood in order to get the most out of these nanomaterials. This thesis will focus on sheet-like 2D nanomaterials, typically derived from layered van der Waals (vdW) crystals. 2D materials researchers initially focused on individual sheets,[4] however liquid phase exfoliation enabled the scalable production of nanosheets in research laboratories, in the form of liquid dispersions.[5] These dispersions or 'inks' could be used to produce networks of billions of interconnected nanosheets. Such networks have properties which depend not only on the nanosheets, but on the junctions between the nanosheets.[6] The networks have been used to produce devices ranging from capacitors[7] and batteries[8] to catalysts[9] and strain gauges.[10] Understanding how electrical conduction in these networks responds to applied strain and how to tune this response will be a key focus of this thesis.

1.2 Research Outline

Printed networks exhibit coating thickness dependent physical phenomena, where the conductivity increases sharply as the thickness increases up to a critical point. This behaviour is known to be a percolation transformation arising from the build-up of a conductive network of nanosheets. It has also been observed that piezoresistive properties can be dependent on the thickness of the network. In Chapter 5, these percolative behaviours of nanosheet networks are investigated. A model for network thickness dependent piezoresistive response is developed and tested. This provides a physical model which can enhance the understanding of this phenomenon in nanosheet networks and guide future researchers in engineering the piezoresistive response of nanosheet networks.

It has been observed that network electrical properties can be modulated by tuning the length and thickness of nanosheets in a network. In liquid phase exfoliation (LPE) dispersions, the aspect ratio of nanosheets is confined to a narrow range due to the exfoliation mechanism, however there is a broad range of nanosheet sizes in the

polydisperse suspension. As a result, a range of nanosheet sizes can be extracted using centrifugation methods. In Chapter 6, films of nanosheets above the percolation thickness regime are prepared with nanosheet thicknesses ranging from 3 nm to 20 nm, and the electrical and piezoresistive properties of the films are investigated. This reveals pathways to enable the modulation of the piezoresistive response of a network by changing the nanosheet thickness.

Nanosheets come in a wide range of sizes depending on the preparation method. Liquid phase exfoliation and electrochemical exfoliation (EE) yield flakes of significantly different aspect ratios and, as a result, the structure of the networks produced differs greatly. A key difference is observed in the contact between the nanosheets. In LPE, there are point-like contacts between jammed nanosheets, while the EE nanosheets form conformal vdW contacts. It is important to understand the impact of these morphological differences in such networks. In Chapter 7 the effect of LPE vs. EE nanosheets on conduction and piezoresistance in spray coated networks is investigated. These properties are also studied in the percolative regime, where it is shown that these percolation effects are observed in both LPE and EE networks, despite significant morphological differences.

In nanosheet networks, it is known that both the nanosheets and the junctions contribute to the electrical resistance of the coating. A method of measuring the resistance contributions of both, using impedance spectroscopy, has opened the possibility of directly measuring these effects in devices. In Chapter 8, through conducting this impedance measurement at different applied strain values, it is possible to probe the effect of strain on the nanosheets and the junctions in the network. This provides insight into the effect of strain on nanosheet networks and offers a new technique to study piezoresistance, by measuring the nanosheet and junction contributions directly.

"Scientists have become the bearers of the torch of discovery in our quest for knowledge."

Stephen Hawking

Chapter 2
2D Materials Properties, Preparation and Processing

2.1 Nanomaterials

Many eras of human civilisation have been described by the materials that defined their most significant technological advances, including the stone age, bronze age, iron age, and now, the silicon age is catching on. However, a new class of materials are coming to the forefront: nanomaterials.

The launching point for several of the significant advances in this field can be traced back to a lecture given by Feynman titled "There's Plenty of Room at the Bottom,"[1] at the end of which he set out challenges to inspire developments in nanoscale fabrication and devices. However, nanomaterials have been found in pigments[11] and medicines[12] used by ancient civilisations and have even been discovered in ancient Damascus steel blades.[13]

A nanomaterial is defined as a material with at least one dimension less than 100 nm. The properties of a material change as the size is reduced, with the dimensionality of a material given by the number of dimensions greater than 100 nm. This has given rise to 0D nanoparticles, 1D nanorods and nanotubes, and the focus of this work: 2D nanosheets. Some allotropes of carbon provide an insightful introduction to nanomaterials, such as fullerene 'buckeyballs,' with all dimensions less than 100 nm, carbon nanotubes (CNTs),

which have one dimension greater than 100 nm, and graphene, atomically thin sheets of carbon atoms.[14] These three structures are shown in Figure 2.1C.

These novel materials have exceptional properties because of their increased surface-to-volume ratio and quantum confinement effects, leading to advances in catalysis,[15] batteries,[16] and electronics.[17] Researchers are now investigating the incorporation of these materials into the mainstream semiconductor industry to push Moore's law even further.[18]

2.1.1 2D Materials

Since the time of Democritus, who thought about breaking matter up into smaller and smaller units to arrive at the base building blocks which he called "atomos", meaning indivisible, scientists have sought to study smaller, thinner materials in the quest for novel physical phenomena.[1] Crystals of layered materials have been known and extensively used for hundreds of years, with some reports of graphite being used as a lubricant to line cannon ball moulds, and molybdenum disulphide being used extensively as a dry lubricant.[19] This low friction arises because of the weak out-of-plane bonding in layered crystals, which allows the sheets to slide past each other, along with incommensurability in stacking between layers which can occur in the bulk crystal.[20] This weak bonding arises due to anisotropy in the bonding of layered crystals, with strong covalent bonding in the plane of the atomic layers and weak vdW bonding between the sheets in the out-of-plane direction.

Layered materials with weak out-of-plane bonding offer potential to separate the individual 2D layers, while ideally leaving the basal plane of the individual sheets intact. Based on reports from Lev Landau and the Mermin-Wagner theorem, large stable atomically thin nanosheets were theorised to be thermodynamically impossible.[21, 22] However, once exfoliated, these materials were observed to self-stabilise by undulations and corrugations, rather than tearing themselves apart.[23] It was correctly predicted, by

exfoliating, that the surface of these 2D nanosheets would be pristine and free of dangling bonds,[24] due to the weak vdW forces holding them together. This has enabled the development of the fruitful field of 2D materials. Using density functional theory methods, theoreticians have developed a library of layered materials they believe to be suitable for exfoliation into 2D nanosheets, with 9,306 materials listed as of 2023.[25]

2.1.2 Graphene

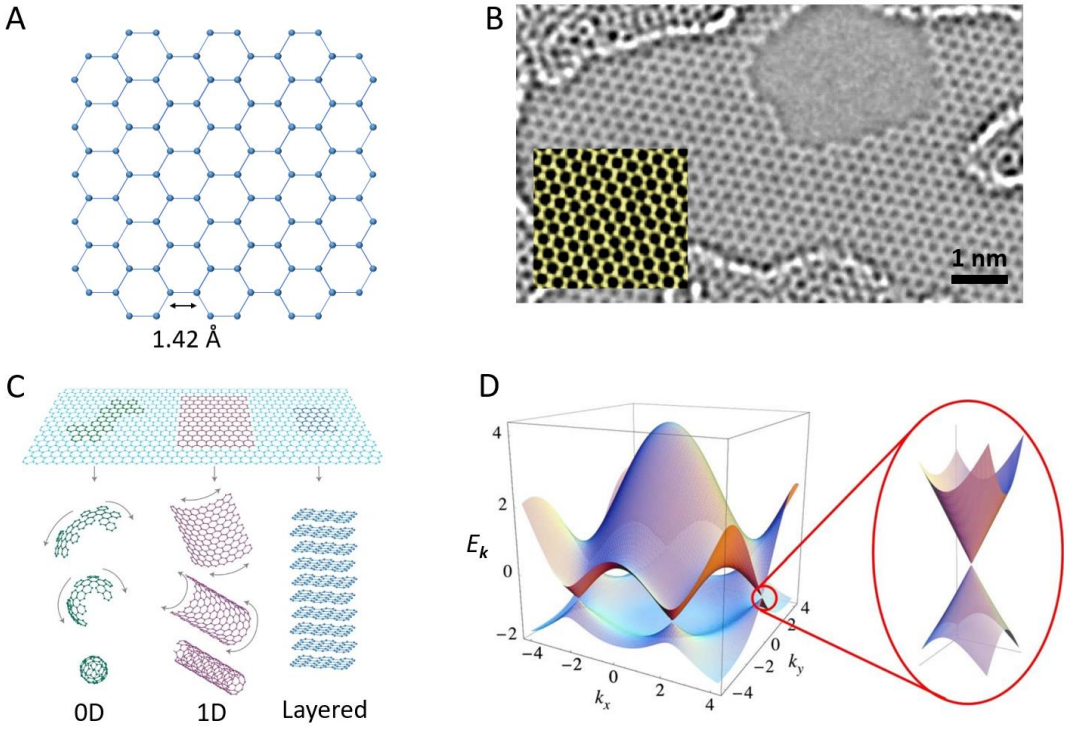

Figure 2.1: Graphene. A) Schematic showing the hexagonal structure of carbon atoms in graphene, with an inter-atomic distance of 1.42 Å. B) Transmission electron micrograph of graphene, adapted from Girit et al.[26] C) Low-dimensional carbon nanomaterials, adapted from Geim et al.[14] D) Electron dispersions for a honeycomb lattice, with the inset showing a magnified view of the cones at the Dirac point. Adapted from Castro Neto et al.[27]

Graphene truly is the prototypical 2D material, composed of a single atomic layer of carbon atoms arranged in a hexagonal lattice, Figure 2.1A. In 2004, the seminal graphene 'Scotch-tape' paper was published by the Manchester group.[4] Soon thereafter, graphene

was found to have superlative properties in many areas including electrical conduction,[27] mechanical strength,[28] and thermal conduction.[29] The hexagonal structure was also observed using transmission electron microscopy, shown in Figure 2.1B.[26] As a result of the impact of isolating monolayer graphene, the Nobel prize in Physics was awarded to Andre Geim and Kostya Novoselov in 2010, "for groundbreaking experiments regarding the two-dimensional material graphene."[30]

However, monolayers of graphite layered crystals had long been postulated. B.C. Brodie considered that, with sufficient division, graphite would yield "minute flat plates" in 1859.[31] With the advent of X-ray diffraction analysis, working independently, Hull,[32] Debye,[33] and an Irish scientist, J.D. Bernal reported on the crystal structure of graphite, noting that the "atoms of carbon lie in planes" and that the planes are composed of "nets of hexagons".[34] The ABAB stacking in graphite layers was named after Bernal. The carbon-carbon bond distance in the basal plane was determined to be 1.42 Å.[34]

As the layered structure of graphite was known, scientists began to imagine and theorise as to the potential properties of graphite at the monolayer limit. In 1947, P.R. Wallace reported on the theoretical semi metallic band structure of what is now called graphene.[35] However, as mentioned previously, it was believed that such 2D crystalline sheets could not exist in a planar state without a substrate, as the thermal vibrations would destroy any long range order in a 2D lattice.[21, 22] These theories were valid, however it was observed that graphene nanosheets are stabilised by their intrinsic ripples and corrugations.[23, 36]

The properties of graphene are strongly related to the hybridised bonding of the carbon atomic orbitals when arranged in a planar hexagonal lattice. The 2s, $2p_x$, and $2p_y$ orbitals hybridise into a σ bonding orbital. This sp^2 hybridised bonding yields strong covalent bonds which enhance the in-plane mechanical properties. The out-of-plane $2p_z$ orbital of

each atom hybridise to form a π bonding orbital. In graphene, this π bonding orbital is half filled, and as a result charge can flow in the nanosheet.

Expanding this theory to include the hexagonal lattice and a tight binding model, results in a linear dispersion relation at the Γ point, known as the Dirac cone.[4] As the electron's effective mass is defined with respect to the curvature of the dispersion relation, the Dirac cone yields an electron with zero effective mass, or a "massless fermion." This cone is shown in Figure 2.1D.[27] As the conduction and valence bands touch with negligible overlap at the Γ point, graphene is said to be a semimetal.[4, 27]

Given that every atom in a graphene monolayer is a surface atom, this yields a specific surface area of 2,630 m^2/g, leading to applications in electrical double layer capacitors.[37] However, it is also poised to deliver impact in sectors including healthcare,[38]electronics,[39] and aviation.[40]

2.1.3 Hexagonal Boron Nitride (h-BN)

Interestingly, a second layered crystal material also exhibits a similar honeycomb hexagonal structure: hexagonal boron nitride (h-BN). This synthetic material is formed from boron and nitrogen atoms, which occupy alternating positions in the hexagonal lattice as in Figure 2.2A. h-BN has long been used in the cosmetics and beauty industry. After the mechanical exfoliation of graphene, this "white graphene" layered crystal was the obvious next step and in less than a year it was isolated in monolayer form.[41]

Interestingly, monolayer h-BN does not exhibit the semi metallic electronic properties of graphene; instead, it is an insulator with an direct bandgap of order 6.1 eV.[42] This band gap opening comes about due to the electronegativity of the nitrogen atoms in the structure,[43] which introduces a polar-covalent nature to the boron-nitrogen bond.[44] Hence the valence band has largely nitrogen p-orbital character, while the conduction band is largely based on the boron p-orbital character.[45] As h-BN nanosheets are optically

transparent,[46] atomically flat,[47] and have low gas-permeability,[48] they are frequently used to encapsulate nanosheet devices.[49] h-BN is also used as a substrate for other 2D nanosheets,[50] and the nanosheets can be used as a dielectric layer.[24]

2.1.4 Transition Metal Dichalcogenides (TMDs)

Transition metal dichalcogenides (TMDs) are a class of layered crystals composed of three-atom thick covalently bonded nanosheets, which are held together by vdW forces between the sheets. The nanosheet layers take the form X-M-X, where a layer of transition metal atoms (M) are sandwiched between two layers of chalcogen atoms (X=S, Se or Te).[51] The structure of TMDs was first reported for Molybdenum Disulfide (MoS_2) in its mineral form 'Molybdenite' by Linus Pauling in 1923.[52] This is a broad class of materials with a wide variety of electronic properties ranging from semi-metallic to semiconducting depending on the choice of metal and chalcogen atoms making up the nanosheets,[53] Figure 2.2B. This variation arises from the differing occupancy of the d-orbitals in the transition metal.[54]

TMDs are polymorphic, meaning they can exist in three primary structural units, the 1T tetrahedral packing, 2H hexagonal packing, and 3R rhombohedral packing.[55] It is also possible to distort the stacking configurations of the elemental layers within the structure. An example of this is the 1T' phase, where metal-metal bonds are formed through dimerisation in the middle layer in 1T phase group VI TMDs,[51] as shown in Figure 2.2C. By changing the structural stacking type and hence the transition metal coordination, the electronic properties of the nanosheets are modified.

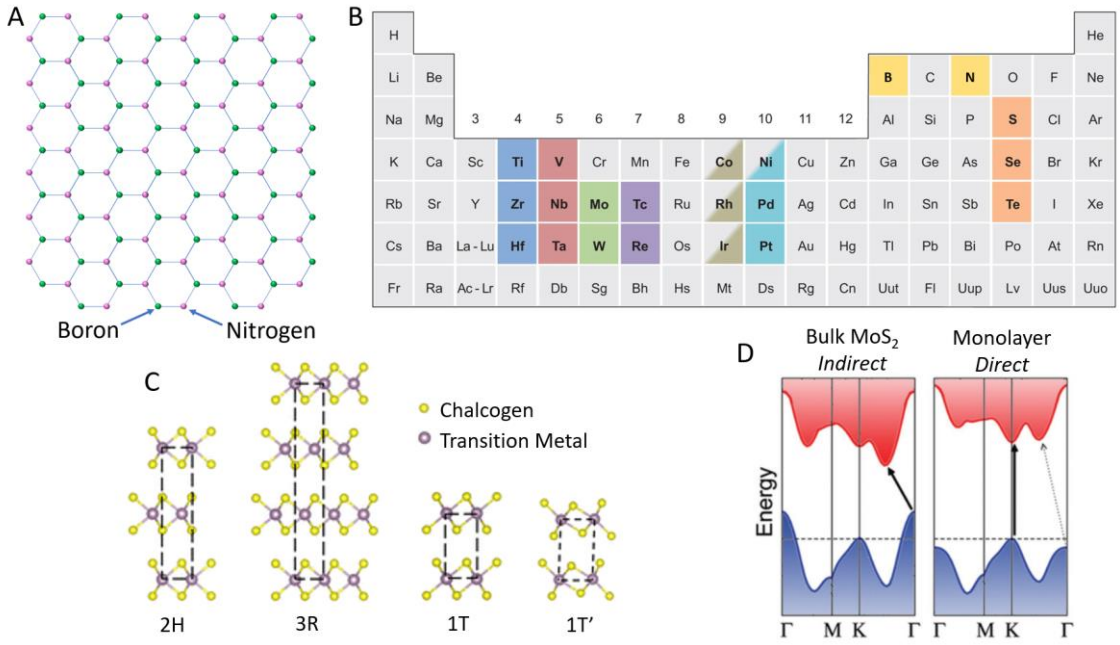

Figure 2.2: Materials Beyond Graphene. A) Schematic of h-BN hexagonal monolayer lattice. B) Periodic table highlighting boron, nitrogen, transition metals capable of forming TMDs, and the chalcogens (S, Se and Te), adapted from Chhowalla et al.[54] C) TMD polytypes, with unit cells defined by the dashed lines. Adapted from Dai et al.[56] D) MoS_2 band diagrams for the bulk and monolayer limits. Adapted from Bonaccorso et al.[57]

Transition metal dichalcogenides have attracted much attention for their electronic properties, but also for their optoelectronic properties. For example, MoS_2 exhibits photoluminescence at the monolayer limit due to an indirect to direct bandgap transition with decreasing thickness, Figure 2.2D.[58] Additionally, by varying the choice of metal and chalcogen, specific desirable properties such as bandgap can be tuned.[59]

To date, TMDs are finding applications across a variety of fields including catalysts for the hydrogen evolution reaction,[60] biosensing,[61] photodetectors,[62] printed transistors,[63] and memristors.[64] Interestingly, monolayer MoS_2 was reported in 1986,[65] almost 20 years before the report of monolayer graphene using the Scotch-tape method.[4] These synthesis methods will be discussed in the following sections.

2.2 2D Material Synthesis Routes

In order to access the properties of 2D nanomaterials, they must first be prepared in a manner which preserves their exceptional qualities. Currently there are two approaches under which all techniques can be classified. The top-down approach where the weaker vdW bonds between the sheets in a layered crystal are broken, yielding individual nanosheets, and the bottom-up approach where a material is grown in a controlled manner, maintaining the required dimensionality.[3] The foundations of these approaches will be outlined below, by discussing mechanical exfoliation and chemical vapour deposition (CVD) techniques, followed by an outline of 2D nanosheet exfoliation in liquid media.

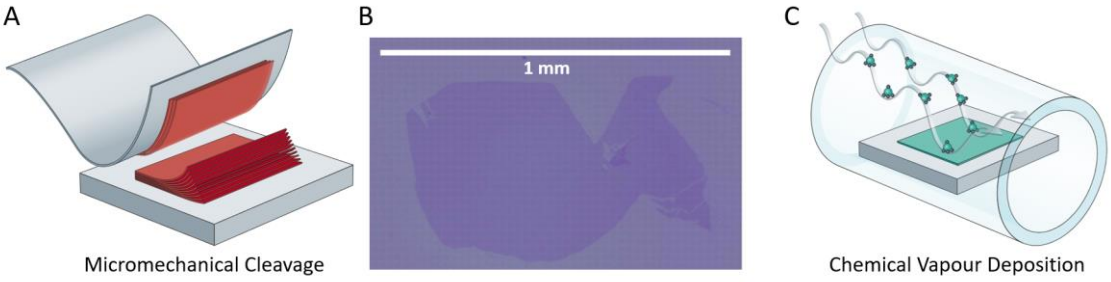

Figure 2.3: 2D Synthesis Methods. A) Diagram showing micromechanical cleavage using scotch tape. Adapted from Mannix et al.[66] B) Optical microscope image of a millimetre scale micromechanically exfoliated nanosheet. Reproduced from Geim et al.[67] C) Illustration of chemical vapour deposition growth of a nanosheet. Adapted from Mannix et al.[66]

2.2.1 Micromechanical Cleavage

This technique, also known as the 'Scotch-tape method' came to the fore when it was used to isolate monolayer graphene in 2004.[4] However, this technique was used to cleave crystals of MoS_2 to thicknesses of less than 100 Å in studies dating back to 1963.[68] In

1999, Lu *et al*. postulated that single atomic layers of graphite could be isolated by rubbing graphite against a flat surface.[69]

The technique is relatively simple in theory, using an adhesive tape to cleave nanosheets from the top surface of a layered crystal, illustrated in Figure 2.3A. As the vdW bonds between the layers are weaker than the in-plane covalent bonds, the nanosheets are delaminated along the basal plane. Repeating the process on the cleaved section, it is possible to continue thinning the crystal towards the monolayer limit. Nanosheets on the millimetre scale have been produced using this method[67, 70] (Figure 2.3B), and can be transferred onto a variety of substrates[71] or stacked with different nanosheets to form heterostructures as desired.[72] This technique has yielded monolayers of graphene, h-BN, TMDs, and more.[41, 70] To date this method is the best route towards high quality, large area, few-layer nanosheets,[73] suited to academic studies of fundamental materials properties. However, its industrial application is hampered by the low throughput and scalability.[74]

2.2.2 Chemical Vapour Deposition (CVD)

This bottom-up nanosheet growth method has shown promise in producing high quality nanosheets at a wafer scale. Large-area growth been reported for graphene,[75, 76] along with some transition metal dichalcogenides, namely MoS_2,[77] WS_2,[78] and WSe_2.[79] The CVD process operates by flowing molecular gas over a metal foil in a high temperature furnace. The gas adsorbs to the metal foil, nucleating the growth of 2D structures, as shown in Figure 2.3C. Through tuning the growth parameters, these can range from polycrystalline films to large single crystals.[67]

This technique gained traction alongside the rise of the semiconductor industry, due to the necessity for high quality thin films.[80, 81] Since then, it has become an integral process in microprocessor production, where much research has been conducted into film

uniformity and deposition parameters including gas concentration, temperature, and the deposition environment.[80] This gives CVD grown 2D materials the advantage of industry compatibility and facilitates process integration, without the need for excessive capital investment to incorporate 2D materials into the next generation of electronic and optoelectronic devices.[17, 38] Conventional CVD does face several challenges, including the production yield being limited by the size of the furnace, requirements for hazardous precursors, and toxic by-products. Additionally, the energy intensive high temperatures limit the choice of substrate, with the transfer process required to remove the grown material from the foil having the potential to introduce defects to the nanosheets.[82]

2.3 Exfoliation in Liquids

While the previously mentioned methods for 2D nanosheet production have their merits, the work presented in this thesis focuses on solution processed nanosheets. Solution based approaches to exfoliation have enabled the scalable production of nanosheets from bulk layered crystal precursors. These methods also have the added advantage of being able to leverage techniques for working with liquids, including but not limited to centrifugation, spray coating, chemistry in solutions, and spectroscopic techniques for liquid samples.

Exfoliation approaches in liquid can include Hummer's method to produce graphene oxide,[83] and MXene synthesis with solution based chemical etching of MAX phase.[84] However, for this thesis, the two liquid-based exfoliation techniques of specific interest are ultrasonication and electrochemical exfoliation.

2.3.1 Liquid Phase Exfoliation (LPE)

Liquid phase exfoliation (LPE) of 2D nanosheets was first reported on in 2008 by the Coleman group,[5] only four years after the initial report of mechanical exfoliation of graphene.[4] The advantages of this technique include its scalability and applicability to a wide variety of layered crystals.[85] LPE mechanically delaminates nanosheets from a bulk

layered crystal, suspended in a stabilising liquid,[5] the nature of which will be discussed in more detail in later sections. This delamination occurs using ultrasonic or shear energy to overcome the vdW forces between the layers.[86, 87] This technique has been used to exfoliate a broad range of layered crystals, including graphite,[5] h-BN,[88] TMDs,[89] black phosphorous,[90] MoO_3,[91] and SnP_3.[8] More recently, work has been carried out to produce nanosheets from non-layered, non-vdW bonded materials using liquid phase exfoliation.[92]

Ultrasonication

Paul Langevin initially developed the piezoelectric quartz transducer which produced ultrasonic waves to detect submarines in 1917.[93] However, ultrasonication was later commercialised in civilian applications for surface cleaning 1950s, before the mechanism of cavitation cleaning was fully understood.[94] To exfoliate using ultrasonication, a transducer converts mechanical oscillations into ultrasonic waves in a liquid.[86] These ultrasonic waves drive exfoliation of layered crystals in a liquid medium by vibrational energy and cavitation,[89] as shown in Figure 2.4A.

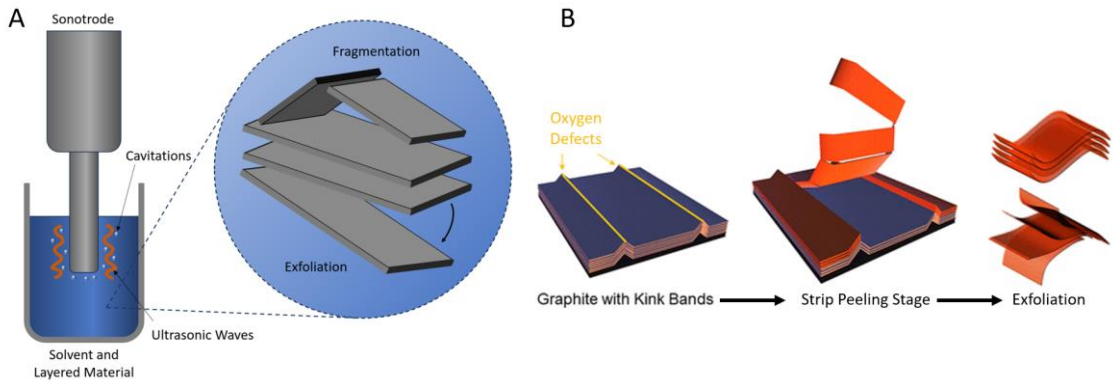

Figure 2.4: Ultrasonic Exfoliation. A) Schematic of an LPE setup, with sonic energy applied to a dispersion of layered material and solvent from a sonotrode. Inset shows nanosheet fragmentation and exfoliation. B) Schematic of the three stages of ultrasonic exfoliation, kink band formation, peeling, and exfoliation. Adapted from Li et al.[95]

Through *in situ* monitoring of the fragmentation and exfoliation of graphite flakes, Li *et al*. outline the three mechanistic stages in the ultrasonication process.[95] They are as follows: firstly, the rupturing of large flakes and the formation of kink bands, secondly, the peeling of thin graphite strips between kink bands, and finally, the exfoliation and fragmentation of thin graphite strips, producing few layer graphene nanosheets. These steps are shown in Figure 2.4B.

In the initial stage, the large flakes are rapidly broken into smaller flakes through existing defects, while the surface of the crystal also shows the formation of kink band ridges, in particular along the zig-zag orientation.[95] These ridges, visible with an optical microscope, are attributed to the increase in temperature[96] and local in-plane compression[97] as bubbles collapse during cavitation.[74] Additionally, the transfer of waves to the liquid-solid interface induces elliptical surface acoustic wave oscillations of atoms near to the surface of the crystal,[98] contributing to ridge formation.

In the second stage, peeling is observed between these reactive kink bands. Notably, the cracks propagate mostly along the zig-zag direction. This is due to kink bands along these directions having an increased likelihood of inducing stacking faults.[99] As the graphite strips are peeled from the parent crystal, trenches of roughly 400 nm are left behind, with steps observed on the edges.[95] It is worth noting that zigzag kink bands are also more chemically reactive[99] than the basal plane, and oxygen species are observed to be chemically bonded at these sites.[95] This suggests potential sonochemical processes[100] along with the purely mechanical processes.[5]

In the final stage of the ultrasonic exfoliation process, both exfoliation and fragmentation of the nanosheets occurs. When there are fewer than 30 layers, kink band formation likelihood is decreased,[99] hence fragmentation of the sheets through an edge tearing

mechanism dominates.[101] Simultaneously, the exfoliation primarily occurs by interlayer sliding and solvent intercalation.[5]

From experimental measurements of the size and thickness of LPE nanosheets, it was found that the nanosheet aspect ratio was approximately constant for all nanosheets in the dispersion, for a range of materials and solvents.[102] Following these observations, it was found that the size-thickness relationship in ultrasonicated nanosheets is essentially fixed and dependent on the anisotropy of the in-plane and out-of-plane bonding strength of the crystal,[103] and the surface energy ratio of the edge plane and basal plane of the material.[102] It was further observed that this exfoliation occurs without functionalising or introducing basal plane defects to the nanosheets.[104]

Through this process, a challenge arises from the resulting polydispersity of nanosheet sizes. Nanosheets exfoliated in NMP using a sonic tip range from monolayer to ~50 layer flakes, with nanosheet lengths ranging from ~30 nm to 1,500 nm.[102] Such dispersions typically have lognormal particle size distributions.[105] This also limits the yield of typically desirable monolayer graphene sheets. LPE offers a cheap and scalable method to produce large quantities of polydisperse nanosheets, which can be used to mechanically reinforce polymers.[106]

2.3.2 Electrochemical Exfoliation (EE)

Electrochemical exfoliation (EE) is an exfoliation method based on the intercalation of a guest species between the layers in a vdW crystal. This method has risen to prominence in the field of solution processed 2D materials predominantly because of its impact on printed electronics. The technique also offers a practical route to overcome the near-constant aspect ratio limitations of LPE dispersions, while also producing thinner and larger nanosheets with significantly higher aspect ratios.

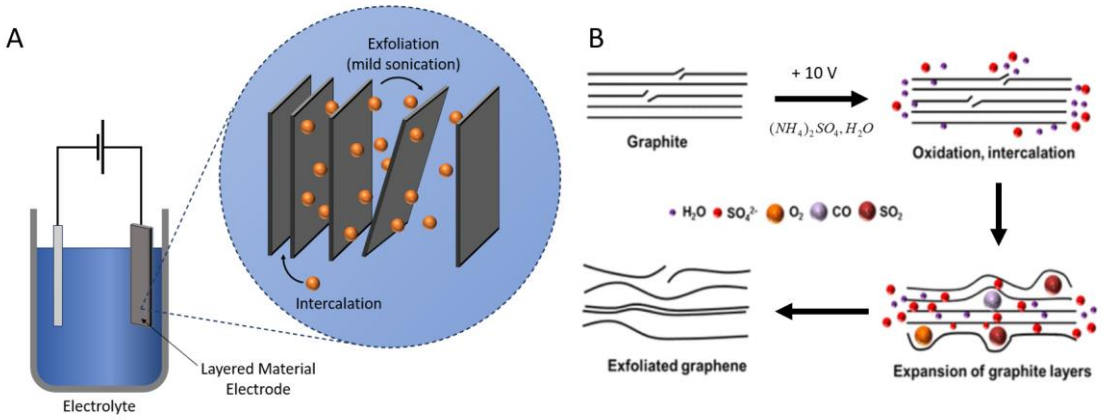

Figure 2.5: Electrochemical Exfoliation. A) Schematic of an electrochemical exfoliation cell setup, with inset of the intercalation into the sheets and nanosheet exfoliation. B) Illustration of the steps involved in electrochemically exfoliating graphene nanosheets using SO_4^{2-} intercalation. Adapted from Parvez et al.[107]

This process occurs in two steps, as illustrated in Figure 2.5A. Firstly, the intercalation of the ions or molecules into the bulk crystal and, secondly, the exfoliation of the intercalated material by bath sonication.[56] The intercalation of these particles between the layers expands the gaps between the individual nanosheets, thus reducing the strength of the vdW attraction between the layers.[108] Hence, there is a smaller energy barrier to overcome to separate the sheets in the exfoliation step and the nanosheets delaminate as larger and thinner nanosheets.[107]

An early report of ion intercalation and sonication assisted exfoliation of single-layer MoS_2 dates back to 1986, where Lithium ions were intercalated into crystals by soaking in hexane and n-butyllithium. The expanded crystals were subsequently ultrasonicated in water, producing what was reported as a 'monolayer'.[65] Unfortunately, secondary processes can occur with Li^+ ions intercalated in the crystal which can induce structural transformations from the desired 2H phase to the 1T phase.[109]

This technique and the associated processes can be broad and varied, as researchers try to enhance flake lateral size, reduce thickness, and minimise basal plane damage, functionalisation, and structural reorganisation. This has been the subject of many review articles.[108, 110] It has been found that some intercalating species, such as bulky, organic molecules, avoid inducing the structural transformations but will not spontaneously intercalate between the layers.[111] By using a two electrode electrochemical cell with the layered crystal as the working electrode and the intercalant dispersed in the electrolyte solution, the intercalant species can be driven between the layers through the application of a potential between the crystal and the counter electrode.[108] This work focuses on SO_4^{2-} anion and organic alkylammonium cation intercalant species, which encompass anodic and cathodic intercalation respectively.[111]

SO_4^{2-} Anion Intercalation

The SO_4^{2-} anion has been used extensively in the electrochemical exfoliation of graphite to graphene,[107, 112-117] with inorganic salts including ammonium, sodium, and potassium sulfate used as a source of ions in the aqueous electrolyte. SO_4^{2-} is preferred as it has an increased exfoliation efficiency compared to other aqueous anion salt solutions.[107] Typically, a potential of +10 V is applied across the cell to drive the SO_4^{2-} between the graphitic layers, as shown in Figure 2.5B.

$$LM + xSO_4^{2-} \rightarrow (SO_4)_x LM + xe^-$$

The mechanism is theorised to proceed through the formation of oxygen and hydroxyl radicals by oxidation in the electrochemical cell. These open the edges and grain boundaries of the graphite crystal by oxidative cleavage,[118] promoting ion intercalation, but these can also induce defects in the nanosheets. Once intercalated, the reduction of SO_4^{2-} ion and water self-oxidation within the crystal produce SO_2 and O_2 gas, which

expands the interlayer spacing.[107, 119] This expanded crystal is then gently sonicated, in an ultrasonic bath, to produce a nanosheet dispersion.[111]

Organic Alkylammonium Cation Intercalation

As previously mentioned, Li^+ ions have been used as intercalant species for exfoliating layered materials. This process of gas formation and hydration, along with charge injection from lithium intercalation, can damage 2D nanosheets, in particular TMD semiconductors, where the semiconducting to metallic transition occurs. Lin *et al*. devised an intercalation strategy using organic alkylammonium cations which did not destroy the semiconducting behaviour in the exfoliation process.[120]

In cathodic exfoliation a negative bias is applied across the cell to drive the alkylammonium ions (R_4N^+) into the layered crystal. The intercalation proceeds as follows.[111]

$$LM + xR_4N^+ + xe^- \rightarrow (R_4N)_x LM$$

As these organic molecular species are larger than elemental ions, they can expand the layered crystal to a greater extent, reducing the interlayer vdW forces even further.[121] Using alkylammonium ions also reduces the damage in the nanosheets and prevents phase transition.[120, 121]

The mechanistic reasons behind the reduction in damage lie in the dimension of the ions and the reactions occurring when exfoliating the expanded crystals. Firstly, the long organic chains help to expand the nanosheets and have dimensions almost an order of magnitude greater than the Li^+ ions, yet these larger ions carry an equivalent charge. Hence, the electron injection ratio from the ions is decreased below the phase transition threshold of 0.29 e^- per formula unit for MoS_2.[122] Secondly, the exfoliation process of the intercalated layered crystal also does not evolve gases and is purely based on solvent diffusion between the layers of the crystal, which results in less damage to the

nanosheets.[121, 123] Both of these electrochemical processes will leave ions in solution, and so washing steps can be necessary to remove any residual ions which may be undesirable in device applications of the nanosheet inks.[124]

2.4 Solvent Stabilisation

In solution processed nanosheet dispersions, choice of solvent is key to producing stable nanosheet dispersions. When nanosheets are in a liquid dispersion, there are two situations which can occur; either the nanosheets are energetically drawn towards the other nanosheets in the dispersion or towards the solvent molecules in the dispersion.[125] These two cases are known as aggregation and solvent stabilisation of the nanosheet dispersion, respectively.

In understanding this process energetically, solubility theory can be used. This is despite the fact that nanosheet dispersions are not strictly solutions, but instead colloidal dispersions. The first step is to understand the mixing of the nanosheets with the solvent molecules at constant temperature and pressure, using the Gibbs free energy of mixing, ΔG_{mix}.[126]

$$\Delta G_{mix} = \Delta H_{mix} - T\Delta S_{mix} \qquad \text{(Eq. 2.1)}$$

In this equation ΔH_{mix} is the enthalpy of mixing, T is the temperature, and ΔS_{mix} is the entropy of mixing. For the mixing process to occur spontaneously, the condition that $\Delta G_{mix} \leq 0$ must be achieved to avoid spontaneous aggregation. As nanosheets are large in comparison to the stabilising solvents, entropy of mixing is assumed to be small, relative to the enthalpy of mixing.[127] In most cases, the stability of nanosheet dispersions is optimised through understanding and minimising the enthalpy of mixing.[89, 104]

For solvent-solute interactions, the enthalpy of mixing per unit volume can be written as follows, where V_{mix} is the volume, ϕ is the solvent volume fraction, k is Boltzmann's

constant, v_0 is the molecular volume of the solvent, and χ is the Flory-Huggins parameter.

$$\frac{\Delta H_{mix}}{V_{mix}} = \chi\phi(1-\phi)kT / v_0 \qquad \text{(Eq. 2.2)}$$

As ΔH_{mix} needs to be minimised, it is simple to show that the Flory-Huggins parameter for the system must be minimised. This parameter encompasses the energetics of the particle-particle, solvent-solvent, and particle-solvent interactions.[125]

$$\chi_{AB} = -\frac{z}{2}\frac{(2\varepsilon_{AB} - \varepsilon_{AA} - \varepsilon_{BB})}{kT} \qquad \text{(Eq. 2.3)}$$

In this equation, z represents the coordination number, ε denotes the pairwise interaction, and the solute and solvent are represented by A and B respectively. From this equation it can be seen that the interaction parameter will be positive if ε_{AA} or ε_{BB} are dominant, leading to aggregation. As a result, the solute-solvent interaction must dominate for stable dispersions, keeping χ_{AB} negative.

The Flory-Huggins interaction parameter can also be approximated from the Hildebrand solubility parameters. These Hildebrand solubility parameters, $\delta_{i,T}$, are calculated as follows: $\delta_{i,T} = \sqrt{E_{T,C}/V}$.[128] Here $E_{T,C}$ is the total cohesive energy density, measured using the heat of vaporisation.[129] This parameter gives a numerical value, which can assist in predicting solubility.[130]

$$\chi \approx \frac{v_0}{kT}(\delta_{A,T} - \delta_{B,T})^2 \qquad \text{(Eq. 2.4)}$$

This model worked well as an initial approximation to predict solubility; however, it was not reliable for polar solvents.[128] As a result, Hansen separated the cohesive energy density into dispersive, D, polar, P, and hydrogen bonding, H, interactions, from which the Hansen components can be extracted.[131]

$$E_{C,T} = E_{C,D} + E_{C,P} + E_{C,H} \rightleftharpoons \delta_T^2 = \delta_D^2 + \delta_P^2 + \delta_H^2 \quad \text{(Eq. 2.5)}$$

Finally, rewriting the Flory-Huggins parameter in terms of all three interactions, a model for predicting solubility in colloidal dispersions has been reached, as shown by Eq. 2.6.[132] This suggests that each of the three parameters must be approximately matched to minimise the difference between the surface energy of the nanosheets and the solvent, yielding a stable dispersion.

$$\chi \approx \frac{v_0}{kT}\left[(\delta_{D,A} - \delta_{D,B})^2 + \frac{(\delta_{P,A} - \delta_{P,B})^2}{4} + \frac{(\delta_{H,A} - \delta_{H,B})^2}{4}\right] \quad \text{(Eq. 2.6)}$$

This model was verified for nanosheet dispersions by Coleman *et al.,* and in the case of LPE graphene the Hansen parameters have been estimated to be $\delta_{D,graphene} \approx 18$ MPa$^{1/2}$, $\delta_{P,graphene} \approx 10$ MPa$^{1/2}$, and $\delta_{H,graphene} \approx 7$ MPa$^{1/2}$.[104]

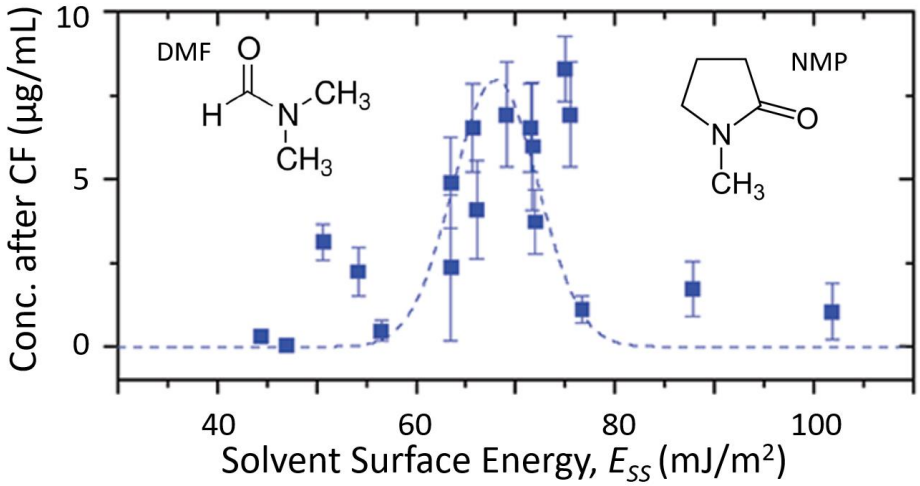

Figure 2.6: Solvent Stability. Plot of dispersed graphene concentration vs. solvent surface energy for LPE graphene exfoliations post centrifugation. Inset molecular diagrams of DMF and NMP molecules. Adapted from Coleman.[104]

Based on extensive studies to identify the optimal solvents for exfoliating graphene and other 2D nanosheets across a range of solvent surface energies (Figure 2.6), n-methyl-2-pyrrolidone (NMP) and dimethylformamide (DMF) proved to yield the most desirable

nanosheet dispersions, with good stability post exfoliation.[5, 86, 89, 104] However, a brief look at the safety data sheets for these materials highlights the toxicity of these solvents.[133, 134] As a result, investigations are underway to find safer solvents for exfoliation, including dihydrolevoglucosenone (Cyrene™).[135]

2.5 Size Selection

As previously mentioned, the liquid dispersion from the exfoliation consists of flakes with polydisperse lengths and thicknesses, as shown in Figure 2.7A. It is possible to separate these flakes into size bands using centrifugation methods, which is particularly useful in nanosheet networks where size has been shown to play an important role in certain applications. Specific examples include monolayer enriched MoS_2 inks required for photoluminescence,[136] smaller nanosheets for catalytic applications,[9] and large nanosheets for mechanically reinforcing polymer composites.[106] There are two primary methods used to separate bulk dispersions into several fractions based on the nanosheet sizes. These involve separation based on buoyancy and sedimentation rate.

2.5.1 Density Gradient Ultracentrifugation (DGU)

Density gradient ultracentrifugation (DGU) makes use of the differences in buoyant density of nanosheets in a dispersion to separate them by size. By using a density graded medium, where the density of the medium increases further down in the centrifuge tube, the nanosheets in dispersion will sediment near their isopycnic (equal density) point.[111] As nanosheets are typically denser than the liquid medium, they are coated with surfactant molecules to reduce the net density, which also allows for nanosheets to be sorted by thickness.[137] DGU was initially used in biochemistry to separate subcellular components,[138] however Hersam *et al*. used this technique to separate aqueous polydisperse CNT dispersions by nanotube diameter[139] and to sort graphene nanosheets according to their thickness.[140] Unfortunately, this technique is limited by low yields,

complicated procedures to prevent the extraction of the wrong nanosheet fraction, and the risk of contamination from the density graded medium and the adsorbed surfactant molecules. These contaminants and adsorbed species have negative effects on electronic devices prepared using the nanosheet inks.[141]

2.5.2 Liquid Cascade Centrifugation (LCC)

In a sedimentation-based separation process, such as liquid cascade centrifugation (LCC), the particles in a suspension are separated according to their sedimentation rate in a medium with uniform density. In such a medium, this sedimentation rate, s, was described by Svedberg,[142] using Equation 2.7. The sedimentation coefficient is the ratio of the particle velocity to acceleration and can be thought of as the time taken for a nanomaterial to sediment. In this equation, m is the particle mass, ρ is the solvent density, V is the volume of 1 gram of material in the suspension, and f is the frictional coefficient.[57] As a result, it is simple to see that the sedimentation rate is dependent on the nanosheet mass along with the drag forces it experiences in suspension.

$$s = \frac{m(1-\rho V)}{f} \qquad \text{(Eq. 2.7)}$$

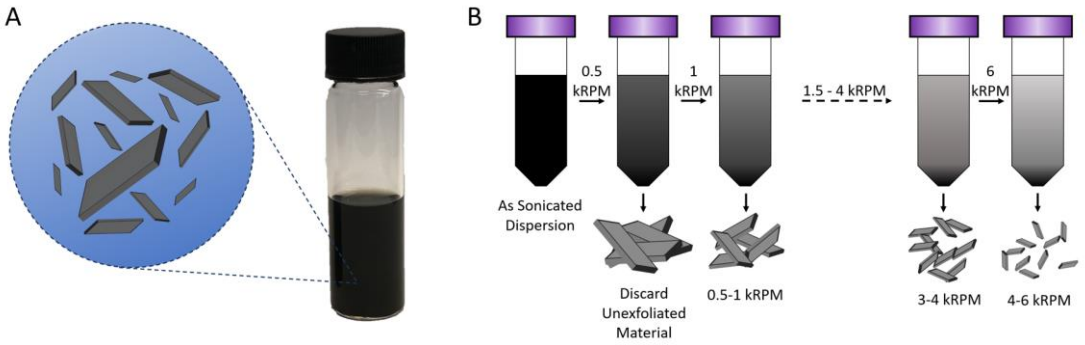

Figure 2.7. Liquid Cascade Centrifugation. A) Photograph of ink, with schematic showing the polydisperse nature of the nanosheet sizes within the as-exfoliated dispersion. B) Schematic showing the LCC process, where fractions containing successively smaller nanosheets are sedimented from the nanosheet dispersion.

During centrifugation, the higher mass large nanosheets sediment more quickly, leaving the smaller, thinner nanosheets in suspension. In a method similar to gas-separation centrifugation cascades, the suspended material can be separated from the sedimented material and centrifuged again. Through repeated centrifugations, the larger flakes are progressively removed, leaving smaller and thinner nanosheets in the dispersion.[136]

The steps involved in LCC are represented in Figure 2.7B. Here, the as-sonicated dispersion is centrifuged at a relatively low speed to sediment the largest, thickest nanosheets and some of the unexfoliated starting material. The supernatant is removed without resuspending any of the sedimented material. The supernatant is then centrifuged at a higher speed, to sediment the largest nanosheets remaining in the suspension.[136] The supernatant is again removed from the vial and transferred on to another centrifugation cycle at higher speed, while the sediment left behind now contains nanosheets which have been selected between two centrifugation speeds. This process is repeated at progressively increasing centrifugation speeds to extract a series of nanosheet sediments, which are successively smaller and thinner. The sediments can be resuspended in a variety of solvents, suitable for printing as inks, with only mild sonication required to resuspend the nanosheets.[143]

Using this LCC solution processing technique, Backes *et al*. successfully enriched the monolayer volume fraction in a LPE WS_2 dispersion from <10% to 75%.[136] This was achieved by removing the larger, thicker flakes, leaving a majority of monolayer sheets in suspension. Such a size selection technique is invaluable when working with TMDs, due to their layer-dependent optoelectronic properties.[58] Additionally, it enables studies where it is desirable to have narrower nanosheet size distributions, such as studies on the effect of nanosheet thickness.[144-147]

The power of this technique is its accessibility and simplicity, in particular when compared to DGU. However, monolayers tend to be very small and, depending on trapping speeds used, the distribution can be broad. Additionally, for applications where large monolayers are desirable, LCC of LPE material will not provide suitable monolayers as the aspect ratio of nanosheets in LPE dispersions is roughly constant across all nanosheet sizes.

"A scientist looking at non-scientific problems is just as dumb as the next guy."

Richard Feynman

Chapter 3
Film Deposition and Characterisation

3.1 Nanosheet Film Deposition

Since the first reports of liquid dispersions of exfoliated nanosheets, many researchers have sought to prepare high quality films of nanosheets to take advantage of the nanomaterial properties and form-factor benefits. These nanomaterial dispersions, coupled with printing technologies, including inkjet[148, 149] and aerosol jet printing,[150, 151] have led to the development of the field of 2D material inks.[56, 57, 111, 152-154]

In lab based studies, it was found that spray coating was an effective technique for prototyping printed devices[155] without the strict ink preparation requirements of inkjet and aerosol jet printing. However, these techniques have struggled to fabricate highly aligned nanosheet films[6] and, as a result, techniques such as spin coating[120, 156] and nanosheet self-assembly at interfaces[157, 158] have been investigated.

3.1.1 Spray Coating

Spray coating is a printing technique which has found application in a variety of industries from industrial manufacturing to artistic painting. This is largely attributed to the relative simplicity and scalability of this technique. The key step towards controlled

liquid atomisation using compressed gas and a needle regulator, as shown in Figure 3.1A, was taken by Frank E. Stanley in 1876.[159] This technique grew in popularity for over a century from his original use in retouching photographs to current applications in large scale surface coating.[160]

In 2004, the first report of the spray coating technique being used to deposit CNTs on a substrate was published.[161] Since this report, the scientific community have utilised this technique to achieve large area coating, particularly in applications where precise patterning is not required. The technique has now been used to prepare films from various nanomaterials, including CNTs,[162] Ag nanowires,[155] quantum dots,[163] and nanosheets.[164]

A schematic of the spray coating process, which involves taking a liquid ink and depositing it on a substrate, is shown in Figure 3.1B. The key stages are as follows. Ink is loaded into the reservoir, where it is gravity fed into the nozzle. As the trigger action is activated, the needle is retracted, which allows ink to flow and releases the N_2 back pressure through the nozzle.[165] At this stage, small droplets of the ink are sheared off, resulting in an aerosol emerging from the nozzle.[155] The spray plume is projected towards a substrate, which is usually heated to promote droplet evaporation, minimising droplet coalescence on the surface. Large area films can be prepared by mounting the spray gun into a remote gantry and rastering the desired spray area.[166] Film thickness can be controlled by varying the number of spray passes. Films can be patterned onto a substrate, with the use of a shadow mask to define the spray region, with 200 μm features routinely sprayed in laboratory settings.[63]

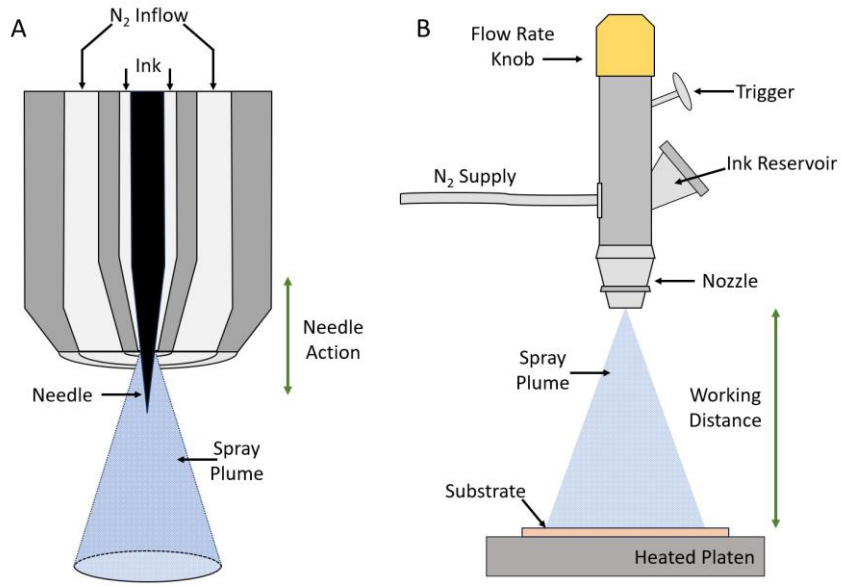

Figure 3.1: Spray Coating. A) Illustration of a spray gun nozzle, showing the ink and N_2 flow, and needle action. B) Schematic of the overall spray gun, depositing ink in the form of spray plume onto a heated substrate.

This technique is also very useful as it is compatible with a wide variety of substrates and solvents. The range of rigid and flexible substrates, which can be prepatterned with deposited electrodes, enables spray printing to thrive in producing films for electrical characterisation, as well as for applications in flexible devices. Typically, nanomaterials can be sprayed directly from suspension, without the need for additives in the ink, which simplifies the ink production and reduces potential contaminants in the final films. Ideally, low boiling point solvents are chosen to speed up the rate of evaporation on the substrate.

Despite the relative simplicity of the spray coating operation, there are still many parameters which can be fine-tuned to optimise film deposition and uniformity. These include the geometrical considerations of spray working distance, the speed at which the gun is rastered across the substrate, the temperature of the substrate, solvent choice, the nozzle diameter, the ink flow rate, and the N_2 back pressure.[155, 167] The working distance

changes the area of the aerosol plume, modulating the mass deposited per unit area. The substrate temperature is critical to promote evaporation of the solvent, while the nozzle size and flow rate determine the droplet density. If the substrate is oversaturated with ink while spraying, the uniformity of the coating can be altered.

However, in their study on the uniformity of spray coated AgNW films, Scardaci *et al*. identified that N_2 back pressure played a crucial role.[155] They found that by increasing the pressure from 15 to 30 PSI, there was a significant increase in the film uniformity. This uniformity was ascribed to the smaller particle sizes created as higher pressures increase the fluid velocity in the nozzle. Additionally, the particle distribution was found to be more homogeneous, with a smaller mean particle size, compared to the broader distribution of large particles aerosolised at lower pressures. The key to uniformity is that the smaller particles evaporate more quickly, reducing the opportunity for particle reaggregation at the surface, which negatively impacts the film uniformity.[155]

This deposition technique is relatively simple and can be used to coat large areas, however it is not a direct write printing technique; hence, for device applications, features must be defined using stencil masks. This can result in wasted material and poses the risk of scratching the film when removing the mask. Smaller features can be directly written using inkjet printing[168] and aerosol jet printing (AJP) techniques. AJP has been able to print traces of silver nanoparticles with widths of 10 μm.[169] However for the studies reported in this thesis, fine printed features were not necessary. Spray printing is also compatible with deposition onto a wide range of flexible substrates,[167, 170, 171] which is a key requirement when studying the piezoresistance of films.

3.1.2 Liquid-Liquid Interfacial Assembly

To control the morphology of nanosheet networks towards high alignment and low porosity (<5%), it is necessary to consider the deposition technique being utilised. As spray coating of LPE nanosheets forms films with poor alignment,[172] to increase basal plane alignment of nanosheets, it was suggested that assembling the nanosheets at a liquid-liquid interface would promote alignment parallel to the substrate at the interface.[173] These assembled films could then be transferred onto a substrate by lifting the substrate through the interface. It is this lifting of the film parallel to the surface that has given rise to the secondary name for this technique, the Langmuir-Schaefer method.[124, 147, 174]

The Langmuir-Schaefer method for film formation maintains a substrate orientation parallel to the interface during film formation, which contrasts with the perpendicular substrate-interface orientation in Langmuir-Blodgett deposition. Langmuir and Schaefer first reported this technique in 1938, when working on the assembly and transfer of protein films.[175] However they assembled their films at a liquid-air interface. For nanoparticle film formation, assembling a film at the interface between two immiscible liquids has proven successful,[176] as it promotes densely tiled nanosheet films with very good alignment and doesn't require specialised equipment.[158] Film assembly at the liquid-liquid interface has been demonstrated for a wide range of nanomaterials, including Au nanoparticles (NPs),[177] CdSe NPs,[178] CNTs,[173], graphene,[179] WSe_2,[180] and MoS_2.[158]

Properties of the Interface

The theory of self-assembling nanoparticle layers at interfaces was introduced by Pieranski in 1980.[181] This concept was merged with the field of Pickering emulsions[182] to confine nanoparticle films at the interface between immiscible liquids. The driving

force towards film assembly at the interface is a reduction in the Helmholtz free energy, based on the interfacial surface tension of the system,[183] as the film forms at the interface. However, the overall change in energy is related to the square of the particle radius.[176, 184] Hence, smaller particles are less well bound to the interface, leading to the observation of the 'liquid like' nature of nanoparticle assemblies at the interface.[185] For rounded disks, similar to nanosheets, the interfacial binding is increased as the particle aspect ratio increases.[186] It has been shown that the energy to remove a 1 μm^2 2D nanosheet from the interface is of the order of 10^7 k_BT.[158] As the interfacial energy is minimised when the liquid-liquid interface coated with nanomaterials is maximised, nanosheets are driven to align,[187] forming tiled layers at the interface.[158]

2D Nanosheet Films

Assembly of aligned films of 2D nanosheets at the liquid-liquid interface was initially reported where the nanosheets were dispersed in one of the immiscible liquids and, using sonication or mechanical shaking of the liquid, the nanosheets were driven to the liquid-liquid interface.[179] More recently, injecting 2D nanosheets directly into the interface between two liquids has been reported.[180, 188]

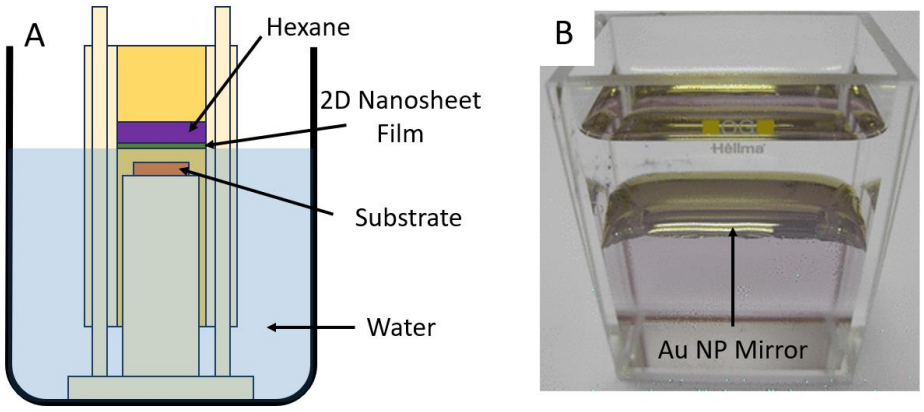

Figure 3.2: Interfacial Assembly. A) Schematic of the liquid-liquid assembly setup used to create aligned films and transfer them onto the desired substrates. B) Gold NP film assembled at a heptane/dichloroethane-water interface, adapted from Fang et al.[189]

In this work, the method used is similar to that reported by Neilson *et al*.[158] and Carey *et al*.[124] where films are assembled by direct injection at the water-hexane liquid-liquid interface, followed by the lifting of the substrate through the interface parallel to the plane of the film. A schematic of the apparatus is shown above in Figure 3.2A, with the water in blue, the substrate in orange, hexane in purple, and the 2D material film at the interface in green. In practice, to raise the substrate through the interface, instead of mechanically moving the substrate, the water is pumped out from below, slowly lowering the interface past the substrate in a controlled process.[147] Key parameters to control film uniformity in this process include ink concentration, volume, choice of solvents, and choice of immiscible liquid to form the interface.

This technique has enabled the preparation of very thin, tiled nano-networks over centimetre scale areas,[158] shown in Figure 3.2B.[189] In order to form thicker films, the film can be dried and passed through another interfacially assembled film.[147] This opens up opportunities for forming pinhole free films of nanosheets[111] with minimal thickness, ideal for dielectric applications,[7] as well as the potential to build hetero-stacks by building up layers of different materials to form devices.[72]

3.2 Spectroscopic Techniques

3.2.1 UV-Visible Spectroscopy

Ultraviolet-visible spectroscopy (UV-Vis) is an optical characterisation technique which studies the absorption of electromagnetic radiation in the ultraviolet (UV) and visible region of the spectrum by materials.[190] Light can also scatter from materials and so the extinction, $\varepsilon(\lambda)$, of a material is defined to be the sum of light absorption, $\alpha(\lambda)$, and scattering, $\sigma(\lambda)$.

$$\varepsilon(\lambda) = \alpha(\lambda) + \sigma(\lambda) \qquad \text{(Eq. 3.1)}$$

This relatively simple non-destructive technique was pioneered as a laboratory analytical technique by Beckman in 1941.[191] However, this technique must acknowledge the work of Wollaston and Fraunhofer, who reported the spectral lines in solar spectra in the early 1800s.[192] The absorbance of light by a material can give information into the electronic structure of a material, owing to the origins of the light absorption processes where the incident light carries enough energy to induce ground to excited state transition. In theory, these transitions occur at discrete energies and should appear as peaks in absorption. However, for colloidal nanosheet dispersions, peak broadening can occur through inter nanosheet interactions, diffusing the peaks into bands. Broadening is also attributed to solute-solvent interactions and scattering.[193]

Spectrophotometer Operation

The operation of a spectrophotometer is relatively simple. It is built from three key components: a light source, a monochromator, and a detector, as shown in Figure 3.3. The sample dispersion is placed in a quartz cuvette, of known path length, transparent in the wavelength range of interest.

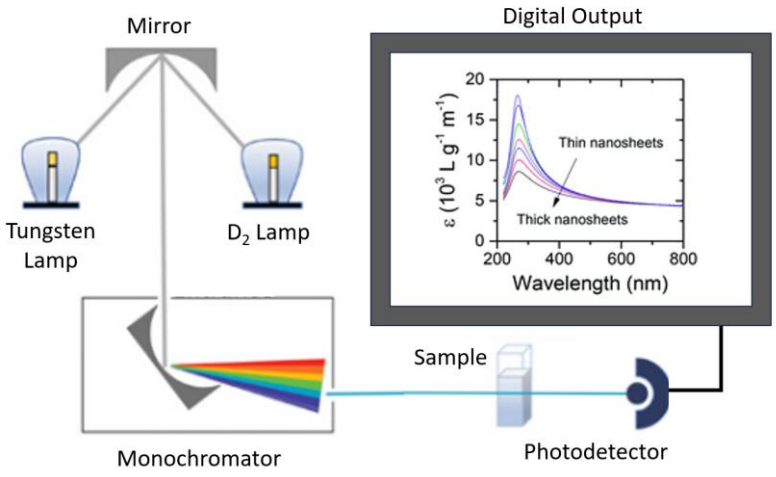

Figure 3.3: UV- Spectrophotometer. Schematic of key components adapted from Rocha et al.[194] Inset spectra of size selected LPE graphene nanosheets reproduced from Backes et al.[195]

The light sources used typically cannot span the full wavelength range of the spectrophotometer, so two sources are used. A deuterium lamp is used as the UV source and a tungsten lamp is used for the visible range wavelengths. The monochromator consists of a diffraction grating, which spreads the beam according to its constituent wavelengths. Using a narrow slit, a small range of wavelengths are chosen and focused into a parallel beam which passes through the sample.[190] Finally, the detector is an InGaAs photodiode, which detects the incident light intensity. By measuring a background intensity, I_0, for a cuvette containing only the solvent used, followed by the sample transmitted intensity, I_T, it is possible to determine the absorbance, A, of the sample, using the Beer-Lambert law, as shown below.

$$A = -\log\left(\frac{I_T}{I_0}\right) = -\log(T) = \varepsilon(\lambda)cl \qquad \text{(Eq. 3.2)}$$

Additionally, from the absorbance, the transmission, T, and the concentration of the dispersion, c, can be determined provided the optical path length of the cuvette, l, and the extinction coefficient, $\varepsilon(\lambda)$, which will depend on the wavelength of light, are known. It can be seen that the absorbance scales linearly with increasing concentration.

UV-Vis of Nanosheets

By measuring the UV-Vis spectra of nanosheet dispersions, it is possible to probe billions of nanosheets, resulting in an ensemble response. This is compared to hundreds of nanosheets which can reasonably be analysed for atomic force microscopy (AFM) or transmission electron microscopy (TEM) characterisations.[87, 196] By taking graphene dispersions of known concentrations, Backes *et al*. developed a spectroscopic metric relating the extinction coefficient to the concentration of the graphene dispersion.[195] For LPE graphene, this was determined to be ε_{750} = 5,450 L.g^{-1}.m^{-1}. A wavelength of 750 nm was chosen, as they noted that some of the spectral features modulated with the nanosheet

length and thickness of the nanosheets in dispersion, but the absorbance at 750 nm was invariant to such effects.

For graphene, the aromatic $\pi \rightarrow \pi^*$ transition, typically found in the wavelength range of 230-330 nm, is the characteristic peak that is most easily observed by UV-Vis.[197] In LPE dispersions, the relative intensity of this peak increases as the nanosheets become smaller and thinner,[195] as shown in the inset of Figure 3.3. For semiconducting materials, there is a significant increase in absorption once the photon energy exceeds the optical bandgap of the material, and peaks are often observed at the excitonic energy levels.[198]

3.2.2 Raman Spectroscopy

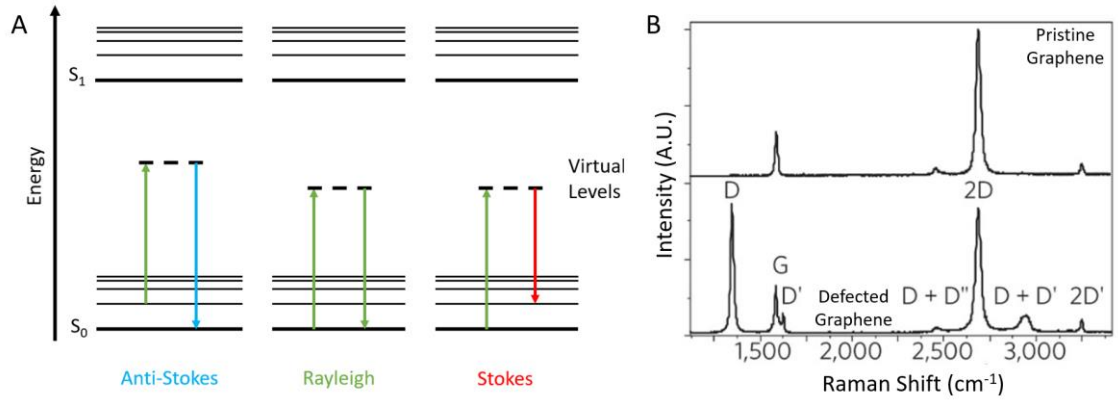

Figure 3.4: Raman Spectroscopy. A) Scattering transitions showing Rayleigh, Stokes and anti-Stokes scattering phenomena., adapted from ref [199]. B) Raman spectra of pristine and defected graphene, with key peaks labelled, adapted from Ferrari et al.[200]

Raman scattering is an optical effect first reported by Sir C.V. Raman in 1928,[201] which enables analysis of the local crystalline order of a material. The phenomenon arises from an inelastic scattering process, where a photon is incident on a sample and is scattered from an optical phonon in the sample, resulting in a change in the photon's energy. This scattering phenomenon is very weak, with the scattered intensity being between 10^{-6} and 10^{-12} of the incident intensity.[202] As a result, this technique benefited greatly from the

development of the laser.[203] However, for 2D nanomaterials, the sample can be damaged if the laser illumination intensity is too extreme.[204]

For a perfectly elastic transition, the incident and scattered photon have the same energy and wavelength. This is known as Rayleigh scattering and is the dominant scattering process due to the wavelength of light being significantly larger than the atoms in the crystal. For a small proportion of the incident photons, the dipole moment induces lattice vibrations. These scattering events are Raman scattered as they will have given or lost energy to the system in the form of an optical phonon. The measured Raman shift is usually cited as a wavenumber, ν, and can be calculated using the following equation, where λ_i is the incident wavelength and λ_s is the scattered wavelength.

$$\nu = \frac{1}{\lambda_i} - \frac{1}{\lambda_s} \qquad \text{(Eq. 3.3)}$$

The change in photon energy when the light scatters is linked to the spacings in the vibrational levels of the crystal,[203] as shown in Figure 3.4A. It can be seen that quantised amounts of energy can be lost from the photon (Stokes) or gained by the photon (anti-Stokes), however the intensity of Stokes scattering is higher as a result of the increased occupation of the ground state before illumination.[203] For a vibrational transition to be Raman active, there must be a change in the polarisability of the material, inducing a temporary dipole as a result of the lattice vibration. If there is no change in polarisability, the vibrational mode is said to be Raman inactive, however these vibrations can be probed using infrared (IR) spectroscopy. Whether a lattice vibration will be Raman or IR active can be determined for solid crystals using the point group symmetry.[205]

In terms of operation, the instrumentation is based on an optical microscope coupled with a laser system, several gratings and mirrors, and a detector. The monochromatic laser beam is focused on the surface of the sample being investigated. The scattered light is

passed through a Rayleigh filter to remove elastically scattered photons and then through a diffraction grating before being detected. As mentioned, care must be taken when choosing the laser power to avoid laser induced sample damage. Ideally, <1 mW should be used for 2D material networks.

The Raman active modes of interest in graphene are the E_{2g} and the A_{1g} vibrational modes, observed in Raman spectra as the G and D peaks, as shown in Figure 3.4B. These are related to the in-plane and out-of-plane vibrations respectively.[200] As the D peak mode requires a defect for activation,[206] the defectiveness of the basal plane of the nanosheet has been linked to relative intensity of the D and G Raman peaks.[200] In TMD materials, the characteristic peaks can be used to analyse the phase of the material, as they change significantly between 2H and 1T structures due to changes in local crystalline structure. Of interest in the 2H phase of MoS_2 are the signature A_{1g} and the E^1_{2g} vibrational modes.[207]

3.3 Microscopic Techniques

3.3.1 Electron Microscopy

Conventional visible wavelength light microscopes have resolving powers which are at best limited by the diffraction of the light waves. Shorter wavelength beams can be used to image with higher resolution.[208] As electrons can be considered to act as waves, with a wavelength dependent on the applied accelerating potential, an increase in momentum decreases the wavelength, following the de Broglie equation, Eq. 3.5. This enables the generation of nanometre scale electron beams, which probe the sample.

$$\lambda = h / p \qquad \text{(Eq. 3.5)}$$

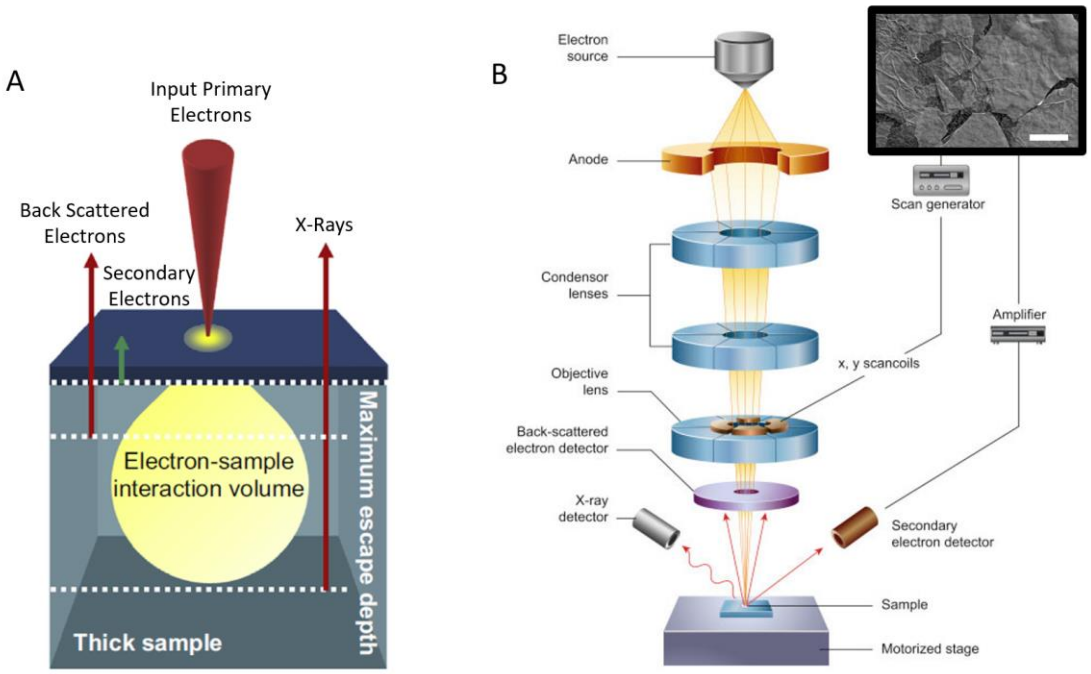

Figure 3.5: Scanning Electron Microscopy. A) Interaction volume of the primary electron beam showing signals emitted from the surface of the sample, adapted from Inkson.[208] B) Schematic of an electron microscope, adapted from Inkson.[208] Scale bar on SEM image of $PtSe_2$ nanosheet network measures 2 µm.

Scanning Electron Microscopy (SEM)

First reported in 1942,[209] SEM has lower resolution than transmission electron microscopy, which was initially a disadvantage. That was until the power of this technique in characterising surfaces and their morphology was realised. Using an electron beam to probe a sample has the benefit of increased material-beam interactions due to the negative charge on the electron interacting strongly with matter, within the sample-interaction volume shown in Figure 3.5A. The size of this volume is dictated by the material and the accelerating voltage. This results in three main signals returning from the sample: the back scattered electrons, secondary electrons (which are generated within the material), and X-rays.[210] Each of these can be independently interpreted to give different information on the sample.

The SEM operates under a vacuum and uses electromagnetic lenses and apertures to focus an accelerating beam of electrons from an electron source (usually a field emission tungsten tip) into a probe with a diameter of several nanometres. This probe beam is rastered across the sample using xy-scan coils and the signal at each point is recorded and output as a surface image, as shown in Figure 3.5B.[208] As previously mentioned, different signals come out of the sample, which are collected using a variety of detectors.

The back scattered electrons are reflected back along the original path and are useful for differentiating materials by atomic number. The X-rays are emitted in every direction from the sample surface, and so X-ray spectrometers located inside the chamber can count rays of different energies using energy dispersive X-ray (EDX) analysis.[211]

Secondary electrons are lower energy particles generated within the samples. When imaging using relatively low accelerating potentials (<5 kV), only electrons generated within the top ~20 nm can escape the sample.[208] These are useful for this work when looking at the surface topography, as there is enhanced surface emission of secondary electrons from slopes and edges. The secondary electrons are detected using an Everhart-Thornley detector mounted to one side of the vacuum chamber. This detector attracts electrons using an electrically biased grid, before hitting a scintillator, with the signal amplified using a photomultiplier tube.[212]

Focused Ion Beam SEM (FIB-SEM) Nanotomography

For further morphological characterisation of the material, in particular internal microscopic structure including porosity, alignment, and pore size and shape, a focused ion beam (FIB) of gallium ions can be used to mill away material exposing the internal structure, within the SEM chamber. Through careful selection of milling speed and potential, issues such as curtaining and redeposition (pore filling in) can be minimised. Using a SEM, the newly exposed internal structure gives a 2D cross sectional

representation of the interior structure of the material. In 2D nanosheet based materials this has been successfully used to study alignment and porosity.[124, 213]

However, to fully understand the internal microstructure of a material, a 3D representation is significantly more useful to study pore networks and connectivity and tortuosity of conductive material pathways. In 2024, Gabbett & Doolan *et al*. reported a technique where successive slices were milled from the exposed cross section, imaging the newly exposed cross section using SEM between slices. A platinum capping pad reduces milling inhomogeneity. This generated an image stack of 100's of slices through the material, with a spacing of 15 nm between successive cross sections. Using advanced image analysis techniques and machine learning, the image stack was segmented into material and pore components, and 3D reconstructions of the material and pore network were generated.[146] In this form, computational analysis of the 3D structure provides more in-depth morphological understanding of a nanomaterial-based film.

3.3.2 Optical Profilometry

Optical profilometry is a non-contact 3D surface topography measurement technique based on the interference of light waves.[214] Tactile contact surface topography measurement techniques such as stylus profilometry and atomic force microscopy are well established, however these are limited by measurement speed and can damage the specimen being tested[215, 216] (Figure 3.6C&D). It has also been shown that 3D surface analysis has more reliability and less parameter variance compared to 2D line scans.[217]

Interferometric techniques utilise the phenomenon of interference fringe generation. This occurs when light from a common source is separated, usually using a beam splitter, and travels along two separate optical paths which recombine prior to detection. Depending on the difference in path length, the light waves can constructively or destructively interfere, leading to bright and dark fringes.[218]

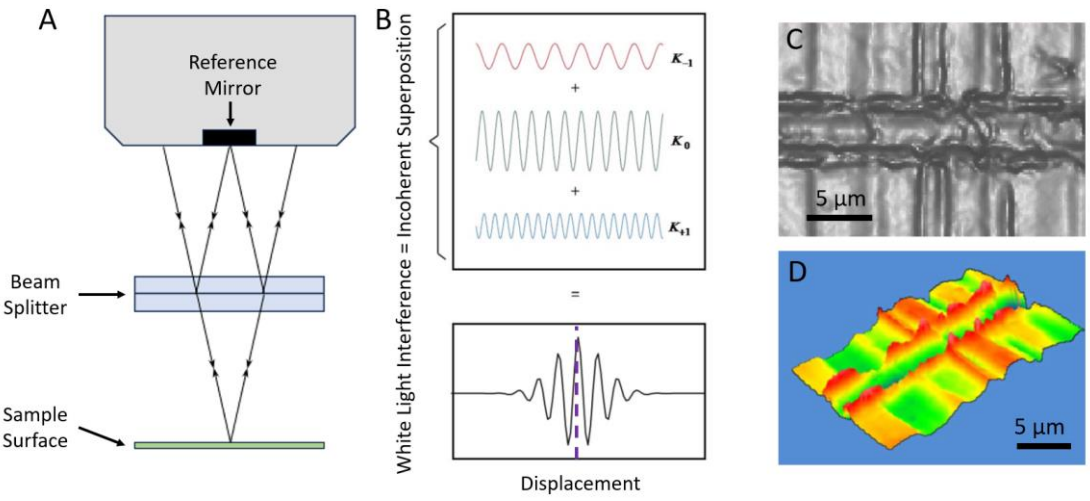

Figure 3.6: Optical Profilometry. A) Schematic of a Mirau objective lens. B) Diagram of WLI correlogram for each pixel, and how it can be broken into distinct interference patterns by wavelength. Adapted from de Groot.[219] *C) Trench left by a stylus profilometer, imaged using a microscope and a 3D surface reconstruction of the scratch. Adapted from de Groot.*[216]

Georges Sagnac proposed using a sample's surface as one reflector to incorporate the surface topography information into the wavefront, which then interferes with the reference beam in a Michelson geometry, in 1911.[220] André Mirau developed a new, more compact configuration for interferometry in 1949.[221] This configuration placed the reference surface mirror within the objective, on the optical axis, as shown in Figure3.6A. This is now most common objective lens design for measuring high magnification interferometry.

White Light Interferometry (WLI)

WLI, as the name suggests, illuminates the sample with a white light source which has a short coherence length, passed through a Mirau objective lens, with the reconstructed image detected by a charge coupled device (CCD) detector. The broad range of wavelengths leads to the interference term being appreciable over a small range of depths and facilitates the identification of the point of greatest contrast in the fringes, which is

located at the point of perfect focus,[219] as shown in Figure 3.6B. In practice, the sample is slightly tilted in order to have the interference fringes travel across the sample as it is moved relative to the objective lens along the z-axis, using a piezo crystal. By identifying the z-value of perfect focus for each pixel as the sample is moved, a 3D representation of the surface can be generated.[214] Points which have the same z-displacement of perfect focus sit at the same height in the output 3D representation.[218] Using computer software, the scan can be levelled as desired.

Phase Shift Interferometry (PSI)

PSI operates in a similar manner to WLI, with a few key differences. Firstly, the light source used has a much narrower wavelength range, approaching the monochromatic limit. This is achieved by placing an optical filter in the light path. This expands the envelope of the interference fringes imaged by the system when scanning in the z-axis. Secondly, PSI requires much flatter surfaces due to the challenges with identifying step heights approaching the wavelength of the incident light.[218] PSI has the advantage of increased precision for samples with smaller step height features. Finally, a phase shift is induced in the reference beam and the interference pattern is imaged across the scan range.

For PSI, the reference beam is phase shifted in known increments, typically $\Delta\psi = \pi / 2$. Sampling rates of at least two images per phase cycle are required to meet the Nyquist requirement, and so the mirror motion is of the order of tenths of microns between images.[216] This is achieved by moving a reference mirror using a piezoelectric actuator. A range of algorithms have been generated to convert the phase shifted intensities at each pixel into the phase from which the surface height can be determined.[222]

The random noise is typically on the order of 0.34 nm for PSI scans, however there are challenges in stitching the heights together, as the algorithm always returns phase values

within a range of 2π. Hence, unwrapping algorithms are required to remove the spikes or false edge discontinuities in the height profiles.[222] This is why PSI is limited in application for films which have large step heights. WLI is limited in precision of thickness measurement, however, the method does have an advantage compared to PSI as it is able to accurately generate surface scans of speckled surfaces,[216] typical of films of nanosheets, while PSI is suitable for thin films of highly aligned nanosheets.

3.4 Electrical Characterisation

In measuring the electrical resistance of a specimen, it is necessary to go back to basics, recalling Ohm's Law which states that the ratio of voltage to current in a component in an electrical circuit at constant temperature is a constant, known as the resistance, $R = V / I$. Hence, the potential to drive a fixed current or vice-versa is typically measured to extract the resistance of a sample.[223] The two primary configurations, two-probe and four-probe, used to complete these measurements are outlined below. Additionally, in electrical measurements it is important to specify if the measurement is for a direct current (DC) or alternating current (AC) system, particularly because the impedance (AC form of resistance) can vary at different modulation frequencies.[224] This is the premise of impedance spectroscopy.

3.4.1 Two-Probe Configuration

When measuring the DC electrical resistance of a sample, the two-probe configuration is the simplest setup. In this case, the length of the channel is given simply by the distance between the electrodes, and the resistance is determined from the ratio of the voltage across to current through the sample. However, as the electrodes and the contacts between the electrodes are in series with the specimen, they can contribute to the electrical resistance measured.[225]

3.4.2 *Four-Probe Configuration*

In this configuration, a constant current is driven through the sample using the two outer 'source' electrodes. Simultaneously the potential drop between the two middle 'sense' electrodes is measured. The resistance is then calculated from the applied current and the change in voltage. As the voltage is measured with practically no current due to the high impedance of the voltmeter across the middle electrodes,[225] the contribution of contact resistance is removed from the measurement. The channel length, L_{Ch}, is given by distance between sense electrodes, as shown in Figure 3.7.

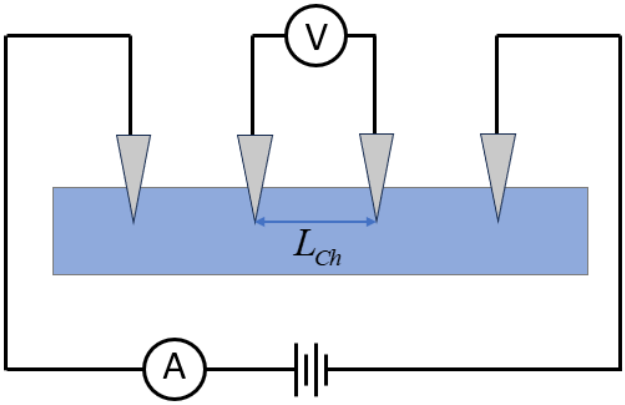

Figure 3.7: Four-Probe Testing. Schematic of a four-probe test setup, with a high impedance voltmeter connected between the inner two 'sense' electrodes and power supply running a constant current, measured by an ammeter, in series through the outer 'source' electrodes.

From these measurements the conductivity, σ_{Net}, and resistivity, ρ_{Net}, of the network can be determined, as written in Equation 3.6. Here, channel width is expressed as W_{Ch} and network thickness is t_{Net}.

$$\sigma_{Net} = \frac{1}{\rho_{Net}} = \frac{1}{R}\frac{1}{t_{Net}}\frac{L_{Ch}}{W_{Ch}} \qquad \text{(Eq. 3.6)}$$

3.4.3 *Impedance Spectroscopy*

The previous electrical techniques utilise DC sources to probe the electronic properties of the materials. However, under the application of AC inputs, materials can have different responses depending on the frequency of the input signal. Using these phenomena, it is possible to model materials using equivalent circuits, where the components in these circuits correspond to physical elements and phenomena in the material.[147, 224]

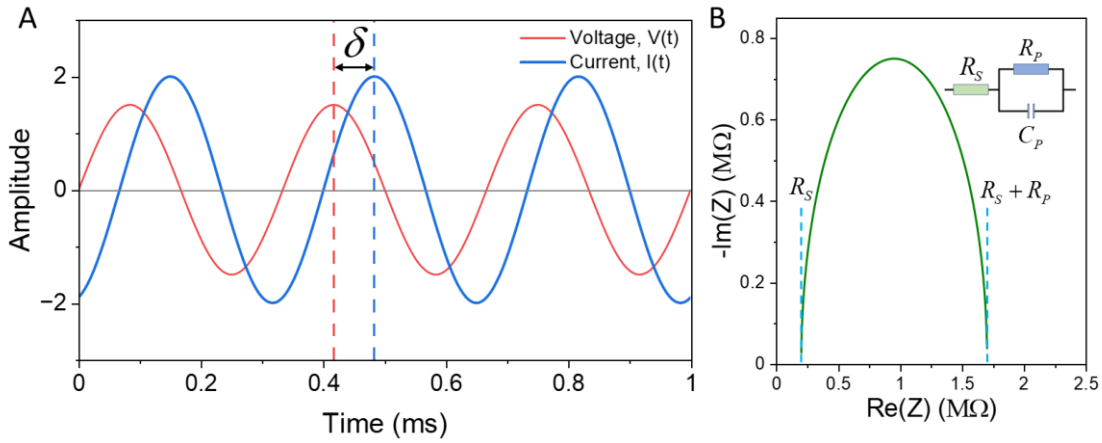

Figure 3.8: Impedance Spectroscopy. A) Plot of oscillating voltage input (red) and measured current response (blue), with a phase shift (δ). B) Nyquist plot for a simple Randles circuit (inset), showing the two intercepts of the semicircle at R_S *and* $R_S + R_P$ *on the* $\mathrm{Re}(Z)$ *axis.*

In practice, impedance spectroscopy applies a sinusoidal AC potential across the device and measures the current response to the alternating potential, as shown in Figure 3.8A.[226, 227] This measurement is repeated for different frequencies of input potential, typically ranging over several orders of magnitude of frequency. The phase shift and magnitude of the current response can be converted to real and imaginary impedance to extract information about the system. The mathematical basis for this is outlined below.

The voltage input can be written as follows, $V(\omega) = \mathrm{Re}(V_0 e^{i\omega t})$, with V_0 representing the voltage amplitude, ω representing the angular frequency, and t representing the time. The measured current output has the following functional form, $I(\omega) = \mathrm{Re}(I_0 e^{i(\omega t - \delta)})$, with current amplitude I_0 and phase shift δ, with respect to the voltage input. Using Ohm's law, the impedance, Z, which is a complex quantity, can be extracted as follows.

$$Z = \frac{V}{I} = \frac{V_0}{I_0} e^{i\delta}, |Z| = \frac{V_0}{I_0} \quad \text{(Eq. 3.7)}$$

Using de Moivre's theorem to divide the impedance into real and imaginary components:

$$Z = \mathrm{Re}(Z) + i\,\mathrm{Im}(Z) = |Z|\cos(\delta) + i|Z|\sin(\delta) \quad \text{(Eq. 3.8)}$$

The real and imaginary impedance can be plotted as a function of angular frequency to give the Bode plot. Plotting Re(Z) vs -Im(Z) is known as the Nyquist plot (Figure 3.8B). These plots can be interpreted by fitting mathematical models derived from the responses of hypothetical circuit models. Of particular interest is a modified Randles equivalent circuit, shown in Figure 3.8B inset. The representation of elements of a nanosheet network by circuit components will be discussed in Chapter 4.

3.5 Tensile Testing

As previously mentioned, materials have driven many advances in human history, with the ability to produce stronger, lighter, and more complex materials proving advantageous to the civilisations with access to such technologies. During the industrial revolution, Tredgold and Fairbairn developed methods of controlling the applied forces for testing materials using hydraulic and screw driven machines.[228] In 1882, Johannsen invented the universal testing machine capable of conducting compression, tensile, and bending tests on materials. This standardisation across the field helped with optimising of material properties and comparing novel materials to existing materials.[229]

In material mechanical characterisation, the applied force per unit cross sectional area (stress, σ) and the fractional length change (strain, ε) are important parameters to measure.[223] A tensile tester measures the stress applied to a material to induce a given strain. In this way, the Young's modulus can be extracted as the slope of the stress vs. strain plot in the linear region, where the intercept is zero,[223, 229] as shown in Figure 3.9. The tensile tester can simultaneously measure the distance between the clamps and the force applied on the load cell, and can be driven to specific stress or strain values, as well as conducting cyclic mechanical testing of materials.

The critical component of the tester is the load cell, a highly sensitive gauge which is calibrated to measure internal strain of the cell, and relate it to an applied force value. This usually operates using strain gauges in a Wheatstone bridge configuration. Mechanical deformation leads to extension or compression of the strain gauges in the load cell, which changes the voltage output of the Wheatstone bridge in a manner which is proportional to the deformation.[230]

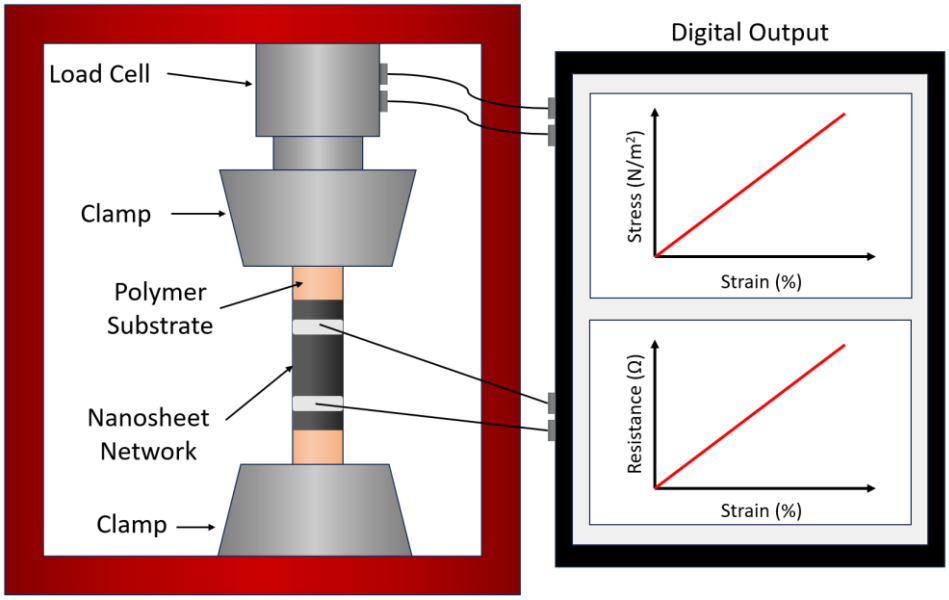

Figure 3.9: Tensile Testing. Schematic of a tensile tester, with simultaneous electrical measurements for electromechanical testing of materials.

When changing the displacement of the clamps, to vary the crosshead displacement, the input from the load cell can be input into a proportional-integral-derivative (PID) system to maintain a constant force application.[229] For the work in this thesis, all samples were position controlled rather than force controlled.

Additional components can be integrated into tensile testing setups to enhance their characterisation capabilities. These include humidity and thermal chambers, video cameras to observe the sample at the point of failure, and electrical probe stations to investigate piezoresistive responses. To measure piezoresistor devices, the sample is mounted in the clamps of the tensile tester, while the two-probe resistance of the sample is simultaneously measured.[166] This enables the measurement of a specimen's electrical resistance as a function of applied strain.

"If I have seen further, it is by standing on the shoulders of Giants."

Issac Newton

Chapter 4

Networks, Percolation, and Piezoresistance

4.1 Nanosheet Networks

When nanosheet ink dispersions are deposited onto substrates, the resulting film is composed of billions of individual nanosheets, each of which has the potential to be in contact with several neighbouring nanosheets.[6] By building up the film, the sheets form pathways across the span of the film. This building up phenomena can be mathematically modelled by percolation theory which will be discussed later in this chapter.

Some could argue that nanosheet networks are an intrinsic part of everyday life. They are one of the first things discovered by children when they go to school, in drawing lines with their graphite pencils (being generous with the definition of a nanosheet). This visible mark is simply a drawing or a letter to a young student but, with careful study, the physics of nanosheet networks can open a range of avenues in electronics, sensing, and catalysis.[231]

4.1.1 Directly Written Nano-Networks

Taking a lead from these networks fabricated in the classroom, several teams have taken the approach of drawing networks of layered crystal platelets using graphite pencils and

by rubbing TMD powders.[232-234] These films, typically drawn onto paper, have shown potential applications as humidity,[235] strain,[236, 237] and temperature sensors.[238, 239] These networks exploit the rough, porous surface of the paper substrate to exfoliate the crystal, breaking the weak vdW bonds through abrasion of the crystal against the substrate surface. However, in this thesis, the primary focus is on nanosheet networks fabricated from dispersions of nanosheets.

4.1.2 Composites

One of the earlier suggested routes to fabricate a system of connected pathways of nanosheets across a device was in nanocomposite materials. Nanocomposites had gained significant traction with CNTs, in terms of exploiting the properties of nanomaterials for applications, in particular enhancing conductivity and mechanical properties of polymer systems.[240] In nanocomposites, the nanosheets are dispersed in a polymeric matrix through processes such as solution blending[241] and melt processing.[242] The properties of the nanosheet network vary with the volume fraction of nanosheets in the composite. For these composite networks, the polymer can induce mechanical and electrical hysteresis as the material is strained and can dope the nanosheets. Lower conductivities are expected for composites, compared with polymer-free networks, as a result of the polymer layer coating the nanosheets.[243] With regard to network morphology, in nanocomposites, nanosheets can be distributed throughout the network, with random orientation or with specific alignment. Additionally, it is possible that phase segregation can occur in nanocomposites leading to areas of high and low loading of nanosheets.[166, 244] Polymer-free films can still behave like composites with pores acting as an insulating matrix, allowing for some models initially presented for composite materials to be utilised more generally.

4.1.3 Early Networks

Initial approaches to producing networks of nanosheets from exfoliated dispersions involved many tried and tested solution processing techniques, including vacuum filtration,[5] drop casting,[245] and spin coating.[246] These methods were effective in preparing films of nanosheets that are referred to as networks.[6] It was possible to analyse morphological properties including alignment and network porosity with these networks.[172] They were also suitable for testing network properties including electrical conductivity,[5] piezoresistance,[247] film transparency,[248] gas sensitivity,[90] and catalytic activity.[9]

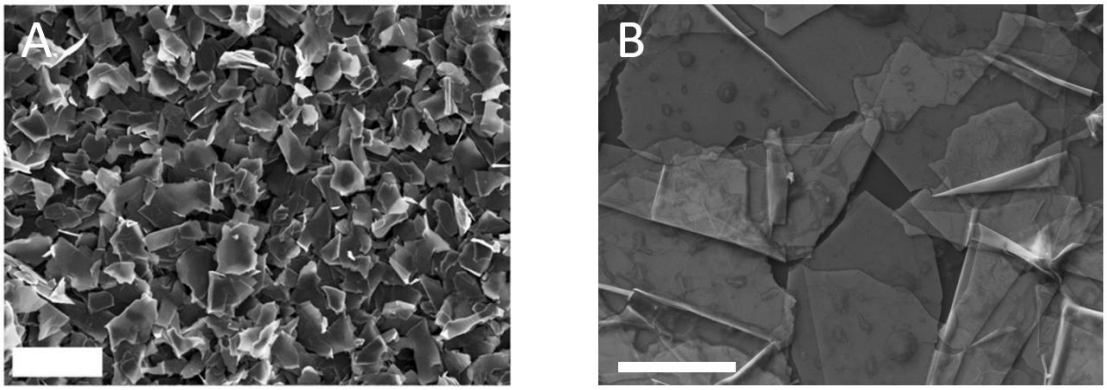

Figure 4.1: Network Imaging. A) SEM image of the top surface of a spray coated LPE graphene network. Adapted from Gabbett & Doolan et al.[146] B) SEM image of the top surface of a liquid-liquid interface assembled EE MoS_2 network. Adapted from Carey et al.[124] Scale bar in both images measures 2 µm.

Network conductivity effects could be observed through changing the nanosheet dimensions,[6] changing the network thickness[249] (for very thin films), and through post processing steps to lower porosity and increase alignment such as calendaring[172] and photonic annealing.[250] However, these relatively simple network production techniques faced challenges including scalability, film uniformity, material loss, inability to define

patterns for the nanosheet network, and difficulties in transferring the films onto arbitrary substrates.

4.1.4 Printed Networks

As a result of these challenges, printing techniques rose in prominence for producing devices from 2D nanosheet dispersions or so called 'inks,' as introduced in Chapter 3. These printing techniques include spray coating, inkjet printing, and aerosol jet printing to produce networks of nanosheets. Unfortunately, these deposition techniques tend to yield disordered nanosheet networks with poor alignment and considerable porosity, particularly for LPE nanosheet inks,[146] as observed in Figure 4.1A. They do however enable the production of large scale, patterned networks, with a wide range of potential substrates. These substrates range from rigid Si/SiO_2 chips to flexible polymers,[251, 252] textiles,[253, 254] and even biological substrates including skin and leaves with transfer processes.[255] The substrate choice can also affect the network properties,[171] offering an alternative tuning option. Additionally, droplet size, ink rheology, pressure, and substrate temperature can play a part as discussed for spray coating.[155] This can be a challenge in optimising network properties, but also offers potential routes to modulate nanosheet networks, potentially unlocking interesting physical phenomena. This has proven pivotal in producing devices including capacitors,[7] diodes,[256] and transistors[63] from 2D nanosheet inks.

4.1.5 Self-Assembled Networks

More recently it was found that highly aligned nanosheet networks with large conformal overlapping nanosheets yielded enhanced electrical performance, in particular enhanced mobility.[257] One of the best synthetic routes to produce such networks from nanosheet dispersions is using self-assembly of nanosheets at an interface and transferring the network onto a substrate.[124, 147, 158] These networks have exceptionally low porosity and

are highly aligned, and conformal inter-flake contact can be observed using SEM,[124] as in Figure 4.1B.

4.1.6 What is a Network?

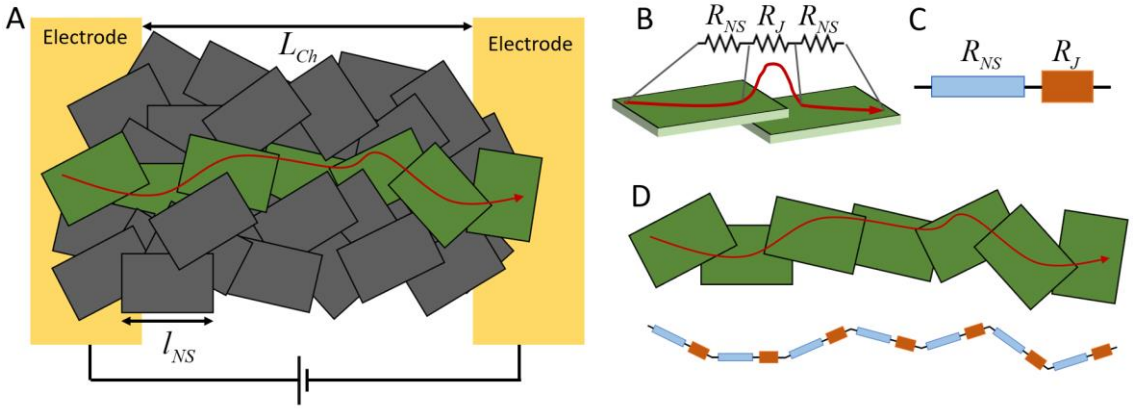

Figure 4.2: Nanosheet Networks. A) Schematic of a nanosheet network between two electrodes, showing the conductive pathway in green. B) Schematic of two nanosheets in contact showing the nanosheet resistance and junction resistance component of the pathway. C) A nanosheet junction pair, represented as a pair of resistors in series. D) Schematic of the conductive pathway, which can be represented as a chain of pairs of resistors, with each pair having a nanosheet resistance and a junction resistance contribution.

Having introduced the concept of nanosheet networks, it is necessary to strictly define the key components. For a network of millions or even billions of nanosheets deposited on a substrate with electrodes at either end of the device (Figure 4.2A), one can imagine an electron's journey through the network. This starts off at the electrode and moves across a junction to a conductive nanosheet. Despite being conductive, this nanosheet will still have some intrinsic nanosheet resistance, R_{NS}.[6] Travelling across the nanosheet, it eventually must migrate beyond the confines of the initial sheet and onto the next by moving across a junction between neighbouring conductive sheets (Figure 4.2B&C). This junction will have an associated junction resistance, R_J, and a junction capacitance, C_J.

The mechanisms of charge transport across the junction will be discussed in a later section. Repeating this process of crossing pairs of nanosheets and junctions thousands of times, eventually the electron finds its way through the network to the second electrode.[147] A visualisation of this is shown in Figure 4.2D.

Network Resistivity Model

Based on this charge carrier's journey, conduction through a nanosheet network can be understood from a theoretical perspective. This model was initially derived for semiconducting or conducting materials,[6, 147] however, when the number of charge carriers, n_{NS}, is large, simplifications can be made. This yields the expression for network resistivity, ρ_{Net}, shown in Equation 4.1.

$$\rho_{Net} \approx \frac{\left[\rho_{NS} + 2t_{NS}R_J\right]}{(1-P_{Net})} \qquad \text{(Eq. 4.1)}$$

In this equation, the newly introduced parameters are nanosheet resistivity, ρ_{NS}, nanosheet thickness, t_{NS}, and network porosity, P_{Net}. For simplicity, only the main steps of the derivation are provided here, however the complete derivation is presented in Appendix A.1.

A key concept to reiterate is that each time a charge carrier passes across a nanosheet, it must also travel through a junction. By finding the number of these nanosheet-junction pairs required to cross the network and estimating the voltage drop across the junction and the nanosheet, as well as the time taken to cross each of them, an expression for the time to cross the network can be written. However, this total time taken can also be written in terms of the mobility of the network, μ_{Net}. From this, Equation 4.2 is found.

$$\mu_{Net} \approx \frac{\mu_{NS}}{\left[1+\frac{R_J}{R_{NS}}\right]\left[1+\frac{2}{n_{NS}l_{NS}A_{NS}}\right]} \qquad \text{(Eq. 4.2)}$$

In this equation, the newly introduced parameters are nanosheet mobility, μ_{NS}, nanosheet length, l_{NS}, and nanosheet cross sectional area, A_{NS}, which is defined as $A_{NS} = l_{NS} t_{NS}$.

It is possible to convert network mobility to network resistivity for 2D nanosheet networks using the following expression, $\rho_{Net}^{-1} = (1 - P_{Net}) n_{NS} e \mu_{Net}$, where e is the charge on an electron. For 2D nanosheets, $R_{NS} = \rho_{NS} / (2t_{NS})$, as the path of the charge carrier in the nanosheet is assumed to be half the length of a nanosheet. By substitution of Eq. 4.2 into these expressions, the network resistivity of a nanosheet network can be modelled by Equation 4.3.

$$\rho_{Net} \approx \frac{\left[\rho_{NS} + 2t_{NS} R_J\right]}{(1 - P_{Net})} \left[1 + \frac{2}{n_{NS} t_{NS} l_{NS}^2}\right] \qquad \text{(Eq. 4.3)}$$

In the limit of high n_{NS}, the model can be further simplified, as the second square bracket term will limit to 1. This model assumes a single conductive pathway; however, the same dependences are observed by considering multiple conductive pathways.

From this model it can be seen that nanosheet dimensions play a significant role in network resistivity. Nanosheet length and thickness have been observed to have impacts on nanosheet network based device performance,[258, 259] including for graphene thermoelectric generators[144] and WS_2 transistors.[145] This model can also be used to extract information about nanosheets and junctions from impedance spectra of nanosheet networks, by fitting impedance spectra, such as the Nyquist plot of a MoS_2 network[147] (Figure 4.3A), with a simple circuit. This circuit is made from a resistor representing the nanosheet resistance, in series with a resistor and a constant phase element which are in parallel with each other. These parallel elements represent the junction resistance and capacitance respectively.[147] This will be outlined in Chapter 8. The constant phase

element is used to account for the distribution of junction types and the range of junction capacitances in the network deviating from ideality.[147]

4.1.7 What is a Junction?

Inter nanosheet junctions can take on a variety of forms. Typically, these junctions are narrow vdW gaps between nanosheets in the network, across which charge must travel.[6] Piatti *et al.* carried out a study of inkjet-printed nanosheet networks, and reported that the charge transport processes in graphene and MoS_2 networks are largely attributed to hopping.[260] However, a wide variety of hopping mechanisms have been found, which can vary between materials and based on the measurement temperature.[260-262] In many networks, across a range of nanomaterial dimensions, it has been shown that the key network element limiting the electrical performance is the inter-nanosheet junctions.[6, 124, 147, 263-265] As these junctions act to limit performance, they can hinder networks from achieving the superlative conductivity and mobility values of the constituent nanoparticles. Hence several strategies have been considered to minimise these junctions, including deposition technique and post processing strategies.[6, 266-268]

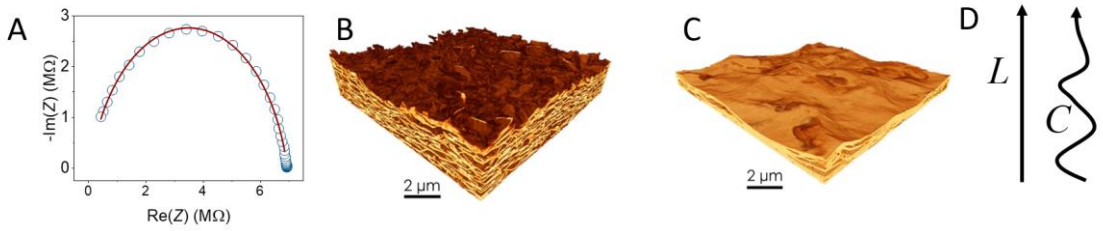

Figure 4.3: Nanosheet Network Junctions and Morphology. A) Plot of the real component of network impedance vs. the negative of the imaginary component of the network impedance for a MoS_2 nanosheet network. Adapted from Gabbett & Kelly et al.[147] 3D reconstructions of B) LPE and C) EE nanosheet networks using FIB-SEM nanotomography. Adapted from Gabbett & Doolan et al.[146] D) Illustration of a straight path length and tortuous path length.

When thinking about these junctions, it is also important to consider the network morphology. In particular, the alignment,[172] porosity,[144] network tortuosity,[269] and nanosheet overlap areas are important parameters which can modulate the network conductivity. When different aspect ratios of nanosheets are used, the alignment and overlap area of the nanosheets changes.[146] For thicker, more rigid nanosheets, a less aligned, jammed network is formed, with point-like contacts observed between the nanosheets (Figure 4.3B). However, large, conformal overlap area junctions are observed for larger, thinner nanosheets which are more flexible and tend to align in the plane of the substrate, this effect can be visualised in Figure 4.3C. Many current approaches are seeking to minimise the inter-nanosheet junction resistances, however there may also be instances where the junction resistance could be useful for device applications. The tortuosity factor, κ, is defined as $\kappa = (C/L)^2$, where L is the linear path and C is the length of the tortuous curved path,[146] as illustrated in Figure 4.3D. For a straight path this will limit towards unity.

4.1.8 Mechanical Deformation of Networks

Mechanical deformation of networks is a relevant consideration in nanosheet networks, with researchers calendaring networks to increase conductivity[270] and straining networks to elicit a piezoresistive response.[271] However the fluid-like nature of these nanosheet networks, with viscosities similar to pitch, results in challenges in studying the mechanics of such systems.[213] Sinnott *et al*. have proposed a method to probe nanosheet network mechanics using a layered compression test.[272] However, they observe interesting anisotropic responses and discover lock-in phenomena as the network is compressed.[273] Of particular interest in such systems is the Poisson ratio, ν, which describes the change in the sample dimension perpendicular to the axis of applied strain. The following equation describes the Poisson ratio for isotropic materials.[274]

$$\nu = -\frac{\varepsilon_{\perp}}{\varepsilon_{\parallel}} \qquad \text{(Eq. 4.4)}$$

In conventional materials the Poisson ratio can take a range of values, with cork having a value close to zero[275] and polyimide reported as 0.39,[276] while natural rubber has ν = 0.50.[277] However, this range has been expanded to include materials with negative Poisson ratios,[278] known as auxetic materials.[279] In nanomaterial networks, the Poisson ratio has been reported to be relatively low, with several reports in the range from -0.1 to 0.1.[280-282] It is theorised that for networks of nanosheets with good alignment, and the potential for sliding motion of the sheets, the Poisson ratio could approach zero.[283-286]

4.1.9 Applications of Nanosheet Networks

As mentioned throughout this section, nanosheet networks have been used in a wide variety of applications, enabling advances in printed electronics, catalysts, and beyond. Most of these device properties are based on thick films which exhibit bulk-like properties; however, these intrinsic properties can deviate with extrinsic behaviour for thicknesses or, in composites, volume fractions below a certain threshold.[287] This is known as percolation, and it can be useful in tuning network properties over orders of magnitude.

4.2 Percolation Theory

Percolation is a mathematical concept which describes scaling, critical phenomena,[288] and geometric features in disordered media. The physical origins can be traced back to the work of Flory and Stockmayer in the 1940s, in studying gelation in polymeric systems.[289] However, the mathematical basis of percolation theory originated in 1957, with the work of Broadbent and Hammersley.[290] It finds many applications in modelling physical phenomena, particularly in disordered or fractal structures. Examples include modelling forest fires,[291] oil fields,[292] and diffusion in disordered media.[293] As a student

who began the PhD journey in 2020, during the COVID-19 pandemic, it was fascinating to see that percolation theory also found a use in modelling the spread of disease in a population.[294]

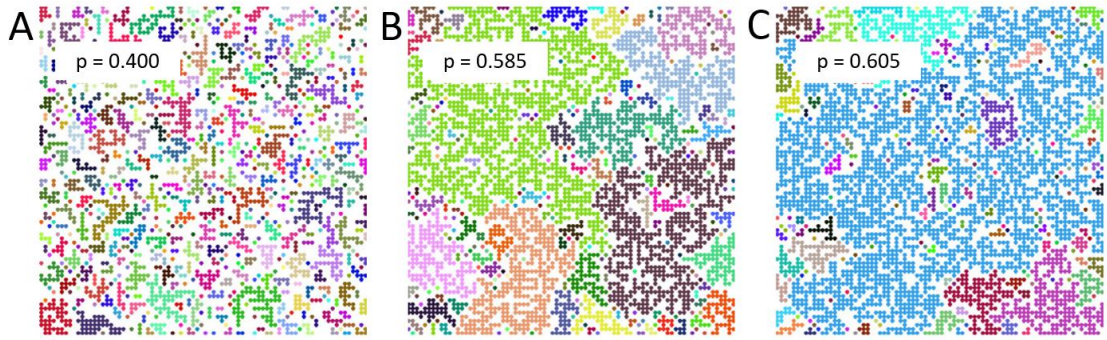

Figure 4.4: Classical Percolation Theory. Site percolation on a square lattice, showing connected clusters each uniquely coloured at different site occupation probabilities. A) P = 0.400. B) P = 0.585. C) P = 0.605. This illustrates the rapid growth from many clusters to one dominant cluster over a small range of occupation probabilities, adapted from Li et al.[288]

4.2.1 Classical Resistor Model

The original use of percolation in conduction utilised resistor models on square lattices which were sufficiently large such as to neglect boundary conditions. In setting up these models, two pathways were developed: the first utilises site occupation to prepare conductive nodes, while the other bond percolation model is set up with bonds between the sites.[295] By changing the probability of site or bond occupation, interesting phenomena were observed, including the growth of connected clusters on the lattice.[296] Once the occupation of conductive sites or conductive bonds reached a threshold value, the cluster formed an infinite cluster with high probability,[290] as visualised in Figure 4.4. From these percolative models, it was possible to derive a mathematical expression for the physical properties. These included a model of the electrical conductivity, σ, across

a network, as a function of the site occupation or volume fraction of conductive elements, ϕ,[297] as presented below.

$$\sigma = \sigma_c(\phi - \phi_c)^n \quad \text{(Eq. 4.5)}$$

Here, the percolation exponent has been theorised to depend only on the dimensionality of the system, with n_{2D} = 4/3 and n_{3D} = 2,[298, 299] however additional dependences have been theorised.[300] It has been reported that the exponent, n, describing such power law scaling as a function of the distance from the critical threshold value, ϕ_c, is identical for site and bond percolation models.[297, 301] This model effectively describes the near-exponential growth in conductivity of such systems above the percolation threshold.

4.2.2 Applications in Nanocomposites

Large portions of the theory are mathematical, focusing on cluster size, dimension and even time dependent phenomena.[288, 297] However, when the scaling theory was applied to nanomaterial networks, the majority of the focus turned to the percolation scaling of conductivity in polymer nanocomposites.[302] This is likely due to the clear and obvious parallels between such a system and a random conductor network in an insulating medium. As the loading of conductive filler particles in a less conductive matrix increases, it is expected that the overall conductivity will increase. However, this occurs in a very sudden transition from insulating to conductive behaviour, owing to the formation of fully connected conductive pathways between the electrodes.[303]

4.2.3 Polymer-Free Networks

In this work, as the focus is on polymer-free networks, percolation is studied with respect to film thickness instead of volume fraction. Percolation phenomena have been observed in electrical data for thin films of polymer-free nanomaterials by several research groups.[248, 304-306] These films typically display a region of sharply increasing conductivity

from a non-conductive state as the film thickness increases, up to a transition point, above which the conductivity saturates,[249, 307] as shown in in Figure 4.5A. Physically, this transition can be thought of in three stages, which occur as the film thickness is increased.

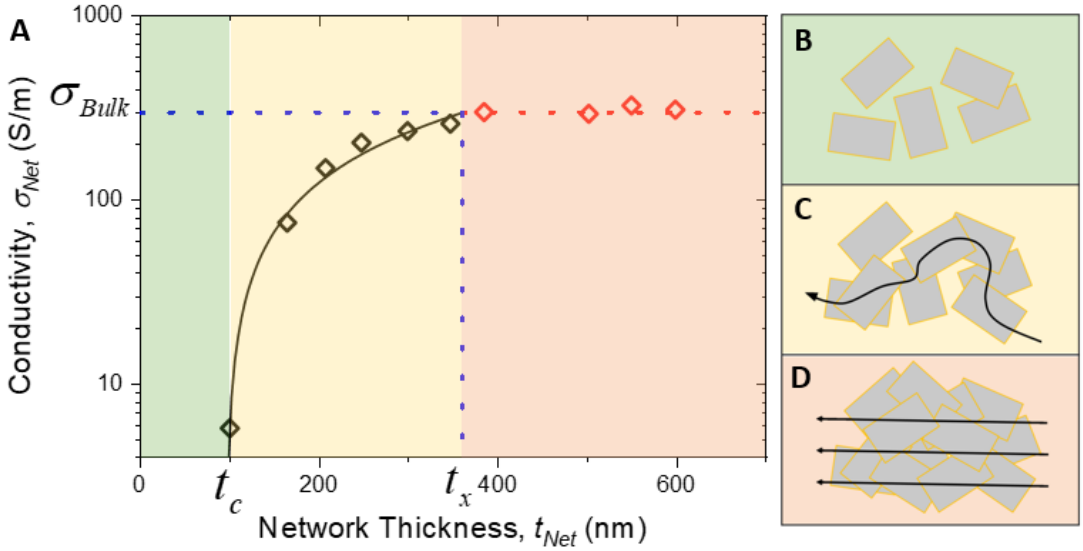

Figure 4.5: Conductivity Percolation in Nanosheet Networks. A) Plot of conductivity vs. network thickness for a spray coated graphene nanosheet network, data from Kelly et al.[307] B) Illustration of a nanosheet network below the percolation threshold. C) Illustration of a nanosheet network in the percolation regime, with an arrow indicating the conductive pathway. D) Illustration of a nanosheet network in the bulk-like regime.

Firstly, when the film thickness is below the percolation threshold (t_c) as shown in Figure 4.5B, the nanosheets form discrete island cluster structures and the early stages of connected pathways. However, there is no long-range connectivity or conductivity in the discontinuous film.[249]

That is up until the second stage where, at the percolation threshold, the first conductive pathway across the length of the film is formed, allowing current to flow. A schematic representation of such a film is shown in Figure 4.5C, with an arrow indicating the tortuous pathway through which the conductive path traverses. As the thickness is further

increased within the percolating region, an increasing number of conductive pathways are formed as gaps in the film are filled in.[307] This results in a super-linear increase in the conductivity of the film in the second stage.

The conductivity increases with the growing number of pathways (Figure 4.5D), until a plateau occurs as the film thickness reaches the bulk-like transition thickness, t_x.[149] Above this thickness, the conductivity is once again an intrinsic property of the material, invariant on thickness.[307] The changes occurring at t_c and t_x are known as critical phenomena, while the mathematical model can be referred to as the percolation scaling theory.[297]

When analysing conductivity as a function of thickness in the percolation regime, a simple model was initially proposed which is based on the model for polymer composites shown above. This model has been modified to allow for film thickness scaling by replacing the volume fraction with film thickness.[149]

$$\sigma = \sigma_A (t - t_c)^n \qquad \text{(Eq. 4.6)}$$

This model works well to describe the percolation conductivity in a nanosheet network, however the σ_A coefficient has no physical meaning. A modified version of this equation has been proposed, for which each parameter has a physical meaning (defined above), as illustrated in Figure 4.5A.[172, 308, 309]

$$\sigma \approx \sigma_B \left(\frac{t - t_c}{t - t_x} \right)^n \qquad \text{(Eq. 4.7)}$$

This enables understanding of the conductivity changes in the percolation regime. Note that there are many challenges in accurately measuring network thickness for nanosheet networks, and as a result not every literature report details the conductivity-thickness behaviour in a manner suitable to extract these parameters. However, several studies report these properties for films of nanomaterials in the percolation regime and a

summary of these is tabulated below. Due to the increased likelihood of sample to sample variability in the electrical data in the percolation regime,[170] fitting the percolation behaviour to extract the percolation exponent can be challenging with some groups not reporting on each of the tabulated parameters.

Table 4.1: Thickness percolation in nanomaterial films.

Author	**Material**	**Deposition**	t_c **(nm)**	t_x **(nm)**	n	σ_B **(S/m)**	**Ref**
Kelly *et al.*	LPE Graphene	AJP	101	360	0.84	300	[307]
Finn *et al*.	Ag NW	Inkjet	255	500	1.1	3×10^4	[168]
De *et al*.	Ag Flakes	Vacuum Filtration	N/A	~1,500	N/A	2.6×10^5	[248]
Müller *et al*.	Au NP	Vacuum Filtration	190	~700	N/A	123	[305]
Scardaci *et al*.	Single Wall CNT	Spray Coating	1.3	~25	0.62	1.7×10^5	[310]
De *et al*.	LPE Graphene	Vacuum Filtration	<5	~20	N/A	1.5×10^4	[247]
De Falco *et al*.	Soot NPs	In-Flame Deposition	<30	~150	N/A	1×10^{-3}	[311]
Ogilvie *et al*.	LPE Graphene	Drop Casting from Emulsion	1,000	2,000	N/A	3,000	[304]
Torrisi *et al*.	LPE Graphene	Inkjet	3	~20	4	100	[149]
Cassidy & Synnatschke *et al*.	EE Graphene	Liquid-Liquid Interfacial Deposition	2	12	3	1.4×10^5	[312]

A model capable of fitting both the bulk-like and percolation regime has been proposed by modifying Eq. 4.7 by Cassidy & Synnatschke *et al*.[312] This enables the entire data set to be used, rather than being strictly limited to the percolation regime. A discussion on the development of this model is included in Appendix A.1.

$$\sigma \approx \sigma_B \left[1 + \frac{1}{4} \left(\frac{t_x - t_c}{t - t_c} \right)^n \right]^{-1} \qquad \text{(Eq. 4.8)}$$

4.2.4 Percolation Exponent

In classical theories of lattice percolation in ideal resistor networks, discussed above, this scaling exponent is only dependent on the dimensionality of the system under investigation. Theoretically, in 3D systems the conductivity scaling exponent is predicted to have a value of 2,[298] and 2D systems should have a value of 4/3.[299] These values can be changed slightly by choice of system and calculation methods.[313] It is worth noting that in Table 4.1, n is rarely precisely in line with these theoretical values. This inconsistency was also observed in a review of over 100 articles showing percolation in CNT composites.[302] Further experimental reports have shown vast disparities in the exponent, with values as high as 9 reported experimentally.[155, 298, 303, 314] This is a significant deviation from the behaviour predicted in the idealised model. In an effort to remedy the disparity between the theoretical predictions and experimental results, Kogut *et al*. demonstrated a link between the percolation exponent of a network and the distribution of junction resistances between the conductive filler particles in the system.[300] They demonstrate that a broader distribution of junction resistances, results in an increase in the percolation exponent.[300]

Interestingly, while the connection between conductivity and percolation theory is plain to see, researchers also identified that, when the networks in the percolation regime were

deformed, the magnitude of the electrical response was enhanced as the percolation threshold was approached from above.

4.3 Piezoresistance

Piezoresistance, the effect of strain on the electrical resistance of a material, was first reported by Lord Kelvin in 1856, when he observed current through an iron wire varied by the application of different tensions.[315] The technological implications of this phenomenon were first recognised and incorporated into patented technologies in the form of a bonded metal wire strain gauge in 1938,[316] and subsequently the metal foil strain gauge which is most commonly used today,[230] illustrated in Figure 4.6A. The modulation in resistance in metals is predominantly due to the reduction in cross sectional area as a result of the Poisson effect, and the increase in length due to the stretching of the sample. The key figure of merit for the piezoresistive effect is the gauge factor, G defined as the fractional change in a sample's electrical resistance, R, per unit strain, ε. A subscript of 0 is used to denote the zero-strain condition.

$$G\varepsilon = \frac{\Delta R}{R_0} \qquad \text{(Eq. 4.9)}$$

Note, this definition this assumes a linear resistance change with strain and, as a result, is only valid in the low-strain regime. The gauge factor can be determined from the slope of the $\Delta R / R_0$ vs. strain plot, as shown in Figure 4.6B.

Having the ability to measure strain using a relatively cheap, mass producible device has enabled advances in many industries, including aviation, automotive, and civil engineering.[230] These metal foils with gauge factor of 2 can typically operate at strains up to 5%. This raises the question as to the key material properties required for piezoresistive devices. Ideally, for strain sensor applications the gauge factor would be high and for stretchable interconnects the gauge factor would be low. Additionally, a

linear electrical response up to a reasonably high strain is ideal.[317] Consistent gauge factor response at different strain rates and after repeated strain and relaxation cycles is necessary, particularly in the aerospace industry where the forces applied to components are cyclic in nature with each take-off and landing.[318, 319]

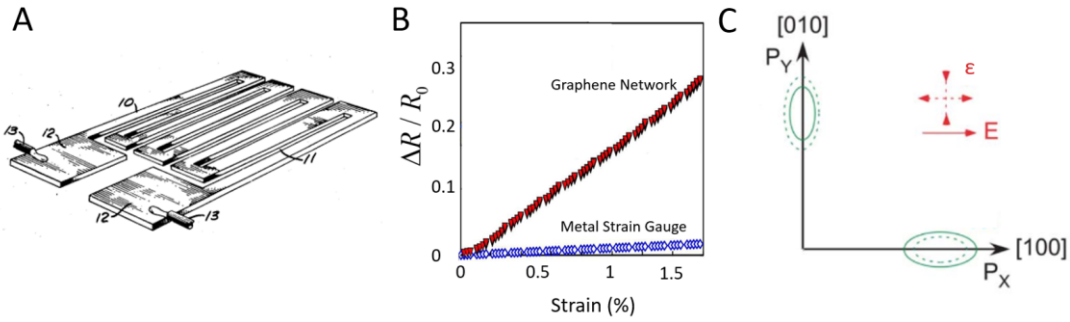

Figure 4.6: Piezoresistive Materials. A) Illustration of a metal foil strain gauge, adapted from van Dyke et al.[320] B) Plot of the fractional change in resistance vs. applied strain for a metal foil strain gauge and a graphene nanosheet network, adapted from Hempel et al.[271] C) Constant energy surfaces, in momentum space, for n-Si, strained and electrically characterised along the (100) axis, with the effect of strain on the constant energy surfaces indicated by dashed lines, adapted from Barlian et al.[321]

This has inspired much research into developing novel alloys, semiconductors, composites, and other classes of materials which have a piezoresistive response, with focuses on optimising these properties.[321-323] Researching this phenomenon is imperative to produce optimised strain gauges for real time health monitoring with wearable technologies,[324-327] and to produce the next generation of flexible electronics with strain invariant conductive interconnects.[328-331]

$$G \approx (1+2\nu) - \frac{1}{\sigma_0}\frac{d\sigma}{d\varepsilon} \approx (1+2\nu) + \frac{1}{\rho_0}\frac{d\rho}{d\varepsilon} \qquad \text{(Eq. 4.10)}$$

The gauge factor equation can be rewritten as shown above,[321] with the derivation shown in Appendix A.1. From this equation it is observed that the geometric effect is tied to the

Poisson ratio, ν, of the material, however if the conductivity, σ,of the material can vary as a function of strain then it is possible to use that as a way of tuning the piezoresistive response. Fortunately, this phenomenon has been observed in several materials systems.

4.3.1 Piezoresistance in Semiconductors

As discussed, the position of the atoms in the unit cell of a material influences the electronic properties. In the case of some TMDs, a significant structural reorganisation from the 2H to 1T phase can lead to a change from semiconducting to semi-metallic electronic properties.[122] Less significant effects can occur with minor lattice deformation, which can result in changes to the number of free electrons and mobility.[332] These effects can be utilised to enhance the geometric gauge factor by introducing an additional change in the material's intrinsic conductivity with strain.

In 1954, the piezoresistive effect was observed in semiconductors by Charles Smith working out of Bell Labs, where n-type Si was found to have a negative gauge factor of -135, while p-type Si had a gauge factor of up to 175.[333] The gauge factor in a semiconductor can be strongly influenced by the doping level and type of dopant, along with the crystallographic direction along which the material is deformed.[334] Additionally, the gauge factor of semiconducting materials is highly temperature dependent,[230] be this from environmental factors or a self-heating effect.[332] Lower doping levels lead to higher gauge factors, ($n < 10^{17}$ cm^{-3}), as the percentage of carriers which move to lower energy levels is higher than for a highly doped semiconductor.[334]

In semiconductor piezoresistors, significant nonlinearity can be observed as strain is increased. It has been reported that by increasing the doping concentration, the resistance, nonlinearity, and temperature dependence can be reduced, however this reduces the gauge factor of the material.[230] Single crystal semiconductor devices are brittle, with strain gauges operating up to 0.1% strain, with an elastic strain range of > 0.5%.

In n-Si, the piezoresistive effect is attributed to the changing band structure with strain along particular axes, as illustrated in Figure 4.6C. The constant energy surfaces are ellipsoids in k-space. As a result, the mobility is direction dependent, when the material is strained along a specific axis (in this case the (001) axis). The ellipsoids along that axis decrease in size while the 4 ellipsoids perpendicular to the axis, which have a higher mobility parallel to the axis of applied strain, increase in size. Hence, the mobility in the axis of straining increases, leading to the negative gauge factor observed in n-Si.[334]

4.3.2 Piezoresistance in Composite Materials

Nanomaterials were initially incorporated into polymer composites for mechanical reinforcement and to enhance the material's conductivity.[240] However, it was also found that they exhibited piezoresistive properties under the application of strain, launching a new field of research: piezoresistive nanocomposites. It is understood that conduction occurs through connected neighbouring conductive particles which extend a conductive pathway between the electrodes in the material,[10, 335] in line with the network model discussed previously.

These composite materials exhibit piezoresistive responses which can vary with a range of factors including filler overlap area, network morphology, and particle alignment.[336] To explain the piezoresistive mechanism in nanocomposites beyond the geometrical response or semiconductor band structure arguments, several mechanisms have been proposed. The first is related to a change in the overlap area or junctions between the nanoparticles as the material is strained, resulting in an overall change in resistance with strain, with the second involving percolation and network structure contributions. These suggested mechanisms can broadly be applied to both composite and polymer-free networks.

Inter-Particle Disconnection and Junctions

For nanoparticle networks, the piezoresistive mechanism has been widely attributed to the change in the junctions between the conductive elements. This has been coined the 'disconnection mechanism' by Souri *et al*.[337] and the effect of junctions has recently been reviewed by Boland.[338] This mechanism proposes that as the material is strained, nanomaterials in the composite move past each other. This movement leads to a reduction in the overlap area or an increase in the distance between the conductive filler particles,[339] reducing the inter-particle conduction and increasing the overall resistance of the network. This has been reported for a wide range of nanoparticle systems.[340-343] Other related approaches involve cracking mechanisms[344] and destroying conductive pathways. Strain dependent tunnelling mechanisms have been proposed for CNT-Ecoflex™ nanocomposites.[345] It has also been possible to combine composite materials with semiconducting fillers to have a piezoresistive response for which the mechanism is a combination of device geometry, inter-nanosheet junctions, and intrinsic semiconductor nanosheet piezoresistivity.[346]

Percolation Effects and Network Structure

As mentioned, networks of nanomaterials can exhibit percolative conductivity. This effect was also observed for piezoresistance in polymer nanocomposites, with rapid increases in gauge factor observed as the percolation threshold is approached from above,[10, 166, 347, 348] as shown in Figure 4.7A. Many research groups attributed this effect to inter-nanosheet charge transport effects similar to the disconnection mechanism, however Garcia *et al*.[299] developed a simple model describing piezoresistance of composite nanomaterials in the percolative regime. This model was derived by differentiating the conductivity percolation equation for nanocomposites with respect to strain, and substituting the result into Equation 4.10. In this model, ϕ is the filler volume

fraction, $\phi_{C,0}$ is the percolation threshold, t is the percolation exponent, and σ_C is the pre-factor of the electrical conductivity percolation scaling with volume fraction.

$$G \approx \left[2 - \left(\frac{d\ln\sigma_C}{d\varepsilon}\right)_0\right] + \left[\left(\frac{dt}{d\varepsilon}\right)_0 \ln\left(\phi - \phi_{C,0}\right)^{-1}\right] + \left[\left(\frac{d\phi_C}{d\varepsilon}\right)_0 \frac{t_0}{\phi - \phi_{C,0}}\right] \qquad \text{(Eq. 4.11)}$$

In this equation, the inter-particle conduction response and geometric piezoresistance are contained within the first square bracket term. The dominant term near the percolation threshold is the third square bracketed term, which is related to the effect of applied strain on the percolative network structure.[299]

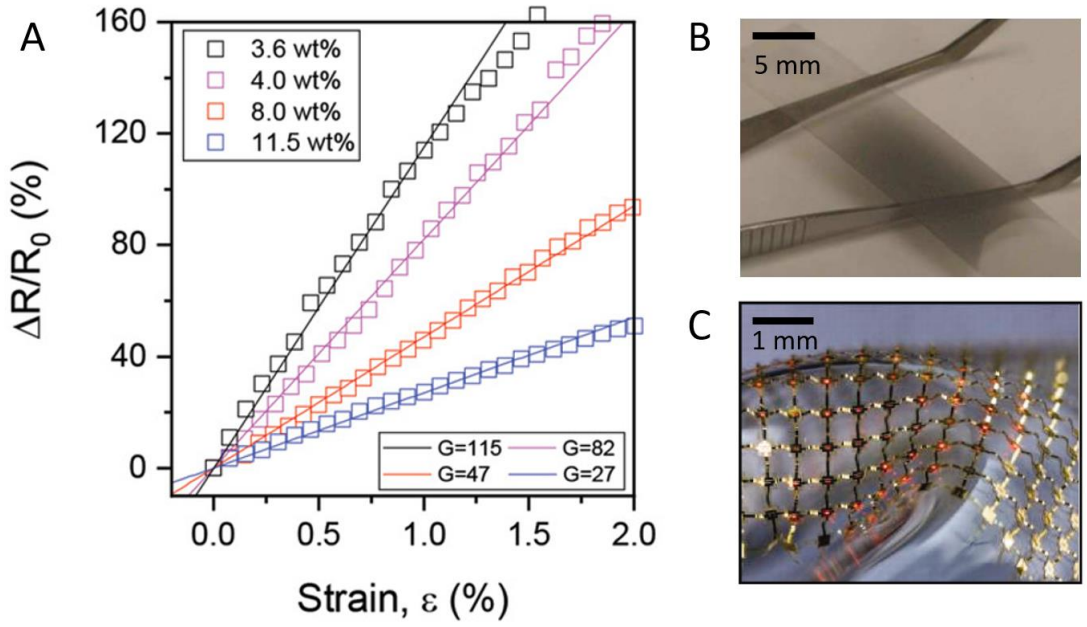

Figure 4.7: Tuning Piezoresistance. A) Plot of fractional change in resistance vs. applied strain for printed networks of graphene-PDMS composites with different volume fractions, reproduced from O'Driscoll et al.[166] B) Photograph of a polymer-free spray coated graphene network on a flexible PET substrate, adapted from Hempel et al.[271] C) Stretchable LED display using a mesh design for flexible interconnects, adapted from Rogers et al.[328]

Challenges with Nanocomposites

Unfortunately, when reviewing the literature for composite piezoresistive materials, the definition of gauge factor in the low-strain limit of linear piezoresistive response has not always been strictly adhered to. This has resulted in several reports of exceptional "gauge factors," reaching several tens of thousands, based on higher strain linear regions.[338] To this end, Boland produced a review of composite piezoresistive devices, in which the gauge factor and linear range were extracted from the raw data available.[336] This gave a range of reported gauge factors 0.01[349] to 2,600.[350]

While piezoresistive responses in nanocomposites can be exceptional, offering potential to deliver high gauge factor wearable strain sensors,[351] it is noteworthy that polymer composite materials have challenges when it comes to hysteresis in the piezoresistive response, along with frequency dependence of the gauge factors.[10, 166] There is also the challenge of polymer matrix getting between the sheets, reducing device conductivity and inducing undesirable mechanical effects.[170] Work has been carried out to minimise this effect by printing the composite materials, which has paved the way towards a printed composite piezoresistor.[166] On closer inspection of the cross sectional imaging of the composite, there is clear phase segregation of the nanosheet and polymer in the device.[166] This is one of the key motivations to return to look at piezoresistance in polymer-free films, in the hope that these undesirable effects would be further minimised.

4.3.3 Piezoresistance in Polymer-Free Films

Carbon microphones were used to convert mechanical deformation to electrical signals and were even used as amplifiers. These can still be found today, over 100 years later. In a description of the operating principle of the microphone, developed by Edison,[352] his biographer, Wills, writes: "when pressure is applied, this deformation changes the contact area between adjacent carbon granules, and hence the electrical resistance."[353] This

mechanism sounds very similar to the proposed disconnection mechanism, where junctions between particles contribute to the piezoresistive response of a network.

Polymer-free nano-networks have been studied for their piezoresistive response, particularly as conductive coatings on flexible substrates.[354] Examples of conductive particles studied include gold nanoparticles,[355] CNTs,[356, 357] graphene,[358-360] TMDs,[361] MXenes,[362] gold nanosheets,[339] and mixtures of different nanomaterials.[170, 363] Such nanomaterial films have no polymer matrix to get between the junctions, which typically results in increased conductivity for polymer-free films.[243] A spray coated graphene film on a flexible polyethylene terephthalate (PET) substrate is shown in Figure 4.7B.[271] Nanomaterial films can also be produced by a variety of methods, and the piezoresistive responses of polymer-free graphene films prepared by different techniques have been tabulated below.

*Table 4.2: Polymer-free graphene piezoresistor gauge factors and linear range reports for a variety of film deposition techniques. *Buckled by substrate pre-strain. **Cracking.*

Name	**Deposition**	**Maximum GF**	**Linear Range (%)**	**Year**	**Ref**
Zhao *et al.*	CVD	300	0.3	2012	[358]
Casiraghi *et al.*	Inkjet	125	1.25	2018	[243]
Wang *et al.**	Scotch-Tape Method	0.55	20	2011	[364]
Zhao *et al*.	PECVD	600	1	2015	[365]
Li *et al*.	Self-Assembly	300	0.5	2016	[157]
Bae *et al.*	CVD	2.7	1.5	2013	[366]
Qiao *et al*.	Laser Scribing	54.7	2	2018	[367]
Hempel *et al*.	Spray Coating	170	1.5	2012	[271]
Garcia *et al*.	Spray Coating	250	0.9	2023	[170]
Neilson *et al.***	Liquid-Liquid	285	20	2023	[368]

In reviewing the literature, the highest gauge factor responses for graphene nanosheet networks are typically observed for the thinnest networks with the highest resistivity. As discussed for composite materials, a range of piezoresistive mechanisms have been suggested. These include changes in junction resistances,[271] cracking of the network,[368] and percolative considerations.[170] It is noted that electrical signal noise varies between devices, and so the ultimate resolution of a piezoresistor depends not only on gauge factor but also on noise in the electrical resistance.[369] However, the magnitude of the noise has not been quantified in any of the studies cited in Table 4.2 when investigating polymer-free graphene piezoresistors, instead focusing on tuning the gauge factor parameter. In order to drive progress in this field, it is necessary to define goals with respect to gauge factor, cyclability, and linear range that the community should be working towards,[336] as well as producing physical models of these phenomena in order to better understand the processes at play when nanosheet networks are strained. These models and community targets would remove the 'stretch and see' approach which currently saturates piezoresistor device literature.

4.3.4 Flexible Electronics

To date, a majority of the work has been conducted on optimising for high gauge factor devices to enable strain sensor applications, however of equal importance when considering piezoresistance in nanosheet networks is optimising for low gauge factor to enable flexible electronic devices[370, 371] and flexible LED arrays, as shown in Figure 4.7C.[328] To date, organic conductors have been proposed as flexible interconnect materials,[372, 373] and it is necessary to refocus the 2D materials field towards flexible electronics if 'all 2D' flexible devices are to become a reality.[374, 375] Some of the lowest gauge factor values have been achieved by depositing the networks on pre-strained substrates, and releasing the strain post deposition, creating ripples which reduce the

effective strain applied to the network during testing.[364, 376] Others have focused on device geometry[324] or have added 1D conductive nanomaterials to bridge gaps in 2D nanosheet networks.[377]

"Equipped with his five senses, man explores the universe around him and calls the adventure Science."

Edwin Powell Hubble

Chapter 5

Effect of Network Thickness on Piezoresistive and Electrical Properties of LPE Nanosheet Networks

The work presented in this chapter has been adapted from the confirmation report and the published work: "Quantifying the Piezoresistive Mechanism in High-Performance Printed Graphene Strain Sensors," published in ACS Applied Materials and Interfaces.[378]

5.1 Introduction

Since the discovery of nanomaterials, and their exciting and superlative properties, researchers have tried to utilise them in technologies that can have a positive impact on society.[379] One area that was initially explored was wearable flexible technologies including deformation,[380] sweat,[381] and chemical sensors.[382] These platforms offer the potential for personalised health monitoring[328] in real time.[324] Over the last decade there has been a significant uptick in wearable health monitoring devices in daily life, tracking exercise recovery, sleep, and even cardiovascular health.[325, 326, 382] Networks of liquid processed nanomaterials have found applications in piezoresistive devices, which display a change in resistance when they are strained. Through understanding and tuning this response, strain gauges and flexible, strain invariant interconnects can be developed. The

figure of merit for the piezoresistive response is the gauge factor (G), $G = (\Delta R / R_0) / \varepsilon$. This is defined strictly in the limit of low strain where the electrical response is linear with strain.[10, 230] Currently the industry standard metal foil gauges which are produced at a large scale[230] have a relatively low G of ~2, as the resistance change is entirely based on the geometrical deformation of the foil.[332]

Incorporating networks of nanomaterials into piezoresistive devices has led to a wide range of reported gauge factors. Reports range from 0.01[349] to 2,600,[350] with the majority of networks found in polymer nanocomposites.[10, 383] Gauge factor has been shown to be linked to network conductivity by the following equation,[332] $G = 2 - (1/\sigma_0)(d\sigma / d\varepsilon)_0$. However, for a piezoresistor to be useful, as well as having high G they also need to have a good linear range, low load/unload hysteresis, and minimal variation of G with frequency, with many teams working to optimise these parameters.[166, 336, 337, 384-388] Nanocomposites tend to have lower conductivities as a result of the polymer coating surrounding the conductive filler.[389] To avoid such issues, and to increase conductivity, the polymer matrix has on occasion been omitted, in favour of a simple polymer-free nanomaterial network.[354-356, 358, 361-363, 390] These types of films can also be printed, enabling different device architectures.[166, 243, 271, 354, 391] Traditionally, the piezoresistive response in nanomaterial networks has been ascribed to strain modulating junctions between conductive particles,[10] however a wide range of potential mechanisms have been postulated.[337]

To date, nanosheet-only piezoresistive films have been fabricated through a range of methods including CVD,[358, 365, 366, 392, 393] drop casting,[157] laser scribing,[367, 394] inkjet printing,[243] and spray coating.[271] In these papers, gauge factors up to ~600 were reported.[365] One disadvantage of such films is that the strain range where the resistance-strain curve is linear is relatively low, <2%.

Nanomaterials, especially graphene, have advantages as printable, scalable, and tuneable piezoresistors. However, the piezoresistive and conductive properties of such films, particularly in the percolation thickness regime, is not universally reported. A physics-based model for the gauge factor response to changing the network thickness in the percolation regime is needed to inform future device optimisation and to provide mechanistic insights into these effects. Current models for network G do not fully consider the network dimension and network conductivity.[299, 359] A gap exists in considering the effect of strain conductivity beyond junction resistance. Detailed characterisation is also lacking on the hysteresis and frequency dependence of the piezoresistive response of polymer-free nanosheet networks.

In this chapter, the effect of network thickness on the electrical and piezoresistive properties of nanosheet networks is investigated, particularly in the percolation regime of thickness. This was conducted by spray coating LPE nanosheets onto flexible substrates to form semi-transparent graphene films. These were characterised electrically and the piezoresistive response was measured, by using a tensile tester to strain the networks. As the networks were in the percolation regime, theoretical models incorporating percolation theory were developed to relate the network thickness, conductivity, and gauge factor of nanosheet networks. The polymer-free networks were also studied for cyclic stability and hysteresis effects when cycling, as well as frequency dependent responses. It is hoped that these results can guide future studies to optimise gauge factor through a mechanistic understanding of the piezoresistive effect in these systems.

5.2 Experimental Procedure

Liquid Phase Exfoliation and Size Selection

Graphene ink was prepared using LPE of graphite flakes (Branwell, graphite grade RFL 99.5, 20 g) in 1-methyl-2-pyrrolidone (Sigma-Aldrich, 200 mL) by tip sonication (200 W, 70% amplitude, 72 h, Hielscher UP200S, 200 W, 24 kHz. This dispersion underwent centrifugation (Hettich Mikro 220R) at 1,500 RPM for 90 min to remove large nanosheets and unexfoliated bulk graphite. The supernatant was vacuum filtered through a 0.45 μm nylon membrane (Sterlitech NY4547100), forming a pellet of graphene. This was washed by adding methanol (Sigma-Aldrich, 30 mL). The residual membrane was dried in a vacuum oven (Fi-Streem Vacuum Oven) at 50 °C overnight. The carbon membrane was weighed (Sartorius Balance), ground into a powder using a mortar and pestle, and resuspended in chloroform (Sigma-Aldrich) by tip sonication for 1 h at 40% amplitude to make a graphene/chloroform dispersion with a concentration of 2 mg/mL. The dispersion concentration and nanosheet thickness were estimated using UV-vis characterisation (Cary 50) as outlined by Backes *et al*.[195] This dispersion was diluted to the required concentrations for spray printing.

Substrate Preparation

Polydimethylsiloxane (PDMS) Sylgard 184 Dow Corning substrates were fabricated by mixing component A (2.00 mL, silicone oil base) and B (200 μL, curing agent) in a 10:1 volume ratio in a polytetrafluoroethylene (PTFE) mould. These were cured in an oven (2 h, 120 °C) after which the cured PDMS was removed from the mould and cut into strips of the required size.

Spray Coating

Thin films of graphene were deposited by spray coating from a modified airbrush (Harder & Steenbeck Infinity Airbrush) which was mounted in a mobile gantry (Janome

JR2300N). The gantry was programmed to raster across a 5 cm × 5 cm area where the substrates were held in place using Kapton tape. The working distance from nozzle to substrates was 10 cm and the nitrogen back pressure was set to 3.5 bar. Films with thickness above 100 nm had well-defined thicknesses that could be measured by a stylus profilometer. Thinner films tend to display more inhomogeneous morphologies. However, the average thicknesses measured for such thin films were reasonably repeatable. For example, a batch of six sprayed films typically displayed a thickness variation of <15 nm.

Thickness Characterisation

Graphene film thickness was characterised using a flatbed scanner (Epson Perfection V700 PHOTO) to determine the optical transmission and thereby extinction. The scanner was previously calibrated using neutral density filters of known transmission. The film extinction was converted to film thickness using the extinction coefficient, which was measured using sprayed films of the same graphene dispersion on glass, whose thicknesses were measured using profilometry. The extinction coefficient was measured for thicker films using between 100 and 250 nm for which the profilometry was more reliable. Very thin films can be somewhat inhomogeneous, making the thickness poorly defined. Measuring the thickness from the optical transmission is equivalent to measuring an average thickness.

Electromechanical Tensile Testing

Printed networks were tested using a Zwick Z0.5 ProLine Tensile Tester (100 N Load Cell). The films were contacted using silver wires attached (using silver paint, Agar Scientific) directly onto the graphene film. Sample dimensions were approximately 5 mm × 25 mm with PDMS thickness in the range of 0.7–1.0 mm. Devices were conditioned by three cycles of a sawtooth profile up to 1% strain before testing. Conditioning is

particularly important as otherwise the initial stretch/release cycle can give an unrepresentative, anomalous electrical response, typically with a higher gauge factor. It is probable that the as-produced network is in a nonequilibrium state and conditioning leads to a slight reorganisation of the network into a more stable state. This final state is likely to have improved connectivity as the total resistance tends to decrease over the conditioning cycle. The resistance was measured using a Keithley KE2601 Source meter controlled by a two-probe LabView program. Electromechanical measurements were made using a maximum strain amplitude of 1%. Straining beyond 1% tended to lead to irreversible cracking or delamination of electrodes. Cyclic measurements were initially performed at 0.6% strain amplitude. However, it was observed that 0.6% strain eventually led to damage to the 45 nm film after repeated cycling. Subsequently, all long cycling experiments on the 45 nm sample were performed with a 0.4% strain amplitude, which could be applied for >3,000 cycles without damage appearing.

The TEM presented in this chapter was carried out by Dr Domhnall O'Suilleabhain, Raman spectroscopy was carried out by Dr Tian Carey and SEM was carried out by Dr Cian Gabbett.

5.3 *Results and Discussion*

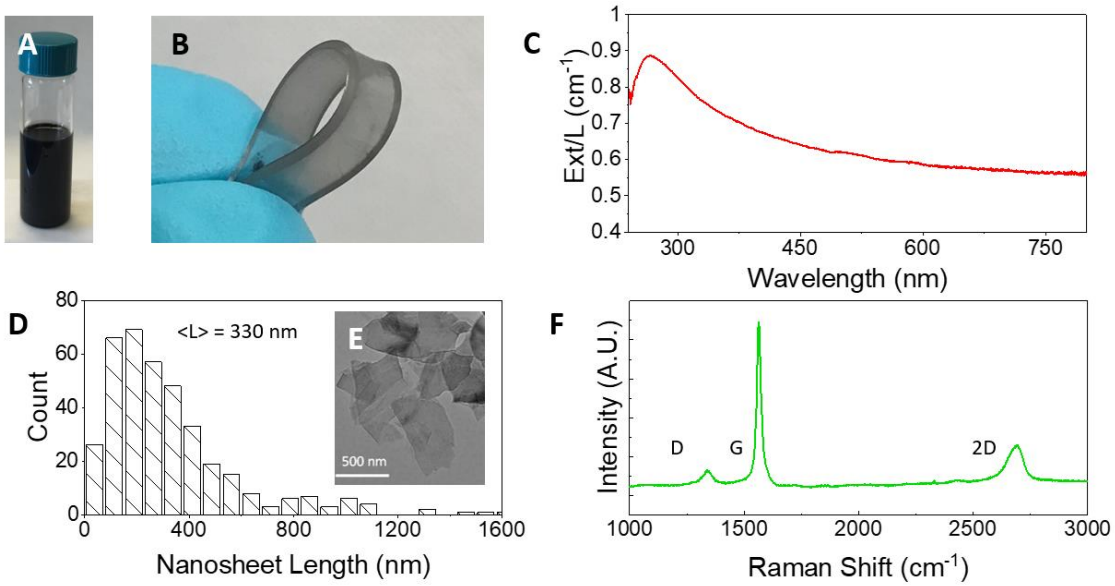

Figure 5.1: Nanosheet Characterisation. A) Photograph of the graphene/chloroform ink. B) Photograph of a printed, semi-transparent graphene film on PDMS substrate. C) Extinction spectrum of the nanosheet ink with the chloroform background removed. D) Histogram of nanosheet length measured from TEM images. E) TEM image of the nanosheets found in the ink. F) Raman spectrum of a nanosheet network produced from ink drop cast onto Si/SiO_2.

The graphene was exfoliated by LPE in NMP and transferred into chloroform as discussed in the experimental procedures. In order to characterise the material and the graphene/chloroform ink (Figure 5.1A), which is suitable for spray coating, various analyses were carried out including UV-Vis spectroscopy, TEM, and Raman spectroscopy. Figure 5.1B shows a thin, spray cast film on a PDMS substrate which has been bent back on itself, showing the flexibility and semitransparency of the deposited film. An extinction spectrum of the ink is shown in Figure 5.1C, showing the characteristic low frequency plateau along with the graphitic $\pi - \pi^*$ transition below 300 nm.[395] From published metrics (ε_{750} = 5,450 L.g^{-1}.m^{-1}),[195] the ink concentration was estimated to be C = 2 mg/mL. The average nanosheet length was measured using TEM,

with the distribution of lengths from 376 measured nanosheets plotted in Figure 5.1D. A representative TEM image is also shown (Figure 5.1E). From this distribution, the mean nanosheet length was determined to be 330 ± 14 nm. The Raman spectrum shown in Figure 5.1F clearly shows the characteristic D, G and 2D graphene peaks. The relatively low D peak intensity, with the D to G peak intensity ratio of $I_D / I_G = 0.15$, indicates that the graphene nanosheets contain very few defects in the basal plane, while the Lorentzian shape of the 2D peak matches the expected shape for few-layer graphene implying electronically decoupled sheets.[195]

5.3.1 Electrical Characterisation

From percolation theory, it is known that the conductivity of a thin nanomaterial network will follow power law behaviour as given by Eq. 5.1, when below the bulk-like critical thickness.

$$\sigma = \sigma_{Bulk}\left(\frac{t - t_c}{t_x - t_c}\right)^n \qquad \text{(Eq. 5.1)}$$

In this study over 50 films with various thicknesses were fabricated by spray coating and their conductivities were measured in the absence of strain, σ_0. In this discussion a subscript "0" indicates at zero-strain. The effective thickness was characterised using optical transmission, by correlating the optical extinction to the measured thickness of films sprayed onto glass (see Appendix A.2).

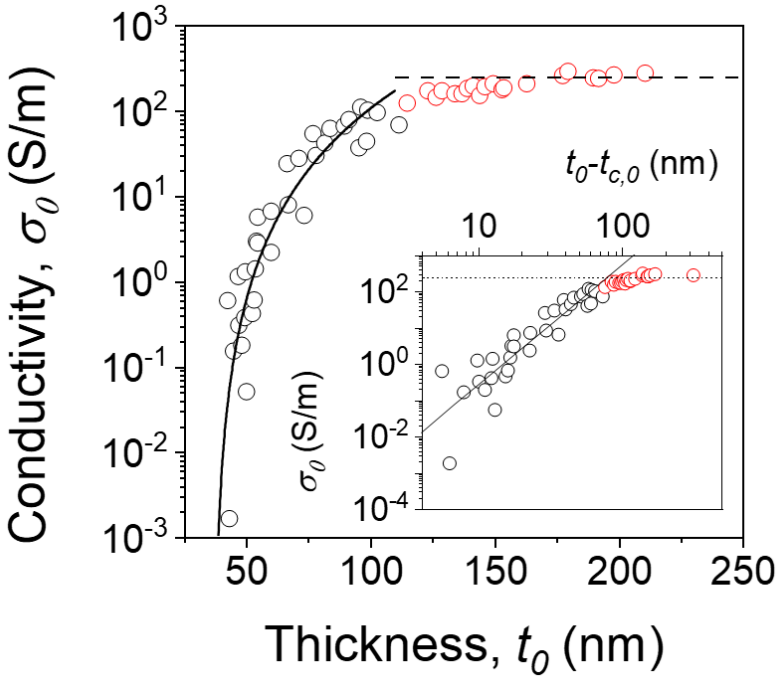

Figure 5.2: Electrical Percolation. Plot of nanosheet film conductivity vs. network thickness, measured at zero-strain. Inset log–log plot of σ_0 *versus* $(t_0 - t_{c,0})$ *with overlaid fit using Eq. 5.1 for* t_0 *< 110 nm. The data for* t_0 *> 110 nm are considered bulk-like and plotted in red with the average value indicated by the dashed line.*

The plot in Figure 5.2 shows conductivity scaling with film thickness, t_0. The conductivity rises with increasing thickness, from ~10^{-3} S/m for films ~ 45 nm thick, rising sharply until a plateau of conductivity at ~ 260 S/m above ~120 nm. Note that no measurable conductivity was found for networks thinner than 40 nm. Inset is a log-log plot of conductivity vs. $(t_0 - t_{c,0})$, used to calculate the fit parameters. This can be explained by noting that in bulk-like systems, conductivity is an intrinsic material property independent of sample dimensions; however, in thin, disordered networks of graphene nanosheets or nanotubes, conductivity is no longer intrinsic.[248] This behaviour has been seen in very thin films of nanomaterials including nanotubes, nanowires, and nanosheets.[248, 249, 307]

Percolation behaviour is largely associated with disorder in the network. The decrease in conductivity with decreasing thickness is linked to the reduction in the number of conductive pathways through the network, up to a critical limit where there is only one conductive pathway, the percolation threshold t_c.

Fitting the data for $t <$ 110 nm, which allows for a transition region from bulk to percolative, a fit (shown in black) is found with $n_0 = 3.3$, $t_{c,0}$ = 37 nm. For the thick films the bulk conductivity, σ_B = 260 S/m, and the crossover point, $t_{x,0}$ = 120 nm, were found. The parameters and their errors are summarised in Table 5.1.

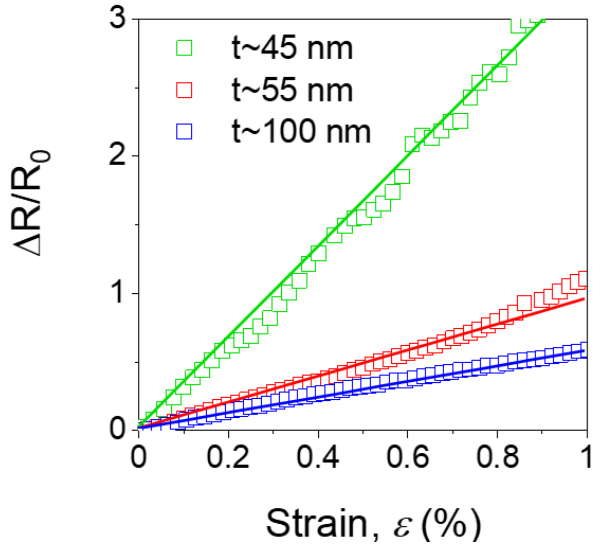

Figure 5.3: Piezoresistive Response. Fractional change in resistance vs. strain for three representative networks of varying film thickness. The solid lines are linear fits.

To investigate the film thickness dependence on gauge factor, the networks analysed in Figure 5.2 were subjected to electromechanical tests, straining from 0% to 1% strain at a rate of 1 %/s. Figure 5.3 shows the electromechanical response of three printed graphene devices of different thicknesses. Minor oscillations observed are due to imperfect application of strain by the tensile tester during testing. From the piezoresistive theory, it is known that at low strain the gauge factor, G, is the slope of the $\Delta R / R_0$ vs. ε plot.

As observed for nanocomposite materials, as the conductivity decreases, the gauge factor increases, shown by the increase in slope in Figure 5.3 as the network thickness is reduced.[299] It was not known if G, like conductivity, shows bulk-like and percolative behaviour across a range of film thicknesses, so more detailed characterisation was required. The linear region in these curves tends to only extend up to the ~0.75-1% strain, limiting their utility to low strain measurements. This is consistent with piezoresistive devices prepared from nanomaterial films with linear ranges <5% strain.[365, 394] A recent study of over 200 literature reported strain sensors found a negative correlation between the gauge factor and the linear sensing range, suggesting that systems with higher gauge factors only have a linear region at low strain.[336]

5.3.2 Scanning Electron Microscopy of Networks

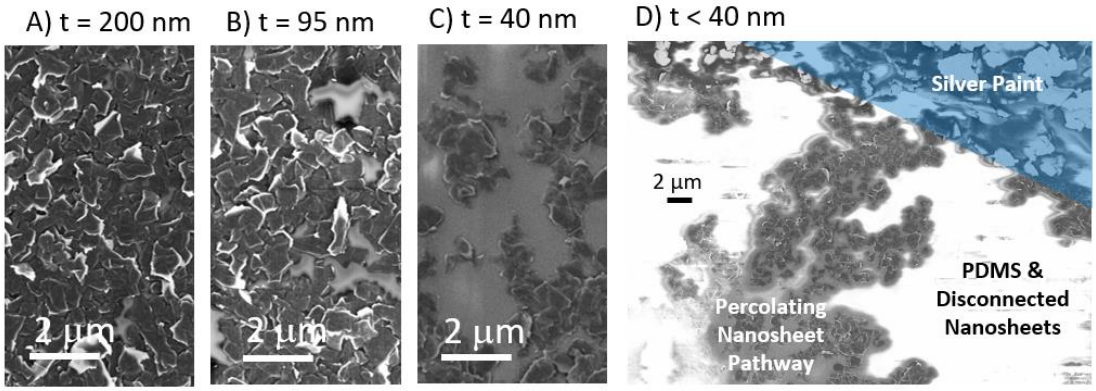

Figure 5.4: Network Imaging. SEM images of three nanosheet networks with thicknesses of A) 200nm, B) 95nm, C) 40nm and D) < 40nm, respectively. The decreasing surface coverage is evident as the thickness is decreased, and the few remaining nanosheet pathways can be seen in the 40 nm sample and percolative conduction to the silver electrode is visualised in the < 40 nm sample.

The ink in Figure 5.1A can be sprayed onto a flexible PDMS substrate to form a thin network on polymer surface. Using SEM this network can be imaged below the

diffraction limit of light.[396] Figure 5.4 shows a selection of SEM images of different networks, each with a different thickness, from different regions on the conductivity-thickness profile (Figure 5.2). From percolation theory, it is expected that for thinner networks there should be fewer conductive pathways across the channel. As the network thickness goes from 200 nm to 40 nm, the morphology of the network changes drastically. Figure 5.4A shows an image of a near-continuous nanosheet network with a thickness of 200 nm in the bulk-like regime, resulting in very few holes through the network. Figure 5.4B shows a t = 95 nm network, which is below the t_x = 120 nm bulk threshold. The network is less uniform, and several gaps can be seen in the network, through which the PDMS substrate can be seen. Figure 5.4C shows a t = 40 nm sprayed network, which is extremely close to the percolation threshold, t_c. This image shows the clear nonuniformities in the network, with disconnected nanosheets, the PDMS substrate, and very few connected current-carrying nanosheets visible on the surface. The nonuniformities are the reason for the percolative conductivity which is observed below t_x and are expected to be pivotal to the increased gauge factor in this regime. With fewer current carrying pathways to depend on, the nonuniform network resistance is more susceptible to strain induced disruption of a few connected pathways, increasing the gauge factor.

Figure 5.4D shows an SEM image of a sprayed network, below percolation, with $t < 40$ nm. As a result, there is no complete bridging connected pathway between the electrodes. However, by imaging near to the silver paint (shaded blue) on the surface, which is connected to the earth, a percolating nanosheet pathway can be clearly identified as the nanosheets in black. The white region is the PDMS substrate and disconnected nanosheets which are unable to join the percolating pathway, and so show a charging effect in the SEM image.

5.3.3 Modelling Gauge Factor

A mathematical model can be derived for the relationship between a percolative nanosheet network's thickness and gauge factor by combining both piezoresistance and percolation theory. It is known that $G \simeq 2-(1/\sigma_0)(d\sigma/d\varepsilon)_0$, however, as Eq. 5.1 was verified above to describe the percolation conductivity of the nanosheet network with respect to network thickness, it may be possible to derive a model for G with respect to network thickness by differentiating Eq. 5.1 with respect to strain.

The complete derivation of the following expression is shown in Appendix A.2.

$$G \simeq \left[2-\left(\frac{d\ln(\sigma_{Bulk})}{d\varepsilon}\right)_0\right]+\left[\ln\left(\frac{t_{x,0}-t_{c,0}}{t_0-t_{c,0}}\right)\left(\frac{dn}{d\varepsilon}\right)_0\right] + \left[\left(\frac{n_0}{t_{x,0}-t_{c,0}}\right)\left\{\left(\frac{dt_x}{d\varepsilon}\right)_0-\left(\frac{dt_c}{d\varepsilon}\right)_0\right\}\right]+\left[\frac{n_0}{t_0-t_{c,0}}\left\{\left(\frac{dt_c}{d\varepsilon}\right)_0-\left(\frac{dt}{d\varepsilon}\right)_0\right\}\right] \quad \text{(Eq. 5.2)}$$

Taking the first three square bracketed terms to be roughly thickness independent, a simplified gauge factor to thickness model can be written (Eq. 5.3). In this simplified model, TNS stands for "thin network sensor". However, this simplified model must be tested on experimental data to validate the assumptions made and to identify which term in the equation is dominant.

$$G \approx G_{TNS}+\frac{t_{TNS}}{t_0-t_{c,0}} \quad \text{(Eq. 5.3)}$$

This model can also be rewritten in terms of conductivity, as in Eq. 5.4. This must also be fitted to experimental data to confirm its ability to accurately model piezoresistive behaviour and to confirm that the fit parameters correspond to the same values as calculated from the conductivity vs. thickness plot in Figure 5.2.

$$G \approx G_{TNS}+\left[\frac{\sigma_{TNS}}{\sigma_0}\right]^{1/n_0} \quad \text{(Eq. 5.4)}$$

Eq. 5.3 suggests that G will increase sharply as the thickness is reduced towards the percolation thickness, t_c, while Eq. 5.4 predicts and explains the power law relationship between G and σ_0 which has been noted by previous authors.[299] According to these equations, the larger the values of the figures of merit, t_{TNS} and σ_{TNS}, the higher the resulting gauge factor.

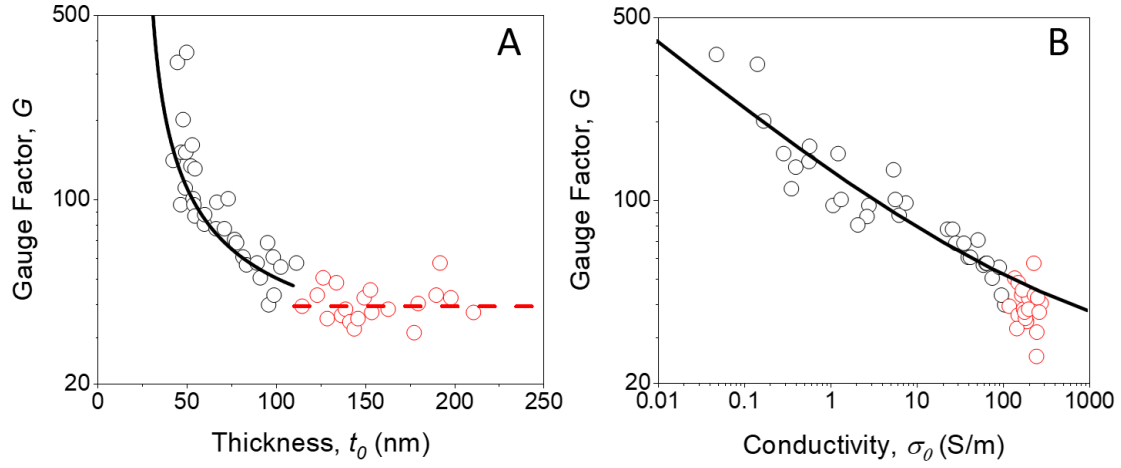

Figure 5.5: Gauge Factor Modelling. A) Plot of gauge factor vs. network thickness with an overlaid fit from Eq. 5.3. B) Plot of gauge factor vs. network conductivity, with overlaid fit from Eq. 5.4. The data for t_0 *> 110 nm are considered bulk-like and plotted in red. Fit parameters are given in Table 5.1.*

In Figure 5.5A, G is plotted as a function of network thickness, and for thinner networks G is highly thickness dependent. This has been alluded to but not explored in detail in a small number of papers.[271, 359, 394] The sharp rise in G as t_c is approached from above is similar to the percolative behaviour shown by the conductivity vs. thickness data. Additionally, G appears to be thickness-independent for network thicknesses above ~120 nm. These results imply that gauge factor has percolative and bulk-like regimes.

In Figure 5.5B, G is plotted against unstrained conductivity and a well-defined power-like decay is observed, as predicted by Eq. 5.4. Similar decays were reported by Hu *et*

al. for epoxy resin/carbon nanotube composites[347] and Garcia *et al.* for Sylgard/graphene composites.[299] This further supports the derived model, which predicts such behaviour, along with providing a link between the behaviour of polymer-free nanosheet networks and nanocomposite strain sensors.

The plots in Figure 5.5 include fits to the model according to Eq. 5.3 and Eq. 5.4, fitting where t_0 is less than 110 nm, consistent with the region in which the electrical percolation data (Figure 5.2) were fitted. The fit parameters for each of these fits are given in Table 5.1.

Table 5.1: Fit parameters from fitting data in Figure 5.2 and Figure 5.5 to the relevant percolation models.

Parameter	**Value**	**Parameter**	**Value**	**Parameter**	**Value**
From σ_0 vs. t_0 (Eq. 5.1)		From G vs. t_0 (Eq. 5.3)		From G vs. σ_0 (Eq. 5.4)	
$\sigma_{B,0}$	260 ± 20 S/m	G_{TNS}	22 ± 4	G_{TNS}	21 ± 5
$t_{c,0}$	37 ± 5 nm	t_{TNS}	2.3 ± 0.3 μm	σ_{TNS}	(3 ± 1) ×10^7 S/m
$t_{x,0}$	120 ± 5 nm	$t_{c,0}$	27 ± 3 nm	n_0	3.7 ± 0.3
n_0	3.3 ± 0.3				

Fitting G vs. t_0, good fit values with relatively low uncertainty were found. Notably, the value of $t_{c,0}$ is very similar, but not identical to the value found from the σ_0 vs. t_0 fitting. Knowing that $t_{TNS} \approx n_0(dt_c/d\varepsilon)_0$, and taking n_0 = 3.3, the value of the derivative $(dt_c/d\varepsilon)_0$ is estimated to be 700 nm, meaning that t_c changes by 7 nm for every percentage of applied strain.

Physically, Eq. 5.3 sheds very interesting light on the factors which dictate the piezoresistive response. When $t_0 \ll t_x$ for high gauge factor thin networks, the second term in Eq. 5.3 dominates, with the magnitude primarily determined by t_{TNS}, which, as

discussed above, scales linearly with $(dt_c / d\varepsilon)_0$. As $(dt_c / d\varepsilon)_0$ is a measure of the change in the percolation threshold with strain, which is essentially a measure of the effect of strain on the network structure, it is concluded that the dominant second term in Eq. 5.3 is linked to network morphology. This is a novel conclusion, as previously it was believed that the dominant piezoresistive effect was the effect of strain on the inter-nanosheet junctions. This effect is contained in the first term in Eq. 5.3.

As shown, G can also be expressed as a function of network conductivity, σ_0, as in Eq. 5.4. This model is fitted to the experimental data in Figure 5.5B and the coefficients are given in Table 5.1. Notably, the values of G_{TNS} and n_0 are consistent with the values estimated from the other fitting equations. The utility of Eq. 5.4 is its prediction of a power law dependence between G and σ_0 which has been alluded to in previous reports.[299]

5.3.4 Cyclability, Hysteresis, and Frequency Dependence

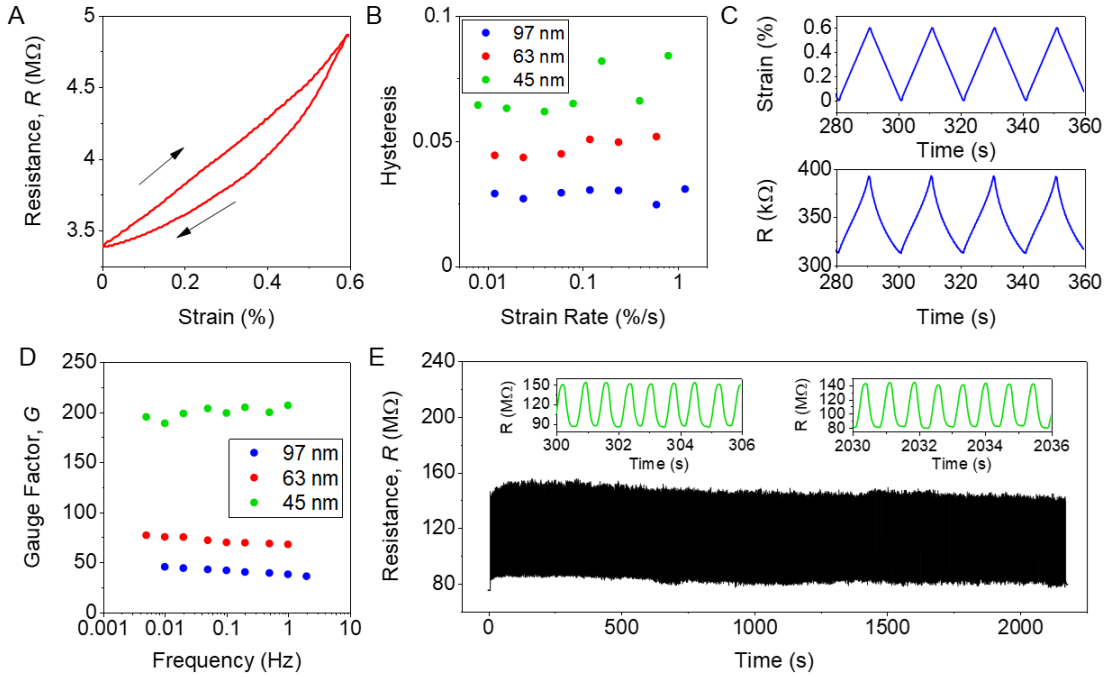

Figure 5.6: Hysteresis and Cyclability Testing. A) Resistance hysteresis profile as a function of strain for the t_0 *= 63 nm film, measured with strain rate of 0.024 %/s. B) Comparison of hysteresis as a function of strain rate for three networks of different thicknesses, showing reasonable stability of hysteresis across two decades of strain rate and an increase in hysteresis at lower thicknesses. C) Cyclic resistance response of 97 nm thick film with 0.05 Hz sawtooth cycling profile with an amplitude from 0% to 0.6%. D) Gauge factor vs. cyclic frequency for three networks, showing near frequency independence from 0.01 Hz to 1 Hz. The strain amplitudes were 0.4% for the 45 nm thick film and 0.6% for the 63 nm and 97 nm films. E) Cyclic testing (sawtooth ~1.5 Hz), 0% to 0.4% strain for 45 nm film showing stability over 3,000 cycles. Inset magnified regions at the start and end of the cycling profile.*

The literature on piezoresistive strain sensors is mostly focused on maximising the gauge factor. However, for practical applications, other factors including low hysteresis, minimum frequency dependence of G and good cyclability over thousands of cycles are important. These factors were investigated and their results are shown in Figure 5.6.

Hysteresis is defined as the area within the hysteresis loop in a resistance vs. strain plot as the device is loaded and released, divided by the area under the resistance vs. strain curve for loading. An example is shown in Figure 5.6A of a 63 nm thick film with a hysteresis of 5% at a strain rate of 0.024 %/s. Hysteresis can be observed when the resistance-strain curve for the release curve does not follow the path traced by the loading curve, implying that the loading process has altered the network structure, at least temporarily.[337, 384] Figure 5.6B shows that the hysteresis across 2 orders of magnitude of strain rate is roughly strain rate independent for three different film thicknesses, all of which show hysteresis less than 10%, with thinner films having a higher hysteresis. Contextualising hysteresis is challenging as some papers measure hysteresis,[397, 398] but very few quote numerical values. However, these results do compare favourably with printed polymer/graphene nanocomposites which have a hysteresis of 15%.[166]

In practical applications, strain gauges must also be able to monitor cyclic straining across a range of frequencies. Hence, frequency invariant gauge factor is imperative across the range and over thousands of cycles. To test this a sawtooth cyclic strain profile, Figure 5.6C (top), was applied to the networks, with the corresponding resistance profile (bottom) showing high cycle to cycle stability of gauge factor. Figure 5.6D shows the dynamic gauge factor vs. frequency for three different network thicknesses, for which all cycles used sawtooth profiles. All three devices show good frequency independence of gauge factor over 2 orders of magnitude of frequency, with the thinnest films having a dynamic gauge factor of $G \approx 200$. Plots of the fractional change in resistance vs. strain, along with stress vs. strain plots for representative samples cyclically deformed across the range of frequencies, are included in Appendix A.2. Once more, frequency dependent gauge factor measurements are rarely reported, however, this data is consistent with the frequency invariant behaviour reported by Li *et al.*[157] and Qiao *et al*.[367]

Figure 5.6E shows the resistance response of the 45 nm thick nanosheet network, over 3,000 cycles, showing great stability, and minimal decay. The inset plots show zoomed in profiles at the start and end of the 3,000-cycle test, showing good fidelity along with stable gauge factors of $G \approx 187$ and $G \approx 184$, respectively. This shows considerable potential for using nanosheet network piezoresistors in commercial applications, however, some encapsulating system will be necessary given that the films are sensitive to scratches and abrasions. It will also be necessary to optimise the resolution of such networks, as the increase in gauge factor observed in the percolation regime is likely competing with an increase in noise in the measured sample resistance.[399]

5.3.5 Literature Comparisons

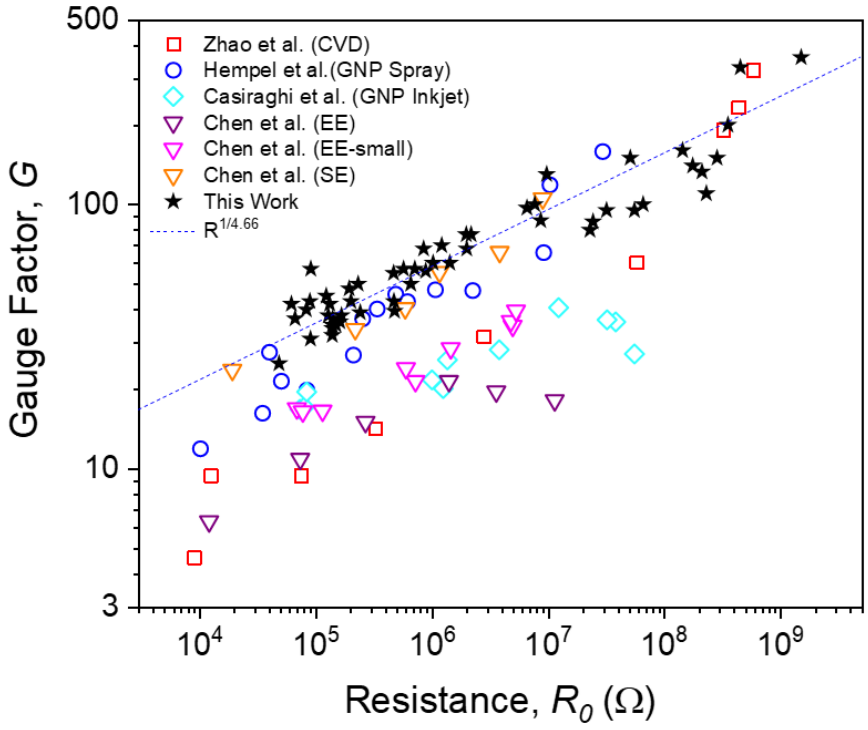

Figure 5.7: Literature Comparisons. Comparison of results with previous literature plotted as gauge factor vs. zero-strain resistance. Papers used in analysis: Zhao et al. (CVD),[358] Hempel et al. (Spray),[271] Casiraghi et al. (Inkjet on paper),[243] Chen et al. (EE / EE-small (sonicated after exfoliation) / Solvent Exfoliated).[360] The dashed line shows power law dependence with an exponent of $1/(n_0+1) = 1/4.66$.

To contextualise the results presented in this chapter, Figure 5.7 shows the comparison between gauge factor data from this research with literature values for graphene-only piezoresistive devices. These include solution processed and CVD grown films. As most papers do not provide the film thickness, making the calculation of conductivity impossible, gauge factors must first be plotted against the zero-strain resistance. The most striking feature of the graph is that the different data sets all show close to power law dependence of gauge factor on resistance. To explain this a short modification was made to the model. The key steps are as follows. Assuming that the network thickness is well above the percolation threshold, ($t_0 \gg t_{c,0}$), the percolation equation yields the dependence $\sigma_0 \propto t_0^{n_0}$. This means that the zero-strain resistance will scale with unstrained film thickness as $R_0 \propto t_0^{-(n_0+1)}$. Making a substitution into Eq. 5.3 returns the relationship $G - G_{TNS} \propto R_0^{1/(n_0+1)}$. When $t_{c,0}$ and G_{TNS} are relatively small, the model predicts the relation $G \propto R_0^{1/(n_0+1)}$. This model can be tested on the existing experimental data, as shown in Figure 5.7, by plotting a line with exponent $1/4.66$, which is consistent with the estimated percolation exponent of 3.66. As mentioned previously, this percolation exponent can be related back to the dimensionality of the system,[299] however, it has been shown that the exponent can increase beyond the theoretical values due to distributions of inter-nanosheet junctions in the network,[300] as is the case in this study.

The model fits well with data collected in this work as well as data from previous nanomaterial-based piezoresistor reports, enabling the percolation exponent of percolative graphene networks to be extracted from piezoresistance measurements on a set of films with unknown thicknesses. Additionally, the devices reported in this chapter are competitive with the best gauge factors for graphene-based strain gauges reported in the literature, even CVD-grown films. This is especially true for the low thickness films,

which have a gauge factor of ~350, which compares well with previously reported graphene networks prepared by drop casting,[394] inkjet printing,[243] spray casting,[271] and self-assembly[157] with low strain gauge factors of ~10, 125, 170, and ~300 respectively. In a 2019 study of 200 nanocomposite strain sensor reports,[336] the gauge factors were ranked, ranging from 0.01 to 2,600.[350] The best graphene thin film device would rank fifth on this scale. While higher gauge factors can be achieved with CVD-grown films, with G = 600 for remote plasma-enhanced chemical vapor deposition (PECVD) grown films,[365] because of the ease of scalable low-cost fabrication and excellent performance, these printed LPE graphene networks have potential to be used in practical low cost applications.

5.4 Conclusions

Based on the results presented in this chapter, many conclusions can be drawn about the physical phenomena at work in nanosheet networks. Of note are the dependences reported for electrical conductivity and piezoresistance with respect to the changing network thickness in the percolation thickness regime. This work demonstrated that the electrical conductivity and gauge factor saturate to their intrinsic values above the bulk-like network thickness in nanosheet networks. However, below this thickness, strong relationships are observed for both conductivity and gauge factor with network thickness. These thickness dependences are both closely related and can be described using models based on percolation theory. These models show that, in the percolation regime, network structure plays a significant part in the piezoresistive response of the network. Additionally, the devices in this study exhibit low hysteresis and frequency independent gauge factor, while also being stable over thousands of cycles, significant for many potential applications.

"Success isn't a result of spontaneous combustion.

You must set yourself on fire."

Arnold H. Glasow

Chapter 6

Effect of Nanosheet Thickness on Conduction and Piezoresistive Response in Nanosheet Networks

The work presented in this chapter has been adapted from the published work: "Quantifying the effect of nanosheet dimensions on the piezoresistive response of printed graphene nanosheet networks," published in Nanoscale Horizons.[400]

6.1 Introduction

As outlined in previous chapters, graphene and the family of 2D materials have attracted attention because of their blend of exciting physical properties and potential for applications.[57, 72, 401, 402] LPE provides a scalable, cost-effective technique to exfoliate layered crystals into nanosheets in liquid mediums and could yield printable inks after necessary solvent exchange or solvent modification steps.[5, 87] These nanosheets can form printed networks from which a range of electronic devices including transistors,[124] solar cells,[403] and diodes[256] can be fabricated. The printability enables the use of flexible substrates, unlocking potential for flexible electronics.[152, 331] However, it is imperative to understand the effect of deformation on such a network to prevent unwanted secondary effects when the devices are in operation.

The response of a film's resistance (R) to strain (ε) is known as the gauge factor (G), as defined in Eq. 6.1.[332] This resistance change is almost always attributed to the effect of strain on the junction resistance,[337, 340, 341, 385] although network morphology effects[378] (Chapter 5), as well as geometrical Poisson effects have been discussed.[385] As these flexible technologies mature, understanding the impact of strain on this resistance will be important to guide new technologies.

$$G = \lim_{\varepsilon \to 0} \left[\frac{\Delta R / R_0}{\varepsilon} \right] \qquad \text{(Eq. 6.1)}$$

To date, significant research has been conducted to optimise the gauge factor in networks of various materials.[10, 166, 336, 338] Combining theoretical models with experimental data has enabled the identification of the key optimisation factors for gauge factor, with links between network resistivity or conductivity and network gauge factor observed readily. Recently, the conductivity of the network has been modulated through a variety of approaches including varying nanosheet loading in nanocomposites,[299] varying ratios of conducting and semiconducting nanosheets in a network,[170] and, as shown in Chapter 5, controlling network thickness in the percolation regime.[378] These are understood theoretically and tested experimentally, linking G and conductivity in each case, casting light on conduction and piezoresistance in each of the systems.

To date a gap in the literature exists regarding a nanosheet parameter that should alter the piezoresistive response in networks. FIB-SEM nanotomography has shown that the size and thickness of the nanosheets can alter the morphology of the networks,[146] while various papers have shown that nanosheet dimensions can significantly impact network resitivity.[145, 146, 258] Additionally, a recent paper has reported a theoretical model which describes the relationship between nanosheet dimensions and network resistivity, as shown in Eq. 4.3.[147] This report also investigates parameters linked to network morphology including junction resistance, tortuosity, and porosity.[147]

In this chapter, the effect of nanosheet dimensions, specifically thickness, on the conduction and piezoresistive properties of printed graphene nanosheet networks is investigated. This was conducted by spray coating size selected nanosheets into networks with thicknesses of a micron or more, ensuring that they display bulk-like resistivity without any percolative effects.[378] This was followed by electrical resistivity and the piezoresistive response measurements on samples from each nanosheet size fraction. Combining these experiments with simple theoretical models, the key limiting factors in network resistivity and piezoresistive response can be identified and quantified for the LPE graphene system, thus providing novel insights into these processes in nano-networks.

6.2 Experimental Procedure

Graphene Exfoliation

Graphite flakes (Asbury, 4 g) were sonicated for 1h in 80 mL n-methyl-2-pyrollidone (Sigma) at 65% power with a horn probe. The suspension was centrifuged (Hettich, 10 cm radius) for 1 h at 6 kRPM. The sediment was resuspended in 80 mL of fresh NMP and sonicated for 9 h at 60 % power, pulsing 4s on 4s off.

Liquid Cascade Centrifugation

To size select the nanosheets, the suspension was centrifuged at 0.5 kRPM for 2 h at 5 °C. The sediment was discarded, and the supernatant was centrifuged at 1 kRPM for 2 h at 5 °C. The sediment was kept and labelled as the "0.5 to 1 kRPM" sample (with the speeds indicating the lower and upper spin speeds used to sediment the nanosheets). The supernatant was then centrifuged at 1.5 kRPM for 2 h at 5 °C. The cycle was repeated at 2, 3, 4, and 6 kRPM, keeping the sediment each time and centrifuging the supernatant at successively higher speeds. The sediments were resuspended in fresh isopropanol (IPA)

and centrifuged at 6 kRPM for 1h at 5 °C. Each sample was finally resuspended in fresh IPA. A schematic of this process is shown in Figure 2.7B.

Characterisation

The nanosheet based inks were characterised using UV-Vis spectroscopy (Cary 50), the nanosheets were spray coated on glass and characterised using Raman spectroscopy (Renishaw inVia Quantor, 532 nm). AFM was used to further characterise the flake thicknesses and lateral size (Digital Instruments Multimode IIIa in tapping mode AFM). The measured thickness was converted to layer number by subtracting 1.0 nm to allow for trapped solvents from the measured thickness and dividing the remainder by 0.95 nm. This layer number was then multiplied by 0.35 nm per layer to get the real thickness, in line with the report by Paton *et* al.[87] SEM of the top surface of the films was conducted using the Zeiss Ultra SEM operating at a potential of 3 keV, and imaging using the secondary electron detector with a working distance of 5 mm.

Film Deposition

Kapton substrates (DuPont Kapton HN, 125 μm) were cleaned using IPA. Compressed N_2 was used to dry the samples before spray coating. The films were spray coated using a Harder & Steenbeck Infinity Airbrush, mounted in a Janome (JR2300N) mobile gantry. The gantry was rastered across a 2 cm × 4 cm area in a serpentine repeating pattern. the N_2 back pressure was set to 40 PSI. The ink concentration was 0.1 mg/mL, 50 mL of ink was sprayed for each device. Ink flow was kept constant at 50 mL/h. The working distance from the airbrush nozzle to substrate was 10 cm.

Thickness Characterisation

Film thickness was measured by scanning an area of each sprayed film using an Optical Profiler (Filmetrics, Profilm3D®) with a 50× Nikon objective lens operating in the white light interferometry mode. This produced a 380 μm × 340 μm image of the film.

Thickness was determined by measuring a scratched region and determining the step height from the substrate to the film surface, across the entire image using the 'Histogram' step height measurement on Profilm Online.

Electromechanical Testing

Devices were tested by contacting the networks with silver paint contacts and silver wires connected to an electrical source meter (Keithley KE2601) in a two-probe electrical test. The resistance was measured as the substrates were strained using a Zwick Z0.5 ProLine Tensile Tester with a 100 N load cell.

The AFM presented in this chapter was carried out by Dr Jose Munuera, Raman spectroscopy was carried out by Dr Tian Carey.

6.3 Results and Discussion

6.3.1 Material Characterisation

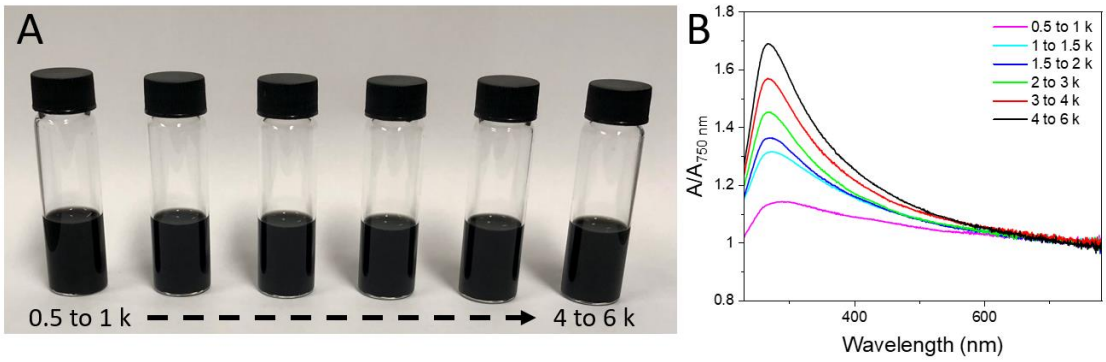

Figure 6.1: Ink Characterisation. A) Photograph of size selected graphene dispersions in IPA. B) UV-Vis spectra of graphene dispersions in different size selection bands.

Dispersions of graphene nanosheets were produced by LPE[5, 86, 104] of graphite powder in NMP. The resultant dispersions were then size selected into various fractions using liquid cascade centrifugation,[136] a process based on repeated centrifugation and separation steps which is shown schematically in Figure 2.7B. Figure 6.1A shows a photograph of the

resulting size selected fractions following a solvent exchange into IPA. An ink concentration of 0.1 mg/mL was chosen for spray coating. Although all inks looked to be identical black liquids, differences between them are observed by measuring their extinction spectra in the UV-visible region as shown in Figure 6.1B. Here, the characteristic π-π* transition peak at ~267 nm is observed as well as the long wavelength plateau.[395] Notably, as the centrifugation speed used to sediment the nanosheets increases, and the nanosheets in the ink become smaller and thinner, the amplitude of the peak relative to the plateau value increases. This observation is in line with observations by Backes *et al*.[195]

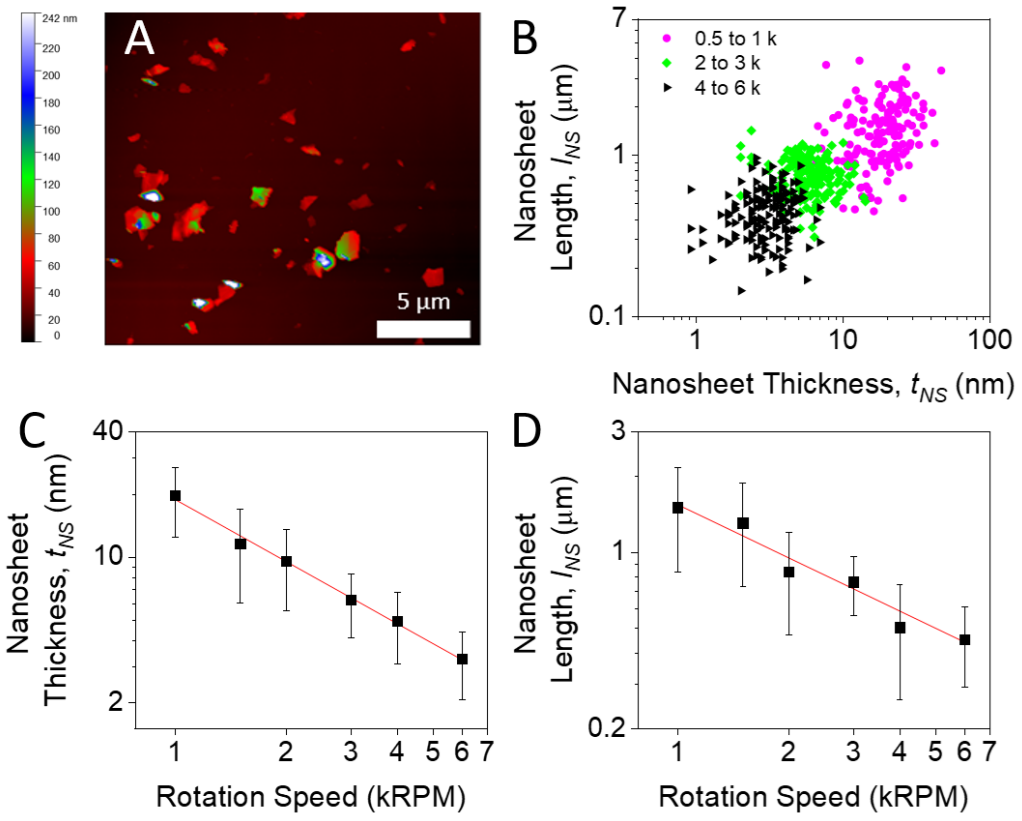

Figure 6.2: Nanosheet Size Characterisation. A) Representative AFM image of graphene nanosheets on a Si/SiO_2 substrate. B) Plot of nanosheet length as a function of nanosheet thickness, where each data point is an individual nanosheet. C) Plot of nanosheet thickness vs. rotation speed. D) Plot of nanosheet length vs. rotation speed. Uncertainty values shown are standard deviations from the AFM distributions.

To enable proper analysis, it is important to measure the lateral size and thickness of the nanosheets in each fraction. To this end, the nanosheet length and thickness distributions were quantified using AFM for all samples, with a representative AFM image shown in Figure 6.2A. When performing AFM of solution processed nanosheets, it is always important to convert the apparent nanosheet thickness to the real thickness.[87, 136, 404, 405] The resultant nanosheet length (l_{NS}) was plotted against nanosheet thickness (t_{NS}) on a flake by flake basis in Figure 6.2B for three of the six fractions studied. The mean values of l_{NS} and t_{NS} were plotted versus the upper RPM used to sediment the fraction of nanosheets in Figure 6.2C&D. These results verify that as the centrifugation speed increases the nanosheets in each fraction become smaller and thinner, decaying as a power law with RPM, as reported previously.[6, 102, 136, 195]

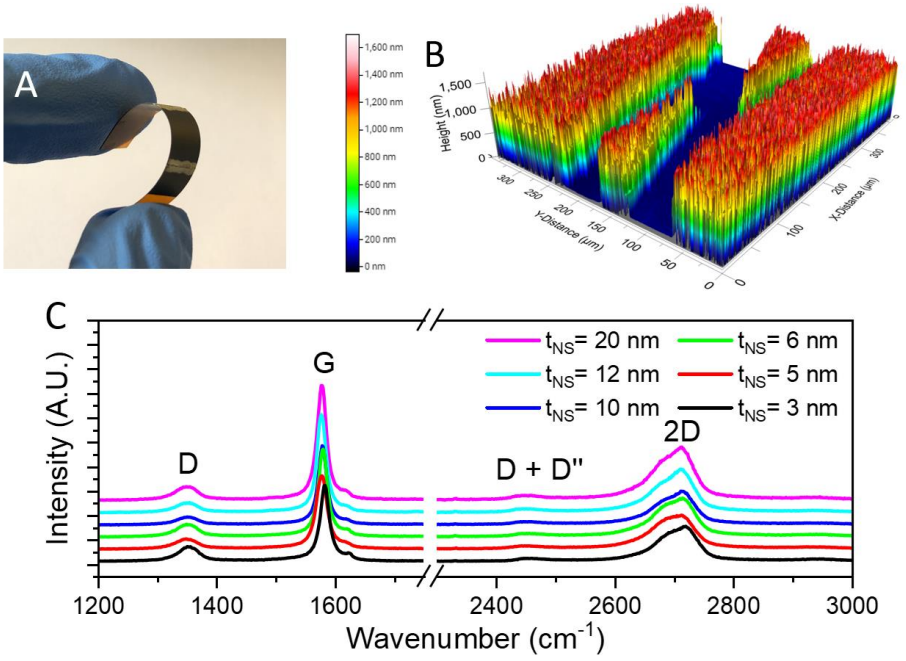

Figure 6.3: Printed Film Characterisation. A) Photograph of a printed graphene film, coated onto a Kapton substrate, bent between two fingers. B) White light interferometry image of a scratch in a printed graphene film, with the top surface showing the top of the film and the bottom showing the substrate. C) Raman spectra of the graphene films prepared with different sizes of nanosheet.

These inks can be used to prepare thin films by a range of solution-deposition methods.[6, 57, 406] Here, films were produced by spray coating onto flexible Kapton substrates (Figure 6.3A), yielding grey opaque films with thickness in the range 1 to 3 μm, as measured by optical profilometry, with a representative 3D profile shown in Figure 6.3B. Such relatively thick films were produced to avoid percolation effects often found in thinner films and to achieve thickness-independent film resistivity.[307] This means that the piezoresistive response will be largely free from effects associated with the influence of strain on the network structure.[378] Raman spectra of the films (Figure 6.3C) showed the characteristic D, G and 2D peaks as well as some evidence of the D + D'' peak,[200] consistent with other reports for liquid phase exfoliated graphene materials.[407]

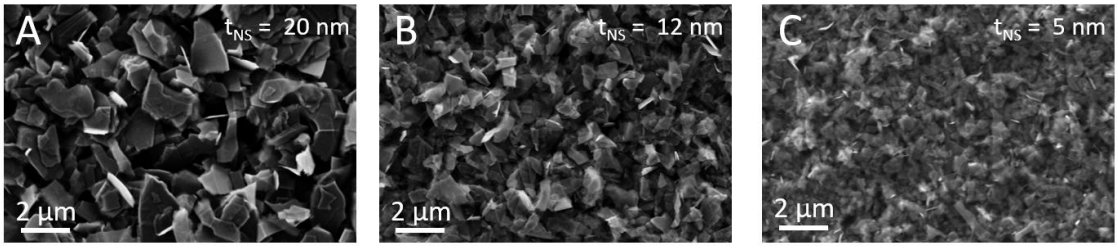

Figure 6.4: Network Imaging. SEM images of the top surfaces of sprayed networks of nanosheets prepared from inks with nanosheet thicknesses of A)20 nm, B) 12 nm, and C) 5 nm.

In order to investigate the microstructure of the spray coated nanosheet films across the range of sizes, SEM images of the top surfaces were taken, as shown in Figure 6.4A-C. No substrate is visible through the network in the images, indicating that a relatively thick film has neem produced. Across each of the sprayed films, considerable disorder with relatively poor flake alignment and significant surface roughness can be observed. These observations are consistent with previously reported spray coated LPE nanosheet networks, which have been shown to yield jammed networks of nanosheets.[146]

6.3.2 Electrical Resistivity of Thick Nanosheet Networks

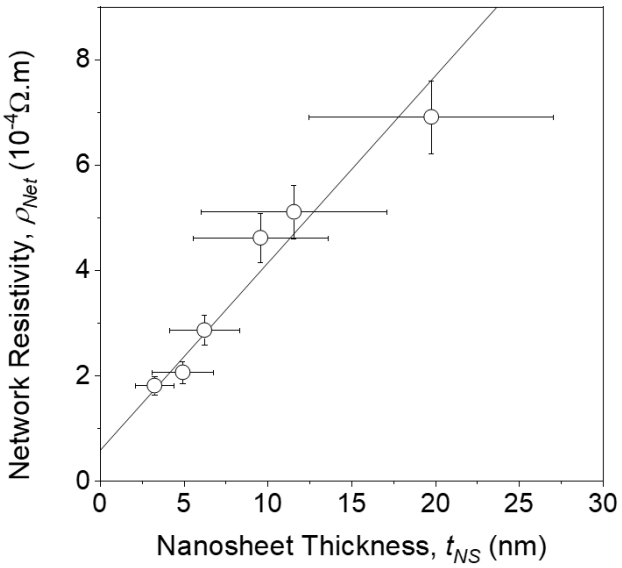

Figure 6.5: Electrical Characterisation. Plot of network resistivity vs. nanosheet thickness showing the increase in resistivity with nanosheet thickness. Linear fit using Equation 6.2.

For electrical measurements, silver electrodes were hand painted to give channel lengths ranging from 0.8-1.0 cm and channel widths in the range of 4–6 mm. When measuring the thin film resistivity at zero strain, values in the range 2-7 $\times 10^{-4}$ Ωm were observed, depending on the dimensions of the nanosheets making up the film. The measured network resistivity, ρ_{NS}, is plotted vs. mean nanosheet thickness, t_{NS}, in Fig 6.5 and shows a well-defined linear trend. For networks of conductive 2D materials which are thick enough to display bulklike conduction, the network resistivity can be modelled using Eq. 6.2.[147]

$$\rho_{Net} \approx \frac{\left[\rho_{NS} + 2t_{NS}R_J\right]}{(1-P_{Net})} \qquad \text{(Eq. 6.2)}$$

Here, ρ_{NS} is the nanosheet resistivity, R_J is the mean junction resistance and P_{Net} is the network porosity. This model fits the data in Figure 6.5 very well. It was necessary to assume the nanosheet network porosity to be P_{Net}=0.5, consistent with reports for sprayed

networks of various LPE nanosheets.[146, 172] This assumption enabled the extraction of the nanosheet resistivity and the junction resistance from this plot. These are found to be: ρ_{NS} = (2.9±1.3) ×10^{-5} Ω.m and R_J = 8.9 ± 1.0 kΩ. These are in line with the previously reported values of ρ_{NS} = 1.7 ×10^{-5} Ω.m and R_J = 3.3 kΩ for LPE graphene, which was exfoliated in a water-surfactant suspension.[147]

In general, resistivity measurements are limited by accurate knowledge of film thickness. Additionally, these systematic errors in film thickness would lead to errors in both the slope and intercept associated with linear fitting to Equation 6.2. For nano-networks, imperfect knowledge of the network porosity and effects of tortuosity can also lead to systematic errors. For this study using Eq. 6.2, tortuosity was assumed to be unimportant, but it can be accounted for in more detailed models.[147] However, taking the ratio of slope to intercept for a ρ_{Net} vs. t_{NS} graph yields a value of $2R_J / \rho_{NS}$ which is free from such errors. Here, from the fit to Figure 6.5, $2R_J / \rho_{NS}$ = 6.13×10^8 m^{-1}.

6.3.3 Piezoresistive Properties of Thick Nanosheet Networks

Using a specially modified tensile tester to measure resistance as a function of applied strain (and stress), the piezoresistive responses of the spray coated films were measured. The gauge factor of the network, G_{Net}, was calculated using Equation 6.1. It was necessary to work at low strain magnitudes, as the gauge factor is defined as the linear response in the limit of low strain. Preliminary results showed the resistance versus strain curves to be linear to almost 1% strain but to preserve the linearity requirement, subsequent measurements were limited to a strain range between 0% and 0.5%. Figure 6.6A shows a plot of fractional resistance change with applied strain for the films made from various nanosheet sizes. These show the expected linearity. It is clear from the figure that, as the thickness of the nanosheet decreases, the slope of the plot (G_{Net}) decreases.

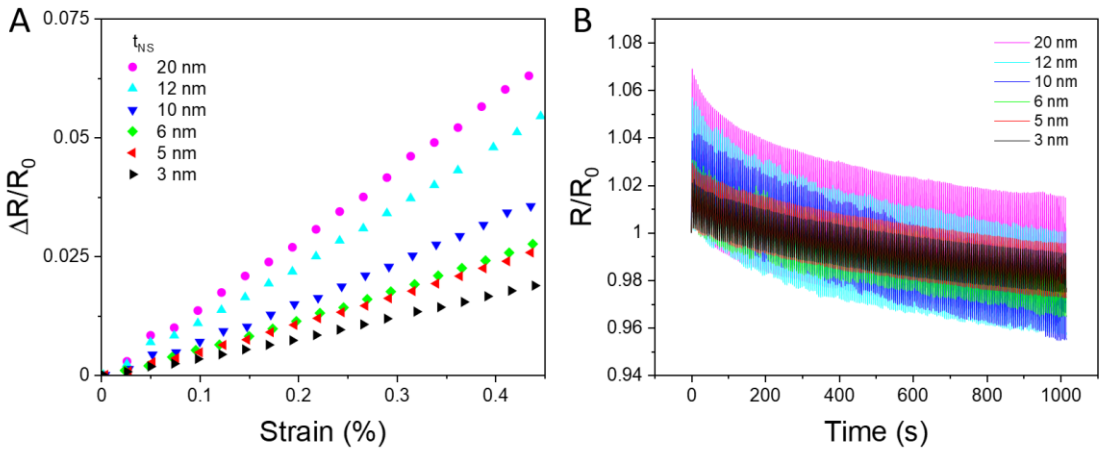

Figure 6.6: Piezoresistive Characterisation. A) Plot of the fractional change in resistance vs. strain for networks prepared with nanosheets of different thicknesses, showing a variation in slope as a function of thickness. Measured with a linear strain rate of 0.2 %/s. B) Plot of normalised resistance vs. time for sawtooth cyclic strain applied to the nanosheet films with an amplitude range from 0% to 0.5% for 200 cycles at a strain rate of 0.2 %/s.

To validate this trend, cyclic testing was performed for the networks produced using nanosheets of each size. The strain was oscillated between 0% and 0.5% in a sawtooth profile for 200 cycles. A representative stress vs. strain plot for a device under cyclic testing is shown in Appendix A.3. Figure 6.6B shows the normalised resistance response for each of the devices. This was an in-phase sawtooth response with minimal hysteresis and good stability, allowing the extraction of a large set of gauge factor values, one for each cycle, which could be treated statistically.

6.3.4 Model Derivation

A theoretical model linking the resistivity of a nanosheet network (in the bulk-like regime) to the nanosheet resistivity, nanosheet thickness and length, network porosity, junction resistance, and the charge carrier density in the nanosheet has been developed, Eq. 6.2. This model also fits well to the experimental data. It is proposed that this model

can be used to derive an expression for the gauge factor of a nanosheet network with bulk-like resistivity.

For any piezoresistive material, the gauge factor can be shown to be related to the rate of change of resistivity with strain.[299] Written such as to apply to a nanosheet network, as presented in Chapter 4, this relationship is given by Equation 6.3:

$$G_{Net} = 2 + \frac{1}{\rho_{Net}} \frac{d\rho_{Net}}{d\varepsilon} \qquad \text{(Eq. 6.3)}$$

Equation 6.3 has previously been successfully used to propose expressions for the gauge factor of polymer nanocomposites,[299] nano-nano composites[170] and thin graphene networks.[378] Differentiating Equation 6.2 with respect to strain, the strain derivative of network resistivity is given by Equation 6.4:

$$\frac{d\rho_{Net}}{d\varepsilon} \approx \frac{\left[\rho_{NS} + 2t_{NS}R_J\right]}{(1-P_{Net})^2} \frac{dP_{Net}}{d\varepsilon} + \frac{\left[d\rho_{NS}/d\varepsilon + 2t_{NS}dR_J/d\varepsilon\right]}{(1-P_{Net})} \qquad \text{(Eq. 6.4)}$$

Substituting this result into Equation 6.3, leaves us with the final expression, which should describe the gauge factor of a network of conductive nanosheets in the bulklike regime.

$$G_{Net} = 2 - \frac{d\ln(1-P_{Net})}{d\varepsilon} + \frac{\left[\frac{1}{\rho_{NS}}\frac{d\rho_{NS}}{d\varepsilon} + \left(\frac{1}{R_J}\frac{dR_J}{d\varepsilon}\right)\left(\frac{2R_J}{\rho_{NS}}\right)t_{NS}\right]}{\left[1 + \left(\frac{2R_J}{\rho_{NS}}\right)t_{NS}\right]} \qquad \text{(Eq. 6.5)}$$

This equation can be used to fit data for the gauge factor, G, as a function of nanosheet thickness, with $(d\rho_{NS}/d\varepsilon)/\rho_{NS}$ and $(dR_J/d\varepsilon)/R_J$ being output as fit parameters. These parameters are of interest as they are linked to the gauge factors associated with the individual nanosheets and junctions (analogous to Equation 6.4).

6.3.5 *Model Fitting*

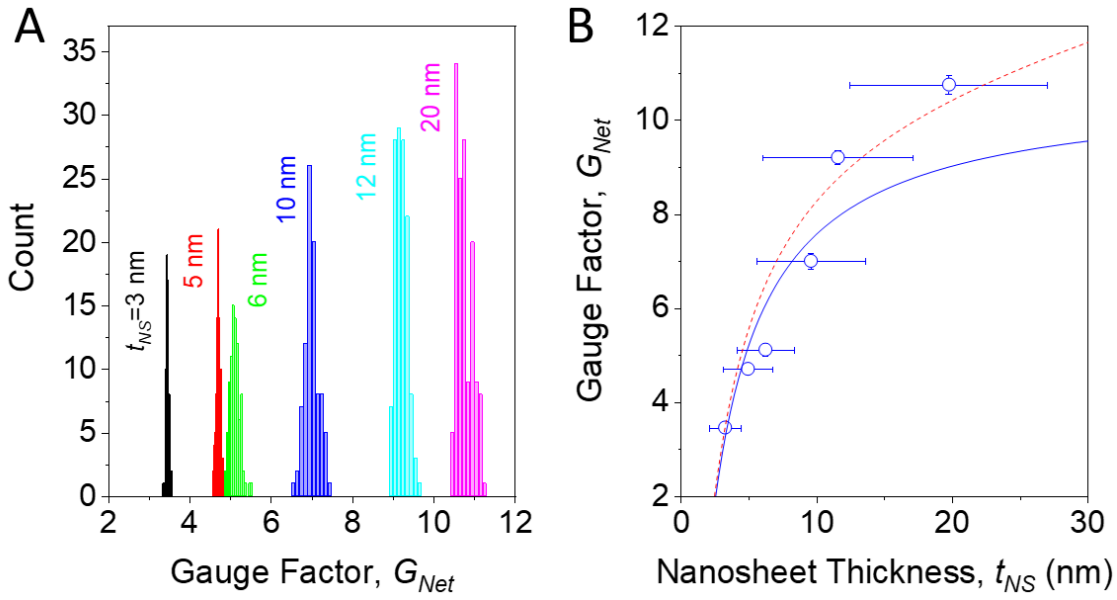

Figure 6.7: Modelling Piezoresistance. A) Histogram showing the distribution in measured gauge factors from the cycling data for each film. B) Plot of gauge factor vs. nanosheet thickness, solid line is the fit to the derived model, dashed line allows for porosity scaling with t_{NS}.

The histograms of extracted gauge factor values from the cyclic testing for each fraction are shown in Figure 6.7A. These histograms are very narrow and allow the mean gauge factor to be determined for each fraction. This is then plotted against nanosheet thickness in Figure 6.7B. This graph clearly shows the network gauge factor to increase with increasing nanosheet thickness.

An effort was made to fit the data in Figure 6.7B using the derived model from Eq. 6.5. This equation has four fit parameters which is too many for accurate fitting, due to our limited data set, restricted by the number of fractions. The number of fit parameters was reduced by one by fixing $2R_J / \rho_{NS}$=6.13×10^8 m^{-1} as extracted from the fit in Figure 6.5. However, even with only three fit parameters, fitting yielded outputs with large associated uncertainty. To remedy this, fitting was attempted whilst fixing the $d\ln(1-P_{Net})/d\varepsilon$ term

at various values between -2 and 2. This process dramatically reduced errors while having limited impact of the other fit parameters (deviation of <25%). The fit parameters are tabulated in Appendix A.3. Thus, $d\ln(1-P_{Net})/d\varepsilon$ was fixed at 0 for the remainder of the fitting process. This fitting process yielded a reasonable trend and outputted the following fit parameters $(d\rho_{NS}/d\varepsilon)/\rho_{NS}$ = -13.6 ± 2.8 and $(dR_J/d\varepsilon)/R_J$ = 8.7 ± 1.1.

This fit works well for thinner nanosheets, however there are deviations from the trend for nanosheet fractions above 10 nm. This is likely as a result of a slight variation with thickness in one of the parameters in Equation 6.5, namely $(d\rho_{NS}/d\varepsilon)/\rho_{NS}$, $(dR_J/d\varepsilon)/R_J$ or $d\ln(1-P_{Net})/d\varepsilon$. The fact that the plot in Figure 6.5 is linear implies that the ratio $2R_J/\rho_{NS}$ does not depend on t_{NS}. The electronic properties of graphene nanosheets greater than a few layers tend to be independent of thickness,[408] implying that in the nanosheets under investigation, ρ_{NS} is thickness independent. Additionally, based on the assumptions of the model in Eq. 6.2, which fits the data well, R_J and as a result, $(dR_J/d\varepsilon)/R_J$ appear to be independent of t_{NS}.

The network porosity has been observed to depend on t_{NS},[144, 146] this implies that there may be a thickness dependence of $d\ln(1-P_{Net})/d\varepsilon$, which would explain the aforementioned discrepancy. To demonstrate this effect, $d\ln(1-P_{Net})/d\varepsilon$ is assumed to scale linearly with nanosheet thickness, as $-7\times10^{7}\ t_{NS}$, while keeping the original fit parameters. This gives the trend shown in Figure 6.7B as a dashed line, in agreement with the data set. This analysis is consistent with the strain independent porosity of thin nanosheets, which was initially assumed, however for larger nanosheets, t_{NS} ~ 20 nm, the network porosity changes by ~1% for every percentage of applied strain. It is hypothesised that this mechanical process occurs by changing the alignment of the

nanosheets which has been shown to alter the porosity of nanosheet networks,[146] however this was not directly measured in this study.

By analogy with Equations 6.1 and 6.3, replacing ρ_{Net} and R_{Net} with ρ_{NS} and R_J respectively, these fit parameters can be understood to be closely related to the gauge factors of individual nanosheets (G_{NS}) and junctions (G_J): $G_{NS} - 2 = (d\rho_{NS} / d\varepsilon) / \rho_{NS}$ and $G_J = (dR_J / d\varepsilon) / R_J$. Hence, it can be written that G_{NS} = -11.6. ± 2.8 and G_J = 8.7 ± 1.1. It is important to note that these values are with respect to applied strain in the network, not the strain experienced by the nanosheet or the junction.

The reasonably high junction gauge factor is relatively straightforward to understand. Inter-nanosheet junctions are expected to change as strain is applied, perhaps altering the charge carriers travel distance between sheets or by reducing the overlap area of the nanosheets. This has traditionally been accepted as the dominant source of piezoresistance in these networks,[340, 341, 385] unless the networks are very thin.[378].

However, detecting the effect of strain on nanosheet resistivity is even more unexpected. To have a measurable nanosheet resistivity change with network strain of the nanosheets is surprising; sheets were expected to slide past one another in response to external stress, without the nanosheets being deformed by the deformation of the network.[213, 409] While there are reports on the effect of applied strain on the individual nanosheet resistances, these reports are for polymeric nanocomposites where stress transfer is mediated by the strong matrix-nanosheet interaction.[346]

Additionally, the negative nanosheet gauge factor is surprising. It has been reported that graphene nanosheets tend to have an intrinsic gauge factor of <10, which is relatively low but positive.[410-413] However, negative gauge factors have been observed for some carbon-based nanostructures, including a negative piezoresistive effect reported by Blazewicz *et al*. when straining graphite fibres.[414] In addition, non-carbon nanosheets such as MoS_2

display strongly negative gauge factors, with $G_{NS} = -50$.[415] This negative nanosheet gauge factor in graphene is an unusual observation and it would be desirable to be able to directly measure the electrical response of the nanosheets to strain for a single network in the future.

Several possible sources of this effect were postulated. It is possible that there is some built in strain in the nanosheets resulting from the network formation. In low strain limit, these residual stresses may be released, returning the nanosheets towards a lower strain state with increasing network strain. Alternatively, it is possible that point contacts between sheets could behave like scattering sites, where one sheet edge presses into the basal plane of another nanosheet. When the network is strained, the sheets are effectively separated, removing the impediment, and hence the nanosheet resistivity decreases.

6.4 Conclusions

The nanosheet thickness dependent electrical and piezoresistive properties of spray coated LPE graphene nanosheet networks were investigated in this chapter. Inks with different nanosheet thicknesses, ranging from ~ 3 nm to ~20 nm, were extracted from a polydisperse LPE exfoliation dispersion through iterative steps of LCC. These inks were characterised spectroscopically, and spray coated films of the inks were studied using SEM. Using a theoretical model, it was possible to extract the nanosheet resistivity and the junction resistance from the plot of network resistivity vs. nanosheet thickness. These parameters were determined to be $\rho_{NS} = (2.9 \pm 1.3) \times 10^{-5}$ Ω.m and $R_J = 8.9 \pm 1.0$ kΩ respectively. It was noted that the piezoresistive response of the networks varied significantly with nanosheet thickness, resulting in the development of a physical model. From this model the nanosheet and junction gauge factors, with respect to strain applied to the network, were extracted to be $G_{NS} = -11.6. \pm 2.8$ and $G_J = 8.7 \pm 1.1$ respectively. The tunability of the gauge factor unlocks potential for nanosheet networks to be

incorporated into devices as flexible interconnects or strain gauges. This study also highlights the significant impact that size selection of nanosheets can have in device optimisation.

"Do not go where the path may lead, go instead

where there is no path and leave a trail."

Ralph Waldo Emerson

Chapter 7

Effect of Nanosheet Aspect Ratio on Conduction and Piezoresistive Response in Nanosheet Networks

7.1 Introduction

To this point, nanosheet networks have been shown to have electrical and piezoresistive properties that vary with network thickness (Chapter 5) and nanosheet thickness (Chapter 6). However, an extensive study is yet to be performed on the effect of changing the aspect ratio of the nanosheets by varying the nanosheet production method. Thus far, LPE nanosheets were used as a model system owing to the ease of scalable production in the laboratory. However, larger, thinner nanosheets, produced by EE methods, have recently been shown to have more conformal and overlapping contacts between the sheets, enabling enhanced electronic device performances compared to LPE nanosheets.[124] It is now imperative to investigate the differences between such systems, from a morphological, electrical, and piezoresistive perspective.

Advances in network characterisation using FIB-SEM nanotomography have enabled more detailed 3D structural characterisation of nanosheet networks.[146] Simultaneously, researchers have been developing techniques to produce and deposit larger, thinner

nanosheets with the objective of reducing inter-nanosheet junction resistances by forming large conformal junctions.[6, 120, 124, 245]

Recent reports suggest that electrical percolation in nanosheets can be modelled across the percolation and bulk regimes,[312] using the following equation shown in Chapter 4:

$$\sigma \approx \sigma_B \left[1 + \frac{1}{4} \left(\frac{t_x - t_c}{t - t_c} \right)^n \right]^{-1} \quad \text{(Eq. 7.1)}$$

This enables key network parameters, including the bulk conductivity and percolation thickness, to be extracted, without needing to prepare and characterise as many samples in the percolation regime, which is challenging and time consuming. An advantage of 2D nanosheet inks is their compatibility with flexible substrates, opening up potential for flexible devices.[375] However, it is important to understand the piezoresistive response of such materials to guide choice of material, as network structure has been found to play a significant part in the piezoresistive response of nanosheet networks.[299]

In this chapter, the morphological, electrical, and piezoresistive properties of printed networks of LPE and EE graphene nanosheets were investigated. The nanosheets were exfoliated and spray coated onto flexible PET substrates. The nanosheets were characterised spectroscopically and microscopically. The structural morphology of the nanosheet and pore networks of both were studied using FIB-SEM nanotomography, yielding quantitative measures of porosity, tortuosity, and alignment. Networks of varying thickness were deposited in order to study the percolative conductivity of networks deposited from inks of different nanosheet aspect ratios. These films were also linearly strained to evaluate the piezoresistive response of the networks. From these analyses, the universality and applicability of the percolation models of nanosheet networks with different nanosheet aspect ratios and network morphologies can be assessed, alongside providing a detailed assessment of the morphological effects of

changing the aspect ratio of nanosheets in printed films. This will provide insights to guide researchers in producing nanosheet devices optimised for morphological, electrical, and piezoresistive properties.

7.2 Experimental Procedure

LPE Graphene Exfoliation

Graphite flakes (Asbury, 4 g) were sonicated in 80 mL n-methyl-2-pyrollidone (Sigma) for 1 h at 65% power. The resulting suspension was centrifuged (Hettich) at 6,000 RPM for 1 h and the sediment was resuspended in 80 mL of n-methyl-2-pyrollidone. This was horn sonicated for 9 h at 60 % power. The suspension was centrifuged for 90 mins at 2,000 RPM to sediment the unexfoliated graphite and the supernatant was centrifuged for 90 mins at 4,000 RPM. The sediment was resuspended in fresh IPA (Sigma) and centrifuged for 60 mins at 6,000 RPM. This washing step was repeated twice. The final sediment was resuspended in IPA and the concentration of the dispersion was determined from UV-Vis measurements with metrics from Backes et al.[195]

EE Graphene Exfoliation

Two pieces of graphite foil (Alfa Aesar, 50 × 30 × 0.254 mm^3) were used as anode and cathode for the EE process. Both electrodes were immersed in 100 mL of 0.1 M aqueous $(NH_4)_2SO_4$ with a constant separation of 2 cm, and a 10 V DC voltage was applied for 30 mins. The current rises steadily during the process, from ~1.1-1.5 A to ~2-2.5 A. The process is repeated using a fresh graphite foil anode, and the expanded material is collected via filtration and repeatedly washed with deionized water (2 L). The expanded material is then transferred to a bottle containing 200 mL of DMF and sonicated for 10 mins (Fisherbrand FB11205, 37 kHz, 100% power). To remove non-exfoliated graphite, the dispersion was centrifuged for 20 mins at 3,000 RPM (Hettich, 10 cm rotor radius) and the supernatant was decanted without redispersion of the sediment. The resulting

dispersion was centrifuged for 90 mins at 6,000 RPM, the supernatant was discarded, and the sediment was redispersed in 20 mL of fresh DMF via brief sonication. The concentration of this ink (~1.5 mg/mL) was determined via UV-Vis measurement.[416] The ink was solvent exchanged to IPA, via 2 cycles of centrifugation (90 mins, 6,000 RPM) and redispersed via brief bath sonication immediately before use.

Nanosheet Characterisation (UV-Vis, Raman, TEM, AFM)

The nanosheet based inks were characterised using UV-Vis spectroscopy (Cary 50). Raman spectra were acquired (using a Renishaw inVia Qontor Raman spectrometer, illuminated by a 532 nm wavelength laser) and averaged over 3 accumulations with a 100× objective of a sample of each ink deposited on glass. An incident power of ~1 mW was used to minimise possible thermal damage. TEM images of the sheets were collected using a JEOL 2100, with an accelerating voltage of 200 kV, in bright field mode. AFM was conducted, using Digital Instruments Multimode IIIa in tapping mode. Inks were drop cast onto Si/SiO_2 substrates coated with (3-aminopropyl)triethoxysilane (APTS) as reported by Karger et al.[417] 10 × 10 μm^2 images were recorded.

Substrate Preparation

Glass substrates (Epredia) were cleaned by a 2-step bath sonication in acetone and IPA (5 mins in each solvent). The substrates were subsequently dried with compressed N_2. PET Substrates were cleaned using IPA and dried with compressed N_2.

Film Deposition

Graphene films were spray coated onto the glass substrates using a modified airbrush (Harder & Steenbeck Infinity Airbrush), mounted in a Janome (JR2300N) mobile gantry. The gantry was programmed to raster across the area of the mask (2 cm × 4 cm), with the serpentine pattern mask attached to the substrate with Kapton tape. The nozzle top substrate working distance was 10 cm and the N_2 back pressure was set to 3.5 bar. The

ink concentration was 0.1 mg/mL for LPE graphene and 0.05 mg/mL for EE graphene, and ink flow was kept constant at 60 mL/h.

Thickness Characterisation

Film thicknesses were determined using a stylus profiler (Veeco Dektak 6m). This had a stylus radius of 12.5 µm, using the force setting at 1 mg, and sampled every 0.2 µm along the profile. For thinner films where stylus profilometry was not suitable, optical profilometry using the Filmetrics Profilm3D® with a 50x Nikon objective lens[418] and flatbed transmission scanning methods[378] (Epson Perfection V700 PHOTO) were used.

Thermal Annealing

To remove residual solvents and increase electrical conductivity, graphene films on glass were thermally annealed in a vacuum chamber (VC2509A) at 350 ºC for 1 h.

Electrical Testing

Four probe DC electrical characterisation was conducted in ambient conditions by contacting silver paint electrodes with probes connected to an electrical source meter (Keithley KE2612A) operating in a four-probe sense mode.

Electromechanical Testing

The nanosheet networks were contacted with silver paint contacts and silver wires connected to an electrical source meter (Keithley KE2601) in a two-probe electrical configuration. The resistance was measured simultaneously with the tensile test carried out with a Zwick Z0.5 ProLine Tensile Tester with a 100 N load cell. Devices were tested between 0% and 0.5% strain with a strain rate of 0.2 %/s.

TEM presented in this chapter was carried out by Dr Mark McCrystall, AFM and EE graphene production and deposition were carried out by Dr Jose Munuera, Raman spectroscopy was carried out by Dr Tian Carey. Cross sectional SEM and FIB-SEM nanotomography were carried out by Dr Cian Gabbett and Luke Doolan.

7.3 Results and Discussion

7.3.1 Ink Characterisation

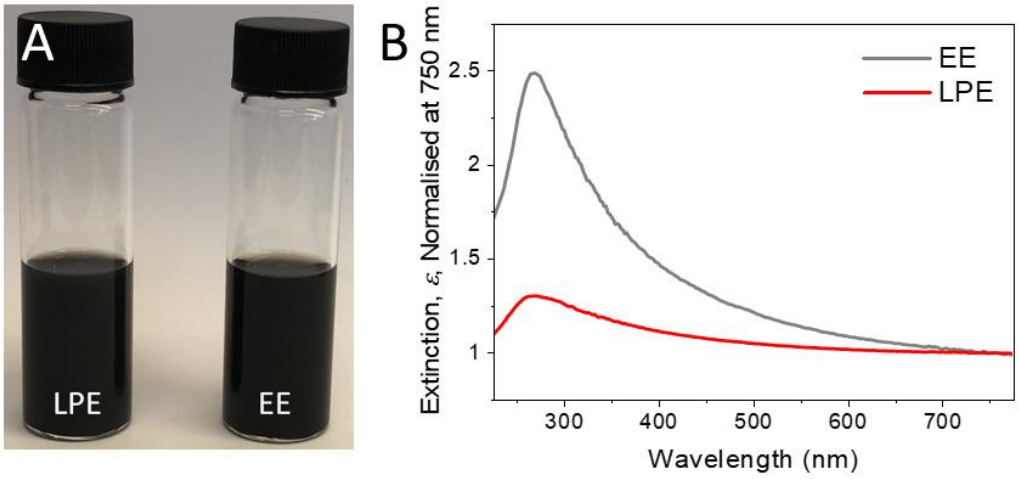

Figure 7.1: Ink Characterisation. A) Photograph of LPE and EE graphene ink dispersions in IPA. B) UV- Vis extinction spectra of LPE and EE nanosheet dispersions.

Inks composed of EE and LPE graphene nanosheets suspended in IPA are shown in Figure 7.1A. These inks are colloidally stable for ~2 weeks, particularly at relatively low concentrations (<0.1 g/L), and are suitable for spray coating to form a thin film on a range of substrates. The extinction spectra of both inks were measured (Fig 7.1B) and they show the characteristic $\pi - \pi^*$ transition peak observed for graphene, along with the plateau at higher wavelengths.[395] These spectra were normalised at 750 nm, in order to compare the relative amplitude of the peaks. The EE material has a significantly increased amplitude, as expected given that the flakes are expected to be thinner and larger than the LPE flakes.[195] This is as a result of the weakened interlaminar bonds in expanded graphite and the gentler bath sonication used to for the EE production process. Transmission electron micrographs in Figure 7.2A&B show that the flakes in both inks are thin and sheet like, as expected for 2D materials. Here the difference in the size of the nanosheets is clearly

seen, with the LPE material having significantly reduced lateral dimensions compared to the EE nanosheets.

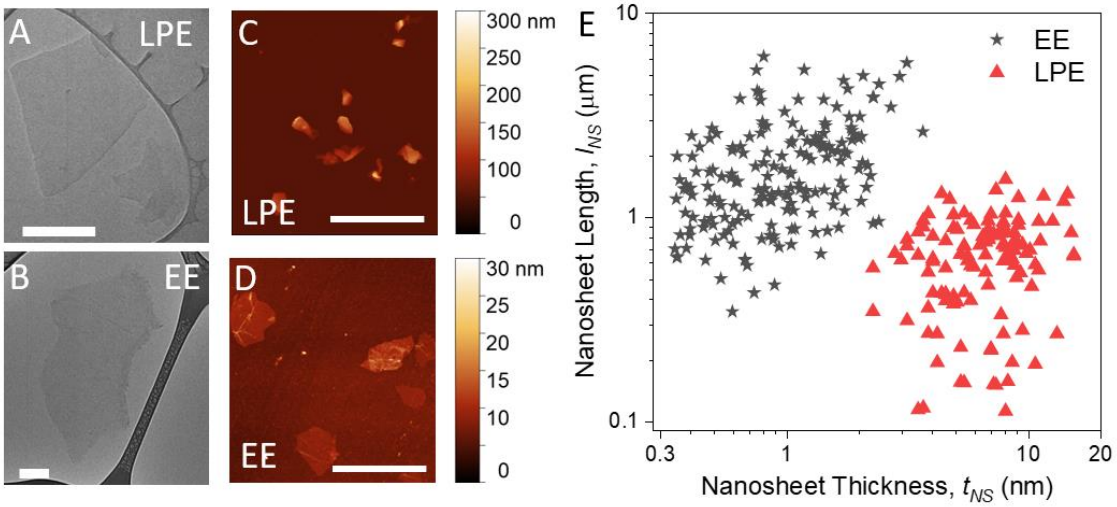

Figure 7.2: Nanosheet Characterisation. Representative TEM images of A) LPE and B) EE nanosheets, scale bar: 250 nm. Representative AFM Images of C) LPE and D) EE nanosheets, scale bar: 5 μm. E) Plot of nanosheet length vs. nanosheet thickness, each data point is an individual nanosheet measured using AFM.

The lateral dimensions of the nanosheets were further characterised using AFM. This enabled the measurement of the nanosheet thickness as well as the nanosheet length. For solution processed nanosheet networks, it is important to account for the difference between the measured thickness and the true thickness of the nanosheets by determining the layer number from AFM metrics. For graphene, each layer has a step height of 0.95 nm, with 1 nm of solvent trapped between the nanosheet and substrate which must also be subtracted. From the layer number, the true nanosheet thickness can be calculated, as each layer has a true thickness of 0.35 nm.[87]

Representative AFM images are shown in Figure 7.2C&D, showing the difference in size and thickness of LPE and EE nanosheets. The plot of nanosheet length vs. layer number in Figure 7.2E shows the differences in nanosheet length and thickness for both

production methods. From this it can be seen that there is no significant overlap between the two nanosheet distributions in the inks. This indicated that the two preparation methods yield nanosheets with significant differences in length and thickness. From these distributions it was possible to extract the mean nanosheet length and thickness for both materials. These are tabulated in Table 7.1. Of note is the significant difference, greater than an order of magnitude, in aspect ratio between the two materials. This is expected to have a significant effect on the conformality of the inter-nanosheet junctions as the larger, thinner nanosheets are more flexible.[6, 419]

Table 7.1: Mean Nanosheet Dimensions from AFM. Reported uncertainty is standard error.

	EE Graphene	**LPE Graphene**
Nanosheet Thickness	1.08 ± 0.05 nm	7.0 ± 0.3 nm
Nanosheet Length	1,880 ± 80 nm	660 ± 30 nm
Nanosheet Aspect Ratio	~1,740	~95

7.3.2 Film Characterisation

Figure 7.3A shows representative cross sectional SEM images of the LPE and EE films spray coated on glass. From these images it is clear that there are significant morphological differences between the two networks, with increased alignment and reduced porosity in the EE network compared to the LPE network. This is in line with expectation as reduced porosity is seen in larger thinner nanosheets,[120, 124, 245] compared to LPE material.[172]

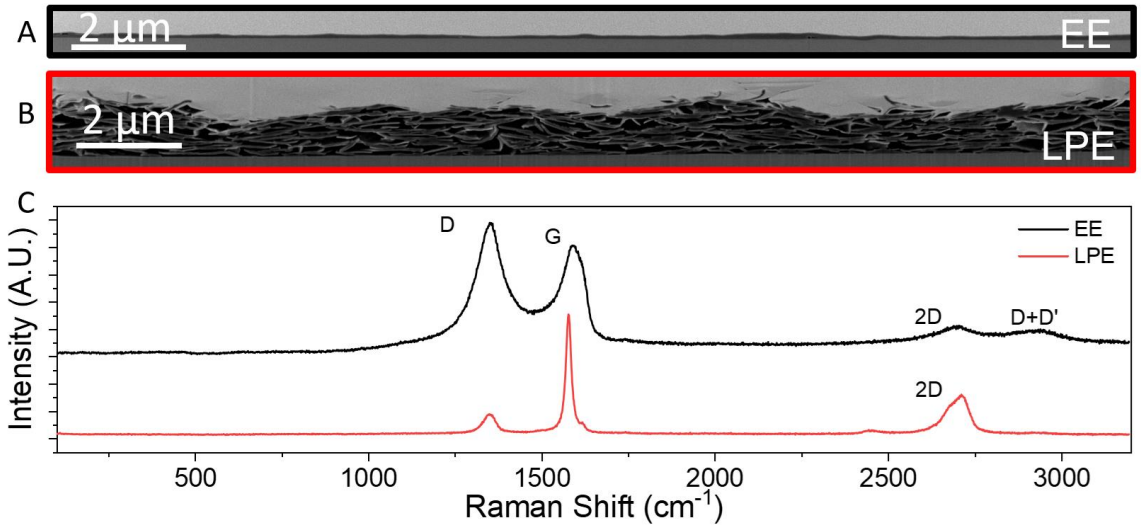

Figure 7.3: Film Characterisation. Cross sectional SEM images of spray coated A) EE and B) LPE nanosheet networks, showing film morphology. C) Raman spectra of LPE and EE films, with an input wavelength of 532 nm, showing the characteristic peaks.

Raman spectra of the nanosheets reveal that there are differences in the local crystallinity of the EE and LPE nanosheets. Most notable is the increased amplitude of the D peak with respect to the G peak in the EE graphene nanosheets compared to the LPE material. The I_D / I_G ratio been linked to increased defectivity in the nanosheets[200] and has been measured to be 1.19 and 0.187 for EE and LPE graphene produced in this study, respectively. This increase in defectivity with respect to the LPE nanosheets has been reported on previously for graphene exfoliated electrochemically using SO_4^{2-} intercalation.[420] This likely arises as a result of oxygen covalently bonding to the carbon atoms during exfoliation.[114]

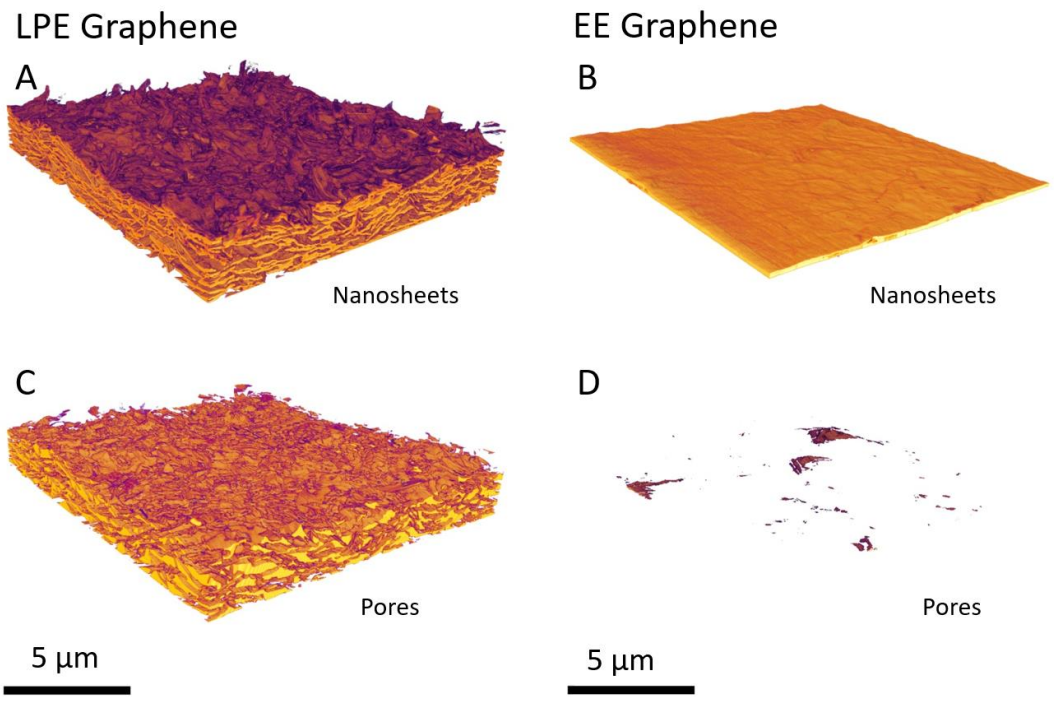

Figure 7.4: Nanosheet and Pore 3D Reconstruction. 3D reconstructions of the nanosheet network and the pore network in both LPE and EE films. Reconstructed from a stack of FIB-SEM nanotomography images.

Using trainable Weka segmentation[421, 422] it was possible to classify individual cross sectional images such as those shown in Figure 7.3A into nanosheet and pore pixels as outlined in Gabbett & Doolan *et al.*[146] These segmented images were stitched together to produce 3D reconstructions of the nanosheet and pore networks of the region of interest for the LPE and EE nanosheet networks, as shown in Figure 7.4. From these representations, the monolithic nature of the EE nanosheet network compared to the highly porous jammed network of LPE nanosheets is evident. Based on these morphological differences, one would expect significant differences in the electrical conductivity of the network, which has been shown to influence the piezoresistance of networks.

The 3D representations enable the quantification of the alignment, porosity, and tortuosity of the networks. This is a significant help in appreciating the differences between these two systems, and the effect nanosheet aspect ratio has on the final deposited film morphology. For the LPE network, the network porosity was measured to be 42.6%, with an in-plane tortuosity factor, κ, of 1.38. For the EE nanosheet network, the highly aligned conformal network had a significantly reduced porosity of 2.2% and a much lower tortuosity factor of 1.05, which is approaching the lower limit of 1. These values compare well to the previously reported values for LPE and EE graphene.[146] These morphological parameters suggest that the networks of EE materials should have a less tortuous path, through a network with fewer pores, increasing the network conductivity. The notable reduction in porosity of EE networks suggests that the nanosheets are in more intimate contact, likely leading to large area conformal junctions between the sheets.

This raises the question of the percolation behaviour of such a network: will the network build up in a percolative manner, as observed for LPE nanosheets in Chapter 5? This was initially characterised by taking top-down SEM of networks of different thicknesses.

7.3.3 Percolation Effects

As nanosheet networks are deposited onto a substrate the film thickness increases. As the thickness of the film increases, the electrical conduction through the network undergoes a percolative transition from insulating, when there are no connected pathways, to a bulk-like conduction state above a critical transition thickness unique to each network. These processes can be observed using SEM to image the networks at different thicknesses in the region of this transition, as shown in Figure 7.5.

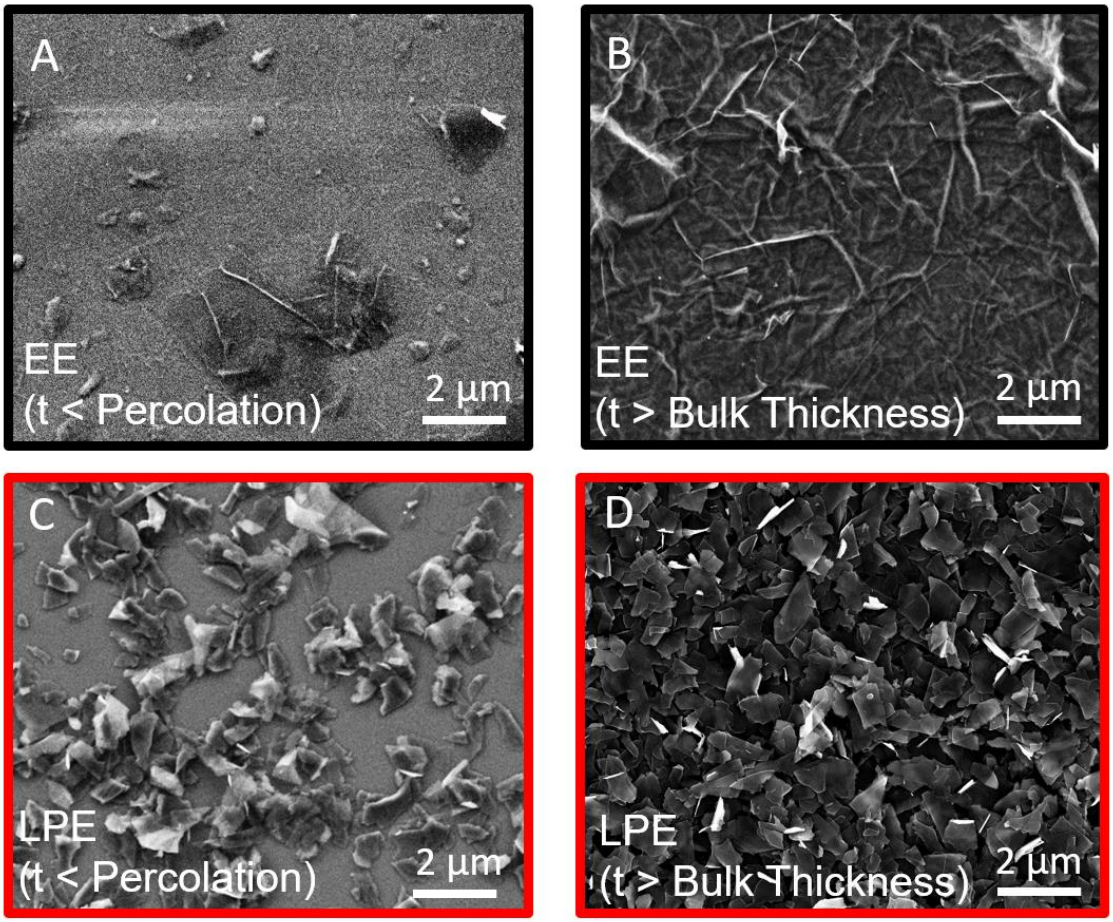

Figure 7.5: Network Imaging. SEM images of the top surface of the nanosheet network above and below the percolation threshold thickness. A) EE nanosheets below percolation. B) EE nanosheets above bulk-like thickness. C) LPE nanosheets below percolation. D) LPE nanosheets above bulk-like thickness.

When the film is very thin and below the percolation threshold for conduction there is no connected pathway between the electrodes and so the substrate is visible, with nanosheets scattered on the surface in isolation or in clusters smaller than the inter-electrode separation. This is observed for both EE and LPE films (Figure 7.5A&C) when the film thickness is less than the percolation threshold. As the film thickness increases the gaps between the nanosheets are filled in with additional material and the network becomes more conductive and no substrate is observed in the top-down SEM images of the

networks (Figure 7.5B&D). These films are significantly above the bulk-like transition thickness.

Interestingly, in comparing both materials, similar fill-in processes occur as the film thickness is increased. However, the EE nanosheets form more conformal, overlapping contacts, with ripples seen on the top surface of the bulk-like sample (Figure 7.5B). The LPE nanosheets retain their discrete nature, forming point-like contacts in a jammed network, without any conformal contacts or rippling observed. This is likely a result of the rigidity increase arising from thicker nanosheets with a smaller aspect ratio.[6, 419] These images and observations are in line with what is expected, based on the 3D reconstructions of the bulk-like networks, where the porosity of the networks is observed to vary greatly depending on the aspect ratio of the initial material.

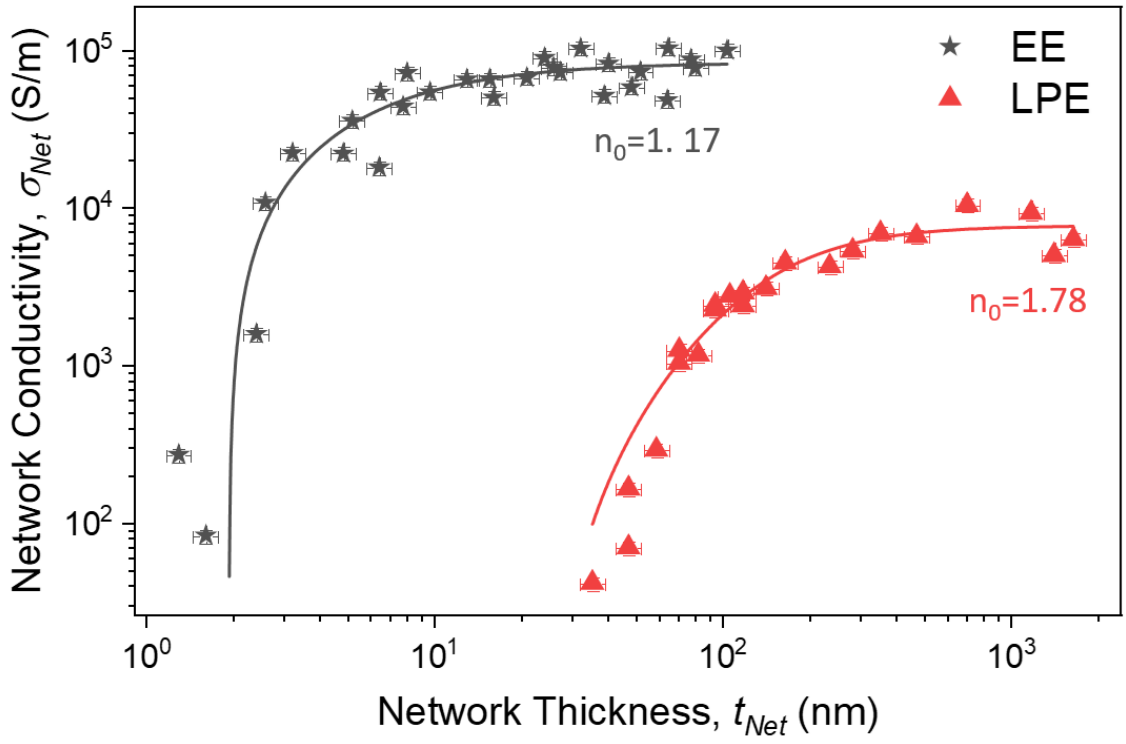

Figure 7.6: Electrical Percolation. Plot of network conductivity vs. network thickness for EE and LPE nanosheet films, with a fit to the percolation model given in Equation 7.1. Fit parameters are shown in Table 7.2.

This percolation scaling with film thickness is well known for LPE networks[248, 307, 378] and nanoparticle thin films.[168, 305, 311, 423] In order to quantify this transition, it is necessary to prepare several samples with different thickness ranging from below the percolation thickness (these should be electrically insulating), through the extrinsic electrical conductivity percolation region where conductivity scales with thickness, and up to a bulk-like thickness where the network conductivity reaches the intrinsic plateau. This requires the careful preparation of many films in order to identify the correct thickness ranges for each material. To enhance the conductivities, samples were post processed by annealing in a vacuum chamber at 350 °C for 1 h in an effort to remove any residual solvents or contaminants between the sheets.[6] Once sufficient data has been collected, the percolation scaling model (Equation 7.1) was applied to extract the key network parameters, as shown in Table 7.2.

Table 7.2: Fit parameters for fitting of data in Figure 7.6 with Equation 7.1.

	EE Networks	**LPE Networks**
$\sigma_{B,0}$	84,000 ± 6,000 S/m	7,700 ± 600 S/m
$t_{c,0}$	1.9 ± 0.8 nm	24 ± 21 nm
$t_{x,0}$	17 ± 5 nm	310 ± 70 nm
n_0	1.17 ± 0.19	1.78 ± 0.20

It should be noted that the n parameter had to be fixed for fitting. In order to identify the optimal n parameter, a range of n values between 1 and 2 were fixed and the data fitted with Equation 7.1. The adjusted R^2 values for each fit was plotted as a function of n, as shown in Appendix A.4. Fitting this data with a quadratic curve enabled the optimal n

value to be determined for both materials along with the associated uncertainty. The fitting in Figure 7.6 was then completed using the optimised n values.

Above the bulk transition thickness, the bulk-like conductivity of LPE and EE nanosheet networks is estimated to be 7,700 ± 600 S/m and 84,000 ± 6,000 S/m respectively. Similar conductivity values were reported for LPE graphene networks by Gabbett & Doolan *et al.*[146] and for EE graphene networks by Marković *et al.*[424] This disparity in bulk conductivities of EE and LPE nanosheets has previously been linked to the differences in the nanosheet thicknesses rather than being an effect of the nanosheet junction resistance decreasing.[146] However the EE network in question had a porosity of 28% compared to 2.2% in this case, with a factor of two difference in the network conductivity. This suggests that decreasing porosity has a non-negligible effect which improves conductivity in nanosheet networks.

From this fitting and the extracted transition thicknesses, it is observed that the thinner, more conformal EE nanosheets form conductive pathways at reduced network thicknesses compared to the LPE nanosheets where the nanosheets are not as aligned in the plane of the substrate. The LPE nanosheets are also thicker and will require a thicker film before all of the gaps in the network are filled in.[168] Similar observations can be made regarding the bulk-like transition point, t_x, in both cases.

In Chapter 5 for LPE nanosheets, the percolation exponent was reported to be > 3. This increased exponent can be attributed to a broader variation of junctions in the network, as a result of a more polydisperse nanosheet size distribution.[300] In this study, a small range of nanosheet sizes were selected by LCC, narrowing the distribution of junctions. As a result, the extracted exponent for the jammed LPE network approaches the theoretical 3D percolation exponent value of 2, while for the monolithic EE graphene network the percolation exponent approaches the theoretical 2D value of 4/3. The

percolation exponent has shown a capability to differentiate the morphological dimensional character of printed nanosheet networks.

7.3.4 Piezoresistive Response

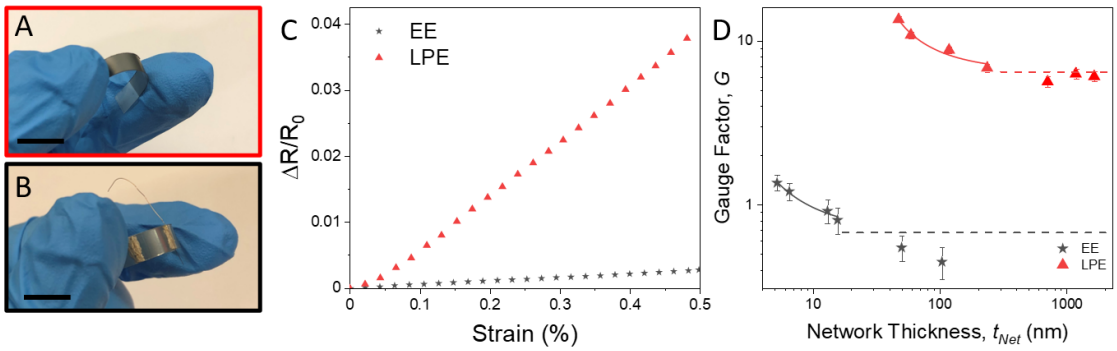

Figure 7.7: Piezoresistive Responses. Photograph of printed films of A) LPE and B) EE nanosheets on PET, bent between two fingers, scale bar: 1 cm. C) Plot of the fractional change in resistance vs. strain for bulk networks prepared with LPE and EE nanosheets. Measured for samples in the bulk thickness regime with a strain rate of 0.2 %/s. D) Plot of gauge factor vs. network thickness, with the solid lines representing the fits to data in the percolation regime, fitted using Equation 7.2, and the extracted G_{TNS} values illustrated using dashed lines.

As the bulk conductivity of the networks varies by an order of magnitude depending on the nanosheet aspect ratio, it was expected that this could lead to differences in the piezoresistive response of the networks, as observed in Chapter 5 and Chapter 6. Previous reports showed that gauge factors of nanosheet networks decreased as the network conductivity increased. Sample networks were spray coated onto PET polymer strips, as shown in Figure 7.7A&B, producing networks on a flexible substrate suitable for tensile testing to measure the piezoresistive response of the networks.

Figure 7.7C shows the fractional change in resistance with strain for a LPE and EE nanosheet network, both of which are above the bulk percolation thickness to avoid any effect percolation may have on the piezoresistive responses. Special care was taken to

avoid the onset of cracking in the networks, which has been shown to significantly increase the piezoresistive response in graphene nanosheet networks.[368] LPE materials have given a linear response up to 1% strain, but to avoid any nonlinearities a strain range of 0% to 0.5% was chosen.

Notably, the LPE network shows considerably increased piezoresistive response (G ~7) compared with the EE network (G ~0.6) at the t_x bulk-like thickness. This is consistent with the prediction of increased G for decreased conductivity. It is proposed that this is a result of the nanosheets in the EE networks sliding past one another more freely, while maintaining the conformal contact between the sheets with large overlapping junctions. The LPE nanosheets are expected to show a larger piezoresistive effect, due to the point-like contacts between the nanosheets in the network, which, when strained, will start to separate, increasing the resistance in the network. Note that the bulk gauge factor for the LPE nanosheet network is consistent with the nanosheet thickness scaling of gauge factor presented in Chapter 6.

In Chapter 5, it was demonstrated that the piezoresistive response of a LPE network can be significantly impacted by the network thickness when $t < t_x$, and that the gauge factor follows a model which can be simplified to the below equation.

$$G \approx G_{TNS} + \frac{t_{TNS}}{t - t_{c,0}} \qquad \text{(Eq. 7.2)}$$

Taking samples of films with thicknesses below the percolation transition for both EE and LPE networks and straining them to 0.5%, it was possible to extract the gauge factor as a function of network thickness below percolation, with the data plotted in Figure 7.7D. Fits to data in the percolation regime are shown as solid lines, while the extracted G_{TNS} values are illustrated as dashed lines. As expected, the LPE material followed the model, with an increase in gauge factor as t_c is approached from above. Interestingly, the EE

networks also followed this percolation model, which validates this model for both point-like and conformal junctions in nanosheet networks, in the percolation regime. However there is some scatter for $t > t_x$, potentially due to substrate effects. This demonstrates that when thicknesses are below t_x for both EE and LPE networks, the network structure is the dominant contributing factor to the increase in piezoresistive response. The fitting parameters are shown in Table 7.3.

Table 7.3: Fit parameters for data shown in Figure 7.7D, using Equation 7.2.

	EE Networks	**LPE Networks**
G_{TNS}	0.68 ± 0.04	6.5 ± 0.5
t_{TNS}	163 ± 18 nm	2.33 ± 0.22 nm
$t_{c,0}$	Fixed at 1.9 nm	Fixed at 24 nm

From this data, it can be observed that the fitting yields a value of t_c consistent with the electrical conductivity fitting, further validating the percolation model for piezoresistance presented in Chapter 5. Note that a similar model, capable of fitting the entire thickness range, was derived using Equation 7.1. This model is presented in Appendix A.4; however, it is unwieldy and the simple model previously presented yields a good fit to the data.

The EE nanosheet network has a bulk gauge factor of 0.68, which is below the gauge factor minimum fixed by the geometric condition $G = 1 + 2\nu$. Note that gauge factors of 0.55 and -2 have been reported for graphene nanoribbons on pre-strained substrates.[364] Furthermore, in Chapter 6, the results demonstrate that the nanosheets can have a negative contribution to the gauge factor of the network. An additional option could be that the EE

graphene network is an auxetic material with a negative Poisson ratio, however the Poisson ratio is predicted to be close to zero for highly aligned nanosheets.

Studying the t_{TNS} values and knowing from Chapter 5 that $t_{TNS} \approx n(dt_c/d\varepsilon)_0$, it is possible to compare the changes in percolation thickness as a function of strain for the two networks. For EE materials $(dt_c/d\varepsilon)_0$ = 2 nm, while for the LPE networks $(dt_c/d\varepsilon)_0$ = 92 nm. These correspond to a 0.02 nm and 0.92 nm change in the percolation thickness for each percent of applied strain. This accounts for a factor of five difference in fractional change in percolation thickness with strain. Considering the highly aligned EE nanosheets observed in the 3D reconstructions, this would suggest that, as the network is being strained, the EE nanosheets are sliding past each other, without greatly reducing the critical network thickness.

7.4 Conclusions

In this chapter, nanosheets of different aspect ratios were produced using LPE in NMP and EE with SO_4^{2-} ions. These nanosheets were size selected using LCC and transferred into IPA to produce inks suitable for spray coating, which were characterised spectroscopically and using AFM. These inks were spray coated to form nanosheet networks on glass and PET substrates. The network structure and morphology of both materials was studied using FIB-SEM nanotomography, yielding 3D reconstructions of the nanosheet and pore networks which could be quantitatively analysed for porosity and tortuosity. Significant differences in bulk conductivities were observed between the LPE and EE networks, in line with previous reports. The networks were also investigated in the percolation thickness regime using SEM and by measuring the electrical conductivity, which enabled the percolation exponent to be extracted, matching the theoretical 2D and 3D exponent for EE and LPE networks respectively. Piezoresistance of the networks was analysed in an attempt to understand the effect of nanosheet network morphology on

piezoresistive response. This showed that the nanosheets exhibited significantly different piezoresistive responses, however both materials showed an increase in gauge factor as the percolation threshold was approached from above. This study indicates that the aspect ratio of the nanosheets making up a network can have a significant impact on the morphological, electrical, and piezoresistive properties of the network, allowing these parameters to be engineered for applications in nanosheet network devices.

"The important thing is not to stop questioning.

Curiosity has its own reason for existing."

Albert Einstein

Chapter 8

Impedance Spectroscopy as a Tool to Characterise Junction Resistance and Nanosheet Resistance in Piezoresistive Networks

The work presented in this chapter has been adapted from the published work: "Using Electrical Impedance Spectroscopy to Separately Quantify the Effect of Strain on Nanosheet and Junction Resistance in Printed Nanosheet Networks," published in Small.[425]

8.1 Introduction

As previously outlined, nanosheet networks are composed of nanosheets and junctions and, under the application of strain, piezoresistive effects are observed at a network level. This results in challenges in converting nanosheet networks into mechanically flexible technologies. These low-cost, printable networks could enable 'Internet-of-Things' connected sensors, flexible displays, and even wearable, real-time health monitoring electronic devices. Enabling further understanding of these technologies has the potential to significantly improve the quality of life of patients, as well as improving diagnostic capabilities for medical professionals.

To date, the piezoresistive effect has been observed in many materials including metal foils,[230] semiconductors,[333] nanocomposites,[10, 166, 335, 346, 426] and nanosheet networks.[271, 360] In these systems, gauge factor has been engineered to enable strain gauge technologies and flexible electrodes, with gauge factors ranging from 0.01 to 2,600.[336, 349, 350] However, the underlying mechanisms behind such devices are broad and varied, ranging from geometric changes to changes in mobility, inter-particle conduction, and even network structure effects in the percolation regime. For nanosheet networks, these mechanistic determinations have been based on using simple physical models to understand the change in network gauge factor as a function of the network volume fraction, thickness, and conductivity. From these analyses, in certain conditions the inter-nanosheet junctions have been theorised to play a significant role in contributing to the piezoresistive response of the network. Such junctions are also proving to be a barrier in achieving theoretical conductivities and mobilities in nanosheet network devices,[257] therefore research has been conducted to measure these directly.

Even without strain, measuring these mean junction resistances has proven to be challenging. Researchers have locally deposited electrodes to measure the junction resistance in crossing pairs of nanotubes[427] and nanowires.[428] However, this approach is not feasible for networks with a vast array of junctions connected in series and in parallel. Conductive AFM can be used to measure junction resistances in networks, however these measurements are limited to sparse networks and the technique is very technically challenging.[264] Recently, an electrical impedance spectroscopy technique capable of measuring the mean nanosheet resistance and mean junction resistance in a nanosheet network has been developed.[147]

In this chapter, the application of this impedance technique to a network of electrochemically exfoliated MoS_2 nanosheets on a flexible substrate, under the

application of mechanical strain, is demonstrated. The networks are deposited from a liquid-liquid interface, creating a thin film of highly aligned nanosheets. These networks were firstly characterised using standard DC piezoresistance analyses including linear and cyclic mechanical deformation. The sample was then analysed using impedance spectroscopy at different applied strains to extract the junction and nanosheet resistance as well as junction capacitance as a function of strain. From this the key components within the network contributing to the piezoresistive effect in this system can be identified. This opens new potential in characterising this effect in nanomaterial systems.

8.2 Experimental Procedure

MoS_2 Exfoliation

EE of the layered MoS_2 crystal used an electrochemical setup consisting of a platinum foil (Alfa Aesar) anode and the bulk crystal as the cathode. The electrolyte consisted of 50 mL propylene carbonate with tetrapropylammonium (TPA) bromide (Sigma-Aldrich) at a concentration of 5 mg/mL. A potential difference of 8 V was applied for 30 mins to expand the layered crystal by ion intercalation. The expanded crystals were washed with DMF to remove any residual bromine and propylene carbonate before bath sonication in DMF with poly(vinylpyrrolidone) (PVP) (MW ~ 40,000, 1 mg/mL) for 5 mins. The dispersion was then centrifuged (Hettich Mikro 220) at 500 RPM for 20 mins to remove unexfoliated materials.

Size Selection

The dispersion was then size selected by centrifuging the supernatant (top 90% of liquid) at 1,000 RPM for 1 h. The sediment, which contains the size selected nanosheets, was resuspended in 2 mL DMF and centrifuged at 10,000 RPM for 1 h. This step was repeated twice to remove the residual PVP. The sediment was then resuspended in 0.5 mL IPA and centrifuged at 10,000 RPM to remove the residual DMF. Following this, the sediment

was redispersed in ~ 0.5 mL of IPA, yielding an MoS_2 dispersion with a concentration of ~ 2.5 mg/mL, which was used to deposit films.

Nanosheet Characterisation

UV-Vis spectroscopy (Perkin Elmer, Lambda 1050) was used to characterise the nanosheet based ink. Drop cast films of MoS_2 ink on Si/SiO_2, annealed at 120 °C for 30 mins, were analysed using Raman spectroscopy (WITec Raman Spectrometer, 523 nm). Electron microscope imagery of the film was carried out with the Zeiss Ultra SEM, with a 3 keV potential (working distance 5 mm), with the secondary electron detector.

Substrate Preparation

Kapton substrates (DuPont brand) were cleaned using IPA. Compressed N_2 was used to dry the samples. Evaporated electrodes (Ti/Au (5 nm/95 nm)) were then deposited using a Temescal evaporator (FC-2000). A shadow mask was used to define the electrode dimensions of L_{Ch} = 100 μm and W_{Ch} = 19.55 mm, with contact pads to facilitate electrical contact after film deposition. Immediately before film deposition, substrates were treated for 3 mins using a UV Ozone Cleaner (Ossila).

Film Deposition

To deposit films using the Langmuir-Schaefer method, a custom setup was used, as described in recent publications.[124, 429] The custom substrate holder, with substrate mounted, was placed in a glass beaker (250 mL) which was filled with DI water until the holder was submerged. Distilled n-Hexane (2 mL) was added to the top of the water, forming a liquid-liquid interface, as shown in Figure 8.1C. The nanosheet ink was injected into the interface using a Pasteur pipette, until uniform coverage was observed by eye. The substrate was lifted through the liquid-liquid interface, transferring the nanosheet film onto the substrate. The substrate was dried at room temperature, before annealing in an Argon atmosphere at 120 °C for 2 h.

Thickness Characterisation

The film thickness of the network was determined using a Filmetrics Profilm3D® optical profiler in phase shift interferometry mode and a 50X Nikon objective lens. Thickness was calculated by taking the step height from the top of the film and a scratch in the film to the Si/SiO_2 substrate below using the histogram measurement protocol on Profilm Online. Si/SiO_2 was used as a substrate as it is more planar for accurately measuring optical interference, as the technique is sensitive to bending of the substrate.

Electromechanical Testing

The samples were mounted in the clamps of a Zwick Z0.5 ProLine Tensile Tester (100 N Load Cell). The tester applied tensile stress to the mounted device. DC electrical characterisation was carried out by connecting the sample to a Keithley (KE2601) electrical source meter in a two-probe setup to measure resistance.

Impedance Spectroscopy Measurements

Impedance spectra were measured using the Keysight E4990E Analyser (max frequency: 30 MHz), with the attached 16047E connector, to connect the sample's wires to the analyser. Short (<5 cm) wires were attached to the gold contact pads on the substrate with conductive silver paint (Ted Pella) to avoid high frequency inductive artifacts. The analyser was calibrated in the open circuit, short circuit, and fixed load (100 Ω standard resistor) conditions. Spectra were collected using the precision setting "speed 3" (instrument setting related to the integration time) and an amplitude of 500 mV.

The UV- Vis spectroscopy presented in this chapter was carried out by Anthony Dawson. Nanosheet exfoliation, film deposition and Raman spectroscopy were carried out by Dr Tian Carey.

8.3 Results and Discussion

8.3.1 Material Characterisation

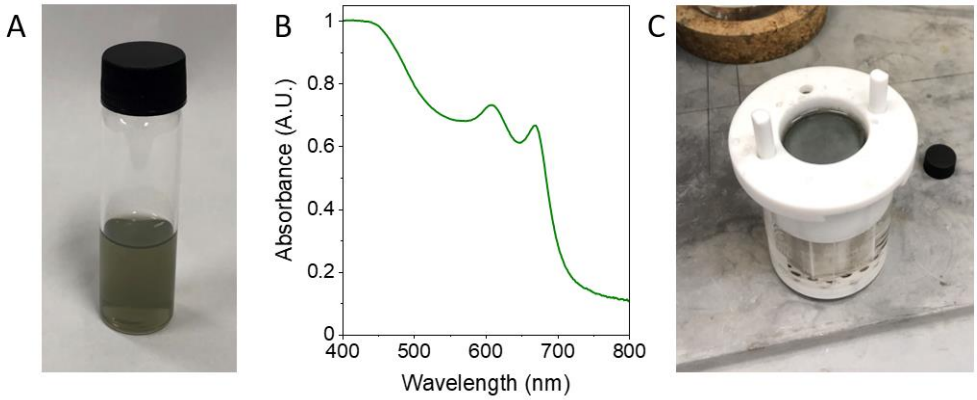

Figure 8.1: Ink Characterisation. A) Photograph of MoS_2 nanosheets dispersed in IPA. B) UV-Vis absorbance spectrum the nanomaterial ink, normalised at 400 nm. C) Photograph of the film deposition setup, with a layer of MoS_2 assembled at the liquid-liquid interface between water and hexane.

In this study, MoS_2 nanosheet networks prepared by EE were used as a model system to characterise network piezoresistance using impedance spectroscopy. The choice of this model system instead of LPE graphene is a result of recent successes in characterising both junction and nanosheet resistance of unstrained networks of MoS_2 nanosheets prepared in a similar manner by Gabbett & Kelly *et al*.[147] Measurable values have not yet been reported from network impedance analysis of LPE nanosheets in the literature. The initial step was to prepare and characterise the nanosheet dispersions used to deposit the networks. EE of bulk layered crystals of MoS_2 was carried out using TPA^+ ions, in line with previous reports of EE MoS_2.[124, 147] The resulting nanosheets were dispersed in IPA to form an ink, with a characteristic green tint from MoS_2, as shown in Figure 8.1A. The dispersion was confirmed to be MoS_2 using the absorbance spectrum, shown in Figure

8.1B, which showed the A and B excitonic absorbance peaks, characteristic of a MoS_2 nanosheet dispersion.[430]

Using the modified interfacial assembly of films at liquid-liquid interfaces, inspired by the Langmuir-Schaeffer deposition method,[124, 147] aligned thin films of nanosheets were deposited on Kapton substrates. This process requires the ink to be injected into a water-hexane interface, where the difference in surface energy promotes the formation of a highly aligned, thin nanosheet network at the interface of the immiscible liquids. The film formed at the interface is shown in Figure 8.1C. This thin network is then deposited onto the substrate by lifting the substrate through the interface. Thicker films can be prepared by repeating the process to build up successive layers. The nanosheet lengths and thicknesses for this standardised preparation of MoS_2 inks are reported in Appendix A.5, extracted from the report of Gabbett & Kelly *et al*.[147]

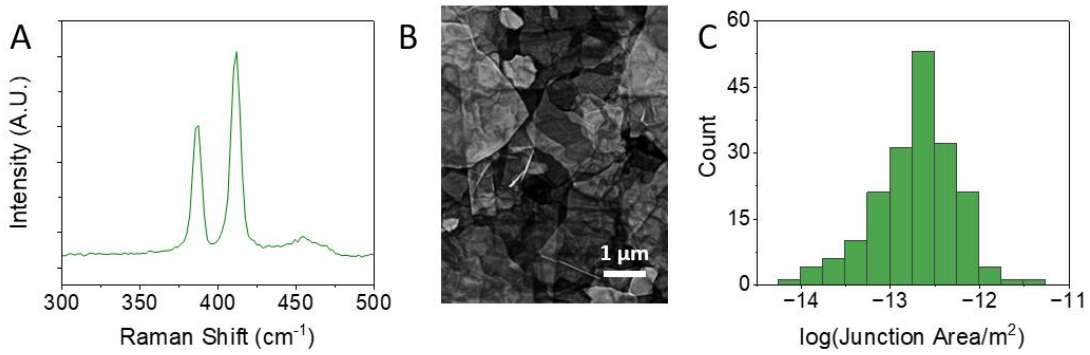

Figure 8.2: Film Characterisation. A) Raman spectrum of the nanosheet film showing characteristic modes. B) SEM of the nanosheet film. C) Histogram showing the measured junction areas for >180 junctions in the film from SEM images.

A Raman spectrum (Figure 8.2A) of the MoS_2 nanosheets deposited onto a Si/SiO_2 by drop casting shows the characteristic A_{1g} and E^1_{2g} Raman active modes of MoS_2.[431, 432] Using SEM, the top surface of the nanosheet network can be imaged and studied, with a representative image showing the as deposited MoS_2 nanosheets on the Kapton substrate

in Figure 8.2B. This SEM image shows large area junctions, where the highly aligned nanosheets conformally overlap with neighbouring nanosheets. This low porosity, aligned, and conformal network morphology is typical of networks of nanosheets exfoliated electrochemically.[124, 147] The formation of such conformal junctions with EE nanosheets, in contrast with LPE nanosheets, is as a result of increased flexibility, due to the reduction in nanosheet thickness, and the ability to form stronger vdW bonds with neighbouring sheets because of their larger nanosheet area.[6] Large conformal junctions exhibit significantly lower junction resistance[147] resulting in increases in network mobilities[120, 245] when compared to LPE nanosheet networks. A recent study by Carey *et al*. demonstrated network mobilities in excess of 10 cm^2/Vs for electrochemically exfoliated TMD nanosheets deposited using the Langmuir-Schaefer inspired method.[124]

It is possible to quantitatively analyse the nanosheet junctions using the top-down SEM images. By identifying the conformal inter-nanosheet junctions and measuring the overlap areas of over 180 such junctions in ImageJ, a distribution of junction areas can be measured. This histogram is plotted in Figure 8.2C, showing a roughly log-normal distribution. The mean junction area, $A_{J,0,}$ was determined to be 0.33 ± 0.03 μm^2. This mean junction overlap area is consistent with the area reported by Gabbett & Kelly *et al*. in their study.[147] Measuring this area will enable deeper analysis of the role of the junctions between the nanosheets in the MoS_2 networks.

8.3.2 Basic Electromechanical Properties (Linear Strain and Cycling)

To evaluate the piezoresistive response of the EE MoS_2 network, the evaporated gold (5 nm/95 nm Ti/Au) bottom contact electrodes were electrically contacted. These defined the channel length, L_{Ch}, and channel width, W_{Ch}, to be 100 μm and 19.55 mm respectively. The network thickness, t_{Net}, was determined to be 19.6 ± 1.2 nm. The zero-

strain resistance was measured to be 1.38 kΩ, yielding a network conductivity, σ_{Net}, of 189.6 S/m. This is roughly in line with the report of Gabbett & Kelly *et al*. who reported 41 S/m on an Si/SiO_2 substrate.[147]

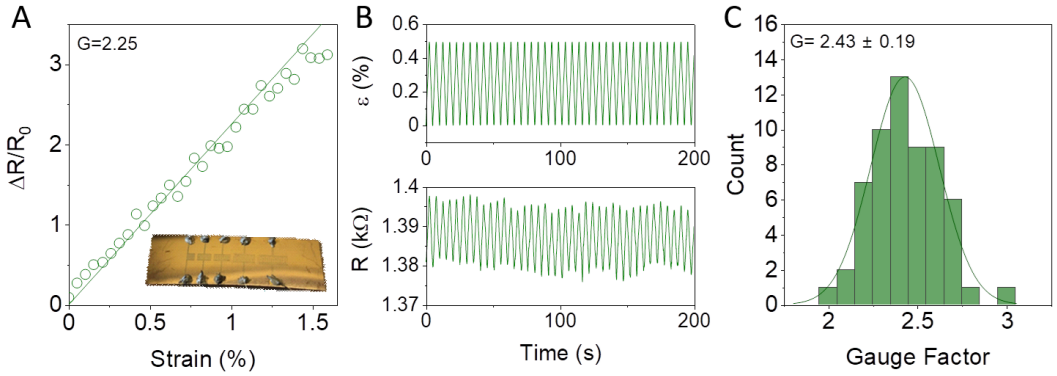

Figure 8.3: DC Piezoresistance. A) Plot of the fractional change in resistance vs. strain. The strain was applied with a strain rate of 0.05 %/s. Inset: a photograph the device. B) Cycling data showing the applied sawtooth strain and the resistance response from the of the film, with an applied strain rate of 0.2 %/s and a strain amplitude of 0% to 0.5%. C) Histogram of measured gauge factors from the cycling measurements.

The first task when measuring piezoresistance of any system is to identify the strain range where the electrical response is linear with strain.[230, 336] This was conducted by mounting the network into the tensile tester and straining the substrate from 0% to 1.6% strain with a strain rate of 0.05 %/s, while using a source meter to measure the resistance. This enabled the plotting of the fractional change in resistance vs. strain as shown in Figure 8.3A. The gauge factor is the slope of this plot in the linear low strain regime and, for this network, G_{Net} was measured to be 2.25, showing a linear range up to 1.2%.

Assessing how this compares to previous reports, similar large aspect ratio EE graphene nanosheets report linear ranges up to 1.5%, with G_{Net} of 6.[360] These gauge factors are lower than those reported with LPE nanosheets,[378] consistent with the results of Chapter

7. Comparing with MoS_2 nanosheets, Chu *et al*. investigated MoS_2 nanosheets coated onto carbon fibres, reporting a linear range of 0.8%, however they did not report on the network gauge factor.[426]

In any piezoresistive system, a key consideration is the reliability and cyclability of the material while maintaining a similar responsiveness to strain. To characterise this cyclic response, repeated sawtooth strain cycles were applied to the network while measuring the DC resistance of the film. In order to ensure that all of the response was within the linear piezoresistive regime, the strain amplitude was set between 0% and 0.5% strain, with a strain rate of 0.2 %/s. The strain profile and resistive response are shown in Figure 8.3B. The electrical response of the network matches the strain input, as it also displays a sawtooth profile and is in phase with the strain profile. This cyclic measurement technique also allows for the effects of random signal noise to be minimised when measuring the gauge factor as the gauge factor is averaged across several cycles.

The minimum and maximum measured resistance values ($R_{n,0}$ and $R_{n,\varepsilon_{Max}}$ respectively) for each strain cycle number, denoted by n, can be extracted from the resistance vs. time plot. These correspond to the unstrained and maximally strained resistances of the network. As the cycling amplitude was carefully chosen to be in the linear regime, the gauge factor of each cycle can be calculated using the following expression:

$$G_n \approx \left(\frac{R_{n,\varepsilon_{Max}} - R_{n,0}}{R_{n,0}\varepsilon_{\max}} \right) \qquad \text{(Eq. 8.1)}$$

The gauge factor was calculated from the profile for more than 50 cycles, and the distribution of gauge factors, ranging from 2 to 3, was plotted as a histogram, as shown in Figure 8.3C. From this distribution the average gauge factor was determined to be 2.43 ± 0.19. This value is consistent with the value extracted from the slope of the plot in Figure 8.3A.

These are relatively low gauge factors, in line with previous observations for highly aligned nanosheets. In order to develop a complete understanding of the system, it is necessary to consider the models of conduction in nanosheet networks presented by Gabbett & Kelly *et al*. They state that for low porosity, doped nanosheets the network resistivity can be approximated by Equation 8.2, as shown in Appendix A.5.

$$\rho_{Net} \approx 2t_{NS}\left[R_{NS} + R_J\right] \qquad \text{(Eq. 8.2)}$$

By substituting this equation into Equation 4.10, it is possible to relate the gauge factor response to the nanosheet resistances and junction resistances. Note that nanosheet networks are mechanically anisotropic, hence the in-plane (ν_y) and out-of-plane (ν_z) Poisson ratios are expected to be different. This will have an impact on the first term, which must be considered when the gauge factor is low. This yields Equation 8.3, for which the full derivation has been included in Appendix A.5.

$$G_{Net} = \left(1 + \nu_y + \nu_z\right) + \frac{dR_{NS}/d\varepsilon + dR_J/d\varepsilon}{R_{NS,0} + R_{J,0}} \qquad \text{(Eq. 8.3)}$$

This equation can be thought of as two distinct parts. The first term is related to the piezoresistive response arising from dimensional changes with deformation ($G_{Dimensional}$). The second term describes the piezoresistive response intrinsic to the network ($G_{Intrinsic}$). This model suggests that nanosheet networks, in the absence of any intrinsic network contribution, will exhibit a piezoresistive response of $G_{Net} = (1 + \nu_y + \nu_z)$ purely due to the geometric effects. It is unclear whether the gauge factor of the MoS_2 network under investigation is purely due to these geometric effects or if there is an intrinsic piezoresistance in the system. Hence, it is necessary to measure R_{NS} and R_J, along with their strain derivatives for the network, to understand the role of $G_{Intrinsic}$.

8.3.3 Impedance Spectroscopy of a Network at Different Strain Magnitudes

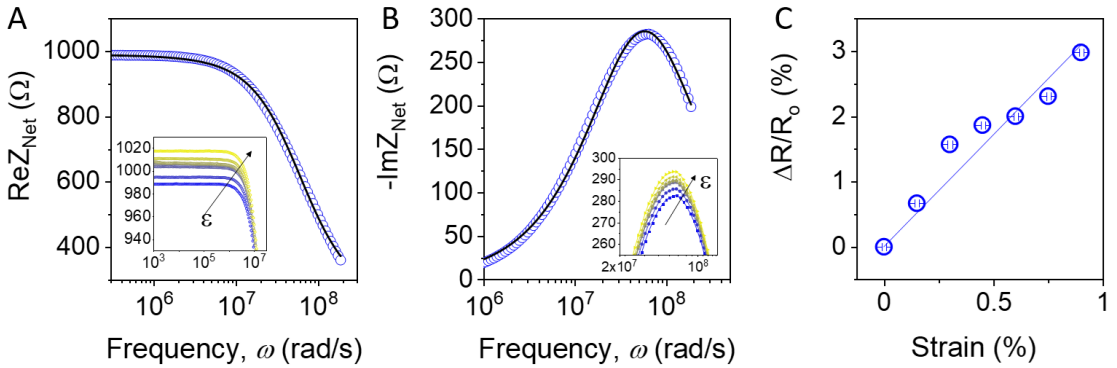

Figure 8.4: AC Characterisation. A) Plot of the real component of network impedance vs. angular frequency. Inset: plot for different applied strains. B) Plot of the imaginary component of network impedance vs. angular frequency. Inset: plot for different applied strains. C) Plot of fractional change of the low frequency impedance vs. applied strain, the AC equivalent to Figure 8.3A.

The impedance spectroscopy technique measures the electrical response of a material across a range of applied AC voltages. In this way, it is able to increase the range of data collected about the sample compared to DC resistance measurements, opening up opportunities to extract more information about the sample. Knowing that the AC impedance takes a complex value, it is possible to extract both the real ($\mathrm{Re}\,Z_{Net}$) and imaginary ($-\mathrm{Im}\,Z_{Net}$) impedance values. In Figure 8.4A and 8.4B, these impedance values are plotted against the AC angular frequency, ω. The spectrum of $\mathrm{Re}\,Z_{Net}$ has a low frequency plateau, which falls off rapidly at higher frequencies, and the $-\mathrm{Im}\,Z_{Net}$ spectrum has a peak with a maximum at relatively high frequency, close to the fall off point of the $\mathrm{Re}\,Z_{Net}$ plateau. These impedance spectra were measured for the nanosheet network at different strain magnitudes, ranging from 0% strain to 0.9%. In practice, the spectral profiles at different strain values were broadly similar to those measured in the

unstrained state. The only significant differences were the plateau region of the $\mathrm{Re}\,Z_{Net}$ spectra and near to the peak of the $-\mathrm{Im}\,Z_{Net}$ spectra. These regions have been scaled in for the plots inset in Figure 8.4A and 8.4B.

Prior to completing detailed analysis and fitting of the spectra, the real impedance at low frequencies was extracted for each strain magnitude, as these are roughly equivalent to the DC resistance.[147] From qualitative observations of the inset in Figure 8.4A the plateau resistance in $\mathrm{Re}\,Z_{Net}$ steadily increases with strain. Formalising this analysis, the fractional change in resistance can be determined using the following equation. $\left([\mathrm{Re}\,Z_{Net}(\varepsilon)-\mathrm{Re}\,Z_{Net}(\varepsilon=0)]/\mathrm{Re}\,Z_{Net}(\varepsilon=0)\right)_{\omega\to 0}=\Delta R/R_0$. These values are plotted against the strain, as shown in Figure 8.4C. From this plot, a gauge factor of 3.4 ± 0.2 was found, which is reasonably consistent with the values extracted from the DC analysis.

Equivalent circuit models are generally used to fit impedance spectra, with the shape of the spectrum guiding the choice of suitable equivalent circuit. Based on the shapes of the measured spectra, the equivalent circuit model chosen for the system is composed of a resistor, R_S, which is in series with a combination of a resistor and a capacitor in parallel, R_P and C_P,[147, 433] as shown in Figure 8.5A. This type of circuit has previously been used to model nanosheet networks, where these individual circuit elements have been ascribed to physical phenomena in the network.[434] In such networks, R_S represents the contributions of nanosheets to the total film resistance, R_P represents the inter-nanosheet junction contribution to the total film resistance, and C_P represents the capacitance of all the junctions in the network.[147]

As the values of R_P and C_P are based on behaviours of a collection of microscopic elements which take a range of values, this can broaden the real and imaginary impedance

spectra.[435] As a result, the impedance spectra must be fitted using the following equations (8.4 A&B), where the capacitor is replaced with a constant phase element, introducing the parameter n.[147, 435] In these equations, n can be related to the distribution of the junction resistance and junction capacitance of the network.[435] When $n = 1$, the system behaves as a simples Randles circuit, however a decrease in n is related to a larger distribution of R_P and C_P.[147]

$$\mathrm{Re}\,Z(\omega) = R_S + \frac{R_P + [1 + (\omega R_P C_P)^n \cos(n\pi/2)]}{1 + 2(\omega R_P C_P)^n \cos(n\pi/2) + (\omega R_P C_P)^{2n}} \quad \text{(Eq. 8.4A)}$$

$$-\mathrm{Im}\,Z(\omega) = \frac{R_P (\omega R_P C_P)^n \sin(n\pi/2)]}{1 + 2(\omega R_P C_P)^n \cos(n\pi/2) + (\omega R_P C_P)^{2n}} \quad \text{(Eq. 8.4B)}$$

By fitting the impedance spectra with these equations, it is possible to extract R_S, R_P, and C_P with $n \sim 0.83$ from the real impedance spectrum, along with R_P and C_P with $n \sim 0.84$ from the imaginary impedance spectrum. However, the parameters of real interest are the microscopic counterparts to these parameters, R_{NS}, R_J, and C_J, which represent the mean values of the resistance of individual nanosheets and junctions as well as the mean capacitance associated with individual junctions respectively. This transformation can be carried out using the conversions shown in Equation 8.5A-C, which have been shown by Gabbett & Kelly *et al.*[147] These equations assume that the nanosheet carrier density is sufficiently high, in order to use the simplified model of network resistivity, which has been validated for EE MoS_2 by previous reports.[124, 147]

$$R_{NS} \approx \frac{W_{Ch} t_{Net}}{L_{Ch}} \frac{(1 - P_{Net})}{2 t_{NS}} R_S \quad \text{(Eq. 8.5A)}$$

$$R_J \approx \frac{W_{Ch} t_{Net}}{L_{Ch}} \frac{(1 - P_{Net})}{2 t_{NS}} R_P \quad \text{(Eq. 8.5B)}$$

$$C_J = R_P C_P / R_J \quad \text{(Eq. 8.5C)}$$

For these conversions, the terms and their associated values are as follows: t_{Net} = (19.6 ± 1.2) nm is the network thickness, L_{Ch} =100 µm and W_{Ch}=19.55 mm are the channel length and width, t_{NS} =3.3 nm is the mean nanosheet thickness, and P_{Net} represents the network porosity (approximated to be zero for EE networks). It was noted that as the substrate was strained, the Poisson effect would lead to changes in W_{Ch} with applied strain, in addition to the expected changes in L_{Ch}. Changes in channel width were accounted for by taking a Poisson ratio of 0.39 for the Kapton substrate,[276] while the out-of-plane Poisson ratio of the aligned nanosheet network is assumed to be negligible ($\nu_Z \approx 0$). As a result, t_{Net} is constant.

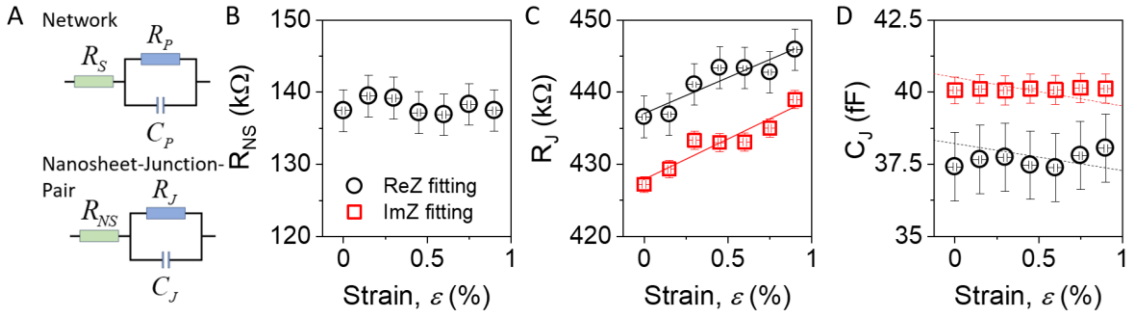

Figure 8.5: Extracted Electrical Parameters. A) Diagram of the equivalent circuits for the overall network and the nanosheet-junction pair. B) Plot of nanosheet resistance vs. strain extracted from fitting real impedance spectra. C) Plot of junction resistance vs. strain extracted from fitting real and imaginary impedance spectra. D) Plot of junction capacitance vs. strain extracted from fitting real and imaginary impedance spectra.

The extracted and converted values of R_{NS}, R_J, and C_J with respect to the applied strain were plotted in Figure 8.5 B-D respectively. Notably, as R_J and C_J could be extracted from both the $\mathrm{Re}\,Z_{Net}$ and the $-\mathrm{Im}\,Z_{Net}$ spectra, they are shown in black for data extracted from fitting $\mathrm{Re}\,Z_{Net}$ and red for data extracted from fitting the $-\mathrm{Im}\,Z_{Net}$. The unstrained

nanosheet resistance value of 138 ± 3 kΩ gives a nanosheet conductivity of 1,000 S/m, slightly higher than that reported by Gabbett & Kelly *et al*.[147]

From Figure 8.5B, it is observed that there is no significant change in the nanosheet resistance as a function of applied strain in the low strain linear regime, up to 0.9%. Thus, it can be stated that $\left(dR_{NS}/d\varepsilon\right)_0 \approx 0$. It is known that individual MoS_2 nanosheets display an intrinsic gauge factor of G_{NS} = -50.[346] As the nanosheet resistance is unchanging, the additional strain applied to the individual nanosheets as the network is strained is believed to be very small. This implies that there is little to no stress transfer to the nanosheets in this particular network. From this result, it is hypothesised that the nanosheets must slide with respect to one another when strain is applied to the network.

The junction resistance values were extracted from fitting of both the real and imaginary spectra, and R_J vs. strain was plotted for both data sets as shown in Figure 8.5C. Note that the R_J values did differ slightly, however the data sets follow the same trend and each data set differs by only ~1% from the common mean of both data sets. The mean unstrained R_J was determined to be 432 ± 3 kΩ. This is slightly lower than previous reports of ~2 MΩ for similar networks.[147] Both data sets display a linear increase in R_J with applied strain in the linear regime, with almost identical slopes of 1,000 ± 170 kΩ and 1,120 ± 160 kΩ, per unit strain. These give an average value of $dR_J / d\varepsilon \approx$ 1,060 ± 170 kΩ, which can be divided by the unstrained junction resistance, to give the junction gauge factor, G_J, of 2.5±0.4. This value is in line with the network gauge factor measured from the DC cyclic strain measurement. Thus, in this system it is concluded that the junctions are modulating the piezoresistive response more significantly than the nanosheets when the network is strained.

As stated previously, it was possible to extract C_J values from the real and imaginary spectra, and so both data sets have been plotted vs. strain in Figure 8.5D. Note that both data sets show very little strain dependence and the measured C_J values are broadly similar, within a few percent of their common mean value.

8.3.4 Sliding Model

With these AC measurements, it is possible to calculate the dimensional and intrinsic contributions to the gauge factor. The dimensional contribution can be written as $G_{Dimensional} = (1+\nu_y+\nu_z)$. ν_y is the Poisson ratio of the Kapton substrate, reported to be 0.39.[276] ν_z is the out-of-plane Poisson ratio of the aligned MoS_2 network, which can be as small as -0.1 to 0.1 in nanomaterial networks[280-282] and could approach zero in a highly aligned network.[283-286] This gives $G_{Dimensional} \approx 1.4$. Substituting the measured values for R_{NS} and R_J, along with their strain derivatives, into the second term in Equation 8.3 yields $G_{Intrinsic}$ = 1.9 ± 0.3. This gives a network gauge factor of G_{Net} 3.3 ± 0.3, in line with the value extracted from Figure 8.4C.

These results are interesting, however having a physical model to help fully understand the process would be desirable. The first key element observed was that the nanosheet resistance remained unchanged with applied strain to the network. Knowing that MoS_2 nanosheets have a significant negative intrinsic piezoresistive response, this indicates that the nanosheets slide past each other instead of deforming in response to the network being strained.

In Appendix A.5, a simple model is derived, which shows that in an aligned nanosheet network where nanosheets can slide past each other, under the application of strain, the average junction area, A_J, can be expressed by Equation 8.6 below.

$$A_J = A_{J,0}\left[1-\frac{(1-f_{J,0})}{f_{J,0}}\varepsilon\right] \quad \text{(Eq. 8.6)}$$

In this equation, the key terms are as follows: $A_{J,0}$ is the average unstrained junction area and $f_{J,0} = A_{J,0} / l_{NS}^2$. The junction resistance can then be expressed as $R_J = (RA)_J / A_J$. In nanosheet networks, $(RA)_J$ is a fundamental property of the junctions. As a result of substitution and using the approximation for small values of x, $(1-x)^{-1} \approx 1+x$, the following model for R_J can be derived:

$$R_J \approx \frac{(RA)_J}{A_{J,0}}\left[1+\frac{(1-f_{J,0})}{f_{J,0}}\varepsilon\right] \quad \text{(Eq. 8.7)}$$

Looking at the dependences in this model, there is a clear linear dependence of junction resistance with strain, as observed in Figure 8.5C. This model also predicts that the ratio of slope to intercept for R_J vs. strain should be equivalent to $(1-f_{J,0})/f_{J,0}$ which has been determined experimentally to be 2.45 ± 0.4, giving $f_{J,0}$ = 0.29 ± 0.05. Note that $f_{J,0} = A_{J,0} / l_{NS}^2$, which can be calculated from the previously measured nanosheet length (1 ± 0.03 μm) and junction area (0.33 ± 0.03 μm^2). This yields a second measurement of $f_{J,0}$ = 0.33 ± 0.04, in excellent agreement with the impedance derived parameters, implying that the simple model can be used to model this system.

Considering the junction capacitance can be written in a similar form, by starting from $C_J = \varepsilon_r \varepsilon_0 A_J / l_J$, where l_J is the spacing between nanosheets at the junction, substitution for A_J yields Equation 8.8.

$$C_J = \varepsilon_r \varepsilon_0 \frac{A_{J,0}}{l_J}\left[1-\frac{(1-f_{J,0})}{f_{J,0}}\varepsilon\right] = C_{J,0}\left[1-\frac{(1-f_{J,0})}{f_{J,0}}\varepsilon\right] \quad \text{(Eq. 8.8)}$$

Plotting this equation using the negative of the slope/intercept ratio found above (Figure 8.5D), it is observed that very little change in capacitance is expected by the model, with the trend falling within the uncertainty of the measured C_J values. However, the expected trend of decreasing C_J with increasing strain predicted by the sliding model is not clearly observed in the measured C_J data. The data potentially shows a plateau or an increasing trend.

It is postulated that there are other effects relevant to the capacitance of the junctions including charge traps at vacancies in the nanosheets,[262, 436] at interfaces,[437, 438] or potentially in surrounding oxides,[439, 440] if present. These will each act as capacitive elements with wide ranges of time constants, introducing a frequency-dependent component to the model circuit system.

This imperfect data shows that the simple model initially proposed for the junction capacitance is not perfect and that, in future, alternative circuit elements must be considered in order to fully describe the nature of the transport across the junctions. This opens exciting research questions for future researchers.

8.4 Conclusions

The piezoresistive properties of highly aligned nanosheet networks prepared from electrochemically exfoliated MoS_2 sheets were investigated in this chapter. These were prepared by assembling nanosheets at a water-hexane interface and depositing them onto a flexible Kapton substrate. These nanosheets were characterised spectroscopically and microscopically. Electromechanical characterisation of the networks measured the resistance change as the networks were strained linearly and with a sawtooth strain profile. Impedance spectroscopy was combined with tensile straining of the network to give insights into the phenomenon of piezoresistance in nanosheet networks. From this analysis, the mean values of nanosheet resistance, junction resistance, and junction

capacitance of the network were directly measured as a function of applied strain. For the MoS_2 network under investigation, it was observed that strain had a significant impact on the inter-nanosheet resistance, while there was no measurable change in the nanosheet resistance. This suggests that the nanosheets slide past one another rather than experiencing the applied strain. This sliding mechanism was verified using a simple physical model of aligned nanosheets sliding past each other.

"The science of today is the technology of tomorrow."

Edward Teller

Chapter 9
Conclusions and Future Work

9.1 Conclusions

In this thesis, nanomaterials and, in particular, networks of 2D nanosheets were discussed. These systems have proven to be useful in a broad array of applications from electronics to catalysts and beyond. The results presented in this work provide insight into methods of tuning the piezoresistance and conductivity of such networks, along with models to predict these behaviours and techniques to directly measure the nanosheet and junction resistances in these systems.

While graphene nanosheet nanocomposite piezoresistors were being investigated, it was observed that despite the high gauge factor values, the conductivities were low and there were challenges with frequency dependent responses and hysteresis effects in the electromechanical response. This motivated the investigation of spray coated polymer-free networks of graphene nanosheets in an effort to mitigate these negative trends, while using learnings from nanocomposite systems. By modulating the thickness of the network, it was possible to prepare films in the percolation regime. Varying the thickness had a measurable effect on the electrical conductivity and piezoresistive response of the nanosheet network, with bulk conductivities of ~260 S/m and maximum gauge factors of

~350. Simple models were developed to relate gauge factor to network thickness and conductivity in the percolation regime. By fitting these models, it was observed that the significant contributing factor augmenting the piezoresistive response in nanosheet networks close to the percolation threshold is the effect of strain on the network structure, and, as a result, the percolation threshold. These devices also displayed cyclic stability over 1,000's of cycles, less than 10% electromechanical hysteresis, and no significant strain rate dependence of gauge factor. These results offer insight into nanosheet networks in the percolation regime, as well as models to study piezoresistance and conduction in networks where polymer components are minimised, removing their associated complications.

Nanosheet networks have found application beyond conductors and piezoresistors and recent reports have observed that network properties can be significantly impacted by the size of the nanosheets making up the network. By way of investigating the effect of nanosheet thickness on conduction and piezoresistance, six different graphene nanosheet inks, with thicknesses ranging from 3 nm to 20 nm, were prepared from a stock LPE dispersion using LCC. Bulk-like films of each size were spray coated onto flexible substrate and the electrical resistivity and piezoresistive response were investigated as a function of nanosheet thickness. The electrical resistivity increased with increasing nanosheet thickness and, using a recently reported model, the nanosheet resistivity and junction resistance were determined to be 2.9×10^{-5} Ωm and 8.9 kΩ respectively. The piezoresistive response also displayed an increase in gauge factor with increasing nanosheet thickness. In order to understand this effect, a new model was developed which could be applied to the data, from which the contribution of the inter-nanosheet junctions and the effect of strain on the nanosheets themselves could be extracted. Interestingly, it was observed that the nanosheets displayed a negative gauge factor. This shows that for

bulk-like nanosheet networks, it is necessary to consider both the inter-nanosheet junctions and the nanosheets themselves when modelling physical phenomena. This also demonstrates another method to tune the conductivity and piezoresistive response of nanosheet networks.

By producing graphene inks from LPE and EE methods, nanosheets of significantly different aspect ratios were produced and spray coated to form networks. Using FIB-SEM nanotomography, the network structures were investigated showing a significantly greater porosity of 42.6% for the LPE network compared to 2.2% for the EE nanosheet network. This representation showed the monolithic EE network structure, while the jammed LPE network had significant porosity and nanosheets were not highly aligned. The bulk EE networks displayed an order of magnitude increase in bulk conductivity compared to the LPE network. This difference has been attributed to a difference in nanosheet thickness, but also to the changes in network porosity. Investigating these networks near their percolation thresholds enabled the percolation exponent, which is linked to the dimensionality of the system, to be extracted. This was in line with the theoretical exponents for 2D and 3D networks for EE and LPE films respectively. Lower gauge factors were observed for the EE networks, which is believed to be a result of the nanosheets sliding past each other in the aligned EE network under the application of external strain. Both systems displayed increases in gauge factor as the percolation threshold was approached from above.

For networks of nanosheets, both the junction and nanosheet resistance must be considered when optimising device performance. Unfortunately, conducting a careful size-selection of nanosheets to extract the resistances of nanosheets and junctions is slow and requires the careful production of many samples. Recent reports of a technique to directly measure the mean nanosheet resistance and junction resistance in a network

inspired this study, enabling the effect of strain on each component of a nanosheet network to be extracted and analysed. The optimal system for this report is a network of electrochemically exfoliated MoS_2 nanosheets deposited from a liquid-liquid interface assembly. Despite the low piezoresistive response of such an aligned nanosheet network, the technique was capable of measuring the junction and nanosheet resistances across a range of strains. No significant effect of strain on the nanosheet resistance was observed, while the inter-nanosheet junctions increased in resistance, with a normalised rate of change of junction resistance with strain of ~2.5. A simple model showed that the measured R_{NS} and R_J data was consistent with highly aligned nanosheets sliding past each other, without transferring stress between the sheets. No two networks of nanosheets are the same, with effects of production method, processing parameters, substrate effects, and environmental factors varying the network electrical and piezoresistive properties. In order to optimise nanosheet network devices, fast, low-cost techniques capable of making direct measurements of the R_{NS} and R_J parameters will be required.

9.2 Future Work

New scientific developments typically unearth many new lines of investigation for curious minds in the scientific community. Based on the outcomes of these projects, it has become clear that there are several projects outstanding which will further the understanding of piezoresistance and conduction in nanosheet networks.

Firstly, repeating some of the studies presented with different 2D material systems to investigate the universality of the models would be a good starting point. This would include varying nanosheet preparation conditions, size distributions of nanosheets, and deposition techniques, and testing the models with semiconducting and perhaps silver nanosheets. In completing these studies, materials systems which display strong dependences on network structure, inter-sheet junctions, or the electronics of the

nanosheets themselves can be explored and reported. This will likely broaden the range of gauge factor values available at a given resistance or thickness value, allowing for materials to be chosen to fit a specific problem or need. Care should be taken that the parameters used to tune piezoresistance do not adversely affect the electrical noise in the system, which could substantially alter the performances of devices.

Secondly, a challenge with polymer-free nanosheet films is their susceptibility to damage from scratches[441] or exposure to environmental conditions including rain or sweat if mounted on a human. In order to mitigate these effects, it would be desirable to develop an encapsulation technique which maintains the film-like properties, while protecting the network from damage. It is important that the encapsulant chosen should maintain the performance advantages of utilising polymer-free networks of nanosheets such as reduced hysteresis and frequency independent piezoresistive response.

Finally, as it is now possible to directly measure the nanosheet and junction resistance of a nanosheet network under the application of strain to gain mechanistic information about the system, opportunities have emerged to explore a wide range of nanomaterial systems. This has been further enhanced with the recent libraries of 2D nanosheets,[442] particularly high aspect ratio nanosheets which have been shown to perform well with impedance spectroscopy.[146] It is worth noting that this technique and the circuit model applied to nanosheet networks are both still under development, and so extensions to the model may be needed in future to fully describe transport across a nanosheet network. In order to tune piezoresistive response, the nanosheets could be functionalised, crosslinked,[213] or doped. Using the impedance technique, the effect of these alterations on the junctions and the nanosheets can be directly quantified.

9.3 Final words

This thesis set out to explore piezoresistance and conduction in nanosheet networks. It has been concluded that nanosheet networks come in a wide variety of network thicknesses, nanosheet sizes, and network morphologies, each of which displays unique responses to strain. Through this research, techniques have been developed to test devices using cyclic testing to probe the gauge factor over several cycles and to directly measure nanosheet and junction resistance variations with strain. Physical models of the effect of network thickness, nanosheet thickness, and network conductivity on the network piezoresistance have been developed and tested. It is hoped that the work in this thesis has a positive impact on the field and opens potential avenues to help further our scientific understanding of such systems.

Appendix

A.1 Literature and Theory

A.1.1 Table of Graphene Film Conductivities

Table A.1: Table of solution processed graphene film conductivities.

Author	**Nanosheet Production**	**Deposition Technique**	**Year**	**Conductivity (S/m)**	**Ref**
Parvez *et al.*	EE	Vacuum Filtration	2013	1.6×10^4	[117]
Clifford *et al.*	Shear Exfoliation	Spray	2024	1.2×10^5	[144]
Cassidy & Synnatschke *et al.*	EE	Liquid-Liquid Assembly	2024	1.3×10^5	[312]
Barwich *et al.*	Shear Exfoliation	Vacuum Filtration and Calendaring	2021	2.2×10^5	[172]
Calabrese *et al.*	LPE	Inkjet		6.25×10^4	[443]
Gabbett & Doolan *et al*.	EE	Spray Coating	2024	4.7×10^4	[146]
Gabbett & Doolan *et al*.	LPE	Spray Coating	2024	8×10^3	[146]
Marković *et al*.	EE	Vacuum Filtration	2016	8.6×10^4	[424]
Majee *et al*.	LPE	Inkjet	2017	2.5×10^4	[444]
Torrisi *et al.*	LPE	Inkjet	2012	1×10^2	[149]

A.1.2 Derivation of Network Resistivity Model

Adapted from SI of Ref[147].

Expressing the length of the tortuous pathway of the chain of conductive nanosheets through the network (L) in terms of the channel length (L_{Ch}) and network tortuosity factor (κ_{Net}), yields the following:

$$L = L_{Ch}\sqrt{\kappa_{Net}}$$

In traversing a nanosheet network, the charge carrier must cross pairs of junctions and nanosheets. Hence the number of nanosheet-junction pairs, N, can be expressed in terms of the distance the charge carrier travels through the nanoparticle, d_{NP} and through the junction, d_J. Note junctions are assumed to be smaller than the nanoparticles.

$$N = \frac{L}{d_{NP} + d_J}, d_{NP} \gg d_J$$

Assuming that each nanosheet-junction pair has equivalent resistance, the potential applied across the network, V, can be divided evenly across each pair of resistors, yielding the potential across each pair, V_P:

$$V_P = V / N = V\left(\frac{d_{NP} + d_J}{L}\right)$$

Dividing the potentials into the junction and nanoparticle components, V_J and V_{NP} respectively, by introducing the junction resistance (R_J) and the nanoparticle resistance (R_{NP}):

$$V_J = \frac{R_J}{R_J + R_{NP}} V_P = \frac{R_J}{R_J + R_{NP}} V\left(\frac{d_{NP} + d_J}{L}\right)$$

$$V_{NP} = \frac{R_{NP}}{R_J + R_{NP}} V\left(\frac{d_{NP} + d_J}{L}\right)$$

The next step is to calculate the time taken to cross the network, τ_{Net}. This can be calculated by dividing the channel length by the effective carrier speed. Note the applied field $E_A = V / L_{Ch}$ and network mobility, μ_{Net}, are introduced.

$$\tau_{Net} = \frac{L_{Ch}}{\mu_{Net} E_A} = \frac{L_{Ch}}{\mu_{Net}} \frac{L_{Ch}}{V}$$

The time can also be calculated as the time taken to cross a nanoparticle (τ_{NP}) added to the time taken to cross a junction (τ_J), multiplied by the number of nanoparticle-junction pairs in the pathway.

$$\tau_{Net} \approx N(\tau_{NP} + \tau_J) = \frac{L}{d_{NP} + d_J}(\tau_{NP} + \tau_J)$$

The time to cross a nanoparticle can be related to the nanoparticle mobility, μ_{NP}, and the applied field across the particle, E_{NP}.

$$\tau_{NP} = \frac{d_{NP}}{\mu_{NP} E_{NP}} = \frac{d_{NP}^2}{\mu_{NP} V_{NP}} = \frac{d_{NP}^2}{\mu_{NP}} \left[\frac{R_J + R_{NP}}{R_{NP}} \frac{L}{(d_{NP} + d_J)V} \right]$$

The time to cross the junction can be determined from the current flowing across the junction, I_J, where e is the elementary charge.

$$\tau_J = \frac{e}{I_J} = \frac{eR_J}{V_J} = e(R_J + R_{NP}) \frac{L}{(d_{NP} + d_J)V}$$

Combining these times, the time to cross a network can be written in terms of nanoparticle and junction parameters.

$$\tau_{Net} \approx \frac{L_{Ch}^2}{\mu_{Net} V} \approx \frac{L}{d_{NP} + d_J} \left(\frac{d_{NP}^2}{\mu_{NP}} \left(\frac{R_J + R_{NP}}{R_{NP}} \frac{L}{(d_{NP} + d_J)V} \right) + e(R_J + R_{NP}) \frac{L}{(d_{NP} + d_J)V} \right)$$

Recalling the definition of network tortuosity:

$$\kappa_{Net} = (L / L_{Ch})^2$$

The equation can be simplified as follows:

$$\frac{1}{\mu_{Net}} = \kappa_{Net} \frac{R_J + R_{NP}}{(d_{NP} + d_J)^2} \left[\frac{d_{NP}^2}{\mu_{NP} R_{NP}} + e \right]$$

$$\mu_{Net} = \frac{(d_{NP} + d_J)^2 / d_{NP}^2}{\left(1 + \frac{R_J}{R_{NP}}\right)} \frac{\mu_{NP} / \kappa_{Net}}{\left[1 + \frac{\mu_{NP} e R_{NP}}{d_{NP}^2}\right]}$$

In order to relate the mobility of the network to the network conductivity, σ_{Net}, the network mobility is multiplied by the network carrier density, n_{Net} and the elementary charge.

$$\sigma_{Net} = \mu_{Net} n_{Net} e$$

At this point, the universality of the system is suspended, and the nanoparticles are restricted to being nanosheets. The distance travelled through a nanosheet is taken to be one half the length of a nanosheet, l_{NS}. Hence the resistance of a nanosheet can also be expressed in terms of the nanosheet resistivity, ρ_{NS}, and the nanosheet thickness, t_{NS}. The nanosheet mobility, μ_{NS}, and nanosheet carrier density, n_{NS}, must also be introduced at this stage. Note that the network carrier density is related to the nanosheet carrier density by the porosity of the network, P.

$$d_{NP} = l_{NS} / 2, R_{NP} = R_{NS} = \rho_{NS} / (2t_{NS}), \mu_{NP} = \mu_{NS} = (n_{NS} e \rho_{NS})^{-1}, n_{Net} = n_{NS}(1-P)$$

Making the required substitutions:

$$\sigma_{Net} \approx \left[\frac{1}{1 + \left(2t_{NS} R_J / \rho_{NS}\right)} \right] \left[\frac{1}{(n_{NS} e \rho_{NS}) \kappa_{Net}} \right] \left[\frac{1}{1 + 2 / \left(n_{NS} t_{NS} l_{NS}^2\right)} \right] n_{NS}(1-P) e$$

This expression can be rewritten in terms of network resistivity, $\rho_{Net} = 1/\sigma_{Net}$.

$$\rho_{Net} \approx \kappa_{Net} \frac{(\rho_{NS} + 2t_{NS} R_J)}{(1-P)} \left[1 + \frac{2}{n_{NS} t_{NS} l_{NS}^2} \right]$$

In this thesis, for electrical characterisation, the network tortuosity is assumed to be ~1.

If n_{NS} is sufficiently large the second term in square brackets is negated

$$\rho_{Net} \approx \frac{(\rho_{NS} + 2t_{NS}R_J)}{(1-P)}$$

If the network porosity is further assumed to be zero, and knowing $\rho_{NS} = 2t_{NS}R_{NS}$, the network resistivity can be written as:

$$\rho_{Net} \approx 2t_{NS}(R_{NS} + R_J)$$

A.1.3 Derivation of Gauge Factor

This derivation is adapted from the SI of Ref[378].

Typically, the gauge factor (G) is defined in terms of resistance (R) and strain (ε), where subscript zero indicates at zero strain.

$$\frac{\Delta R}{R_0} = G\varepsilon$$

Hence, at low strain, this can be rewritten as:

$$G = \frac{1}{R_0}\frac{dR}{d\varepsilon}.$$

Expressing the resistance in terms of the sample length (L), cross sectional area (A) and the conductivity (σ).

$$R = \frac{L}{\sigma A}$$

At low strain, it is assumed that the volume remains constant.

$$AL = A_0L_0$$

Hence resistance can be written as follows:

$$R = \frac{L^2}{\sigma A_0 L_0}$$

Differentiating with respect to strain:

$$\frac{dR}{d\varepsilon} = \frac{1}{A_0 L_0}\left[\frac{2L}{\sigma}\frac{dL}{d\varepsilon} - \frac{L^2}{\sigma^2}\frac{d\sigma}{d\varepsilon}\right]$$

Dividing both sides through by $R_0 = \frac{L_0}{\sigma_0 A_0}$:

$$\frac{1}{R_0}\frac{dR}{d\varepsilon} = \frac{\sigma_0}{L_0^{\,2}}\left[\frac{2L}{\sigma}\frac{dL}{d\varepsilon} - \frac{L^2}{\sigma^2}\frac{d\sigma}{d\varepsilon}\right]$$

In the limit of low strain, $L \approx L_0$ and $\sigma \approx \sigma_0$.

$$\frac{1}{R_0}\frac{dR}{d\varepsilon} \approx \frac{\sigma_0}{L_0^{\,2}}\left[\frac{2L_0}{\sigma_0}\frac{dL}{d\varepsilon} - \frac{L_0^{\,2}}{\sigma_0^{\,2}}\frac{d\sigma}{d\varepsilon}\right] = \frac{2}{L_0}\frac{dL}{d\varepsilon} - \frac{1}{\sigma_0}\frac{d\sigma}{d\varepsilon}$$

Knowing that strain is defined as $\varepsilon = \frac{L - L_0}{L_0}$:

$$G = \frac{1}{R_0}\frac{dR}{d\varepsilon} \approx 2 - \frac{1}{\sigma_0}\left(\frac{d\sigma}{d\varepsilon}\right)_0$$

This derivation assumes a Poisson ratio of 0.5, however without this assumption, the equation can be written as follows, from Fiorillo *et al*.[332]

$$G \approx (1 + 2\nu) - \frac{1}{\sigma_0}\left(\frac{d\sigma}{d\varepsilon}\right)_0$$

A.1.4 Conductivity Percolation with Physical Parameters

$$\sigma = \sigma_0 (t - t_c)^n$$

At the bulk transition thickness, t_x, the conductivity reaches the bulk conductivity of the network, σ_B.

$$\sigma(t_x) = \sigma_B = \sigma_0 (t_x - t_c)^n$$

Rearranging this expression:

$$\sigma_0 = \sigma_B (t_x - t_c)^{-n}$$

Substituting back into the original equation:

$$\sigma = \sigma_B \left(\frac{t - t_c}{t_x - t_c} \right)^n$$

A.1.5 Conductivity Percolation Across the Full Thickness Range

Previous reports for thin film conductivities and resistivities integrated surface roughness and scattering phenomena when fitting data across the complete thickness range. Typically, these equations consist of two terms, the first describing the bulk material and the second describing a modification due to these phenomena. Cassidy and Synnatschke *et al*. proposed the following equation for resistivity, where the denominator of the second term incorporates percolation scaling.

$$\rho = \rho_B + \frac{\rho_0}{(t - t_c)^n}$$

In specific limiting cases the film thickness dependence matches the Fuchs-Sondheimer model[445] along with recent models proposed by Zhou *et al*.[446]

At t_x, the conductivity is 80% of σ_B:

$$\sigma(t_x) = 0.8\sigma_B$$

$$\rho(t_x) = 5\rho_B / 4 = \rho_B + \frac{\rho_0}{(t_x - t_c)^n}$$

$$\rho_0 = \rho_B (t_x - t_c)^n / 4$$

$$\rho \approx \rho_B + \frac{\rho_B (t_x - t_c)^n}{4(t - t_c)^n} \approx \rho_B \left[1 + \frac{1}{4} \left(\frac{t_x - t_c}{t - t_c} \right)^n \right]$$

$$\sigma \approx \sigma_B \left[1 + \frac{1}{4} \left(\frac{t_x - t_c}{t - t_c} \right)^n \right]^{-1}$$

A.2 Experimental 1

A.2.1 Model Derivation

This derivation is adapted from the SI of Ref[378].

The thickness dependence of conductivity in the percolation regime (σ) can be expressed in terms of network thickness (t), percolation thickness (t_c), the percolation exponent (n), and a proportionality constant (σ_c):

$$\sigma = \sigma_c (t - t_c)^n$$

It has been observed that conductivity can saturate above a critical thickness (t_x) and a more complete form of the expression is given below, where σ_{Bulk} is the bulk conductivity of the network above the bulk-like transition thickness (t_x).

$$\sigma = \sigma_{Bulk} \left(\frac{t - t_c}{t_x - t_c} \right)^n$$

It is known that:

$$G \simeq 2 - \frac{1}{\sigma_0} \left(\frac{d\sigma}{d\varepsilon} \right)_0$$

Differentiating σ with respect to strain gives:

$$\frac{d\sigma}{d\varepsilon} = \frac{\partial\sigma}{\partial\varepsilon} + \frac{\partial\sigma}{\partial\sigma_{Bulk}} \frac{d\sigma_{Bulk}}{d\varepsilon} + \frac{\partial\sigma}{\partial n} \frac{dn}{d\varepsilon} + \frac{\partial\sigma}{\partial t_x} \frac{dt_x}{d\varepsilon} + \frac{\partial\sigma}{\partial t} \frac{dt}{d\varepsilon} + \frac{\partial\sigma}{\partial t_c} \frac{dt_c}{d\varepsilon}$$

Writing out each partial derivative:

$$\frac{\partial\sigma}{\partial\varepsilon} = 0$$

$$\frac{\partial\sigma}{\partial\sigma_{Bulk}} = \left(\frac{t - t_c}{t_x - t_c} \right)^n$$

$$\frac{\partial\sigma}{\partial n} = \ln\left(\frac{t - t_c}{t_x - t_c} \right) \left(\sigma_{Bulk} \left(\frac{t - t_c}{t_x - t_c} \right)^n \right)$$

$$\frac{\partial \sigma}{\partial t_x} = -\frac{n}{t_x - t_c}\left(\sigma_{Bulk}\left(\frac{t - t_c}{t_x - t_c}\right)^n\right)$$

$$\frac{\partial \sigma}{\partial t} = \frac{n}{t - t_c}\left(\sigma_{Bulk}\left(\frac{t - t_c}{t_x - t_c}\right)^n\right)$$

$$\frac{\partial \sigma}{\partial t_c} = \left(\frac{n}{t_x - t_c} - \frac{n}{t - t_c}\right)\left(\sigma_{Bulk}\left(\frac{t - t_c}{t_x - t_c}\right)^n\right)$$

Substituting each of these derivatives into the previous equation gives:

$$\frac{d\sigma}{d\varepsilon} = \left(\frac{t - t_c}{t_x - t_c}\right)^n \frac{d\sigma_{Bulk}}{d\varepsilon} + \ln\left(\frac{t - t_c}{t_x - t_c}\right)\left(\sigma_{Bulk}\left(\frac{t - t_c}{t_x - t_c}\right)^n\right)\frac{dn}{d\varepsilon} - \frac{n}{t_x - t_c}\left(\sigma_{Bulk}\left(\frac{t - t_c}{t_x - t_c}\right)^n\right)\frac{dt_x}{d\varepsilon}$$
$$+ \frac{n}{t - t_c}\left(\sigma_{Bulk}\left(\frac{t - t_c}{t_x - t_c}\right)^n\right)\frac{dt}{d\varepsilon} + \left(\frac{n}{t_x - t_c} - \frac{n}{t - t_c}\right)\left(\sigma_{Bulk}\left(\frac{t - t_c}{t_x - t_c}\right)^n\right)\frac{dt_c}{d\varepsilon}$$

This equation is simplified by dividing through by $\sigma = \sigma_{Bulk}\left(\frac{t - t_c}{t_x - t_c}\right)^n$:

$$\frac{1}{\sigma}\frac{d\sigma}{d\varepsilon} = \frac{1}{\sigma_{Bulk}}\frac{d\sigma_{Bulk}}{d\varepsilon} + \ln\left(\frac{t - t_c}{t_x - t_c}\right)\frac{dn}{d\varepsilon} - \frac{n}{t_x - t_c}\frac{dt_x}{d\varepsilon} + \frac{n}{t - t_c}\frac{dt}{d\varepsilon} + \left(\frac{n}{t_x - t_c} - \frac{n}{t - t_c}\right)\frac{dt_c}{d\varepsilon}$$

As G is only defined in the limit of low strain, all derivatives are taken in the limit of low strain and let $\sigma \simeq \sigma_0$ and as a result $\sigma_{Bulk} \simeq \sigma_{Bulk,0}$, $n \simeq n_0$, $t_x \simeq t_{x,0}$, $t \simeq t_0$ and $t_c \simeq t_{c,0}$.

$$\frac{1}{\sigma_0}\left(\frac{d\sigma}{d\varepsilon}\right)_0 = \frac{1}{\sigma_{Bulk,0}}\left(\frac{d\sigma_{Bulk}}{d\varepsilon}\right)_0 + \ln\left(\frac{t_0 - t_{c,0}}{t_{x,0} - t_{c,0}}\right)\left(\frac{dn}{d\varepsilon}\right)_0 - \frac{n_0}{t_{x,0} - t_{c,0}}\left(\frac{dt_x}{d\varepsilon}\right)_0$$
$$+ \frac{n_0}{t_0 - t_{c,0}}\left(\frac{dt}{d\varepsilon}\right)_0 + \left(\frac{n_0}{t_{x,0} - t_{c,0}} - \frac{n_0}{t_0 - t_{c,0}}\right)\left(\frac{dt_c}{d\varepsilon}\right)_0$$

This yields the following expression for G:

$$G \simeq 2 - \frac{1}{\sigma_{Bulk,0}}\left(\frac{d\sigma_{Bulk}}{d\varepsilon}\right)_0 - \ln\left(\frac{t_0 - t_{c,0}}{t_{x,0} - t_{c,0}}\right)\left(\frac{dn}{d\varepsilon}\right)_0 + \frac{n_0}{t_{x,0} - t_{c,0}}\left(\frac{dt_x}{d\varepsilon}\right)_0 - \frac{n_0}{t_0 - t_{c,0}}\left(\frac{dt}{d\varepsilon}\right)_0$$
$$- \left(\frac{n_0}{t_{x,0} - t_{c,0}} - \frac{n_0}{t_0 - t_{c,0}}\right)\left(\frac{dt_c}{d\varepsilon}\right)_0$$

Applying the following relation, and by grouping the like terms, G is shown to depend on four terms, each in square brackets:

$$\frac{1}{\sigma_{Bulk}}\frac{d\sigma_{Bulk}}{d\varepsilon} \simeq \frac{d\ln(\sigma_{Bulk})}{d\varepsilon}$$

$$G \simeq \left[2-\left(\frac{d\ln(\sigma_{Bulk})}{d\varepsilon}\right)_0\right]+\left[\ln\left(\frac{t_{x,0}-t_{c,0}}{t_0-t_{c,0}}\right)\left(\frac{dn}{d\varepsilon}\right)_0\right]+\left[\left(\frac{n_0}{t_{x,0}-t_{c,0}}\right)\left\{\left(\frac{dt_x}{d\varepsilon}\right)_0-\left(\frac{dt_c}{d\varepsilon}\right)_0\right\}\right]$$
$$+\left[\frac{n_0}{t_0-t_{c,0}}\left\{\left(\frac{dt_c}{d\varepsilon}\right)_0-\left(\frac{dt}{d\varepsilon}\right)_0\right\}\right]$$

The first three terms can be approximated as thickness independent and can be written in a simplified form as G_{TNS}. Note that the second term does have some thickness dependence, however, this dependence is weak compared to the final term.

$$G_{TNS} \simeq \left[2-\left(\frac{d\ln(\sigma_{Bulk})}{d\varepsilon}\right)_0\right]+\left[\ln\left(\frac{t_{x,0}-t_{c,0}}{t_0-t_{c,0}}\right)\left(\frac{dn}{d\varepsilon}\right)_0\right]+\left[\left(\frac{n_0}{t_{x,0}-t_{c,0}}\right)\left\{\left(\frac{dt_x}{d\varepsilon}\right)_0-\left(\frac{dt_c}{d\varepsilon}\right)_0\right\}\right]$$

The fourth term contains the following difference of derivatives, $\left\{\left(\frac{dt_c}{d\varepsilon}\right)_0-\left(\frac{dt}{d\varepsilon}\right)_0\right\}$

Defining Poisson's ratio as $\nu_{tL}=d\varepsilon_t/d\varepsilon$, where ε_t is the transverse (perpendicular to straining axis) strain, it is straightforward to show that $(dt/d\varepsilon)_0=-\nu_{tL}t_0$. For porous nanostructured films, as previously discussed, the Poisson ratio can be very small (often $-0.1 < \nu_{tL}$,0.1).[280-282] Network thicknesses are also small. This allows the $(dt/d\varepsilon)_0$ term to be neglected.

$$\left(\frac{dt_c}{d\varepsilon}\right)_0 \gg \left(\frac{dt}{d\varepsilon}\right)_0$$

Hence, t_{TNS} can be defined as:

$$t_{TNS} \approx n_0\left(\frac{dt_c}{d\varepsilon}\right)_0$$

This substitution leads to the much simpler expression:

$$G \approx G_{TNS} + \frac{t_{TNS}}{t_0 - t_{c,0}}$$

This expression for G can also be re-expressed in terms of σ_0:

$$\sigma_0 = \sigma_{Bulk,0}\left(\frac{t_0 - t_{c,0}}{t_{x,0} - t_{c,0}}\right)^{n_0}$$

Which can be rewritten as follows:

$$\frac{1}{t_0 - t_{c,0}} = \frac{1}{t_{x,0} - t_{c,0}}\left(\frac{\sigma_{Bulk,0}}{\sigma_0}\right)^{1/n_0}$$

Making the substitution to reintroduce conductivity back into the model:

$$G \approx G_{TNS} + \frac{t_{TNS}}{t_{x,0} - t_{c,0}}\left(\frac{\sigma_{Bulk,0}}{\sigma_0}\right)^{1/n_0}$$

Defining σ_{TNS} simplifies the expression:

$$\sigma_{TNS} = \sigma_{Bulk,0}\left(\frac{t_{TNS}}{t_{x,0} - t_{c,0}}\right)^{n_0}$$

This yields a model relating σ_0 to G.

$$G \approx G_{TNS} + \left[\frac{\sigma_{TNS}}{\sigma_0}\right]^{1/n_0}$$

A.2.2 Relating Gauge Factor to Resistance

From the percolation conductivity equation:

$$\sigma = \sigma_{Bulk}\left(\frac{t - t_c}{t_x - t_c}\right)^n$$

Assuming $t >> t_c$, the simple proportionality can be drawn:

$$\sigma \propto t^n$$

Resistance can be expressed as follows:

$$R = \frac{L}{\sigma t w}$$

Which gives the following proportionality:

$$R \propto \frac{1}{\sigma t} \propto \frac{1}{t^n t} \propto \frac{1}{t^{n+1}}$$

Rearranging for t:

$$t \propto R^{-\frac{1}{n+1}}$$

Substituting this relation into the Gauge factor, network thickness model, maintaining the $t >> t_c$ assumption:

$$G \approx G_{TNS} + \frac{t_{TNS}}{t - t_c} \propto \frac{1}{t}$$

Yielding $G \propto R^{\frac{1}{n+1}}$

A.2.3 Transmission Scanning

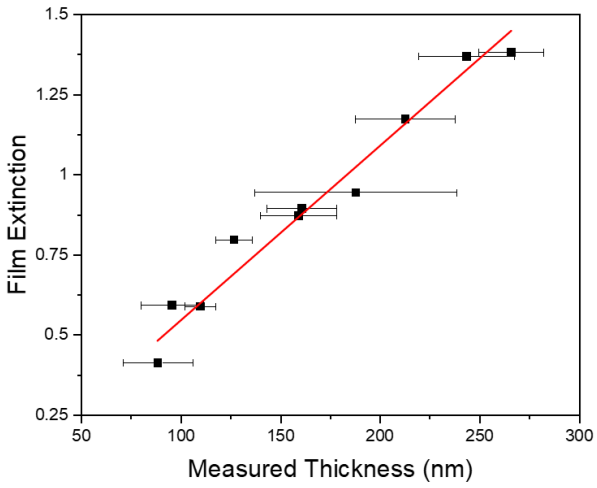

Figure A2.1: Plot of film extinction vs. measured network thickness for LPE graphene sprayed films on glass substrates showing a linear correlation with a slope of (54.5 ± 1.1)×10^{-4} nm^{-1}. Extinction was determined using optical transmission measurements, film thickness was measured by stylus profilometry.

A.2.4 Cyclic Testing

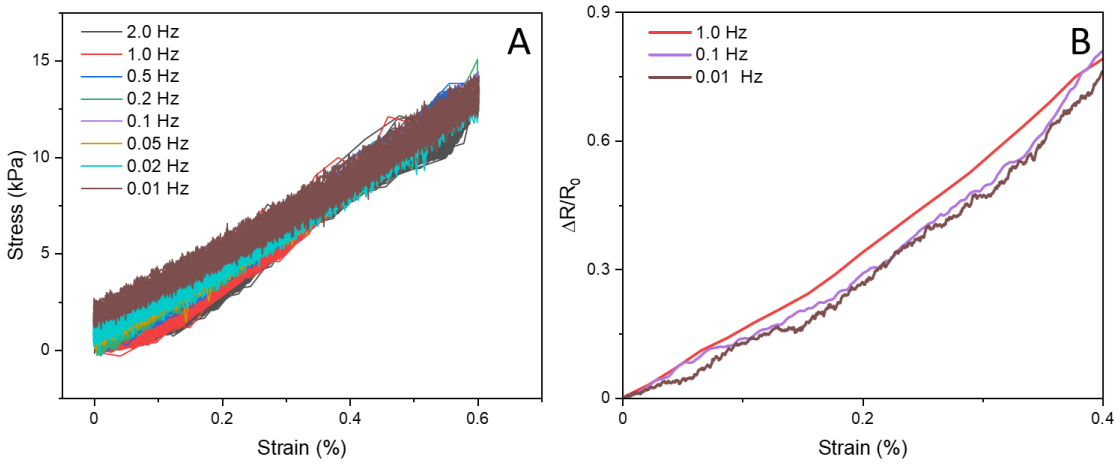

Figure A2.2: A) Plot of applied stress vs. strain, for a PDMS substrate cycled between 0% and 0.6% at a strain rate of across a broad range of cycling frequencies from 0.01 Hz to 2 Hz. B) Plot of the fractional change in resistance vs. strain for a 45 nm thick film, at different cycling frequencies from 0.01 Hz to 1 Hz.

A.3 Experimental 2

A.3.1 AFM Sizes

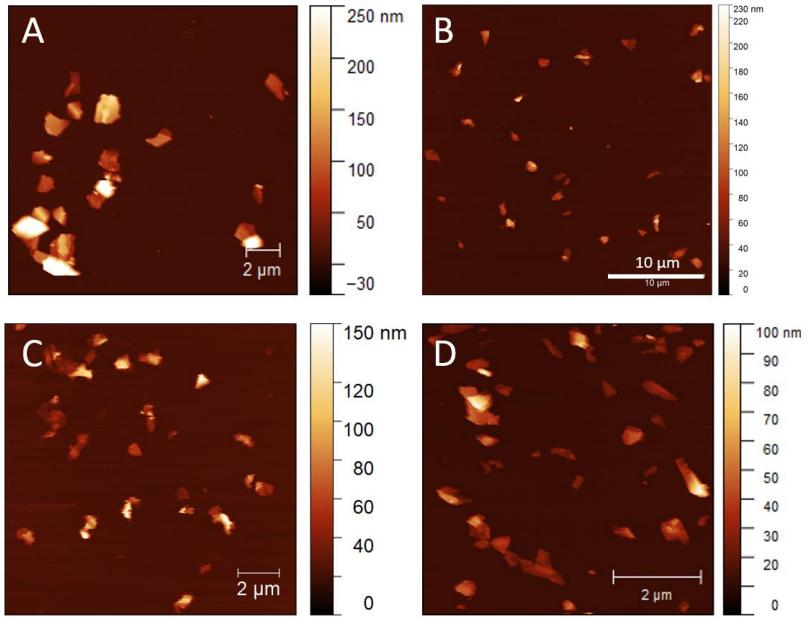

Figure A3.1: Representative AFM images of graphene nanosheets from across the range of size selected fractions. A) 0.5 to 1 kRPM, B) 1 to 1.5 kRPM, C) 2 to 3 kRPM, D) 3 to 4 kRPM.

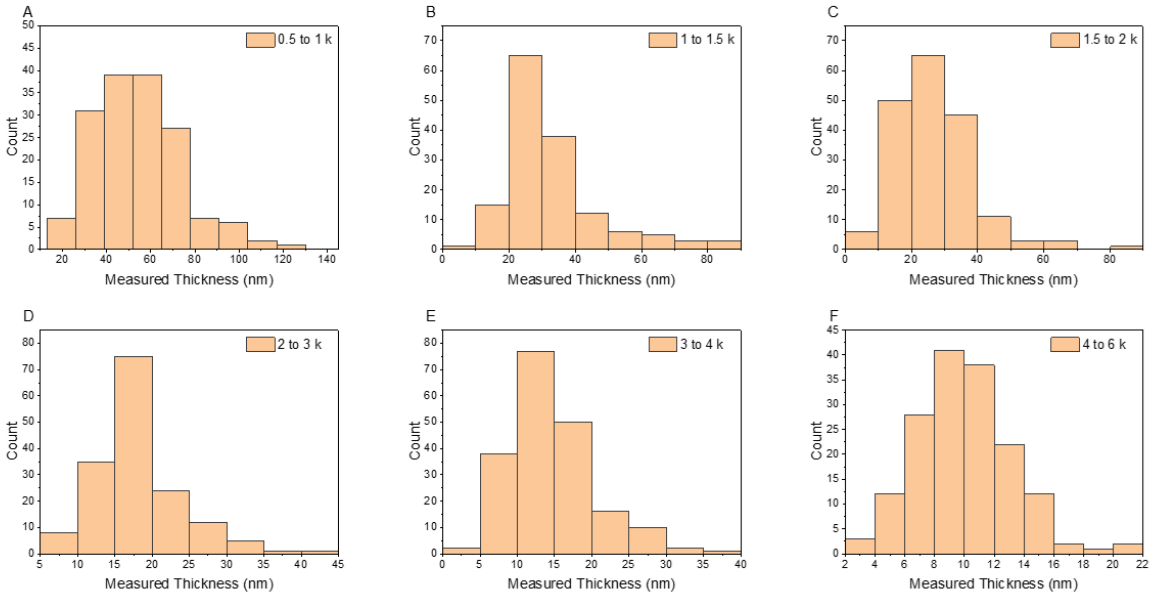

Figure A3.2: Measured apparent thickness distribution histograms for graphene nanosheets measured using AFM from all six size fractions. A) 0.5 to 1 kRPM, B) 1 to 1.5 kRPM, C) 1.5 to 2 kRPM, D) 2 to 3 kRPM, E) 3 to 4 kRPM, F) 4 to 6 kRPM.

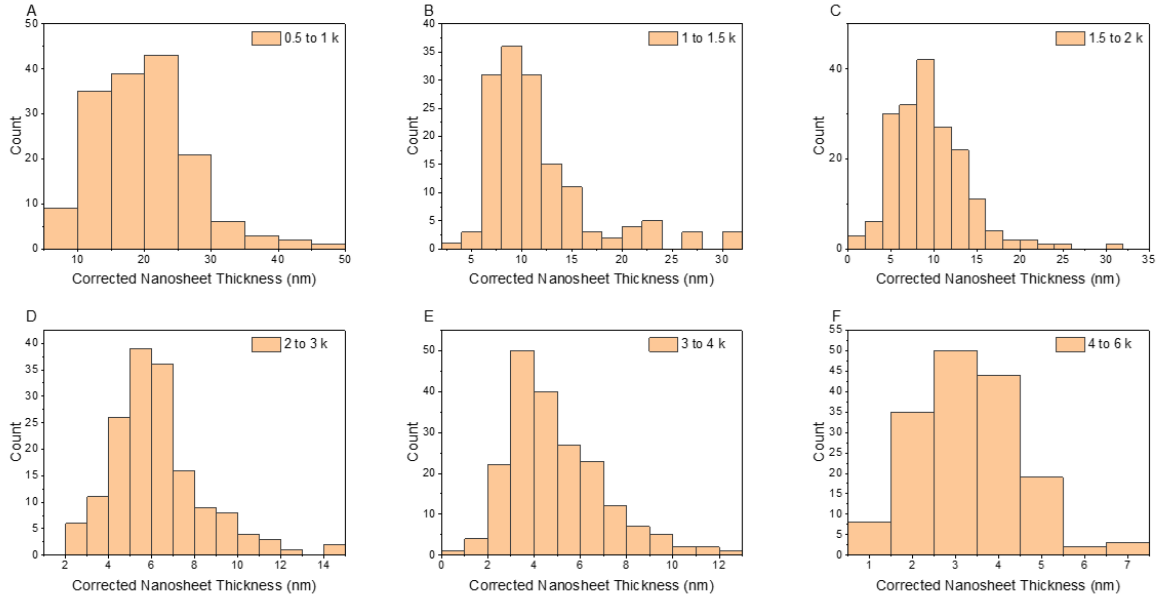

Figure A3.3: Converted nanosheet thickness distribution histograms, converted from the measured thicknesses (Figure A3.2) for all six size fractions. A) 0.5 to 1 kRPM, B) 1 to 1.5 kRPM, C) 1.5 to 2 kRPM, D) 2 to 3 kRPM, E) 3 to 4 kRPM, F) 4 to 6 kRPM.

Table A3.1: Nanosheet sizes determined from AFM for each size fraction.

Centrifugation Trapping Speeds	l_{NS} **(µm)**	**Thickness before correction (nm)**	t_{NS} **(nm)**
0.5 to 1 kRPM	1.50	54.6	19.7
1 to 1.5 kRPM	1.30	32.4	11.6
1.5 to 2 kRPM	0.83	27.0	9.6
2 to 3 kRPM	0.76	17.9	6.2
3 to 4 kRPM	0.50	14.4	4.9
4 to 6 kRPM	0.45	9.8	3.2

A.3.2 Substrate Cycling Mechanics

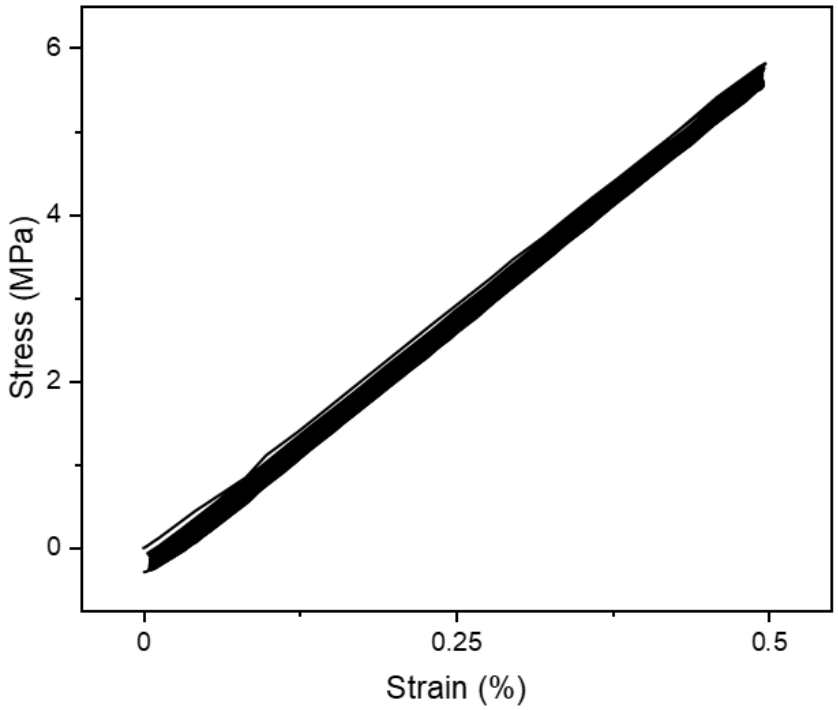

Figure A3.4: Plot of applied stress vs. strain, for a Kapton substrate cycled between 0% and 0.5% at a strain rate of 0.2 %/s for 200 cycles.

A.3.3 Model Derivation

For a bulk-like nanosheet network ($t > t_x$), network resistivity can be modelled as:

$$\rho_{Net} \approx \frac{\left[\rho_{NS} + 2t_{NS}R_J\right]}{(1-P_{Net})}\left[1+\frac{2}{n_{NS}t_{NS}l_{NS}^2}\right]$$

For graphene, the nanosheet carrier density, n_{NS} is large and the above expression can be simplified:

$$\rho_{Net} \approx \frac{\left[\rho_{NS} + 2t_{NS}R_J\right]}{(1-P_{Net})}$$

For a piezoresistive network, the network gauge factor can be written as:

$$G_{Net} = 2+\frac{1}{\rho_{Net}}\frac{d\rho_{Net}}{d\varepsilon}$$

The strain derivative of network resistivity can be linked to piezoresistance, hence $d\rho_{Net}/d\varepsilon$ is calculated:

$$\rho_{Net} \approx \left[\rho_{NS} + 2t_{NS}R_J\right](1-P_{Net})^{-1}$$

$$\frac{d\rho_{Net}}{d\varepsilon} \approx \left[\rho_{NS} + 2t_{NS}R_J\right]\frac{d}{d\varepsilon}(1-P_{Net})^{-1} + (1-P_{Net})^{-1}\frac{d}{d\varepsilon}\left[\rho_{NS} + 2t_{NS}R_J\right]$$

$$= \left[\rho_{NS} + 2t_{NS}R_J\right](1-P_{Net})^{-2}\frac{dP_{Net}}{d\varepsilon} + (1-P_{Net})^{-1}\left[\frac{d\rho_{NS}}{d\varepsilon} + 2t_{NS}\frac{dR_J}{d\varepsilon}\right]$$

$$= \frac{\left[\rho_{NS} + 2t_{NS}R_J\right]}{(1-P_{Net})^2}\frac{dP_{Net}}{d\varepsilon} + \frac{\left[d\rho_{NS}/d\varepsilon + 2t_{NS}dR_J/d\varepsilon\right]}{(1-P_{Net})}$$

Substituting this derivative into the above expression for G_{Net} yields:

$$G = 2 + \frac{\dfrac{\left[\rho_{NS} + 2t_{NS}R_J\right]}{(1-P_{Net})^2}\dfrac{dP_{Net}}{d\varepsilon} + \dfrac{\left[d\rho_{NS}/d\varepsilon + 2t_{NS}dR_J/d\varepsilon\right]}{(1-P_{Net})}}{\dfrac{\left[\rho_{NS} + 2t_{NS}R_J\right]}{(1-P_{Net})}}$$

$$G = 2 + \frac{\left[\rho_{NS} + 2t_{NS}R_J\right]\dfrac{dP_{Net}}{d\varepsilon} + (1-P_{Net})\left[d\rho_{NS}/d\varepsilon + 2t_{NS}dR_J/d\varepsilon\right]}{(1-P_{Net})\left[\rho_{NS} + 2t_{NS}R_J\right]}$$

Simplifying leaves a three term expression for network gauge factor:

$$G = 2 + \frac{\dfrac{dP_{Net}}{d\varepsilon}}{(1-P_{Net})} + \frac{\left[d\rho_{NS}/d\varepsilon + 2t_{NS}dR_J/d\varepsilon\right]}{\left[\rho_{NS} + 2t_{NS}R_J\right]}$$

Modifying the second term using the relation:

$$\frac{\dfrac{dP_{Net}}{d\varepsilon}}{(1-P_{Net})} \approx -\frac{d\ln(1-P_{Net})}{d\varepsilon}$$

And dividing through the third term by ρ_{NS} gives the model:

$$G_{Net} = 2 - \frac{d\ln(1-P_{Net})}{d\varepsilon} + \frac{\left[\dfrac{1}{\rho_{NS}}\dfrac{d\rho_{NS}}{d\varepsilon} + \left(\dfrac{1}{R_J}\dfrac{dR_J}{d\varepsilon}\right)\left(\dfrac{2R_J}{\rho_{NS}}\right)t_{NS}\right]}{\left[1 + \left(\dfrac{2R_J}{\rho_{NS}}\right)t_{NS}\right]}$$

For fitting of the model, the $\left(\dfrac{2R_J}{\rho_{NS}}\right)$ term can be extracted from the thickness dependent resistivity fit, reducing the required number of fit parameters.

A.3.4 Varying Parameters

Table A3.2: Table of fit parameters for fitting Figure 6.7B, where $d\ln(1-P_{Net})/d\varepsilon$ *takes fixed values between -2 and 2.*

$(2R_J/\rho_{NS})$	$d\ln(1-P_{Net})/d\varepsilon$	$(d\rho_{NS}/d\varepsilon)/\rho_{NS}$	$(dR_J/d\varepsilon)/R_J$
6.13×10^8	-2	-11.6 ± 2.8	10.7 ± 1.1
6.13×10^8	-1	-12.6 ± 2.8	9.7 ± 1.1
6.13×10^8	0	-13.6 ± 2.8	8.7 ± 1.1
6.13×10^8	1	-14.6 ± 2.8	7.7 ± 1.1
6.13×10^8	2	-15.6 ± 2.8	6.7 ± 1.1

A.3.5 Positive Nanosheet Gauge Factor

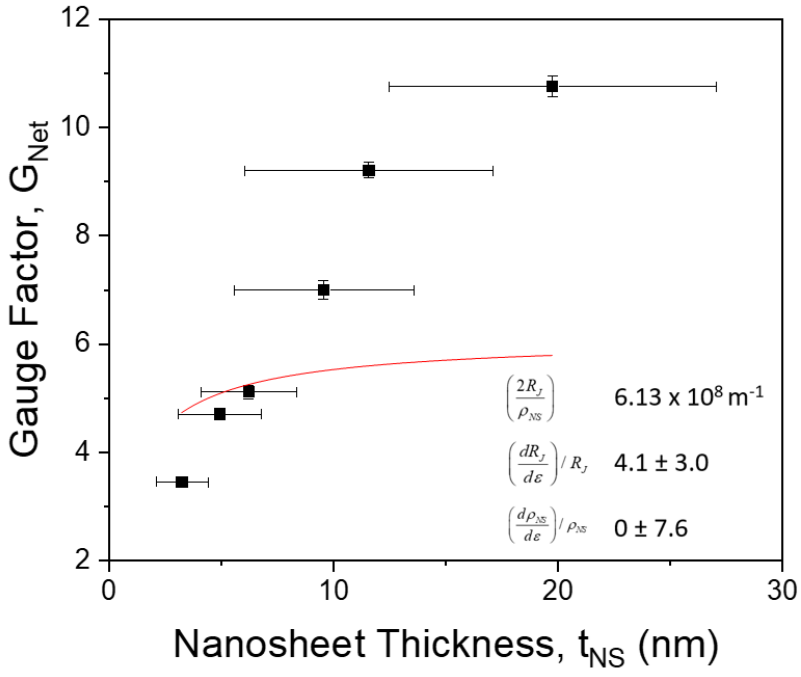

Figure A3.5: Plot of network gauge factor vs. nanosheet thickness, fit where the nanosheet resistivity change with strain is restricted to be positive, showing the poor fit to the model.

A.4 Experimental 3

A.4.1 Optical Profilometry

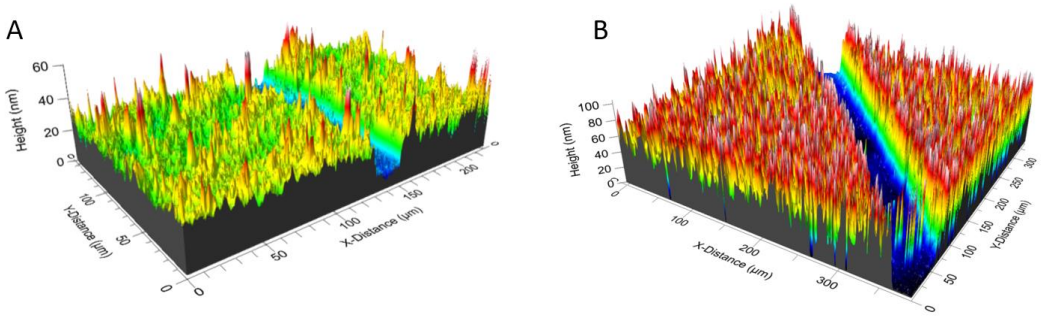

Figure A4.1: Optical Profilometry. 3D top-surface reconstruction A) EE and B) LPE graphene nanosheet spray coated film with a scratch to the substrate, using phase shift interferometry.

A.4.2 Aspect Ratio Histograms

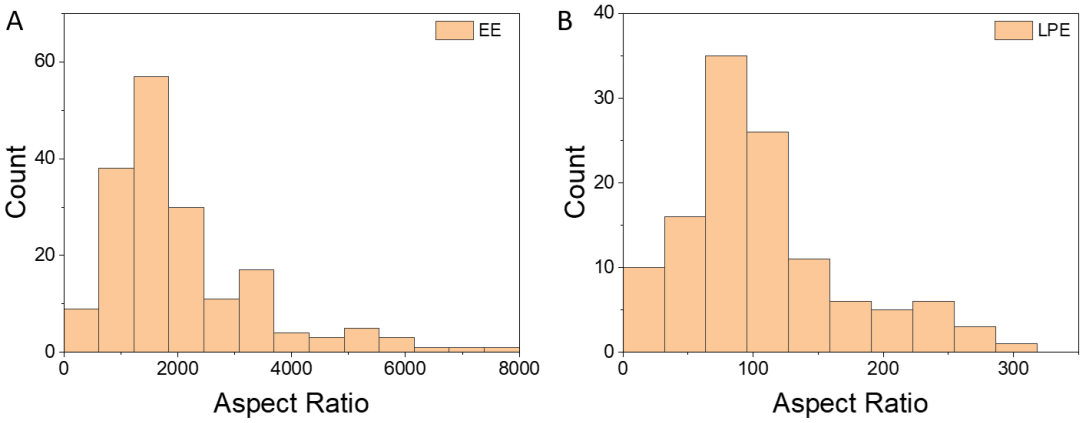

Figure A4.2: Plots of aspect ratio distributions from AFM Measurements of A) EE and B) LPE nanosheet dispersions.

A.4.3 Fitting R^2

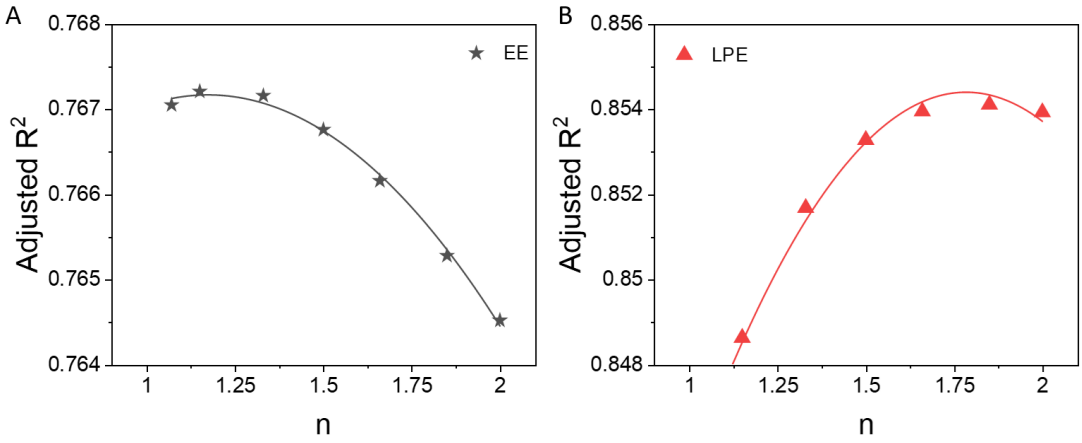

Figure A4.3: Plots of the adjusted R^2 of percolation plots in Figure 7.6 at different values of n *for A) EE and B) LPE nanosheet networks.*

A.4.4 The Extended GF Model

For a network with an intrinsic piezoresistive response:

$$G_{Net} \approx (1+2\nu) - \frac{1}{\sigma_{Net,0}}\left(\frac{d\sigma_{Net}}{d\varepsilon}\right)_0 \approx (1+2\nu) + \frac{1}{\rho_{Net,0}}\left(\frac{d\rho_{Net}}{d\varepsilon}\right)_0$$

The network conductivity and resistivity can be approximated across the entire thickness regime by the following equation:

$$\sigma_{Net} \approx \sigma_B \left[1+\frac{1}{4}\left(\frac{t_x - t_c}{t - t_c}\right)^n\right]^{-1}$$

$$\rho_{Net} \approx \rho_B \left[1+\frac{1}{4}\left(\frac{t_x - t_c}{t - t_c}\right)^n\right]$$

Partially differentiating ρ_{Net} with respect to strain:

$$\left(\frac{d\rho_{Net}}{d\varepsilon}\right)_0 = \left[1+\frac{1}{4}\left(\frac{t_x-t_c}{t-t_c}\right)^n\right]\left(\frac{d\rho_B}{d\varepsilon}\right)_0 + \left[n\frac{\rho_B}{4(t-t_c)}\left(\frac{t_x-t_c}{t-t_c}\right)^{n-1}\right]\left(\frac{dt_x}{d\varepsilon}\right)_0$$
$$-\left[n\frac{\rho_B(t_x-t_c)}{4(t-t_c)^2}\left(\frac{t_x-t_c}{t-t_c}\right)^{n-1}\right]\left(\frac{dt}{d\varepsilon}\right)_0 + \left[\ln\left(\frac{t_x-t_c}{t-t_c}\right)\frac{\rho_B}{4}\left(\frac{t_x-t_c}{t-t_c}\right)^n\right]\left(\frac{dn}{d\varepsilon}\right)_0$$
$$+\left[\frac{\rho_B(n(t_x-t))}{4(t-t_c)^2}\left(\frac{t_x-t_c}{t-t_c}\right)^{n-1}\right]\left(\frac{dt_c}{d\varepsilon}\right)_0$$

Substituting into the equation for the network gauge factor:

$$G_{Net} \approx (1+2\nu) + \frac{1}{\rho_B\left[1+\frac{1}{4}\left(\frac{t_x-t_c}{t-t_c}\right)^n\right]}\left\{\begin{array}{l}\left[1+\frac{1}{4}\left(\frac{t_x-t_c}{t-t_c}\right)^n\right]\left(\frac{d\rho_B}{d\varepsilon}\right)_0 \\ +\left[n\frac{\rho_B}{4(t-t_c)}\left(\frac{t_x-t_c}{t-t_c}\right)^{n-1}\right]\left(\frac{dt_x}{d\varepsilon}\right)_0 \\ -\left[n\frac{\rho_B(t_x-t_c)}{4(t-t_c)^2}\left(\frac{t_x-t_c}{t-t_c}\right)^{n-1}\right]\left(\frac{dt}{d\varepsilon}\right)_0 \\ +\left[\ln\left(\frac{t_x-t_c}{t-t_c}\right)\frac{\rho_B}{4}\left(\frac{t_x-t_c}{t-t_c}\right)^n\right]\left(\frac{dn}{d\varepsilon}\right)_0 \\ +\left[\frac{\rho_B(n(t_x-t))}{4(t-t_c)^2}\left(\frac{t_x-t_c}{t-t_c}\right)^{n-1}\right]\left(\frac{dt_c}{d\varepsilon}\right)_0\end{array}\right\}$$

A.5 Experimental 4

A.5.1 Conversion Parameters

Conversion Parameters

Table A5.1: MoS_2 nanosheet and network parameters extracted from Gabbett & Kelly et al.[147].

Nanosheet and Structural Parameters	
Nanosheet Thickness, t_{NS} (nm)	3.3
Nanosheet Length, l_{NS} (μm)	1
Nanosheet Carrier Density, n_{NS} (m^{-3})	6×10^{23}
Network Porosity, P	0
Network Tortuosity, κ	1

A.5.2 Optical Profilometry

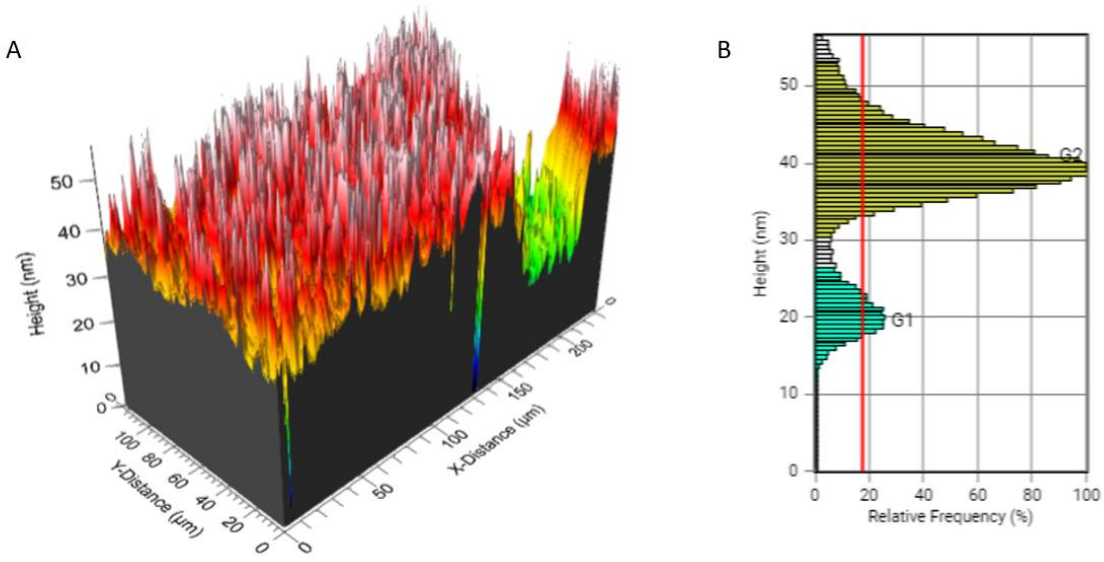

Figure A5.1: Network thickness characterisation. A) 3D top-surface reconstruction of MoS_2 film with a scratch to the substrate, using phase shift interferometry. B) Distribution of pixel height, showing two peaks, lower (green) peak is the substrate, higher (yellow) peak is the surface of the film.

A.5.3 Derivation of Sliding Nanosheets Model

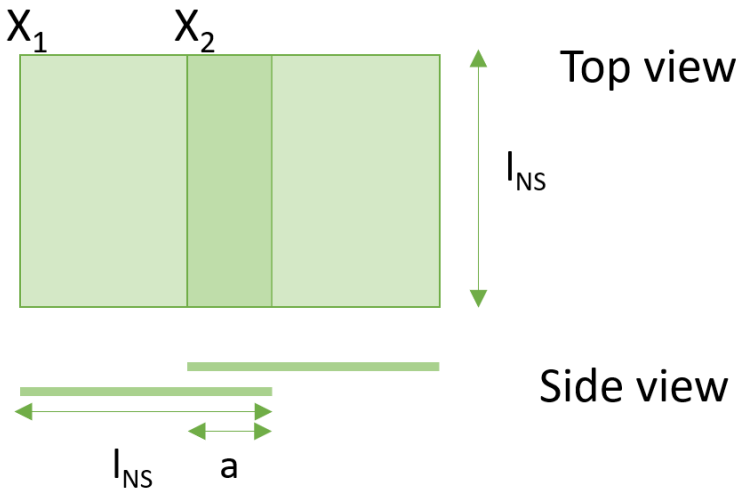

Figure A5.2: Nanosheet overlap schematic, showing top view and side view of two square overlapping nanosheets.

For two partially overlapping square nanosheets of length l_{NS}, as shown in Figure A5.2, where the overlap area is the inter-nanosheet junction, the junction area is defined as $A = al_{NS}$, where a is the length of the overlapping region. The left-hand edges of the nanosheets are located at the X_1 and X_2 positions respectively. Hence the distance between the left-hand edges can be described as:

$$(X_2 - X_1) = \Delta X = l_{NS} - a$$

Applying strain along the x-axis of the system, will move the edges of the nanosheets further apart:

$$\Delta X = (\varepsilon + 1)(\Delta X)_0$$

The subscript zero denotes the unstrained condition.

Assuming that the nanosheets do not change length, but simply slide past each other upon straining, these two expressions can be combined:

$$\Delta X_0(\varepsilon + 1) = l_{NS} - a$$

In the absence of strain, where a_0 is the unstrained value of a:

$$\Delta X_0 = l_{NS} - a_0$$

Hence $(l_{NS} - a_0)(\varepsilon + 1) = l_{NS} - a$.

Multiplying across by l_{NS}, and recalling $A_J = a l_{NS}$:

$$(l_{NS}^2 - a_0 l_{NS})(\varepsilon + 1) = l_{NS}^2 - a l_{NS}$$

$$(l_{NS}^2 - A_{J,0})(\varepsilon + 1) = l_{NS}^2 - A_J$$

Here, $A_{J,0}$ is the unstrained junction resistance.

Rewriting to get an expression for A_J:

$$A_J = A_{J,0}\left[1 - \frac{(l_{NS}^2 - A_{J,0})}{A_{J,0}}\varepsilon\right]$$

Expressing this in terms of the fractional nanosheet area taken up by the junction, $f_{J,0} = A_{J,0} / l_{NS}^2$, yields:

$$A_J = A_{J,0}\left[1 - \frac{(1 - f_{J,0})}{f_{J,0}}\varepsilon\right]$$

R_J can be expressed in terms of A_J, where $(RA)_J$ is a fundamental junction property:

$$R_J = \frac{(RA)_J}{A_J}$$

$$R_J = \frac{(RA)_J}{A_{J,0}}\left[1 - \frac{(1 - f_{J,0})}{f_{J,0}}\varepsilon\right]^{-1}$$

For small values of x, such expressions can be rewritten as $(1 - x)^{-1} \approx 1 + x$:

$$R_J \approx \frac{(RA)_J}{A_{J,0}}\left[1 + \frac{(1 - f_{J,0})}{f_{J,0}}\varepsilon\right]$$

The junction capacitance, C_J, can be similarly derived, starting with the following expression:

$$C_J = \varepsilon_r \varepsilon_0 A_J / l_J$$

Here ε_r represents the relative permittivity and ε_0 represents the permittivity of free space.

$$C_J = \frac{\varepsilon_r \varepsilon_0 A_{J,0}}{l_J}\left[1 - \frac{(1 - f_{J,0})}{f_{J,0}}\varepsilon\right] = C_{J,0}\left[1 - \frac{(1 - f_{J,0})}{f_{J,0}}\varepsilon\right]$$

A.5.4 Geometric Gauge Factor in Anisotropic Materials

It has been shown that for isotropic materials without an intrinsic piezoresistance, the gauge factor can be expressed as $G = 1 + 2\nu$.[332] However, for anisotropic materials, this equation must be slightly modified. Considering an anisotropic sample with sample dimensions L_x, w_y, and t_z in the x, y, and z directions respectively, extension along the x-axis will result in a strain of $\varepsilon_x = (L_x - L_{x,0}) / L_{x,0}$, which rearranges to give $L_x = L_{x,0}(\varepsilon_x + 1)$. Note the subscript zero denotes the unstrained condition. By analogy, the strain dependent values in the y and z directions can be expressed as $w_y = w_{y,0}(\varepsilon_y + 1)$ and $t_z = t_{z,0}(\varepsilon_z + 1)$ respectively.

The strain in the y and z directions depend on the Poisson ratios, such that, $\varepsilon_y = -\nu_y \varepsilon_x$ and $\varepsilon_z = -\nu_z \varepsilon_x$.

Hence, each dimension can be written in terms of ε_x:

$w_y = w_{y,0}(1 - \nu_y \varepsilon_x)$ and $t_z = t_{z,0}(1 - \nu_z \varepsilon_x)$.

The resistance along the x-axis can be written as:

$$R_x = \rho \frac{L_x}{w_y t_z}$$

And the gauge factor can be written as:

$$G = \frac{1}{\varepsilon_x}\left[\frac{R_x - R_{x,0}}{R_{x,0}}\right] = \frac{1}{\varepsilon_x}\left[\frac{L_x / L_{x,0}}{(w_y / w_{y,0})(t_z / t_{y,0})} - 1\right]$$

Rewriting in terms of the applied strain:

$$G = \frac{1}{\varepsilon_x}\left[\frac{(\varepsilon_x + 1)}{(1 - \nu_y \varepsilon_x)(1 - \nu_z \varepsilon_x)} - 1\right]$$

Simplifying the denominator using the observation below for y, and similar for z:

$$\frac{1}{(1 - \nu_y \varepsilon_x)} = (1 - \nu_y \varepsilon_x)^{-1} \approx (1 + \nu_y \varepsilon_x)$$

Yields:

$$G = \frac{1}{\varepsilon_x}\left[(\varepsilon_x + 1)(1 + \nu_y \varepsilon_x)(1 + \nu_z \varepsilon_x) - 1\right]$$

Expanding out the product in square brackets, neglecting terms which include ε_x^2 or higher powers yields:

$$G = 1 + \nu_y + \nu_z$$

For isotropic materials, this equation simplifies to $G = 1 + 2\nu$ as expected.

Bibliography

[1] Feynman, R. P. There's Plenty of Room at the Bottom. *Engineering and Science* **1960**, *23* (5), 22-36.

[2] Pokrajac, L.; Abbas, A.; Chrzanowski, W.; Dias, G. M.; Eggleton, B. J.; Maguire, S.; Maine, E.; Malloy, T.; Nathwani, J.; Nazar, L.; et al. Nanotechnology for a Sustainable Future: Addressing Global Challenges with the International Network4Sustainable Nanotechnology. *ACS Nano* **2021**, *15* (12), 18608-18623. DOI: 10.1021/acsnano.1c10919.

[3] Sergeev, G. B.; Klabunde, K. J. *Nanochemistry*; Elsevier, 2013. DOI: 10.1016/B978-0-444-59397-9.00002-5.

[4] Novoselov, K. S.; Geim, A. K.; Morozov, S. V.; Jiang, D.; Zhang, Y.; Dubonos, S. V.; Grigorieva, I. V.; Firsov, A. A. Electric Field Effect in Atomically Thin Carbon Films. *Science* **2004**, *306* (5696), 666-669. DOI: 10.1126/science.1102896.

[5] Hernandez, Y.; Nicolosi, V.; Lotya, M.; Blighe, F. M.; Sun, Z.; De, S.; McGovern, I. T.; Holland, B.; Byrne, M.; Gun'Ko, Y. K.; et al. High-yield production of graphene by liquid-phase exfoliation of graphite. *Nature Nanotechnology* **2008**, *3* (9), 563-568. DOI: 10.1038/nnano.2008.215.

[6] Kelly, A. G.; O'Suilleabhain, D.; Gabbett, C.; Coleman, J. N. The electrical conductivity of solution-processed nanosheet networks. *Nature Reviews Materials* **2021**. DOI: 10.1038/s41578-021-00386-w.

[7] Kelly, A. G.; Finn, D.; Harvey, A.; Hallam, T.; Coleman, J. N. All-printed capacitors from graphene-BN-graphene nanosheet heterostructures. *Applied Physics Letters* **2016**, *109* (2). DOI: 10.1063/1.4958858.

[8] Tian, R.; Griffin, A.; McCrystall, M.; Breshears, M.; Harvey, A.; Gabbett, C.; Horváth, D. V.; Backes, C.; Jing, Y.; Heine, T.; et al. Liquid Exfoliated SnP3 Nanosheets for Very High Areal Capacity Lithium-Ion Batteries. *Advanced Energy Materials* **2021**, *11* (4), 2002364. DOI: 10.1002/aenm.202002364.

[9] Gholamvand, Z.; McAteer, D.; Harvey, A.; Backes, C.; Coleman, J. N. Electrochemical Applications of Two-Dimensional Nanosheets: The Effect of Nanosheet Length and Thickness. *Chemistry of Materials* **2016**, *28* (8), 2641-2651. DOI: 10.1021/acs.chemmater.6b00009.

[10] Boland, C. S.; Khan, U.; Ryan, G.; Barwich, S.; Charifou, R.; Harvey, A.; Backes, C.; Li, Z.; Ferreira, M. S.; Möbius, M. E.; et al. Sensitive electromechanical sensors using viscoelastic graphene-polymer nanocomposites. *Science* **2016**, *354* (6317), 1257. DOI: 10.1126/science.aag2879.

[11] Murr, L. E. Nanoparticulate materials in antiquity: The good, the bad and the ugly. *Materials Characterization* **2009**, *60* (4), 261-270. DOI: 10.1016/j.matchar.2008.03.012.

[12] Astruc, D. Introduction: Nanoparticles in Catalysis. *Chemical Reviews* **2020**, *120* (2), 461-463. DOI: 10.1021/acs.chemrev.8b00696.

[13] Reibold, M.; Paufler, P.; Levin, A. A.; Kochmann, W.; Pätzke, N.; Meyer, D. C. Carbon nanotubes in an ancient Damascus sabre. *Nature* **2006**, *444* (7117), 286-286. DOI: 10.1038/444286a.

[14] Geim, A. K.; Novoselov, K. S. The rise of graphene. *Nature Materials* **2007**, *6* (3), 183-191. DOI: 10.1038/nmat1849.

[15] Zhou, Z.-Y.; Tian, N.; Li, J.-T.; Broadwell, I.; Sun, S.-G. Nanomaterials of high surface energy with exceptional properties in catalysis and energy storage. *Chemical Society Reviews* **2011**, *40* (7), 4167-4185, 10.1039/C0CS00176G. DOI: 10.1039/C0CS00176G.

[16] Su, X.; Wu, Q.; Li, J.; Xiao, X.; Lott, A.; Lu, W.; Sheldon, B. W.; Wu, J. Silicon-Based Nanomaterials for Lithium-Ion Batteries: A Review. *Advanced Energy Materials* **2014**, *4* (1), 1300882. DOI: 10.1002/aenm.201300882.

[17] Akinwande, D.; Huyghebaert, C.; Wang, C.-H.; Serna, M. I.; Goossens, S.; Li, L.-J.; Wong, H. S. P.; Koppens, F. H. L. Graphene and two-dimensional materials for silicon technology. *Nature* **2019**, *573* (7775), 507-518. DOI: 10.1038/s41586-019-1573-9.

[18] Kim, K. S.; Kwon, J.; Ryu, H.; Kim, C.; Kim, H.; Lee, E.-K.; Lee, D.; Seo, S.; Han, N. M.; Suh, J. M.; et al. The future of two-dimensional semiconductors beyond Moore's law. *Nature Nanotechnology* **2024**. DOI: 10.1038/s41565-024-01695-1.

[19] Winer, W. O. Molybdenum disulfide as a lubricant: A review of the fundamental knowledge. *Wear* **1967**, *10* (6), 422-452. DOI: 10.1016/0043-1648(67)90187-1.

[20] Dienwiebel, M.; Verhoeven, G. S.; Pradeep, N.; Frenken, J. W. M.; Heimberg, J. A.; Zandbergen, H. W. Superlubricity of Graphite. *Physical Review Letters* **2004**, *92* (12), 126101. DOI: 10.1103/PhysRevLett.92.126101.

[21] Landau, L. D. Zur Theorie der phasenumwandlungen II. *Phys. Z. Sowjetunion* **1937**, *11* (545), 26-35.

[22] Mermin, N. D. Crystalline Order in Two Dimensions. *Physical Review* **1968**, *176* (1), 250-254. DOI: 10.1103/PhysRev.176.250.

[23] Fasolino, A.; Los, J. H.; Katsnelson, M. I. Intrinsic ripples in graphene. *Nature Materials* **2007**, *6* (11), 858-861. DOI: 10.1038/nmat2011.

[24] Dean, C. R.; Young, A. F.; Meric, I.; Lee, C.; Wang, L.; Sorgenfrei, S.; Watanabe, K.; Taniguchi, T.; Kim, P.; Shepard, K. L.; et al. Boron nitride substrates for high-quality graphene electronics. *Nature Nanotechnology* **2010**, *5* (10), 722-726. DOI: 10.1038/nnano.2010.172.

[25] Campi, D.; Mounet, N.; Gibertini, M.; Pizzi, G.; Marzari, N. Expansion of the Materials Cloud 2D Database. *ACS Nano* **2023**, *17* (12), 11268-11278. DOI: 10.1021/acsnano.2c11510.

[26] Girit, Ç. Ö.; Meyer, J. C.; Erni, R.; Rossell, M. D.; Kisielowski, C.; Yang, L.; Park, C.-H.; Crommie, M. F.; Cohen, M. L.; Louie, S. G.; et al. Graphene at the Edge: Stability and Dynamics. *Science* **2009**, *323* (5922), 1705-1708. DOI: doi:10.1126/science.1166999.

[27] Castro Neto, A. H.; Guinea, F.; Peres, N. M. R.; Novoselov, K. S.; Geim, A. K. The electronic properties of graphene. *Reviews of Modern Physics* **2009**, *81* (1), 109-162. DOI: 10.1103/RevModPhys.81.109.

[28] Lee, C.; Wei, X.; Kysar, J. W.; Hone, J. Measurement of the Elastic Properties and Intrinsic Strength of Monolayer Graphene. *Science* **2008**, *321* (5887), 385-388. DOI: doi:10.1126/science.1157996.

[29] Balandin, A. A.; Ghosh, S.; Bao, W.; Calizo, I.; Teweldebrhan, D.; Miao, F.; Lau, C. N. Superior Thermal Conductivity of Single-Layer Graphene. *Nano Letters* **2008**, *8* (3), 902-907. DOI: 10.1021/nl0731872.

[30] It's still all about graphene. *Nature Materials* **2011**, *10* (1), 1-1. DOI: 10.1038/nmat2938.

[31] Brodie, B. C. On the Atomic Weight of Graphite. *Philosophical Transactions of the Royal Society of London* **1859**, *149*, 249-259. JSTOR.

[32] Hull, A. W. A New Method of X-Ray Crystal Analysis. *Physical Review* **1917**, *10* (6), 661-696. DOI: 10.1103/PhysRev.10.661.

[33] Dalba, G. Peter J. W. Debye – a whole life devoted to science. *Acta Crystallographica Section A* **2016**, *72* (6), 591-607. DOI: 10.1107/S2053273316013619.

[34] Bernal, J. D.; Bragg, W. L. The structure of graphite. *Proceedings of the Royal Society of London. Series A, Containing Papers of a Mathematical and Physical Character* **1924**, *106* (740), 749-773. DOI: doi:10.1098/rspa.1924.0101.

[35] Wallace, P. R. The Band Theory of Graphite. *Physical Review* **1947**, *71* (9), 622-634. DOI: 10.1103/PhysRev.71.622.

[36] Meyer, J. C.; Geim, A. K.; Katsnelson, M. I.; Novoselov, K. S.; Booth, T. J.; Roth, S. The structure of suspended graphene sheets. *Nature* **2007**, *446* (7131), 60-63. DOI: 10.1038/nature05545.

[37] Stoller, M. D.; Park, S.; Zhu, Y.; An, J.; Ruoff, R. S. Graphene-Based Ultracapacitors. *Nano Letters* **2008**, *8* (10), 3498-3502. DOI: 10.1021/nl802558y.

[38] Briggs, N.; Subramanian, S.; Lin, Z.; Li, X.; Zhang, X.; Zhang, K.; Xiao, K.; Geohegan, D.; Wallace, R.; Chen, L.-Q.; et al. A roadmap for electronic grade 2D materials. *2D Materials* **2019**, *6* (2), 022001. DOI: 10.1088/2053-1583/aaf836.

[39] Avouris, P.; Dimitrakopoulos, C. Graphene: synthesis and applications. *Materials Today* **2012**, *15* (3), 86-97. DOI: 10.1016/S1369-7021(12)70044-5.

[40] Raimondo, M.; Guadagno, L.; Speranza, V.; Bonnaud, L.; Dubois, P.; Lafdi, K. Multifunctional graphene/POSS epoxy resin tailored for aircraft lightning strike protection. *Composites Part B: Engineering* **2018**, *140*, 44-56. DOI: 10.1016/j.compositesb.2017.12.015.

[41] Novoselov, K. S.; Jiang, D.; Schedin, F.; Booth, T. J.; Khotkevich, V. V.; Morozov, S. V.; Geim, A. K. Two-dimensional atomic crystals. *Proceedings of the National Academy of Sciences* **2005**, *102* (30), 10451-10453. DOI: 10.1073/pnas.0502848102.

[42] Elias, C.; Valvin, P.; Pelini, T.; Summerfield, A.; Mellor, C. J.; Cheng, T. S.; Eaves, L.; Foxon, C. T.; Beton, P. H.; Novikov, S. V.; et al. Direct band-gap crossover in epitaxial monolayer boron nitride. *Nature Communications* **2019**, *10* (1), 2639. DOI: 10.1038/s41467-019-10610-5.

[43] Yin, D.; Yang, Y.; Yang, Y.; Fang, H. A novel fullerene-like B30N30 structure: Stability and electronic property. *Carbon* **2016**, *102*, 273-278. DOI: 10.1016/j.carbon.2016.02.063.

[44] Seyyed Fakhrabadi, M. M. Comment on 'Molecular structure-dependent deformations in boron nitride nanostructures subject to an electrical field'. *Journal of Physics D: Applied Physics* **2016**, *49* (10), 108001. DOI: 10.1088/0022-3727/49/10/108001.

[45] McDougall, N. L.; Partridge, J. G.; Nicholls, R. J.; Russo, S. P.; McCulloch, D. G. Influence of point defects on the near edge structure of hexagonal boron nitride. *Physical Review B* **2017**, *96* (14), 144106. DOI: 10.1103/PhysRevB.96.144106.

[46] Caldwell, J. D.; Aharonovich, I.; Cassabois, G.; Edgar, J. H.; Gil, B.; Basov, D. N. Photonics with hexagonal boron nitride. *Nature Reviews Materials* **2019**, *4* (8), 552-567. DOI: 10.1038/s41578-019-0124-1.

[47] Fu, D.; Zhao, X.; Zhang, Y.-Y.; Li, L.; Xu, H.; Jang, A. R.; Yoon, S. I.; Song, P.; Poh, S. M.; Ren, T.; et al. Molecular Beam Epitaxy of Highly Crystalline Monolayer

Molybdenum Disulfide on Hexagonal Boron Nitride. *Journal of the American Chemical Society* **2017**, *139* (27), 9392-9400. DOI: 10.1021/jacs.7b05131.

[48] Li, L. H.; Cervenka, J.; Watanabe, K.; Taniguchi, T.; Chen, Y. Strong Oxidation Resistance of Atomically Thin Boron Nitride Nanosheets. *ACS Nano* **2014**, *8* (2), 1457-1462. DOI: 10.1021/nn500059s.

[49] Ma, K. Y.; Kim, M.; Shin, H. S. Large-Area Hexagonal Boron Nitride Layers by Chemical Vapor Deposition: Growth and Applications for Substrates, Encapsulation, and Membranes. *Accounts of Materials Research* **2022**, *3* (7), 748-760. DOI: 10.1021/accountsmr.2c00061.

[50] Lee, J. S.; Choi, S. H.; Yun, S. J.; Kim, Y. I.; Boandoh, S.; Park, J.-H.; Shin, B. G.; Ko, H.; Lee, S. H.; Kim, Y.-M.; et al. Wafer-scale single-crystal hexagonal boron nitride film via self-collimated grain formation. *Science* **2018**, *362* (6416), 817-821. DOI: doi:10.1126/science.aau2132.

[51] Manzeli, S.; Ovchinnikov, D.; Pasquier, D.; Yazyev, O. V.; Kis, A. 2D transition metal dichalcogenides. *Nature Reviews Materials* **2017**, *2* (8), 17033. DOI: 10.1038/natrevmats.2017.33.

[52] Dickinson, R. G.; Pauling, L. The Crystal Structure of Molybdenite. *Journal of the American Chemical Society* **1923**, *45* (6), 1466-1471. DOI: 10.1021/ja01659a020.

[53] Samadi, M.; Sarikhani, N.; Zirak, M.; Zhang, H.; Zhang, H.-L.; Moshfegh, A. Z. Group 6 transition metal dichalcogenide nanomaterials: synthesis, applications and future perspectives. *Nanoscale Horizons* **2018**, *3* (2), 90-204, 10.1039/C7NH00137A. DOI: 10.1039/C7NH00137A.

[54] Chhowalla, M.; Shin, H. S.; Eda, G.; Li, L.-J.; Loh, K. P.; Zhang, H. The chemistry of two-dimensional layered transition metal dichalcogenide nanosheets. *Nature Chemistry* **2013**, *5* (4), 263-275. DOI: 10.1038/nchem.1589.

[55] Wang, Q. H.; Kalantar-Zadeh, K.; Kis, A.; Coleman, J. N.; Strano, M. S. Electronics and optoelectronics of two-dimensional transition metal dichalcogenides. *Nature Nanotechnology* **2012**, *7* (11), 699-712. DOI: 10.1038/nnano.2012.193.

[56] Dai, Y.; He, Q.; Huang, Y.; Duan, X.; Lin, Z. Solution-Processable and Printable Two-Dimensional Transition Metal Dichalcogenide Inks. *Chemical Reviews* **2024**, *124* (9), 5795-5845. DOI: 10.1021/acs.chemrev.3c00791.

[57] Bonaccorso, F.; Bartolotta, A.; Coleman, J. N.; Backes, C. 2D-Crystal-Based Functional Inks. *Advanced Materials* **2016**, *28* (29), 6136-6166. DOI: 10.1002/adma.201506410.

[58] Mak, K. F.; Lee, C.; Hone, J.; Shan, J.; Heinz, T. F. Atomically Thin MoS2: A New Direct-Gap Semiconductor. *Physical Review Letters* **2010**, *105* (13), 136805. DOI: 10.1103/PhysRevLett.105.136805.

[59] Chaves, A.; Azadani, J. G.; Alsalman, H.; da Costa, D. R.; Frisenda, R.; Chaves, A. J.; Song, S. H.; Kim, Y. D.; He, D.; Zhou, J.; et al. Bandgap engineering of two-dimensional semiconductor materials. *npj 2D Materials and Applications* **2020**, *4* (1), 29. DOI: 10.1038/s41699-020-00162-4.

[60] Zheng, Z.; Yu, L.; Gao, M.; Chen, X.; Zhou, W.; Ma, C.; Wu, L.; Zhu, J.; Meng, X.; Hu, J.; et al. Boosting hydrogen evolution on MoS2 via co-confining selenium in surface and cobalt in inner layer. *Nature Communications* **2020**, *11* (1), 3315. DOI: 10.1038/s41467-020-17199-0.

[61] Hu, Y.; Huang, Y.; Tan, C.; Zhang, X.; Lu, Q.; Sindoro, M.; Huang, X.; Huang, W.; Wang, L.; Zhang, H. Two-dimensional transition metal dichalcogenide nanomaterials for biosensing applications. *Materials Chemistry Frontiers* **2017**, *1* (1), 24-36, 10.1039/C6QM00195E. DOI: 10.1039/C6QM00195E.

[62] Velusamy, D. B.; Kim, R. H.; Cha, S.; Huh, J.; Khazaeinezhad, R.; Kassani, S. H.; Song, G.; Cho, S. M.; Cho, S. H.; Hwang, I.; et al. Flexible transition metal dichalcogenide nanosheets for band-selective photodetection. *Nature Communications* **2015**, *6* (1), 8063. DOI: 10.1038/ncomms9063.

[63] Kelly, A., G.; Hallam, T.; Backes, C.; Harvey, A.; Esmaeily Amir, S.; Godwin, I.; Coelho, J.; Nicolosi, V.; Lauth, J.; Kulkarni, A.; et al. All-printed thin-film transistors from networks of liquid-exfoliated nanosheets. *Science* **2017**, *356* (6333), 69-73. DOI: 10.1126/science.aal4062.

[64] Ge, R.; Wu, X.; Kim, M.; Shi, J.; Sonde, S.; Tao, L.; Zhang, Y.; Lee, J. C.; Akinwande, D. Atomristor: Nonvolatile Resistance Switching in Atomic Sheets of Transition Metal Dichalcogenides. *Nano Letters* **2018**, *18* (1), 434-441. DOI: 10.1021/acs.nanolett.7b04342.

[65] Joensen, P.; Frindt, R. F.; Morrison, S. R. Single-layer MoS2. *Materials Research Bulletin* **1986**, *21* (4), 457-461. DOI: 10.1016/0025-5408(86)90011-5.

[66] Mannix, A. J.; Kiraly, B.; Hersam, M. C.; Guisinger, N. P. Synthesis and chemistry of elemental 2D materials. *Nature Reviews Chemistry* **2017**, *1* (2), 0014. DOI: 10.1038/s41570-016-0014.

[67] Geim, A. K. Graphene: Status and Prospects. *Science* **2009**, *324* (5934), 1530-1534. DOI: 10.1126/science.1158877.

[68] Frindt, R. F.; Yoffe, A. D. Physical Properties of Layer Structures: Optical Properties and Photoconductivity of Thin Crystals of Molybdenum Disulphide. *Proceedings of the*

Royal Society of London. Series A, Mathematical and Physical Sciences **1963**, *273* (1352), 69-83. JSTOR.

[69] Xuekun, L.; Minfeng, Y.; Hui, H.; Rodney, S. R. Tailoring graphite with the goal of achieving single sheets. *Nanotechnology* **1999**, *10* (3), 269. DOI: 10.1088/0957-4484/10/3/308.

[70] Huang, Y.; Pan, Y.-H.; Yang, R.; Bao, L.-H.; Meng, L.; Luo, H.-L.; Cai, Y.-Q.; Liu, G.-D.; Zhao, W.-J.; Zhou, Z.; et al. Universal mechanical exfoliation of large-area 2D crystals. *Nature Communications* **2020**, *11* (1), 2453. DOI: 10.1038/s41467-020-16266-w.

[71] Castellanos-Gomez, A.; Buscema, M.; Molenaar, R.; Singh, V.; Janssen, L.; van der Zant, H. S. J.; Steele, G. A. Deterministic transfer of two-dimensional materials by all-dry viscoelastic stamping. *2D Materials* **2014**, *1* (1), 011002. DOI: 10.1088/2053-1583/1/1/011002.

[72] Novoselov, K. S.; Mishchenko, A.; Carvalho, A.; Castro Neto, A. H. 2D materials and van der Waals heterostructures. *Science* **2016**, *353* (6298), aac9439. DOI: doi:10.1126/science.aac9439.

[73] Novoselov, K. S.; Fal′ko, V. I.; Colombo, L.; Gellert, P. R.; Schwab, M. G.; Kim, K. A roadmap for graphene. *Nature* **2012**, *490* (7419), 192-200. DOI: 10.1038/nature11458.

[74] Yi, M.; Shen, Z. A review on mechanical exfoliation for the scalable production of graphene. *Journal of Materials Chemistry A* **2015**, *3* (22), 11700-11715, 10.1039/C5TA00252D. DOI: 10.1039/C5TA00252D.

[75] Li, X.; Cai, W.; An, J.; Kim, S.; Nah, J.; Yang, D.; Piner, R.; Velamakanni, A.; Jung, I.; Tutuc, E.; et al. Large-Area Synthesis of High-Quality and Uniform Graphene Films on Copper Foils. *Science* **2009**, *324* (5932), 1312-1314. DOI: 10.1126/science.1171245.

[76] Lee, S.; Lee, K.; Zhong, Z. Wafer Scale Homogeneous Bilayer Graphene Films by Chemical Vapor Deposition. *Nano Letters* **2010**, *10* (11), 4702-4707. DOI: 10.1021/nl1029978.

[77] Jeon, J.; Jang, S. K.; Jeon, S. M.; Yoo, G.; Jang, Y. H.; Park, J.-H.; Lee, S. Layer-controlled CVD growth of large-area two-dimensional MoS2 films. *Nanoscale* **2015**, *7* (5), 1688-1695, 10.1039/C4NR04532G. DOI: 10.1039/C4NR04532G.

[78] Gao, Y.; Liu, Z.; Sun, D.-M.; Huang, L.; Ma, L.-P.; Yin, L.-C.; Ma, T.; Zhang, Z.; Ma, X.-L.; Peng, L.-M.; et al. Large-area synthesis of high-quality and uniform monolayer WS2 on reusable Au foils. *Nature Communications* **2015**, *6* (1), 8569. DOI: 10.1038/ncomms9569.

[79] Li, S.; Wang, S.; Tang, D.-M.; Zhao, W.; Xu, H.; Chu, L.; Bando, Y.; Golberg, D.; Eda, G. Halide-assisted atmospheric pressure growth of large WSe2 and WS2 monolayer crystals. *Applied Materials Today* **2015**, *1* (1), 60-66. DOI: 10.1016/j.apmt.2015.09.001.

[80] Choy, K. L. Chemical vapour deposition of coatings. *Progress in Materials Science* **2003**, *48* (2), 57-170. DOI: 10.1016/S0079-6425(01)00009-3.

[81] Powell, C. F.; Blocher, J. M.; Oxley, J. H. *Vapor Deposition*; John Wiley & Sons, 1966.

[82] Lee, S.-M.; Kim, J.-H.; Ahn, J.-H. Graphene as a flexible electronic material: mechanical limitations by defect formation and efforts to overcome. *Materials Today* **2015**, *18* (6), 336-344. DOI: 10.1016/j.mattod.2015.01.017.

[83] Zaaba, N. I.; Foo, K. L.; Hashim, U.; Tan, S. J.; Liu, W.-W.; Voon, C. H. Synthesis of Graphene Oxide using Modified Hummers Method: Solvent Influence. *Procedia Engineering* **2017**, *184*, 469-477. DOI: 10.1016/j.proeng.2017.04.118.

[84] Lim, K. R. G.; Shekhirev, M.; Wyatt, B. C.; Anasori, B.; Gogotsi, Y.; Seh, Z. W. Fundamentals of MXene synthesis. *Nature Synthesis* **2022**, *1* (8), 601-614. DOI: 10.1038/s44160-022-00104-6.

[85] Hu, C.-X.; Shin, Y.; Read, O.; Casiraghi, C. Dispersant-assisted liquid-phase exfoliation of 2D materials beyond graphene. *Nanoscale* **2021**, *13* (2), 460-484. DOI: 10.1039/D0NR05514J.

[86] Nicolosi, V.; Chhowalla, M.; Kanatzidis Mercouri, G.; Strano Michael, S.; Coleman Jonathan, N. Liquid Exfoliation of Layered Materials. *Science* **2013**, *340* (6139), 1226419. DOI: 10.1126/science.1226419.

[87] Paton, K. R.; Varrla, E.; Backes, C.; Smith, R. J.; Khan, U.; O'Neill, A.; Boland, C.; Lotya, M.; Istrate, O. M.; King, P.; et al. Scalable production of large quantities of defect-free few-layer graphene by shear exfoliation in liquids. *Nature Materials* **2014**, *13* (6), 624-630. DOI: 10.1038/nmat3944.

[88] Zhi, C.; Bando, Y.; Tang, C.; Kuwahara, H.; Golberg, D. Large-Scale Fabrication of Boron Nitride Nanosheets and Their Utilization in Polymeric Composites with Improved Thermal and Mechanical Properties. *Advanced Materials* **2009**, *21* (28), 2889-2893. DOI: 10.1002/adma.200900323.

[89] Coleman, J. N.; Lotya, M.; O'Neill, A.; Bergin, S. D.; King, P. J.; Khan, U.; Young, K.; Gaucher, A.; De, S.; Smith, R. J.; et al. Two-Dimensional Nanosheets Produced by Liquid Exfoliation of Layered Materials. *Science* **2011**, *331* (6017), 568-571. DOI: 10.1126/science.1194975.

[90] Hanlon, D.; Backes, C.; Doherty, E.; Cucinotta, C. S.; Berner, N. C.; Boland, C.; Lee, K.; Harvey, A.; Lynch, P.; Gholamvand, Z.; et al. Liquid exfoliation of solvent-

stabilized few-layer black phosphorus for applications beyond electronics. *Nature Communications* **2015**, *6* (1), 8563. DOI: 10.1038/ncomms9563.

[91] Hanlon, D.; Backes, C.; Higgins, T. M.; Hughes, M.; O'Neill, A.; King, P.; McEvoy, N.; Duesberg, G. S.; Mendoza Sanchez, B.; Pettersson, H.; et al. Production of Molybdenum Trioxide Nanosheets by Liquid Exfoliation and Their Application in High-Performance Supercapacitors. *Chemistry of Materials* **2014**, *26* (4), 1751-1763. DOI: 10.1021/cm500271u.

[92] Kaur, H.; Coleman, J. N. Liquid-Phase Exfoliation of Nonlayered Non-Van-Der-Waals Crystals into Nanoplatelets. *Advanced Materials* **2022**, *34* (35), 2202164. DOI: 10.1002/adma.202202164.

[93] Duck, F. Paul Langevin, U-boats, and ultrasonics. *Physics Today* **2022**, *75* (11), 42-48. DOI: 10.1063/pt.3.5122.

[94] Mason, T. J. Ultrasonic cleaning: An historical perspective. *Ultrasonics Sonochemistry* **2016**, *29*, 519-523. DOI: 10.1016/j.ultsonch.2015.05.004.

[95] Li, Z.; Young, R. J.; Backes, C.; Zhao, W.; Zhang, X.; Zhukov, A. A.; Tillotson, E.; Conlan, A. P.; Ding, F.; Haigh, S. J.; et al. Mechanisms of Liquid-Phase Exfoliation for the Production of Graphene. *ACS Nano* **2020**, *14* (9), 10976-10985. DOI: 10.1021/acsnano.0c03916.

[96] Zhou, G.; Rajak, P.; Susarla, S.; Ajayan, P. M.; Kalia, R. K.; Nakano, A.; Vashishta, P. Molecular Simulation of MoS2 Exfoliation. *Scientific Reports* **2018**, *8* (1), 16761. DOI: 10.1038/s41598-018-35008-z.

[97] Ma, H.; Shen, Z.; Ben, S. Understanding the exfoliation and dispersion of MoS2 nanosheets in pure water. *Journal of Colloid and Interface Science* **2018**, *517*, 204-212. DOI: 10.1016/j.jcis.2017.11.013.

[98] Hess, P. Surface Acoustic Waves in Materials Science. *Physics Today* **2002**, *55* (3), 42-47. DOI: 10.1063/1.1472393.

[99] Rooney, A. P.; Li, Z.; Zhao, W.; Gholinia, A.; Kozikov, A.; Auton, G.; Ding, F.; Gorbachev, R. V.; Young, R. J.; Haigh, S. J. Anomalous twin boundaries in two dimensional materials. *Nature Communications* **2018**, *9* (1), 3597. DOI: 10.1038/s41467-018-06074-8.

[100] Suslick, K. S. Sonochemistry. *Science* **1990**, *247* (4949), 1439-1445. DOI: 10.1126/science.247.4949.1439.

[101] Annett, J.; Cross, G. L. W. Self-assembly of graphene ribbons by spontaneous self-tearing and peeling from a substrate. *Nature* **2016**, *535* (7611), 271-275. DOI: 10.1038/nature18304.

[102] Backes, C.; Campi, D.; Szydlowska, B. M.; Synnatschke, K.; Ojala, E.; Rashvand, F.; Harvey, A.; Griffin, A.; Sofer, Z.; Marzari, N.; et al. Equipartition of Energy Defines the Size–Thickness Relationship in Liquid-Exfoliated Nanosheets. *ACS Nano* **2019**, *13* (6), 7050-7061. DOI: 10.1021/acsnano.9b02234.

[103] Ji, L.-J.; Qin, Y.; Gui, D.; Li, W.; Li, Y.; Li, X.; Lu, P. Quantifying the Exfoliation Ease Level of 2D Materials via Mechanical Anisotropy. *Chemistry of Materials* **2018**, *30* (24), 8732-8738. DOI: 10.1021/acs.chemmater.8b01082.

[104] Coleman, J. N. Liquid Exfoliation of Defect-Free Graphene. *Accounts of Chemical Research* **2013**, *46* (1), 14-22. DOI: 10.1021/ar300009f.

[105] Chacham, H.; Santos, J. C. C.; Pacheco, F. G.; Silva, D. L.; Martins, R. M.; Del'Boccio, J. P.; Soares, E. M.; Altoé, R.; Furtado, C. A.; Plentz, F.; et al. Controlling the Morphology of Nanoflakes Obtained by Liquid-Phase Exfoliation: Implications for the Mass Production of 2D Materials. *ACS Applied Nano Materials* **2020**, *3* (12), 12095-12105. DOI: 10.1021/acsanm.0c02598.

[106] May, P.; Khan, U.; O'Neill, A.; Coleman, J. N. Approaching the theoretical limit for reinforcing polymers with graphene. *Journal of Materials Chemistry* **2012**, *22* (4), 1278-1282, 10.1039/C1JM15467B. DOI: 10.1039/C1JM15467B.

[107] Parvez, K.; Wu, Z.-S.; Li, R.; Liu, X.; Graf, R.; Feng, X.; Müllen, K. Exfoliation of Graphite into Graphene in Aqueous Solutions of Inorganic Salts. *Journal of the American Chemical Society* **2014**, *136* (16), 6083-6091. DOI: 10.1021/ja5017156.

[108] Abdelkader, A. M.; Cooper, A. J.; Dryfe, R. A. W.; Kinloch, I. A. How to get between the sheets: a review of recent works on the electrochemical exfoliation of graphene materials from bulk graphite. *Nanoscale* **2015**, *7* (16), 6944-6956, 10.1039/C4NR06942K. DOI: 10.1039/C4NR06942K.

[109] Kappera, R.; Voiry, D.; Yalcin, S. E.; Branch, B.; Gupta, G.; Mohite, A. D.; Chhowalla, M. Phase-engineered low-resistance contacts for ultrathin MoS2 transistors. *Nature Materials* **2014**, *13* (12), 1128-1134. DOI: 10.1038/nmat4080.

[110] Zhao, M.; Casiraghi, C.; Parvez, K. Electrochemical exfoliation of 2D materials beyond graphene. *Chemical Society Reviews* **2024**, *53* (6), 3036-3064, 10.1039/D3CS00815K. DOI: 10.1039/D3CS00815K.

[111] Rhee, D.; Jariwala, D.; Cho, J. H.; Kang, J. Solution-processed 2D van der Waals networks: Fabrication strategies, properties, and scalable device applications. *Applied Physics Reviews* **2024**, *11* (2). DOI: 10.1063/5.0205192.

[112] Paredes, J. I.; Munuera, J. M. Recent advances and energy-related applications of high quality/chemically doped graphenes obtained by electrochemical exfoliation methods. *Journal of Materials Chemistry A* **2017**, *5* (16), 7228-7242, 10.1039/C7TA01711A. DOI: 10.1039/C7TA01711A.

[113] Munuera, J. M.; Paredes, J. I.; Villar-Rodil, S.; Ayán-Varela, M.; Martínez-Alonso, A.; Tascón, J. M. D. Electrolytic exfoliation of graphite in water with multifunctional electrolytes: en route towards high quality, oxide-free graphene flakes. *Nanoscale* **2016**, *8* (5), 2982-2998, 10.1039/C5NR06882G. DOI: 10.1039/C5NR06882G.

[114] Munuera, J. M.; Paredes, J. I.; Villar-Rodil, S.; Ayán-Varela, M.; Pagán, A.; Aznar-Cervantes, S. D.; Cenis, J. L.; Martínez-Alonso, A.; Tascón, J. M. D. High quality, low oxygen content and biocompatible graphene nanosheets obtained by anodic exfoliation of different graphite types. *Carbon* **2015**, *94*, 729-739. DOI: 10.1016/j.carbon.2015.07.053.

[115] Su, C.-Y.; Lu, A.-Y.; Xu, Y.; Chen, F.-R.; Khlobystov, A. N.; Li, L.-J. High-Quality Thin Graphene Films from Fast Electrochemical Exfoliation. *ACS Nano* **2011**, *5* (3), 2332-2339. DOI: 10.1021/nn200025p.

[116] Yang, S.; Brüller, S.; Wu, Z.-S.; Liu, Z.; Parvez, K.; Dong, R.; Richard, F.; Samorì, P.; Feng, X.; Müllen, K. Organic Radical-Assisted Electrochemical Exfoliation for the Scalable Production of High-Quality Graphene. *Journal of the American Chemical Society* **2015**, *137* (43), 13927-13932. DOI: 10.1021/jacs.5b09000.

[117] Parvez, K.; Li, R.; Puniredd, S. R.; Hernandez, Y.; Hinkel, F.; Wang, S.; Feng, X.; Müllen, K. Electrochemically Exfoliated Graphene as Solution-Processable, Highly Conductive Electrodes for Organic Electronics. *ACS Nano* **2013**, *7* (4), 3598-3606. DOI: 10.1021/nn400576v.

[118] Lu, J.; Yang, J.-x.; Wang, J.; Lim, A.; Wang, S.; Loh, K. P. One-Pot Synthesis of Fluorescent Carbon Nanoribbons, Nanoparticles, and Graphene by the Exfoliation of Graphite in Ionic Liquids. *ACS Nano* **2009**, *3* (8), 2367-2375. DOI: 10.1021/nn900546b.

[119] Liu, N.; Kim, P.; Kim, J. H.; Ye, J. H.; Kim, S.; Lee, C. J. Large-Area Atomically Thin MoS2 Nanosheets Prepared Using Electrochemical Exfoliation. *ACS Nano* **2014**, *8* (7), 6902-6910. DOI: 10.1021/nn5016242.

[120] Lin, Z.; Liu, Y.; Halim, U.; Ding, M.; Liu, Y.; Wang, Y.; Jia, C.; Chen, P.; Duan, X.; Wang, C.; et al. Solution-processable 2D semiconductors for high-performance large-area electronics. *Nature* **2018**, *562* (7726), 254-258. DOI: 10.1038/s41586-018-0574-4.

[121] Wang, S.; Xue, J.; Xu, D.; He, J.; Dai, Y.; Xia, T.; Huang, Y.; He, Q.; Duan, X.; Lin, Z. Electrochemical molecular intercalation and exfoliation of solution-processable two-dimensional crystals. *Nature Protocols* **2023**, *18* (9), 2814-2837. DOI: 10.1038/s41596-023-00865-0.

[122] Li, Y.; Duerloo, K.-A. N.; Wauson, K.; Reed, E. J. Structural semiconductor-to-semimetal phase transition in two-dimensional materials induced by electrostatic gating. *Nature Communications* **2016**, *7* (1), 10671. DOI: 10.1038/ncomms10671.

[123] Wang, C.; He, Q.; Halim, U.; Liu, Y.; Zhu, E.; Lin, Z.; Xiao, H.; Duan, X.; Feng, Z.; Cheng, R.; et al. Monolayer atomic crystal molecular superlattices. *Nature* **2018**, *555* (7695), 231-236. DOI: 10.1038/nature25774.

[124] Carey, T.; Cassidy, O.; Synnatschke, K.; Caffrey, E.; Garcia, J.; Liu, S.; Kaur, H.; Kelly, A. G.; Munuera, J.; Gabbett, C.; et al. High-Mobility Flexible Transistors with Low-Temperature Solution-Processed Tungsten Dichalcogenides. *ACS Nano* **2023**, *17* (3), 2912-2922. DOI: 10.1021/acsnano.2c11319.

[125] Rubenstein, M.; Colby, R. C. *Polymer Physics*; Oxford University Press, 2003.

[126] Atkins, P.; de Paula, J. *Atkins' Physical Chemistry*; Oxford University Press, 2014.

[127] Cao, W.; Wang, J.; Ma, M. Exfoliation of Two-Dimensional Materials: The Role of Entropy. *The Journal of Physical Chemistry Letters* **2019**, *10* (5), 981-986. DOI: 10.1021/acs.jpclett.9b00204.

[128] Hildebrand, J. H.; Prausnitz, J. M.; Scott, R. L. *Regular and Related Solutions: The Solubility of Gases, Liquids, and Solids*; Van Nostrand Reinhold Company, 1970.

[129] Gardon, J. L. Critical review of concepts common to cohesive energy density, surface tension, tensile strength, heat of mixing, interfacial tension, and butt joint strength. *Journal of Colloid and Interface Science* **1977**, *59* (3), 582-596. DOI: 10.1016/0021-9797(77)90053-4.

[130] Hildebrand, J. H.; Scott, R. L. *The Solubility of Nonelectrolytes*; Reinhold Publishing Corporation, 1950.

[131] Hansen, C. M. *The three dimensional solubility parameter and solvent diffusion coefficient: Their importance in surface coating formulation*; Danish Technical Press, 1967.

[132] Lindvig, T.; Michelsen, M. L.; Kontogeorgis, G. M. A Flory–Huggins model based on the Hansen solubility parameters. *Fluid Phase Equilibria* **2002**, *203* (1), 247-260. DOI: 10.1016/S0378-3812(02)00184-X.

[133] Saillenfait, A. M.; Gallissot, F.; Langonné, I.; Sabaté, J. P. Developmental toxicity of N-methyl-2-pyrrolidone administered orally to rats. *Food and Chemical Toxicology* **2002**, *40* (11), 1705-1712. DOI: 10.1016/S0278-6915(02)00115-1.

[134] Stuart, R. Lessons Learned from a Short-Term Exposure to DMF. *ACS Chemical Health & Safety* **2023**, *30* (2), 44-48. DOI: 10.1021/acs.chas.2c00047.

[135] Pan, K.; Fan, Y.; Leng, T.; Li, J.; Xin, Z.; Zhang, J.; Hao, L.; Gallop, J.; Novoselov, K. S.; Hu, Z. Sustainable production of highly conductive multilayer graphene ink for

wireless connectivity and IoT applications. *Nature Communications* **2018**, *9* (1), 5197. DOI: 10.1038/s41467-018-07632-w.

[136] Backes, C.; Szydłowska, B. M.; Harvey, A.; Yuan, S.; Vega-Mayoral, V.; Davies, B. R.; Zhao, P.-l.; Hanlon, D.; Santos, E. J. G.; Katsnelson, M. I.; et al. Production of Highly Monolayer Enriched Dispersions of Liquid-Exfoliated Nanosheets by Liquid Cascade Centrifugation. *ACS Nano* **2016**, *10* (1), 1589-1601. DOI: 10.1021/acsnano.5b07228.

[137] Zhu, J.; Kang, J.; Kang, J.; Jariwala, D.; Wood, J. D.; Seo, J.-W. T.; Chen, K.-S.; Marks, T. J.; Hersam, M. C. Solution-Processed Dielectrics Based on Thickness-Sorted Two-Dimensional Hexagonal Boron Nitride Nanosheets. *Nano Letters* **2015**, *15* (10), 7029-7036. DOI: 10.1021/acs.nanolett.5b03075.

[138] Graham, J. *Biological centrifugation*; Garland Science, 2020.

[139] Green, A. A.; Hersam, M. C. Ultracentrifugation of single-walled nanotubes. *Materials Today* **2007**, *10* (12), 59-60. DOI: 10.1016/S1369-7021(07)70309-7.

[140] Green, A. A.; Hersam, M. C. Solution Phase Production of Graphene with Controlled Thickness via Density Differentiation. *Nano Letters* **2009**, *9* (12), 4031-4036. DOI: 10.1021/nl902200b.

[141] Huang, X.; Leng, T.; Zhang, X.; Chen, J. C.; Chang, K. H.; Geim, A. K.; Novoselov, K. S.; Hu, Z. Binder-free highly conductive graphene laminate for low cost printed radio frequency applications. *Applied Physics Letters* **2015**, *106* (20). DOI: 10.1063/1.4919935.

[142] Svedberg, T.; Pedersen, K. O. *The Ultracentrifuge*; Oxford University Press, 1940.

[143] Barwich, S.; Khan, U.; Coleman, J. N. A Technique To Pretreat Graphite Which Allows the Rapid Dispersion of Defect-Free Graphene in Solvents at High Concentration. *The Journal of Physical Chemistry C* **2013**, *117* (37), 19212-19218. DOI: 10.1021/jp4047006.

[144] Clifford, K.; Ogilvie, S. P.; Amorim Graf, A.; Wood, H. J.; Sehnal, A. C.; Salvage, J. P.; Lynch, P. J.; Large, M. J.; Dalton, A. B. Emergent high conductivity in size-selected graphene networks. *Carbon* **2024**, *218*, 118642. DOI: 10.1016/j.carbon.2023.118642.

[145] Higgins, T. M.; Finn, S.; Matthiesen, M.; Grieger, S.; Synnatschke, K.; Brohmann, M.; Rother, M.; Backes, C.; Zaumseil, J. Electrolyte-Gated n-Type Transistors Produced from Aqueous Inks of WS2 Nanosheets. *Advanced Functional Materials* **2019**, *29* (4), 1804387. DOI: 10.1002/adfm.201804387.

[146] Gabbett, C.; Doolan, L.; Synnatschke, K.; Gambini, L.; Coleman, E.; Kelly, A. G.; Liu, S.; Caffrey, E.; Munuera, J.; Murphy, C.; et al. Quantitative analysis of printed

nanostructured networks using high-resolution 3D FIB-SEM nanotomography. *Nature Communications* **2024**, *15* (1), 278. DOI: 10.1038/s41467-023-44450-1.

[147] Gabbett, C.; Kelly, A. G.; Coleman, E.; Doolan, L.; Carey, T.; Synnatschke, K.; Liu, S.; Dawson, A.; O'Suilleabhain, D.; Munuera, J.; et al. Understanding how junction resistances impact the conduction mechanism in nano-networks. *Nature Communications* **2024**, *15* (1), 4517. DOI: 10.1038/s41467-024-48614-5.

[148] Derby, B. Inkjet Printing of Functional and Structural Materials: Fluid Property Requirements, Feature Stability, and Resolution. *Annual Review of Materials Research* **2010**, *40* (1), 395-414. DOI: 10.1146/annurev-matsci-070909-104502.

[149] Torrisi, F.; Hasan, T.; Wu, W.; Sun, Z.; Lombardo, A.; Kulmala, T. S.; Hsieh, G.-W.; Jung, S.; Bonaccorso, F.; Paul, P. J.; et al. Inkjet-Printed Graphene Electronics. *ACS Nano* **2012**, *6* (4), 2992-3006. DOI: 10.1021/nn2044609.

[150] Jabari, E.; Toyserkani, E. Micro-scale aerosol-jet printing of graphene interconnects. *Carbon* **2015**, *91*, 321-329. DOI: 10.1016/j.carbon.2015.04.094.

[151] Secor, E. B. Principles of aerosol jet printing. *Flexible and Printed Electronics* **2018**, *3* (3), 035002. DOI: 10.1088/2058-8585/aace28.

[152] Huang, Q.; Zhu, Y. Printing Conductive Nanomaterials for Flexible and Stretchable Electronics: A Review of Materials, Processes, and Applications. *Advanced Materials Technologies* **2019**, *4* (5), 1800546. DOI: 10.1002/admt.201800546.

[153] Li, J.; Lemme, M. C.; Östling, M. Inkjet Printing of 2D Layered Materials. *ChemPhysChem* **2014**, *15* (16), 3427-3434. DOI: 10.1002/cphc.201402103.

[154] van Hazendonk, L. S.; Vonk, C. F.; van Grondelle, W.; Vonk, N. H.; Friedrich, H. Towards a predictive understanding of direct ink writing of graphene-based inks. *Applied Materials Today* **2024**, *36*, 102014. DOI: 10.1016/j.apmt.2023.102014.

[155] Scardaci, V.; Coull, R.; Lyons, P. E.; Rickard, D.; Coleman, J. N. Spray Deposition of Highly Transparent, Low-Resistance Networks of Silver Nanowires over Large Areas. *Small* **2011**, *7* (18), 2621-2628. DOI: 10.1002/smll.201100647.

[156] Sakai, N.; Sasaki, T. Guidelines for Arranging 2D Nanosheets into Neatly Tiled Monolayer Films by a Spin-Coating Process. *Langmuir* **2022**, *38* (40), 12399-12407. DOI: 10.1021/acs.langmuir.2c02211.

[157] Li, X.; Yang, T.; Yang, Y.; Zhu, J.; Li, L.; Alam, F. E.; Li, X.; Wang, K.; Cheng, H.; Lin, C.-T.; et al. Large-Area Ultrathin Graphene Films by Single-Step Marangoni Self-Assembly for Highly Sensitive Strain Sensing Application. *Advanced Functional Materials* **2016**, *26* (9), 1322-1329. DOI: 10.1002/adfm.201504717.

[158] Neilson, J.; Avery, M. P.; Derby, B. Tiled Monolayer Films of 2D Molybdenum Disulfide Nanoflakes Assembled at Liquid/Liquid Interfaces. *ACS Appl Mater Interfaces* **2020**, *12* (22), 25125-25134. DOI: 10.1021/acsami.0c03794.

[159] Stanley, F. E. Improvement in Atomizers. USA 1876.

[160] Kim, J.; Lee, T.; Han, J.-H.; Kim, J. H. Possibility of large-area carbon nanotube films formation through spray coating. *Micro and Nano Systems Letters* **2024**, *12* (1), 6. DOI: 10.1186/s40486-023-00193-8.

[161] Ferrer-Anglada, N.; Kaempgen, M.; Skákalová, V.; Dettlaf-Weglikowska, U.; Roth, S. Synthesis and characterization of carbon nanotube-conducting polymer thin films. *Diamond and Related Materials* **2004**, *13* (2), 256-260. DOI: 10.1016/j.diamond.2003.10.026.

[162] Kaempgen, M.; Duesberg, G. S.; Roth, S. Transparent carbon nanotube coatings. *Applied Surface Science* **2005**, *252* (2), 425-429. DOI: 10.1016/j.apsusc.2005.01.020.

[163] Chen, M.; Yu, H.; Kershaw, S. V.; Xu, H.; Gupta, S.; Hetsch, F.; Rogach, A. L.; Zhao, N. Fast, Air-Stable Infrared Photodetectors based on Spray-Deposited Aqueous HgTe Quantum Dots. *Advanced Functional Materials* **2014**, *24* (1), 53-59. DOI: 10.1002/adfm.201301006.

[164] Blake, P.; Brimicombe, P. D.; Nair, R. R.; Booth, T. J.; Jiang, D.; Schedin, F.; Ponomarenko, L. A.; Morozov, S. V.; Gleeson, H. F.; Hill, E. W.; et al. Graphene-Based Liquid Crystal Device. *Nano Letters* **2008**, *8* (6), 1704-1708. DOI: 10.1021/nl080649i.

[165] Dong, Y. L.; Pan, B. A Review of Speckle Pattern Fabrication and Assessment for Digital Image Correlation. *Experimental Mechanics* **2017**, *57* (8), 1161-1181. DOI: 10.1007/s11340-017-0283-1.

[166] O'Driscoll, D. P.; McMahon, S.; Garcia, J.; Biccai, S.; Gabbett, C.; Kelly, A. G.; Barwich, S.; Moebius, M.; Boland, C. S.; Coleman, J. N. Printable G-Putty for Frequency- and Rate-Independent, High-Performance Strain Sensors. *Small* **2021**, *17* (23), e2006542. DOI: 10.1002/smll.202006542.

[167] Carey, T.; Jones, C.; Le Moal, F.; Deganello, D.; Torrisi, F. Spray-Coating Thin Films on Three-Dimensional Surfaces for a Semitransparent Capacitive-Touch Device. *ACS Applied Materials & Interfaces* **2018**, *10* (23), 19948-19956. DOI: 10.1021/acsami.8b02784.

[168] Finn, D. J.; Lotya, M.; Coleman, J. N. Inkjet Printing of Silver Nanowire Networks. *ACS Applied Materials & Interfaces* **2015**, *7* (17), 9254-9261. DOI: 10.1021/acsami.5b01875.

[169] Cai, F.; Chang, Y. H.; Wang, K.; Zhang, C.; Wang, B.; Papapolymerou, J. Low-Loss 3-D Multilayer Transmission Lines and Interconnects Fabricated by Additive

Manufacturing Technologies. *IEEE Transactions on Microwave Theory and Techniques* **2016**, *64* (10), 3208-3216. DOI: 10.1109/TMTT.2016.2601907.

[170] Garcia, J. R.; McCrystal, M.; Horváth, D.; Kaur, H.; Carey, T.; Coleman, J. N. Tuneable Piezoresistance of Graphene-Based 2D:2D Nanocomposite Networks. *Advanced Functional Materials* **2023**, *33* (20), 2214855. DOI: 10.1002/adfm.202214855.

[171] Ruhkopf, J.; Sawallich, S.; Nagel, M.; Otto, M.; Plachetka, U.; Kremers, T.; Schnakenberg, U.; Kataria, S.; Lemme, M. C. Role of Substrate Surface Morphology on the Performance of Graphene Inks for Flexible Electronics. *ACS Applied Electronic Materials* **2019**, *1* (9), 1909-1916. DOI: 10.1021/acsaelm.9b00413.

[172] Barwich, S.; Medeiros de Araújo, J.; Rafferty, A.; Gomes da Rocha, C.; Ferreira, M. S.; Coleman, J. N. On the relationship between morphology and conductivity in nanosheet networks. *Carbon* **2021**, *171*, 306-319. DOI: 10.1016/j.carbon.2020.09.015.

[173] Rodgers, A. N. J.; Rabiu, A. K.; Toth, P. S.; Adams, R. W.; Dryfe, R. A. W. Assembly and electrochemistry of carbon nanomaterials at the liquid-liquid interface. *Electrochimica Acta* **2019**, *308*, 307-316. DOI: 10.1016/j.electacta.2019.04.035.

[174] Kalosi, A.; Demydenko, M.; Bodik, M.; Hagara, J.; Kotlar, M.; Kostiuk, D.; Halahovets, Y.; Vegso, K.; Marin Roldan, A.; Maurya, G. S.; et al. Tailored Langmuir–Schaefer Deposition of Few-Layer MoS2 Nanosheet Films for Electronic Applications. *Langmuir* **2019**, *35* (30), 9802-9808. DOI: 10.1021/acs.langmuir.9b01000.

[175] Langmuir, I.; Schaefer, V. J. Activities of urease and pepsin monolayers. *Journal of the American Chemical Society* **1938**, *60* (6), 1351-1360.

[176] Shi, S.; Russell, T. P. Nanoparticle Assembly at Liquid–Liquid Interfaces: From the Nanoscale to Mesoscale. *Advanced Materials* **2018**, *30* (44), 1800714. DOI: 10.1002/adma.201800714.

[177] Li, Y.-J.; Huang, W.-J.; Sun, S.-G. A Universal Approach for the Self-Assembly of Hydrophilic Nanoparticles into Ordered Monolayer Films at a Toluene/Water Interface. *Angewandte Chemie International Edition* **2006**, *45* (16), 2537-2539. DOI: 10.1002/anie.200504595.

[178] Lin, Y.; Skaff, H.; Böker, A.; Dinsmore, A. D.; Emrick, T.; Russell, T. P. Ultrathin Cross-Linked Nanoparticle Membranes. *Journal of the American Chemical Society* **2003**, *125* (42), 12690-12691. DOI: 10.1021/ja036919a.

[179] Biswas, S.; Drzal, L. T. A Novel Approach to Create a Highly Ordered Monolayer Film of Graphene Nanosheets at the Liquid−Liquid Interface. *Nano Letters* **2009**, *9* (1), 167-172. DOI: 10.1021/nl802724f.

[180] Yu, X.; Prévot, M. S.; Guijarro, N.; Sivula, K. Self-assembled 2D WSe2 thin films for photoelectrochemical hydrogen production. *Nature Communications* **2015**, *6* (1), 7596. DOI: 10.1038/ncomms8596.

[181] Pieranski, P. Two-Dimensional Interfacial Colloidal Crystals. *Physical Review Letters* **1980**, *45* (7), 569-572. DOI: 10.1103/PhysRevLett.45.569.

[182] Pickering, S. U. CXCVI.—Emulsions. *Journal of the Chemical Society, Transactions* **1907**, *91* (0), 2001-2021, 10.1039/CT9079102001. DOI: 10.1039/CT9079102001.

[183] Zeppieri, S.; Rodríguez, J.; López de Ramos, A. L. Interfacial Tension of Alkane + Water Systems. *Journal of Chemical & Engineering Data* **2001**, *46* (5), 1086-1088. DOI: 10.1021/je000245r.

[184] Binks, B. P.; Lumsdon, S. O. Influence of Particle Wettability on the Type and Stability of Surfactant-Free Emulsions. *Langmuir* **2000**, *16* (23), 8622-8631. DOI: 10.1021/la000189s.

[185] Lin, Y.; Böker, A.; Skaff, H.; Cookson, D.; Dinsmore, A. D.; Emrick, T.; Russell, T. P. Nanoparticle Assembly at Fluid Interfaces: Structure and Dynamics. *Langmuir* **2005**, *21* (1), 191-194. DOI: 10.1021/la048000q.

[186] Binks, B. P.; Horozov, T. S. *Colloidal Particles at Liquid Interfaces*; Cambridge University Press, 2006. DOI: DOI: 10.1017/CBO9780511536670.

[187] Neilson, J. Liquid-Liquid Assembled 2D Materials for Large-Area Electronics. Ph.D., The University of Manchester (United Kingdom), England, 2021.

[188] Jia, B.; Wang, Q.; Zhang, W.; Lin, B.; Yuan, N.; Ding, J.; Ren, Y.; Chu, F. A new oil/water interfacial assembly of sulphonated graphene into ultrathin films. *RSC Advances* **2014**, *4* (65), 34566-34571, 10.1039/C4RA05160B. DOI: 10.1039/C4RA05160B.

[189] Fang, P.-P.; Chen, S.; Deng, H.; Scanlon, M. D.; Gumy, F.; Lee, H. J.; Momotenko, D.; Amstutz, V.; Cortés-Salazar, F.; Pereira, C. M.; et al. Conductive Gold Nanoparticle Mirrors at Liquid/Liquid Interfaces. *ACS Nano* **2013**, *7* (10), 9241-9248. DOI: 10.1021/nn403879g.

[190] Pavia, D. L.; Lampman, G. M.; Kriz, G. S.; Vyvyan, J. R. *Introduction to Spectroscopy, 5th Edition*; Cengage Learning, USA, 2015.

[191] Mukhopadhyay, R. The Rise of Instruments during World War II. *Analytical Chemistry* **2008**, *80* (15), 5684-5691. DOI: 10.1021/ac801205u.

[192] Teichmann, J.; Stinner, A. From William Hyde Wollaston to Alexander von Humboldt - Star Spectra and Celestial Landscape. *Annals of Science* **2014**, *71* (1), 27-60. DOI: 10.1080/00033790.2012.739709.

[193] Owen, T. *Fundamentals of modern UV-visible spectroscopy*; Agilent Technologies, 2000.

[194] Rocha, F. S.; Gomes, A. J.; Lunardi, C. N.; Kaliaguine, S.; Patience, G. S. Experimental methods in chemical engineering: Ultraviolet visible spectroscopy—UV-Vis. *The Canadian Journal of Chemical Engineering* **2018**, *96* (12), 2512-2517. DOI: 10.1002/cjce.23344.

[195] Backes, C.; Paton, K. R.; Hanlon, D.; Yuan, S.; Katsnelson, M. I.; Houston, J.; Smith, R. J.; McCloskey, D.; Donegan, J. F.; Coleman, J. N. Spectroscopic metrics allow in situ measurement of mean size and thickness of liquid-exfoliated few-layer graphene nanosheets. *Nanoscale* **2016**, *8* (7), 4311-4323. DOI: 10.1039/c5nr08047a.

[196] Kubetschek, N.; Backes, C.; Goldie, S. Algorithm for Reproducible Analysis of Semiconducting 2D Nanomaterials Based on UV-VIS Spectroscopy. *Advanced Materials Interfaces* **2024**, 2400311. DOI: 10.1002/admi.202400311.

[197] Abdolkarimi-Mahabadi, M.; Bayat, A.; Mohammadi, A. Use of UV-Vis Spectrophotometry for Characterization of Carbon Nanostructures: a Review. *Theoretical and Experimental Chemistry* **2021**, *57* (3), 191-198. DOI: 10.1007/s11237-021-09687-1.

[198] Fox, M. *Optical Properties of Solids*; Oxford University Press, 2001.

[199] *What is the Stokes Shift*. Edinburgh Instruments, https://www.edinst.com/blog/what-is-the-stokes-shift/ (accessed 09/05/2024).

[200] Ferrari, A. C.; Basko, D. M. Raman spectroscopy as a versatile tool for studying the properties of graphene. *Nature Nanotechnology* **2013**, *8* (4), 235-246. DOI: 10.1038/nnano.2013.46.

[201] Raman, C. V.; Krishnan, K. S. A New Type of Secondary Radiation. *Nature* **1928**, *121* (3048), 501-502. DOI: 10.1038/121501c0.

[202] Zhang, S.-L. *Raman Spectroscopy and its Application in Nanostructures*; Wiley, 2012. DOI: 10.1002/9781119961659.

[203] Ferraro, J. R.; Nakamoto, K.; Brown, C. W. *Introductory Raman Spectroscopy (Second Edition)*; Academic Press, 2003. DOI: 10.1016/B978-012254105-6/50005-6.

[204] Ma, X.; Guo, P.; Yi, C.; Yu, Q.; Zhang, A.; Ji, J.; Tian, Y.; Jin, F.; Wang, Y.; Liu, K.; et al. Raman scattering in the transition-metal dichalcogenides of 1T'-MoTe2, Td-MoTe2,

and Td-WTe2. *Physical Review B* **2016**, *94* (21), 214105. DOI: 10.1103/PhysRevB.94.214105.

[205] Jacobs, P. *Group Theory with Applications in Chemical Physics*; Cambridge University Press, UK, 2005.

[206] Ferrari, A. C.; Robertson, J. Interpretation of Raman spectra of disordered and amorphous carbon. *Physical Review B* **2000**, *61* (20), 14095-14107. DOI: 10.1103/PhysRevB.61.14095.

[207] Li, H.; Zhang, Q.; Yap, C. C. R.; Tay, B. K.; Edwin, T. H. T.; Olivier, A.; Baillargeat, D. From Bulk to Monolayer MoS2: Evolution of Raman Scattering. *Advanced Functional Materials* **2012**, *22* (7), 1385-1390. DOI: 10.1002/adfm.201102111.

[208] Inkson, B. J. 2 - Scanning electron microscopy (SEM) and transmission electron microscopy (TEM) for materials characterization. In *Materials Characterization Using Nondestructive Evaluation (NDE) Methods*, Hübschen, G., Altpeter, I., Tschuncky, R., Herrmann, H.-G. Eds.; Woodhead Publishing, 2016; pp 17-43.

[209] Zworykin, V. K. The scanning electron microscope. *Scientific American* **1942**, *167* (3), 111-113.

[210] Joy, D. C.; Joy, C. S. Low voltage scanning electron microscopy. *Micron* **1996**, *27* (3), 247-263. DOI: 10.1016/0968-4328(96)00023-6.

[211] Goldstein, J. I.; Newbury, D. E.; Michael, J. R.; Ritchie, N. W. M.; Scott, J. H. J.; Joy, D. C. *Scanning Electron Microscopy and X-Ray Microanalysis*; Springer New York, 2017.

[212] Goodhew, P. J.; Humphreys, J.; Beanland, R. *Electron Microscopy and Analysis, Third Edition*; Taylor & Francis, 2000.

[213] Sinnott, A. D.; Kelly, A.; Gabbett, C.; Munuera, J.; Doolan, L.; Möbius, M.; Ippolito, S.; Samorì, P.; Coleman, J. N.; Cross, G. L. W. Mechanical Properties of Conducting Printed Nanosheet Network Thin Films Under Uniaxial Compression. *Advanced Materials* **2024**, *36* (9), 2306954. DOI: 10.1002/adma.202306954.

[214] de Groot, P.; de Lega, X. C. Scanning interferometry for thin film thickness and surface measurements. USA 2008.

[215] Leach, R. K. *The measurement of surface texture using stylus instruments*; 2; Teddington, 2014. http://eprintspublications.npl.co.uk/2041/.

[216] de Groot, P. Principles of interference microscopy for the measurement of surface topography. *Adv. Opt. Photon.* **2015**, *7* (1), 1-65. DOI: 10.1364/AOP.7.000001.

[217] Lonardo, P. M.; Trumpold, H.; De Chiffre, L. Progress in 3D Surface Microtopography Characterization. *CIRP Annals* **1996**, *45* (2), 589-598. DOI: 10.1016/S0007-8506(07)60513-7.

[218] Hariharan, P. *Basics of interferometry*; Elsevier Academic Press, 2006.

[219] de Groot, P. Coherence Scanning Interferometry. In *Optical Measurement of Surface Topography*, Leach, R. Ed.; Springer Berlin Heidelberg, 2011; pp 187-208.

[220] Sagnac, G. Strioscope et striographe interférentiels - Forme interférentielle de la méthode optique des stries. *Radium (Paris)* **1911**, *8* (7), 241-253.

[221] Mirau, André H. Interferometer. USA 1950.

[222] de Groot, P. Derivation of algorithms for phase-shifting interferometry using the concept of a data-sampling window. *Appl. Opt.* **1995**, *34* (22), 4723-4730. DOI: 10.1364/AO.34.004723.

[223] Callister, W. D.; Rethwisch, D. G. *Materials Science and Engineering*; Wiley, 2014.

[224] Lazanas, A. C.; Prodromidis, M. I. Electrochemical Impedance Spectroscopy─A Tutorial. *ACS Measurement Science Au* **2023**, *3* (3), 162-193. DOI: 10.1021/acsmeasuresciau.2c00070.

[225] Tumanski, S. *Principles of Electrical Measurement*; Taylor & Francis, USA, 2006.

[226] Witte, R. A. *Spectrum and network measurements*; nstitution of Engineering and Technology, 2014.

[227] Dalley, J. W.; Riley, W. F.; McConnell, K. G. *Instrumentation for engineering measurements*; Wiley, 1993.

[228] Spectrographic. *Exploring the Evolution of Tensile Testing: Unravelling the History of Material Strength Assessment*. 2024. https://www.linkedin.com/pulse/exploring-evolution-tensile-testing-unravelling-c4zrc/ (accessed 06/07/2024).

[229] Davis, J. R. *Tensile Testing*; ASM International, 2004.

[230] Window, A. L. *Strain Gauge Technology*; Springer, 1992.

[231] Pinilla, S.; Coelho, J.; Li, K.; Liu, J.; Nicolosi, V. Two-dimensional material inks. *Nature Reviews Materials* **2022**, *7* (9), 717-735. DOI: 10.1038/s41578-022-00448-7.

[232] Mazaheri, A.; Lee, M.; van der Zant, H. S. J.; Frisenda, R.; Castellanos-Gomez, A. MoS2-on-paper optoelectronics: drawing photodetectors with van der Waals

semiconductors beyond graphite. *Nanoscale* **2020**, *12* (37), 19068-19074, 10.1039/D0NR02268C. DOI: 10.1039/D0NR02268C.

[233] Nutting, D.; Felix, J. F.; Tillotson, E.; Shin, D.-W.; De Sanctis, A.; Chang, H.; Cole, N.; Russo, S.; Woodgate, A.; Leontis, I.; et al. Heterostructures formed through abraded van der Waals materials. *Nature Communications* **2020**, *11* (1), 3047. DOI: 10.1038/s41467-020-16717-4.

[234] Kurra, N.; Dutta, D.; Kulkarni, G. U. Field effect transistors and RC filters from pencil-trace on paper. *Physical Chemistry Chemical Physics* **2013**, *15* (21), 8367-8372, 10.1039/C3CP50675D. DOI: 10.1039/C3CP50675D.

[235] Zhang, Y.; Duan, Z.; Zou, H.; Ma, M. Drawn a facile sensor: A fast response humidity sensor based on pencil-trace. *Sensors and Actuators B: Chemical* **2018**, *261*, 345-353. DOI: 10.1016/j.snb.2018.01.176.

[236] Lin, C.-W.; Zhao, Z.; Kim, J.; Huang, J. Pencil Drawn Strain Gauges and Chemiresistors on Paper. *Scientific Reports* **2014**, *4* (1), 3812. DOI: 10.1038/srep03812.

[237] Kang, T.-K. Tunable piezoresistive sensors based on pencil-on-paper. *Applied Physics Letters* **2014**, *104* (7), 073117. DOI: 10.1063/1.4866440.

[238] Dinh, T.; Phan, H.-P.; Dao, D. V.; Woodfield, P.; Qamar, A.; Nguyen, N.-T. Graphite on paper as material for sensitive thermoresistive sensors. *Journal of Materials Chemistry C* **2015**, *3* (34), 8776-8779, 10.1039/C5TC01650A. DOI: 10.1039/C5TC01650A.

[239] Lee, M.; Mazaheri, A.; van der Zant, H. S. J.; Frisenda, R.; Castellanos-Gomez, A. Drawing WS2 thermal sensors on paper substrates. *Nanoscale* **2020**, *12* (43), 22091-22096, 10.1039/D0NR06036D. DOI: 10.1039/D0NR06036D.

[240] Kinloch, I. A.; Suhr, J.; Lou, J.; Young, R. J.; Ajayan, P. M. Composites with carbon nanotubes and graphene: An outlook. *Science* **2018**, *362* (6414), 547-553. DOI: 10.1126/science.aat7439.

[241] Melly, S. K.; Liu, L.; Liu, Y.; Leng, J. Active composites based on shape memory polymers: overview, fabrication methods, applications, and future prospects. *Journal of Materials Science* **2020**, *55* (25), 10975-11051. DOI: 10.1007/s10853-020-04761-w.

[242] Armstrong, G. An introduction to polymer nanocomposites. *European Journal of Physics* **2015**, *36* (6), 063001. DOI: 10.1088/0143-0807/36/6/063001.

[243] Casiraghi, C.; Macucci, M.; Parvez, K.; Worsley, R.; Shin, Y.; Bronte, F.; Borri, C.; Paggi, M.; Fiori, G. Inkjet printed 2D-crystal based strain gauges on paper. *Carbon* **2018**, *129*, 462-467. DOI: 10.1016/j.carbon.2017.12.030.

[244] Zhou, S.; Wang, L.; Lu, Z.; Ding, Q.; Wang, S. C.; Wood, R. J. K.; Xue, Q. Tailoring microstructure and phase segregation for low friction carbon-based nanocomposite coatings. *Journal of Materials Chemistry* **2012**, *22* (31), 15782-15792, 10.1039/C2JM30918A. DOI: 10.1039/C2JM30918A.

[245] Carey, T.; Maughan, J.; Doolan, L.; Caffrey, E.; Garcia, J.; Liu, S.; Kaur, H.; Ilhan, C.; Seyedin, S.; Coleman, J. N. Knot Architecture for Biocompatible and Semiconducting 2D Electronic Fiber Transistors. *Small Methods* **2024**, *n/a* (n/a), 2301654. DOI: 10.1002/smtd.202301654.

[246] Tang, Q.; Tang, Z.; Wu, J.; Lin, J.; Oh, I. Highly conducting multilayer films from graphene nanosheets by a spin self-assembly method. *Journal of Materials Chemistry* **2011**, *21* (14), 5378-5385, 10.1039/C0JM04055J. DOI: 10.1039/C0JM04055J.

[247] De, S.; King, P. J.; Lotya, M.; O'Neill, A.; Doherty, E. M.; Hernandez, Y.; Duesberg, G. S.; Coleman, J. N. Flexible, Transparent, Conducting Films of Randomly Stacked Graphene from Surfactant-Stabilized, Oxide-Free Graphene Dispersions. *Small* **2010**, *6* (3), 458-464. DOI: 10.1002/smll.200901162.

[248] De, S.; King, P. J.; Lyons, P. E.; Khan, U.; Coleman, J. N. Size Effects and the Problem with Percolation in Nanostructured Transparent Conductors. *ACS Nano* **2010**, *4* (12), 7064-7072. DOI: 10.1021/nn1025803.

[249] De, S.; Coleman, J. N. The effects of percolation in nanostructured transparent conductors. *MRS Bulletin* **2011**, *36* (10), 774-781. DOI: 10.1557/mrs.2011.236 From Cambridge University Press Cambridge Core.

[250] Arapov, K.; Bex, G.; Hendriks, R.; Rubingh, E.; Abbel, R.; de With, G.; Friedrich, H. Conductivity Enhancement of Binder-Based Graphene Inks by Photonic Annealing and Subsequent Compression Rolling *Advanced Engineering Materials* **2016**, *18* (7), 1234-1239. DOI: 10.1002/adem.201500646.

[251] Gao, Y.; Shi, W.; Wang, W.; Leng, Y.; Zhao, Y. Inkjet Printing Patterns of Highly Conductive Pristine Graphene on Flexible Substrates. *Industrial & Engineering Chemistry Research* **2014**, *53* (43), 16777-16784. DOI: 10.1021/ie502675z.

[252] Banerjee, I.; Faris, T.; Stoeva, Z.; Harris, P. G.; Chen, J.; Sharma, A. K.; Ray, A. K. Graphene films printable on flexible substrates for sensor applications. *2D Materials* **2017**, *4* (1), 015036. DOI: 10.1088/2053-1583/aa50f0.

[253] Carey, T.; Cacovich, S.; Divitini, G.; Ren, J.; Mansouri, A.; Kim, J. M.; Wang, C.; Ducati, C.; Sordan, R.; Torrisi, F. Fully inkjet-printed two-dimensional material field-effect heterojunctions for wearable and textile electronics. *Nature Communications* **2017**, *8* (1), 1202. DOI: 10.1038/s41467-017-01210-2.

[254] Islam, M. R.; Afroj, S.; Beach, C.; Islam, M. H.; Parraman, C.; Abdelkader, A.; Casson, A. J.; Novoselov, K. S.; Karim, N. Fully printed and multifunctional graphene-

based wearable e-textiles for personalized healthcare applications. *iScience* **2022**, *25* (3), 103945. DOI: 10.1016/j.isci.2022.103945.

[255] Sollami Delekta, S.; Östling, M.; Li, J. Wet Transfer of Inkjet Printed Graphene for Microsupercapacitors on Arbitrary Substrates. *ACS Applied Energy Materials* **2019**, *2* (1), 158-163. DOI: 10.1021/acsaem.8b01225.

[256] Liu, S.; Ding, E.-X.; Kelly, A. G.; Doolan, L.; Gabbett, C.; Kaur, H.; Munuera, J.; Carey, T.; Garcia, J.; Coleman, J. N. Solution processed, vertically stacked hetero-structured diodes based on liquid-exfoliated WS2 nanosheets: from electrode-limited to bulk-limited behavior. *Nanoscale* **2022**, *14* (42), 15679-15690, 10.1039/D2NR04196K. DOI: 10.1039/D2NR04196K.

[257] Neilson, J.; Caffrey, E.; Cassidy, O.; Gabbett, C.; Synnatschke, K.; Schneider, E.; Munuera, J. M.; Carey, T.; Rimmer, M.; Sofer, Z.; et al. Production of Ultrathin and High-Quality Nanosheet Networks via Layer-by-Layer Assembly at Liquid–Liquid Interfaces. *ACS Nano* **2024**, *18* (47), 32589-32601. DOI: 10.1021/acsnano.4c09745.

[258] Large, M. J.; Ogilvie, S. P.; Amorim Graf, A.; Lynch, P. J.; O'Mara, M. A.; Waters, T.; Jurewicz, I.; Salvage, J. P.; Dalton, A. B. Large-Scale Surfactant Exfoliation of Graphene and Conductivity-Optimized Graphite Enabling Wireless Connectivity. *Advanced Materials Technologies* **2020**, *5* (7), 2000284. DOI: 10.1002/admt.202000284.

[259] Yakimchuk, E.; Soots, R.; Kotin, I.; Antonova, I. 2D printed graphene conductive layers with high carrier mobility. *Current Applied Physics* **2017**, *17* (12), 1655-1661. DOI: 10.1016/j.cap.2017.09.012.

[260] Piatti, E.; Arbab, A.; Galanti, F.; Carey, T.; Anzi, L.; Spurling, D.; Roy, A.; Zhussupbekova, A.; Patel, K. A.; Kim, J. M.; et al. Charge transport mechanisms in inkjet-printed thin-film transistors based on two-dimensional materials. *Nature Electronics* **2021**, *4* (12), 893-905. DOI: 10.1038/s41928-021-00684-9.

[261] Shlimak, I. *Is Hopping a Science?*; WORLD SCIENTIFIC, 2015. DOI: doi:10.1142/9522.

[262] Ippolito, S.; Urban, F.; Zheng, W.; Mazzarisi, O.; Valentini, C.; Kelly, A. G.; Gali, S. M.; Bonn, M.; Beljonne, D.; Corberi, F.; et al. Unveiling Charge-Transport Mechanisms in Electronic Devices Based on Defect-Engineered MoS2 Covalent Networks. *Advanced Materials* **2023**, *35* (15), 2211157. DOI: 10.1002/adma.202211157.

[263] Guyot-Sionnest, P. Electrical Transport in Colloidal Quantum Dot Films. *The Journal of Physical Chemistry Letters* **2012**, *3* (9), 1169-1175. DOI: 10.1021/jz300048y.

[264] Nirmalraj, P. N.; Lyons, P. E.; De, S.; Coleman, J. N.; Boland, J. J. Electrical Connectivity in Single-Walled Carbon Nanotube Networks. *Nano Letters* **2009**, *9* (11), 3890-3895. DOI: 10.1021/nl9020914.

[265] Nirmalraj, P. N.; Lutz, T.; Kumar, S.; Duesberg, G. S.; Boland, J. J. Nanoscale Mapping of Electrical Resistivity and Connectivity in Graphene Strips and Networks. *Nano Letters* **2011**, *11* (1), 16-22. DOI: 10.1021/nl101469d.

[266] Aigner, W.; Bienek, O.; Falcão, B. P.; Ahmed, S. U.; Wiggers, H.; Stutzmann, M.; Pereira, R. N. Intra- and inter-nanocrystal charge transport in nanocrystal films. *Nanoscale* **2018**, *10* (17), 8042-8057, 10.1039/C8NR00250A. DOI: 10.1039/C8NR00250A.

[267] Kagan, C. R.; Murray, C. B. Charge transport in strongly coupled quantum dot solids. *Nature Nanotechnology* **2015**, *10* (12), 1013-1026. DOI: 10.1038/nnano.2015.247.

[268] Lanigan, D.; Thimsen, E. Contact Radius and the Insulator–Metal Transition in Films Comprised of Touching Semiconductor Nanocrystals. *ACS Nano* **2016**, *10* (7), 6744-6752. DOI: 10.1021/acsnano.6b02190.

[269] Epstein, N. On tortuosity and the tortuosity factor in flow and diffusion through porous media. *Chemical Engineering Science* **1989**, *44* (3), 777-779. DOI: 10.1016/0009-2509(89)85053-5.

[270] He, P.; Cao, J.; Ding, H.; Liu, C.; Neilson, J.; Li, Z.; Kinloch, I. A.; Derby, B. Screen-Printing of a Highly Conductive Graphene Ink for Flexible Printed Electronics. *ACS Applied Materials & Interfaces* **2019**, *11* (35), 32225-32234. DOI: 10.1021/acsami.9b04589.

[271] Hempel, M.; Nezich, D.; Kong, J.; Hofmann, M. A novel class of strain gauges based on layered percolative films of 2D materials. *Nano Lett* **2012**, *12* (11), 5714-5718. DOI: 10.1021/nl302959a.

[272] Sinnott, A. D.; Kelly, A.; Gabbett, C.; Moebius, M.; Coleman, J. N.; Cross, G. L. W. Pressure-dependent mechanical properties of thin films under uniaxial strain via the layer compression test. *Journal of Materials Research* **2024**, *39* (2), 273-282. DOI: 10.1557/s43578-023-01221-4.

[273] Sinnott, A. D. Mechanical Characterisation of Printed Nanosheet Network Thin Films. Trinity College Dublin, 2024. http://hdl.handle.net/2262/107314.

[274] Mott, P. H.; Roland, C. M. Limits to Poisson's ratio in isotropic materials. *Physical Review B* **2009**, *80* (13), 132104. DOI: 10.1103/PhysRevB.80.132104.

[275] Fortes, M. A.; Teresa Nogueira, M. The poison effect in cork. *Materials Science and Engineering: A* **1989**, *122* (2), 227-232. DOI: 10.1016/0921-5093(89)90634-5.

[276] Chen, M. J. Pressure-volume-temperature and wave propagation studies of polyimide films. University of Massachussetts Amherst, 1998.

[277] Anderson, M. L.; Mott, P. H.; Roland, C. M. The Compression of Bonded Rubber Disks. *Rubber Chemistry and Technology* **2004**, *77* (2), 293-302. DOI: 10.5254/1.3547824.

[278] Greaves, G. N.; Greer, A. L.; Lakes, R. S.; Rouxel, T. Poisson's ratio and modern materials. *Nature Materials* **2011**, *10* (11), 823-837. DOI: 10.1038/nmat3134.

[279] Evans, K. E.; Alderson, A. Auxetic Materials: Functional Materials and Structures from Lateral Thinking! *Advanced Materials* **2000**, *12* (9), 617-628. DOI: 10.1002/(SICI)1521-4095(200005)12:9<617::AID-ADMA617>3.0.CO;2-3.

[280] Kim, K. H.; Oh, Y.; Islam, M. F. Mechanical and Thermal Management Characteristics of Ultrahigh Surface Area Single-Walled Carbon Nanotube Aerogels. *Advanced Functional Materials* **2013**, *23* (3), 377-383. DOI: 10.1002/adfm.201201055.

[281] Mecklenburg, M.; Schuchardt, A.; Mishra, Y. K.; Kaps, S.; Adelung, R.; Lotnyk, A.; Kienle, L.; Schulte, K. Aerographite: Ultra Lightweight, Flexible Nanowall, Carbon Microtube Material with Outstanding Mechanical Performance. *Advanced Materials* **2012**, *24* (26), 3486-3490. DOI: 10.1002/adma.201200491.

[282] Wu, Y.; Yi, N.; Huang, L.; Zhang, T.; Fang, S.; Chang, H.; Li, N.; Oh, J.; Lee, J. A.; Kozlov, M.; et al. Three-dimensionally bonded spongy graphene material with super compressive elasticity and near-zero Poisson's ratio. *Nature Communications* **2015**, *6* (1), 6141. DOI: 10.1038/ncomms7141.

[283] Woo, S.; Park, H. C.; Son, Y.-W. Poisson's ratio in layered two-dimensional crystals. *Physical Review B* **2016**, *93* (7), 075420. DOI: 10.1103/PhysRevB.93.075420.

[284] Zhan, H.; Guo, D.; Xie, G. Two-dimensional layered materials: from mechanical and coupling properties towards applications in electronics. *Nanoscale* **2019**, *11* (28), 13181-13212, 10.1039/C9NR03611C. DOI: 10.1039/C9NR03611C.

[285] Fan, Y.; Xiang, Y.; Shen, H.-S. Temperature-Dependent Mechanical Properties of Graphene/Cu Nanocomposites with In-Plane Negative Poisson's Ratios. *Research* **2020**, *2020*. DOI: doi:10.34133/2020/5618021.

[286] Rawson, S. D.; Bayram, V.; McDonald, S. A.; Yang, P.; Courtois, L.; Guo, Y.; Xu, J.; Burnett, T. L.; Barg, S.; Withers, P. J. Tailoring the Microstructure of Lamellar Ti3C2Tx MXene Aerogel by Compressive Straining. *ACS Nano* **2022**, *16* (2), 1896-1908. DOI: 10.1021/acsnano.1c04538.

[287] McAteer, D.; Gholamvand, Z.; McEvoy, N.; Harvey, A.; O'Malley, E.; Duesberg, G. S.; Coleman, J. N. Thickness Dependence and Percolation Scaling of Hydrogen Production Rate in MoS2 Nanosheet and Nanosheet–Carbon Nanotube Composite Catalytic Electrodes. *ACS Nano* **2016**, *10* (1), 672-683. DOI: 10.1021/acsnano.5b05907.

[288] Li, M.; Liu, R.-R.; Lü, L.; Hu, M.-B.; Xu, S.; Zhang, Y.-C. Percolation on complex networks: Theory and application. *Physics Reports* **2021**, *907*, 1-68. DOI: 10.1016/j.physrep.2020.12.003.

[289] Flory, P. J. Molecular Size Distribution in Three Dimensional Polymers. I. Gelation1. *Journal of the American Chemical Society* **1941**, *63* (11), 3083-3090. DOI: 10.1021/ja01856a061.

[290] Broadbent, S. R.; Hammersley, J. M. Percolation processes: I. Crystals and mazes. *Mathematical Proceedings of the Cambridge Philosophical Society* **1957**, *53* (3), 629-641. DOI: 10.1017/S0305004100032680 From Cambridge University Press Cambridge Core.

[291] Malarz, K.; Kaczanowska, S.; KuŁAkowski, K. ARE FOREST FIRES PREDICTABLE? *International Journal of Modern Physics C* **2002**, *13* (08), 1017-1031. DOI: 10.1142/S0129183102003760.

[292] King, P. R.; Buldyrev, S. V.; Dokholyan, N. V.; Havlin, S.; Lee, Y.; Paul, G.; Stanley, H. E. Applications of statistical physics to the oil industry: predicting oil recovery using percolation theory. *Physica A: Statistical Mechanics and its Applications* **1999**, *274* (1), 60-66. DOI: 10.1016/S0378-4371(99)00327-1.

[293] Grigor'ev, V. N. Diffusion in solid helium (A review). *Low Temperature Physics* **1997**, *23* (1), 3-14. DOI: 10.1063/1.593334.

[294] Croccolo, F.; Roman, H. E. Spreading of infections on random graphs: A percolation-type model for COVID-19. *Chaos, Solitons & Fractals* **2020**, *139*, 110077. DOI: 10.1016/j.chaos.2020.110077.

[295] Kirkpatrick, S. Percolation and Conduction. *Reviews of Modern Physics* **1973**, *45* (4), 574-588. DOI: 10.1103/RevModPhys.45.574.

[296] Saberi, A. A. Recent advances in percolation theory and its applications. *Physics Reports* **2015**, *578*, 1-32. DOI: 10.1016/j.physrep.2015.03.003.

[297] Stauffer, D.; Aharony, A. *Introduction to Percolation theory*; Taylor & Francis, 1994.

[298] Johner, N.; Grimaldi, C.; Balberg, I.; Ryser, P. Transport exponent in a three-dimensional continuum tunneling-percolation model. *Physical Review B* **2008**, *77* (17). DOI: 10.1103/PhysRevB.77.174204.

[299] Garcia, J. R.; O'Suilleabhain, D.; Kaur, H.; Coleman, J. N. A Simple Model Relating Gauge Factor to Filler Loading in Nanocomposite Strain Sensors. *ACS Applied Nano Materials* **2021**, *4* (3), 2876-2886. DOI: 10.1021/acsanm.1c00040.

[300] Kogut, P. M.; Straley, J. P. Distribution-induced non-universality of the percolation conductivity exponents. *Journal of Physics C: Solid State Physics* **1979**, *12* (11), 2151-2159. DOI: 10.1088/0022-3719/12/11/023.

[301] Radicchi, F.; Castellano, C. Breaking of the site-bond percolation universality in networks. *Nature Communications* **2015**, *6* (1), 10196. DOI: 10.1038/ncomms10196.

[302] Bauhofer, W.; Kovacs, J. Z. A review and analysis of electrical percolation in carbon nanotube polymer composites. *Composites Science and Technology* **2009**, *69* (10), 1486-1498. DOI: 10.1016/j.compscitech.2008.06.018.

[303] Balberg, I.; Azulay, D.; Toker, D.; Millo, O. Percolation and Tunneling in Composite Materials. *International Journal of Modern Physics B* **2004**, *18* (15), 2091-2121. DOI: 10.1142/S0217979204025336.

[304] Ogilvie, S. P.; Large, M. J.; O'Mara, M. A.; Sehnal, A. C.; Amorim Graf, A.; Lynch, P. J.; Cass, A. J.; Salvage, J. P.; Alfonso, M.; Poulin, P.; et al. Nanosheet-Stabilized Emulsions: Near-Minimum Loading and Surface Energy Design of Conductive Networks. *ACS Nano* **2022**, *16* (2), 1963-1973. DOI: 10.1021/acsnano.1c06519.

[305] Müller, K. H.; Wei, G.; Raguse, B.; Myers, J. Three-dimensional percolation effect on electrical conductivity in films of metal nanoparticles linked by organic molecules. *Physical Review B* **2003**, *68* (15), 155407. DOI: 10.1103/PhysRevB.68.155407.

[306] McManus, D.; Vranic, S.; Withers, F.; Sanchez-Romaguera, V.; Macucci, M.; Yang, H.; Sorrentino, R.; Parvez, K.; Son, S.-K.; Iannaccone, G.; et al. Water-based and biocompatible 2D crystal inks for all-inkjet-printed heterostructures. *Nature Nanotechnology* **2017**, *12* (4), 343-350. DOI: 10.1038/nnano.2016.281.

[307] Kelly, A. G.; Vega-Mayoral, V.; Boland, J. B.; Coleman, J. N. Whiskey-phase exfoliation: exfoliation and printing of nanosheets using Irish whiskey. *2D Materials* **2019**, *6* (4), 045036. DOI: 10.1088/2053-1583/ab3892.

[308] Cunningham, G.; Lotya, M.; McEvoy, N.; Duesberg, G. S.; van der Schoot, P.; Coleman, J. N. Percolation scaling in composites of exfoliated MoS2 filled with nanotubes and graphene. *Nanoscale* **2012**, *4* (20), 6260-6264. DOI: 10.1039/C2NR31782F.

[309] Wu, J.; McLachlan, D. S. Percolation exponents and thresholds obtained from the nearly ideal continuum percolation system graphite-boron nitride. *Physical Review B* **1997**, *56* (3), 1236-1248. DOI: 10.1103/PhysRevB.56.1236.

[310] Scardaci, V.; Coull, R.; Coleman, J. N. Very thin transparent, conductive carbon nanotube films on flexible substrates. *Applied Physics Letters* **2010**, *97* (2). DOI: 10.1063/1.3462317.

[311] De Falco, G.; Commodo, M.; Barra, M.; Chiarella, F.; D'Anna, A.; Aloisio, A.; Cassinese, A.; Minutolo, P. Electrical characterization of flame-soot nanoparticle thin films. *Synthetic Metals* **2017**, *229*, 89-99. DOI: 10.1016/j.synthmet.2017.05.008.

[312] Cassidy, O.; Synnatschke, K.; Munuera, J.; Gabbett, C.; Carey, T.; Doolan, L.; Caffrey, E.; Coleman Jonathan, N. Layer-by-layer assembly yields thin graphene films with near theoretical conductivity. *Submitted* **2024**.

[313] Sahimi, M.; Hughes, B. D.; Scriven, L. E.; Davis, H. T. Critical exponent of percolation conductivity by finite-size scaling. *Journal of Physics C: Solid State Physics* **1983**, *16* (16), L521. DOI: 10.1088/0022-3719/16/16/004.

[314] Balberg, I.; Azulay, D.; Goldstein, Y.; Jedrzejewski, J. Possible origin of the smaller-than-universal percolation-conductivity exponent in the continuum. *Phys Rev E* **2016**, *93* (6), 062132. DOI: 10.1103/PhysRevE.93.062132.

[315] Thomson, W. XXXI. The Bakerian lecture.-On the electro-dynamic qualities of metals. *Philosophical Transactions of the Royal Society of London* **1856**, *146*, 649-751. DOI: doi:10.1098/rstl.1856.0031.

[316] Simmons, J. E. E. Material testing apparatus. 1942.

[317] Chung, D. D. L. A critical review of piezoresistivity and its application in electrical-resistance-based strain sensing. *Journal of Materials Science* **2020**, *55* (32), 15367-15396. DOI: 10.1007/s10853-020-05099-z.

[318] Cowles, B. A. High cycle fatigue in aircraft gas turbines—an industry perspective. *International Journal of Fracture* **1996**, *80* (2), 147-163. DOI: 10.1007/BF00012667.

[319] Crawley, E. F. Intelligent structures for aerospace - A technology overview and assessment. *AIAA Journal* **1994**, *32* (8), 1689-1699. DOI: 10.2514/3.12161.

[320] van Dyke, W. D.; Dennis, P. A. Metal foil type strain gauge and method of making same. USA 1948.

[321] Barlian, A. A.; Park, W. T.; Mallon, J. R.; Rastegar, A. J.; Pruitt, B. L. Review: Semiconductor Piezoresistance for Microsystems. *Proceedings of the IEEE* **2009**, *97* (3), 513-552. DOI: 10.1109/JPROC.2009.2013612.

[322] Park, J.; You, I.; Shin, S.; Jeong, U. Material Approaches to Stretchable Strain Sensors. *ChemPhysChem* **2015**, *16* (6), 1155-1163. DOI: 10.1002/cphc.201402810.

[323] Trung, T. Q.; Lee, N.-E. Flexible and Stretchable Physical Sensor Integrated Platforms for Wearable Human-Activity Monitoringand Personal Healthcare. *Advanced Materials* **2016**, *28* (22), 4338-4372. DOI: 10.1002/adma.201504244.

[324] Kim, D.-H.; Lu, N.; Ma, R.; Kim, Y.-S.; Kim, R.-H.; Wang, S.; Wu, J.; Won, S. M.; Tao, H.; Islam, A.; et al. Epidermal Electronics. *Science* **2011**, *333* (6044), 838. DOI: 10.1126/science.1206157.

[325] Jiang, Y.; Ma, J.; Shen, L.; Zhang, W.; Yang, K.; Zhu, B.; Yang, Y.; Ma, H.; Chen, X.; Bai, S.; et al. Chemresistor Smart Sensors from Silk Fibroin-Graphene Composites for Touch-free Wearables. *ACS Applied Materials & Interfaces* **2023**, *15* (40), 47196-47207. DOI: 10.1021/acsami.3c07913.

[326] Lu, L.; Zhang, J.; Xie, Y.; Gao, F.; Xu, S.; Wu, X.; Ye, Z. Wearable Health Devices in Health Care: Narrative Systematic Review. *JMIR Mhealth Uhealth* **2020**, *8* (11), e18907. DOI: 10.2196/18907.

[327] Garcia, J.; Caffrey, E.; Doolan, L.; Horvath, D. V.; Carey, T.; Gabbett, C.; Coleman, J. N. Near Room Temperature Production of Segregated Network Composites of Carbon Nanotubes and Regolith as Multifunctional, Extra-Terrestrial Building Materials. *Small* **2024**, *n/a* (n/a), 2310954. DOI: 10.1002/smll.202310954.

[328] Rogers, J. A.; Someya, T.; Huang, Y. Materials and Mechanics for Stretchable Electronics. *Science* **2010**, *327* (5973), 1603. DOI: 10.1126/science.1182383.

[329] Li, M.; Wu, Y.; Zhang, L.; Wo, H.; Huang, S.; Li, W.; Zeng, X.; Ye, Q.; Xu, T.; Luo, J.; et al. Liquid metal-based electrical interconnects and interfaces with excellent stability and reliability for flexible electronics. *Nanoscale* **2019**, *11* (12), 5441-5449, 10.1039/C8NR09503E. DOI: 10.1039/C8NR09503E.

[330] Agcayazi, T.; Chatterjee, K.; Bozkurt, A.; Ghosh, T. K. Flexible Interconnects for Electronic Textiles. *Advanced Materials Technologies* **2018**, *3* (10), 1700277. DOI: 10.1002/admt.201700277.

[331] Dang, W.; Vinciguerra, V.; Lorenzelli, L.; Dahiya, R. Printable stretchable interconnects. *Flexible and Printed Electronics* **2017**, *2* (1), 013003. DOI: 10.1088/2058-8585/aa5ab2.

[332] Fiorillo, A. S.; Critello, C. D.; Pullano, S. A. Theory, technology and applications of piezoresistive sensors: A review. *Sensors and Actuators A: Physical* **2018**, *281*, 156-175. DOI: 10.1016/j.sna.2018.07.006.

[333] Smith, C. S. Piezoresistance Effect in Germanium and Silicon. *Physical Review* **1954**, *94* (1), 42-49. DOI: 10.1103/PhysRev.94.42.

[334] Mason, W. P. *Crystal Physics of Interaction Processes*; Academic Press, NYC, 1966.

[335] Boland, C. S.; Khan, U.; Backes, C.; O'Neill, A.; McCauley, J.; Duane, S.; Shanker, R.; Liu, Y.; Jurewicz, I.; Dalton, A. B.; et al. Sensitive, High-Strain, High-Rate Bodily

Motion Sensors Based on Graphene–Rubber Composites. *ACS Nano* **2014**, *8* (9), 8819-8830. DOI: 10.1021/nn503454h.

[336] Boland, C. S. Stumbling through the Research Wilderness, Standard Methods To Shine Light on Electrically Conductive Nanocomposites for Future Healthcare Monitoring. *ACS Nano* **2019**, *13* (12), 13627-13636. DOI: 10.1021/acsnano.9b06847.

[337] Souri, H.; Banerjee, H.; Jusufi, A.; Radacsi, N.; Stokes, A. A.; Park, I.; Sitti, M.; Amjadi, M. Wearable and Stretchable Strain Sensors: Materials, Sensing Mechanisms, and Applications. *Advanced Intelligent Systems* **2020**, *2* (8), 2000039. DOI: 10.1002/aisy.202000039.

[338] Boland, C. S. Performance Analysis of Solution-Processed Nanosheet Strain Sensors – A Systematic Review of Graphene and MXene Wearable Devices. *Nanotechnology* **2024**.

[339] Lim, G.-H.; Lee, N.-E.; Lim, B. Highly sensitive, tunable, and durable gold nanosheet strain sensors for human motion detection. *Journal of Materials Chemistry C* **2016**, *4* (24), 5642-5647, 10.1039/C6TC00251J. DOI: 10.1039/C6TC00251J.

[340] Amjadi, M.; Pichitpajongkit, A.; Lee, S.; Ryu, S.; Park, I. Highly Stretchable and Sensitive Strain Sensor Based on Silver Nanowire–Elastomer Nanocomposite. *ACS Nano* **2014**, *8* (5), 5154-5163. DOI: 10.1021/nn501204t.

[341] Song, J.; Tan, Y.; Chu, Z.; Xiao, M.; Li, G.; Jiang, Z.; Wang, J.; Hu, T. Hierarchical Reduced Graphene Oxide Ridges for Stretchable, Wearable, and Washable Strain Sensors. *ACS Applied Materials & Interfaces* **2019**, *11* (1), 1283-1293. DOI: 10.1021/acsami.8b18143.

[342] Wu, J.; Ma, Z.; Hao, Z.; Zhang, J. T.; Sun, P.; Zhang, M.; Liu, Y.; Cheng, Y.; Li, Y.; Zhong, B.; et al. Sheath–Core Fiber Strain Sensors Driven by in-Situ Crack and Elastic Effects in Graphite Nanoplate Composites. *ACS Applied Nano Materials* **2019**, *2* (2), 750-759. DOI: 10.1021/acsanm.8b01926.

[343] Souri, H.; Bhattacharyya, D. Wearable strain sensors based on electrically conductive natural fiber yarns. *Materials & Design* **2018**, *154*, 217-227. DOI: 10.1016/j.matdes.2018.05.040.

[344] Wang, S.; Xiao, P.; Liang, Y.; Zhang, J.; Huang, Y.; Wu, S.; Kuo, S.-W.; Chen, T. Network cracks-based wearable strain sensors for subtle and large strain detection of human motions. *Journal of Materials Chemistry C* **2018**, *6* (19), 5140-5147, 10.1039/C8TC00433A. DOI: 10.1039/C8TC00433A.

[345] Amjadi, M.; Yoon, Y. J.; Park, I. Ultra-stretchable and skin-mountable strain sensors using carbon nanotubes–Ecoflex nanocomposites. *Nanotechnology* **2015**, *26* (37), 375501. DOI: 10.1088/0957-4484/26/37/375501.

[346] Biccai, S.; Boland, C. S.; O'Driscoll, D. P.; Harvey, A.; Gabbett, C.; O'Suilleabhain, D. R.; Griffin, A. J.; Li, Z.; Young, R. J.; Coleman, J. N. Negative Gauge Factor Piezoresistive Composites Based on Polymers Filled with MoS2 Nanosheets. *ACS Nano* **2019**, *13* (6), 6845-6855. DOI: 10.1021/acsnano.9b01613.

[347] Hu, N.; Karube, Y.; Arai, M.; Watanabe, T.; Yan, C.; Li, Y.; Liu, Y.; Fukunaga, H. Investigation on sensitivity of a polymer/carbon nanotube composite strain sensor. *Carbon* **2010**, *48* (3), 680-687. DOI: 10.1016/j.carbon.2009.10.012.

[348] Carcia, P. F.; Suna, A.; Childers, W. D. Electrical conduction and strain sensitivity in RuO2 thick film resistors. *Journal of Applied Physics* **1983**, *54* (10), 6002-6008. DOI: 10.1063/1.331779.

[349] Han, L.; Lu, X.; Wang, M.; Gan, D.; Deng, W.; Wang, K.; Fang, L.; Liu, K.; Chan, C. W.; Tang, Y.; et al. A Mussel-Inspired Conductive, Self-Adhesive, and Self-Healable Tough Hydrogel as Cell Stimulators and Implantable Bioelectronics. *Small* **2017**, *13* (2), 1601916. DOI: 10.1002/smll.201601916.

[350] Lee, W. S.; Kim, D.; Park, B.; Joh, H.; Woo, H. K.; Hong, Y.-K.; Kim, T.-i.; Ha, D.-H.; Oh, S. J. Multiaxial and Transparent Strain Sensors Based on Synergetically Reinforced and Orthogonally Cracked Hetero-Nanocrystal Solids. *Advanced Functional Materials* **2019**, *29* (4). DOI: 10.1002/adfm.201806714.

[351] Ates, H. C.; Nguyen, P. Q.; Gonzalez-Macia, L.; Morales-Narváez, E.; Güder, F.; Collins, J. J.; Dincer, C. End-to-end design of wearable sensors. *Nature Reviews Materials* **2022**, *7* (11), 887-907. DOI: 10.1038/s41578-022-00460-x.

[352] Edison, T. A. Speaking-telegraph. 1877.

[353] Wills, I. Instrumentalizing Failure: Edison's Invention of the Carbon Microphone. *Annals of Science* **2007**, *64* (3), 383-409. DOI: 10.1080/00033790601160515.

[354] Lee, D.; Hong, H. P.; Lee, C. J.; Park, C. W.; Min, N. K. Microfabrication and characterization of spray-coated single-wall carbon nanotube film strain gauges. *Nanotechnology* **2011**, *22* (45), 455301. DOI: 10.1088/0957-4484/22/45/455301.

[355] Herrmann, J.; Müller, K. H.; Reda, T.; Baxter, G. R.; Raguse, B.; de Groot, G. J. J. B.; Chai, R.; Roberts, M.; Wieczorek, L. Nanoparticle films as sensitive strain gauges. *Applied Physics Letters* **2007**, *91* (18). DOI: 10.1063/1.2805026.

[356] Grow, R. J.; Wang, Q.; Cao, J.; Wang, D.; Dai, H. Piezoresistance of carbon nanotubes on deformable thin-film membranes. *Applied Physics Letters* **2005**, *86* (9). DOI: 10.1063/1.1872221.

[357] Yamada, T.; Hayamizu, Y.; Yamamoto, Y.; Yomogida, Y.; Izadi-Najafabadi, A.; Futaba, D. N.; Hata, K. A stretchable carbon nanotube strain sensor for human-motion detection. *Nature Nanotechnology* **2011**, *6* (5), 296-301. DOI: 10.1038/nnano.2011.36.

[358] Zhao, J.; He, C.; Yang, R.; Shi, Z.; Cheng, M.; Yang, W.; Xie, G.; Wang, D.; Shi, D.; Zhang, G. Ultra-sensitive strain sensors based on piezoresistive nanographene films. *Applied Physics Letters* **2012**, *101* (6). DOI: 10.1063/1.4742331.

[359] Yao, H.; Hempel, M.; Hsieh, Y. P.; Kong, J.; Hofmann, M. Characterizing percolative materials by straining. *Nanoscale* **2019**, *11* (3), 1074-1079. DOI: 10.1039/c8nr09120j.

[360] Chen, Z.; Ming, T.; Goulamaly, M. M.; Yao, H.; Nezich, D.; Hempel, M.; Hofmann, M.; Kong, J. Enhancing the Sensitivity of Percolative Graphene Films for Flexible and Transparent Pressure Sensor Arrays. *Advanced Functional Materials* **2016**, *26* (28), 5061-5067. DOI: 10.1002/adfm.201503674.

[361] Yan, W.; Fuh, H.-R.; Lv, Y.; Chen, K.-Q.; Tsai, T.-Y.; Wu, Y.-R.; Shieh, T.-H.; Hung, K.-M.; Li, J.; Zhang, D.; et al. Giant gauge factor of Van der Waals material based strain sensors. *Nature Communications* **2021**, *12* (1), 2018. DOI: 10.1038/s41467-021-22316-8.

[362] Yang, Y.; Shi, L.; Cao, Z.; Wang, R.; Sun, J. Strain Sensors with a High Sensitivity and a Wide Sensing Range Based on a Ti3C2Tx(MXene) Nanoparticle–Nanosheet Hybrid Network. *Advanced Functional Materials* **2019**, *29* (14). DOI: 10.1002/adfm.201807882.

[363] Yang, Z.; Wang, D. Y.; Pang, Y.; Li, Y. X.; Wang, Q.; Zhang, T. Y.; Wang, J. B.; Liu, X.; Yang, Y. Y.; Jian, J. M.; et al. Simultaneously Detecting Subtle and Intensive Human Motions Based on a Silver Nanoparticles Bridged Graphene Strain Sensor. *ACS Appl Mater Interfaces* **2018**, *10* (4), 3948-3954. DOI: 10.1021/acsami.7b16284.

[364] Wang, Y.; Yang, R.; Shi, Z.; Zhang, L.; Shi, D.; Wang, E.; Zhang, G. Super-Elastic Graphene Ripples for Flexible Strain Sensors. *ACS Nano* **2011**, *5* (5), 3645-3650. DOI: 10.1021/nn103523t.

[365] Zhao, J.; Wang, G.; Yang, R.; Lu, X.; Cheng, M.; He, C.; Xie, G.; Meng, J.; Shi, D.; Zhang, G. Tunable Piezoresistivity of Nanographene Films for Strain Sensing. *ACS Nano* **2015**, *9* (2), 1622-1629. DOI: 10.1021/nn506341u.

[366] Bae, S.-H.; Lee, Y.; Sharma, B. K.; Lee, H.-J.; Kim, J.-H.; Ahn, J.-H. Graphene-based transparent strain sensor. *Carbon* **2013**, *51*, 236-242. DOI: 10.1016/j.carbon.2012.08.048.

[367] Qiao, Y.; Wang, Y.; Tian, H.; Li, M.; Jian, J.; Wei, Y.; Tian, Y.; Wang, D. Y.; Pang, Y.; Geng, X.; et al. Multilayer Graphene Epidermal Electronic Skin. *ACS Nano* **2018**, *12* (9), 8839-8846. DOI: 10.1021/acsnano.8b02162.

[368] Neilson, J.; Cataldi, P.; Derby, B. Graphene-Based Transparent Flexible Strain Gauges with Tunable Sensitivity and Strain Range. *ACS Applied Nano Materials* **2023**, *6* (23), 21763-21774. DOI: 10.1021/acsanm.3c03967.

[369] Ramírez, J.; Urbina, A. D.; Kleinschmidt, A. T.; Finn, M.; Edmunds, S. J.; Esparza, G. L.; Lipomi, D. J. Exploring the limits of sensitivity for strain gauges of graphene and hexagonal boron nitride decorated with metallic nanoislands. *Nanoscale* **2020**, *12* (20), 11209-11221, 10.1039/D0NR02270E. DOI: 10.1039/D0NR02270E.

[370] Akinwande, D.; Petrone, N.; Hone, J. Two-dimensional flexible nanoelectronics. *Nature Communications* **2014**, *5* (1), 5678. DOI: 10.1038/ncomms6678.

[371] Daus, A.; Vaziri, S.; Chen, V.; Köroğlu, Ç.; Grady, R. W.; Bailey, C. S.; Lee, H. R.; Schauble, K.; Brenner, K.; Pop, E. High-performance flexible nanoscale transistors based on transition metal dichalcogenides. *Nature Electronics* **2021**, *4* (7), 495-501. DOI: 10.1038/s41928-021-00598-6.

[372] Liu, K.; Ouyang, B.; Guo, X.; Guo, Y.; Liu, Y. Advances in flexible organic field-effect transistors and their applications for flexible electronics. *npj Flexible Electronics* **2022**, *6* (1), 1. DOI: 10.1038/s41528-022-00133-3.

[373] Ling, H.; Liu, S.; Zheng, Z.; Yan, F. Organic Flexible Electronics. *Small Methods* **2018**, *2* (10), 1800070. DOI: 10.1002/smtd.201800070.

[374] Orts Mercadillo, V.; Chan, K. C.; Caironi, M.; Athanassiou, A.; Kinloch, I. A.; Bissett, M.; Cataldi, P. Electrically Conductive 2D Material Coatings for Flexible and Stretchable Electronics: A Comparative Review of Graphenes and MXenes. *Advanced Functional Materials* **2022**, *32* (38), 2204772. DOI: 10.1002/adfm.202204772.

[375] Moses, O. A.; Gao, L.; Zhao, H.; Wang, Z.; Lawan Adam, M.; Sun, Z.; Liu, K.; Wang, J.; Lu, Y.; Yin, Z.; et al. 2D materials inks toward smart flexible electronics. *Materials Today* **2021**, *50*, 116-148. DOI: 10.1016/j.mattod.2021.08.010.

[376] Rhee, D.; Han, B.; Jung, M.; Kim, J.; Song, O.; Kang, J. Hierarchical Nanoscale Structuring of Solution-Processed 2D van der Waals Networks for Wafer-Scale, Stretchable Electronics. *ACS Applied Materials & Interfaces* **2022**, *14* (51), 57153-57164. DOI: 10.1021/acsami.2c16738.

[377] Yang, C.; Huang, W.; Lin, Y.; Cao, S.; Wang, H.; Sun, Y.; Fang, T.; Wang, M.; Kong, D. Stretchable MXene/Carbon Nanotube Bilayer Strain Sensors with Tunable Sensitivity and Working Ranges. *ACS Applied Materials & Interfaces* **2024**, *16* (23), 30274-30283. DOI: 10.1021/acsami.4c04770.

[378] Caffrey, E.; Garcia, J. R.; O'Suilleabhain, D.; Gabbett, C.; Carey, T.; Coleman, J. N. Quantifying the Piezoresistive Mechanism in High-Performance Printed Graphene Strain Sensors. *ACS Applied Materials & Interfaces* **2022**, *14* (5), 7141-7151. DOI: 10.1021/acsami.1c21623.

[379] Haleem, A.; Javaid, M.; Singh, R. P.; Rab, S.; Suman, R. Applications of nanotechnology in medical field: a brief review. *Global Health Journal* **2023**, *7* (2), 70-77. DOI: 10.1016/j.glohj.2023.02.008.

[380] Lipomi, D. J.; Vosgueritchian, M.; Tee, B. C. K.; Hellstrom, S. L.; Lee, J. A.; Fox, C. H.; Bao, Z. Skin-like pressure and strain sensors based on transparent elastic films of carbon nanotubes. *Nature Nanotechnology* **2011**, *6* (12), 788-792. DOI: 10.1038/nnano.2011.184.

[381] Childs, A.; Mayol, B.; Lasalde-Ramírez, J. A.; Song, Y.; Sempionatto, J. R.; Gao, W. Diving into Sweat: Advances, Challenges, and Future Directions in Wearable Sweat Sensing. *ACS Nano* **2024**, *18* (36), 24605-24616. DOI: 10.1021/acsnano.4c10344.

[382] Vaghasiya, J. V.; Mayorga-Martinez, C. C.; Pumera, M. Wearable sensors for telehealth based on emerging materials and nanoarchitectonics. *npj Flexible Electronics* **2023**, *7* (1), 26. DOI: 10.1038/s41528-023-00261-4.

[383] O'Mara, M. A.; Ogilvie, S. P.; Large, M. J.; Graf, A. A.; Sehnal, A. C.; Lynch, P. J.; Salvage, J. P.; Jurewicz, I.; King, A. A. K.; Dalton, A. B. Ultrasensitive Strain Gauges Enabled by Graphene-Stabilized Silicone Emulsions. *Advanced Functional Materials* **2020**, *30* (32). DOI: 10.1002/adfm.202002433.

[384] Luo, Z.; Hu, X.; Tian, X.; Luo, C.; Xu, H.; Li, Q.; Li, Q.; Zhang, J.; Qiao, F.; Wu, X.; et al. Structure-Property Relationships in Graphene-Based Strain and Pressure Sensors for Potential Artificial Intelligence Applications. *Sensors* **2019**, *19* (5). DOI: 10.3390/s19051250.

[385] Amjadi, M.; Kyung, K.-U.; Park, I.; Sitti, M. Stretchable, Skin-Mountable, and Wearable Strain Sensors and Their Potential Applications: A Review. *Advanced Functional Materials* **2016**, *26* (11), 1678-1698. DOI: 10.1002/adfm.201504755.

[386] Zheng, Q.; Lee, J.-h.; Shen, X.; Chen, X.; Kim, J.-K. Graphene-based wearable piezoresistive physical sensors. *Materials Today* **2020**, *36*, 158-179. DOI: 10.1016/j.mattod.2019.12.004.

[387] Sui, X.; Downing, J. R.; Hersam, M. C.; Chen, J. Additive manufacturing and applications of nanomaterial-based sensors. *Materials Today* **2021**. DOI: 10.1016/j.mattod.2021.02.001.

[388] Li, X.; Chai, Y. Design and applications of graphene-based flexible and wearable physical sensing devices. *2D Materials* **2020**, *8* (2). DOI: 10.1088/2053-1583/abcbe6.

[389] Trindade, G. F.; Wang, F.; Im, J.; He, Y.; Balogh, A.; Scurr, D.; Gilmore, I.; Tiddia, M.; Saleh, E.; Pervan, D.; et al. Residual polymer stabiliser causes anisotropic electrical conductivity during inkjet printing of metal nanoparticles. *Communications Materials* **2021**, *2* (1). DOI: 10.1038/s43246-021-00151-0.

[390] Ren, J.; Wang, C.; Zhang, X.; Carey, T.; Chen, K.; Yin, Y.; Torrisi, F. Environmentally-friendly conductive cotton fabric as flexible strain sensor based on hot press reduced graphene oxide. *Carbon* **2017**, *111*, 622-630. DOI: 10.1016/j.carbon.2016.10.045.

[391] Lee, J.; Lim, M.; Yoon, J.; Kim, M. S.; Choi, B.; Kim, D. M.; Kim, D. H.; Park, I.; Choi, S. J. Transparent, Flexible Strain Sensor Based on a Solution-Processed Carbon Nanotube Network. *ACS Appl Mater Interfaces* **2017**, *9* (31), 26279-26285. DOI: 10.1021/acsami.7b03184.

[392] Feng, W.; Zheng, W.; Gao, F.; Chen, X.; Liu, G.; Hasan, T.; Cao, W.; Hu, P. Sensitive Electronic-Skin Strain Sensor Array Based on the Patterned Two-Dimensional α-In2Se3. *Chemistry of Materials* **2016**, *28* (12), 4278-4283. DOI: 10.1021/acs.chemmater.6b01073.

[393] Wagner, S.; Yim, C.; McEvoy, N.; Kataria, S.; Yokaribas, V.; Kuc, A.; Pindl, S.; Fritzen, C.-P.; Heine, T.; Duesberg, G. S.; et al. Highly Sensitive Electromechanical Piezoresistive Pressure Sensors Based on Large-Area Layered PtSe2 Films. *Nano Letters* **2018**, *18* (6), 3738-3745. DOI: 10.1021/acs.nanolett.8b00928.

[394] Tian, H.; Shu, Y.; Cui, Y. L.; Mi, W. T.; Yang, Y.; Xie, D.; Ren, T. L. Scalable fabrication of high-performance and flexible graphene strain sensors. *Nanoscale* **2014**, *6* (2), 699-705. DOI: 10.1039/c3nr04521h.

[395] Uran, S.; Alhani, A.; Silva, C. Study of ultraviolet-visible light absorbance of exfoliated graphite forms. *AIP Advances* **2017**, *7* (3). DOI: 10.1063/1.4979607.

[396] Poole, C. P.; Owens, F. J. *Introduction to Nanotechnology*; Wiley, 2003.

[397] Jeong, Y. R.; Park, H.; Jin, S. W.; Hong, S. Y.; Lee, S.-S.; Ha, J. S. Highly Stretchable and Sensitive Strain Sensors Using Fragmentized Graphene Foam. *Advanced Functional Materials* **2015**, *25* (27), 4228-4236. DOI: 10.1002/adfm.201501000.

[398] Shi, X.; Liu, S.; Sun, Y.; Liang, J.; Chen, Y. Lowering Internal Friction of 0D–1D–2D Ternary Nanocomposite-Based Strain Sensor by Fullerene to Boost the Sensing Performance. *Advanced Functional Materials* **2018**, *28* (22), 1800850. DOI: 10.1002/adfm.201800850.

[399] Soliveres, S.; Gyani, J.; Delseny, C.; Hoffmann, A.; Pascal, F. 1⁄f noise and percolation in carbon nanotube random networks. *Applied Physics Letters* **2007**, *90* (8), 082107. DOI: 10.1063/1.2709853.

[400] Caffrey, E.; Munuera, J. M.; Carey, T.; Coleman, J. N. Quantifying the effect of nanosheet dimensions on the piezoresistive response of printed graphene nanosheet networks. *Nanoscale Horizons* **2024**, 10.1039/D4NH00224E. DOI: 10.1039/D4NH00224E.

[401] Khan, K.; Tareen, A. K.; Aslam, M.; Wang, R.; Zhang, Y.; Mahmood, A.; Ouyang, Z.; Zhang, H.; Guo, Z. Recent developments in emerging two-dimensional materials and their applications. *Journal of Materials Chemistry C* **2020**, *8* (2), 387-440, 10.1039/C9TC04187G. DOI: 10.1039/C9TC04187G.

[402] Ferrari, A. C.; Bonaccorso, F.; Fal'ko, V.; Novoselov, K. S.; Roche, S.; Bøggild, P.; Borini, S.; Koppens, F. H. L.; Palermo, V.; Pugno, N.; et al. Science and technology roadmap for graphene, related two-dimensional crystals, and hybrid systems. *Nanoscale* **2015**, *7* (11), 4598-4810, 10.1039/C4NR01600A. DOI: 10.1039/C4NR01600A.

[403] Bellani, S.; Bartolotta, A.; Agresti, A.; Calogero, G.; Grancini, G.; Di Carlo, A.; Kymakis, E.; Bonaccorso, F. Solution-processed two-dimensional materials for next-generation photovoltaics. *Chemical Society Reviews* **2021**, *50* (21), 11870-11965, 10.1039/D1CS00106J. DOI: 10.1039/D1CS00106J.

[404] Backes, C.; Smith, R. J.; McEvoy, N.; Berner, N. C.; McCloskey, D.; Nerl, H. C.; O'Neill, A.; King, P. J.; Higgins, T.; Hanlon, D.; et al. Edge and confinement effects allow in situ measurement of size and thickness of liquid-exfoliated nanosheets. *Nature Communications* **2014**, *5* (1), 4576. DOI: 10.1038/ncomms5576.

[405] Griffin, A.; Harvey, A.; Cunningham, B.; Scullion, D.; Tian, T.; Shih, C.-J.; Gruening, M.; Donegan, J. F.; Santos, E. J. G.; Backes, C.; et al. Spectroscopic Size and Thickness Metrics for Liquid-Exfoliated h-BN. *Chemistry of Materials* **2018**, *30* (6), 1998-2005. DOI: 10.1021/acs.chemmater.7b05188.

[406] Hu, G.; Kang, J.; Ng, L. W. T.; Zhu, X.; Howe, R. C. T.; Jones, C. G.; Hersam, M. C.; Hasan, T. Functional inks and printing of two-dimensional materials. *Chemical Society Reviews* **2018**, *47* (9), 3265-3300, 10.1039/C8CS00084K. DOI: 10.1039/C8CS00084K.

[407] Haar, S.; Ciesielski, A.; Clough, J.; Yang, H.; Mazzaro, R.; Richard, F.; Conti, S.; Merstorf, N.; Cecchini, M.; Morandi, V.; et al. A Supramolecular Strategy to Leverage the Liquid-Phase Exfoliation of Graphene in the Presence of Surfactants: Unraveling the Role of the Length of Fatty Acids. *Small* **2015**, *11* (14), 1691-1702. DOI: 10.1002/smll.201402745.

[408] Ferrari, A. C.; Meyer, J. C.; Scardaci, V.; Casiraghi, C.; Lazzeri, M.; Mauri, F.; Piscanec, S.; Jiang, D.; Novoselov, K. S.; Roth, S.; et al. Raman spectrum of graphene and graphene layers. *Physical Review Letters* **2006**, *97* (18), 187401. DOI: 187401

10.1103/PhysRevLett.97.187401.

[409] Manikas, A. C.; Pastore Carbone, M. G.; Woods, C. R.; Wang, Y.; Souli, I.; Anagnostopoulos, G.; Hadjinicolaou, M.; Novoselov, K. S.; Galiotis, C. Stress transfer at the nanoscale on graphene ribbons of regular geometry. *Nanoscale* **2019**, *11* (30), 14354-14361, 10.1039/C9NR03166A. DOI: 10.1039/C9NR03166A.

[410] Smith, A. D.; Niklaus, F.; Paussa, A.; Vaziri, S.; Fischer, A. C.; Sterner, M.; Forsberg, F.; Delin, A.; Esseni, D.; Palestri, P.; et al. Electromechanical Piezoresistive Sensing in Suspended Graphene Membranes. *Nano Letters* **2013**, *13* (7), 3237-3242. DOI: 10.1021/nl401352k.

[411] Huang, M. Y.; Pascal, T. A.; Kim, H.; Goddard, W. A.; Greer, J. R. Electronic-Mechanical Coupling in Graphene from in situ Nanoindentation Experiments and Multiscale Atomistic Simulations. *Nano Letters* **2011**, *11* (3), 1241-1246. DOI: 10.1021/nl104227t.

[412] Zhu, S. E.; Ghatkesar, M. K.; Zhang, C.; Janssen, G. Graphene based piezoresistive pressure sensor. *Applied Physics Letters* **2013**, *102* (16). DOI: 10.1063/1.4802799.

[413] Benameur, M. M.; Gargiulo, F.; Manzeli, S.; Autès, G.; Tosun, M.; Yazyev, O. V.; Kis, A. Electromechanical oscillations in bilayer graphene. *Nature Communications* **2015**, *6* (1), 8582. DOI: 10.1038/ncomms9582.

[414] Blazewicz, S.; Patalita, B.; Touzain, P. Study of piezoresistance effect in carbon fibers. *Carbon* **1997**, *35* (10), 1613-1618. DOI: 10.1016/S0008-6223(97)00120-6.

[415] Manzeli, S.; Allain, A.; Ghadimi, A.; Kis, A. Piezoresistivity and Strain-induced Band Gap Tuning in Atomically Thin MoS2. *Nano Letters* **2015**, *15* (8), 5330-5335. DOI: 10.1021/acs.nanolett.5b01689.

[416] Ayán-Varela, M.; Paredes, J. I.; Guardia, L.; Villar-Rodil, S.; Munuera, J. M.; Díaz-González, M.; Fernández-Sánchez, C.; Martínez-Alonso, A.; Tascón, J. M. D. Achieving Extremely Concentrated Aqueous Dispersions of Graphene Flakes and Catalytically Efficient Graphene-Metal Nanoparticle Hybrids with Flavin Mononucleotide as a High-Performance Stabilizer. *ACS Applied Materials & Interfaces* **2015**, *7* (19), 10293-10307. DOI: 10.1021/acsami.5b00910.

[417] Karger, L.; Synnatschke, K.; Settele, S.; Hofstetter, Y. J.; Nowack, T.; Zaumseil, J.; Vaynzof, Y.; Backes, C. The Role of Additives in Suppressing the Degradation of Liquid-Exfoliated WS2 Monolayers. *Advanced Materials* **2021**, *33* (42), 2102883. DOI: 10.1002/adma.202102883.

[418] Kelly, A. G.; Sheil, S.; Douglas-Henry, D. A.; Caffrey, E.; Gabbett, C.; Doolan, L.; Nicolosi, V.; Coleman, J. N. Transparent Conductors Printed from Grids of Highly Conductive Silver Nanosheets. *ACS Applied Materials & Interfaces* **2023**, *15* (33), 39864-39871. DOI: 10.1021/acsami.3c07459.

[419] Wang, G.; Dai, Z.; Xiao, J.; Feng, S.; Weng, C.; Liu, L.; Xu, Z.; Huang, R.; Zhang, Z. Bending of Multilayer van der Waals Materials. *Physical Review Letters* **2019**, *123* (11), 116101. DOI: 10.1103/PhysRevLett.123.116101.

[420] Munuera, J. M.; Paredes, J. I.; Villar-Rodil, S.; Castro-Muñiz, A.; Martínez-Alonso, A.; Tascón, J. M. D. High quality, low-oxidized graphene via anodic exfoliation with table salt as an efficient oxidation-preventing co-electrolyte for water/oil remediation and capacitive energy storage applications. *Applied Materials Today* **2018**, *11*, 246-254. DOI: 10.1016/j.apmt.2018.03.002.

[421] Arganda-Carreras, I.; Kaynig, V.; Rueden, C.; Eliceiri, K. W.; Schindelin, J.; Cardona, A.; Sebastian Seung, H. Trainable Weka Segmentation: a machine learning tool for microscopy pixel classification. *Bioinformatics* **2017**, *33* (15), 2424-2426. DOI: 10.1093/bioinformatics/btx180.

[422] Schindelin, J.; Arganda-Carreras, I.; Frise, E.; Kaynig, V.; Longair, M.; Pietzsch, T.; Preibisch, S.; Rueden, C.; Saalfeld, S.; Schmid, B.; et al. Fiji: an open-source platform for biological-image analysis. *Nature Methods* **2012**, *9* (7), 676-682. DOI: 10.1038/nmeth.2019.

[423] Sabayev, V.; Croitoru, N.; Inberg, A.; Shacham-Diamand, Y. The evolution and analysis of electrical percolation threshold in nanometer scale thin films deposited by electroless plating. *Materials Chemistry and Physics* **2011**, *127* (1), 214-219. DOI: 10.1016/j.matchemphys.2011.01.061.

[424] Marković, Z. M.; Budimir, M. D.; Kepić, D. P.; Holclajtner-Antunović, I. D.; Marinović-Cincović, M. T.; Dramićanin, M. D.; Spasojević, V. D.; Peruško, D. B.; Špitalský, Z.; Mičušik, M.; et al. Semi-transparent, conductive thin films of electrochemical exfoliated graphene. *RSC Advances* **2016**, *6* (45), 39275-39283, 10.1039/C6RA04250C. DOI: 10.1039/C6RA04250C.

[425] Caffrey, E.; Carey, T.; Doolan, L.; Dawson, A.; Coleman, E.; Sofer, Z.; Cassidy, O.; Gabbett, C.; Coleman, J. N. Using Electrical Impedance Spectroscopy to Separately Quantify the Effect of Strain on Nanosheet and Junction Resistance in Printed Nanosheet Networks. *Small* **2024**, *n/a* (n/a), 2406864. DOI: 10.1002/smll.202406864.

[426] Chu, J.; Bissett, M. A.; Young, R. J. MoS2 Nanosheet-Coated Carbon Fibers as Strain Sensors in Epoxy Composites. *ACS Applied Nano Materials* **2021**, *4* (9), 9181-9189. DOI: 10.1021/acsanm.1c01723.

[427] Fuhrer, M. S.; Nygård, J.; Shih, L.; Forero, M.; Yoon, Y. G.; Mazzoni, M. S. C.; Choi, H. J.; Ihm, J.; Louie, S. G.; Zettl, A.; et al. Crossed nanotube junctions. *Science* **2000**, *288* (5465), 494-497. DOI: 10.1126/science.288.5465.494.

[428] Bellew, A. T.; Manning, H. G.; da Rocha, C. G.; Ferreira, M. S.; Boland, J. J. Resistance of Single Ag Nanowire Junctions and Their Role in the Conductivity of Nanowire Networks. *Acs Nano* **2015**, *9* (11), 11422-11429. DOI: 10.1021/acsnano.5b05469.

[429] Lee, K.; Szydłowska, B. M.; Hartwig, O.; Synnatschke, K.; Tywoniuk, B.; Hartman, T.; Tomašević-Ilić, T.; Gabbett, C. P.; Coleman, J. N.; Sofer, Z.; et al. Highly conductive and long-term stable films from liquid-phase exfoliated platinum diselenide. *Journal of Materials Chemistry C* **2023**, *11* (2), 593-599, 10.1039/D2TC03889G. DOI: 10.1039/D2TC03889G.

[430] Wilcoxon, J. P.; Newcomer, P. P.; Samara, G. A. Synthesis and optical properties of MoS2 and isomorphous nanoclusters in the quantum confinement regime. *Journal of Applied Physics* **1997**, *81* (12), 7934-7944. DOI: 10.1063/1.365367.

[431] Zhou, K.-G.; Withers, F.; Cao, Y.; Hu, S.; Yu, G.; Casiraghi, C. Raman Modes of MoS2 Used as Fingerprint of van der Waals Interactions in 2-D Crystal-Based Heterostructures. *ACS Nano* **2014**, *8* (10), 9914-9924. DOI: 10.1021/nn5042703.

[432] Lee, C.; Yan, H.; Brus, L. E.; Heinz, T. F.; Hone, J.; Ryu, S. Anomalous Lattice Vibrations of Single- and Few-Layer MoS2. *ACS Nano* **2010**, *4* (5), 2695-2700. DOI: 10.1021/nn1003937.

[433] Garrett, M. P.; Ivanov, I. N.; Gerhardt, R. A.; Puretzky, A. A.; Geohegan, D. B. Separation of junction and bundle resistance in single wall carbon nanotube percolation networks by impedance spectroscopy. *Applied Physics Letters* **2010**, *97* (16), 163105. DOI: 10.1063/1.3490650.

[434] Moore, D. C.; Jawaid, A.; Busch, R.; Brothers, M.; Miesle, P.; Miesle, A.; Rao, R.; Lee, J.; Beagle, L. K.; Motala, M.; et al. Ultrasensitive Molecular Sensors Based on Real-Time Impedance Spectroscopy in Solution-Processed 2D Materials. *Advanced Functional Materials* **2022**, *32* (12), 2106830. DOI: 10.1002/adfm.202106830.

[435] Boukamp, B. A. Distribution (function) of relaxation times, successor to complex nonlinear least squares analysis of electrochemical impedance spectroscopy? *Journal of Physics-Energy* **2020**, *2* (4). DOI: 10.1088/2515-7655/aba9e0.

[436] Zhao, Y.; Tripathi, M.; Čerņevičs, K.; Avsar, A.; Ji, H. G.; Gonzalez Marin, J. F.; Cheon, C.-Y.; Wang, Z.; Yazyev, O. V.; Kis, A. Electrical spectroscopy of defect states and their hybridization in monolayer MoS2. *Nature Communications* **2023**, *14* (1), 44. DOI: 10.1038/s41467-022-35651-1.

[437] Guo, Y.; Wei, X.; Shu, J.; Liu, B.; Yin, J.; Guan, C.; Han, Y.; Gao, S.; Chen, Q. Charge trapping at the MoS2-SiO2 interface and its effects on the characteristics of MoS2 metal-oxide-semiconductor field effect transistors. *Applied Physics Letters* **2015**, *106* (10), 103109. DOI: 10.1063/1.4914968.

[438] Jeong, Y.; Lee, H. J.; Park, J.; Lee, S.; Jin, H.-J.; Park, S.; Cho, H.; Hong, S.; Kim, T.; Kim, K.; et al. Engineering MoSe2/MoS2 heterojunction traps in 2D transistors for multilevel memory, multiscale display, and synaptic functions. *npj 2D Materials and Applications* **2022**, *6* (1), 23. DOI: 10.1038/s41699-022-00295-8.

[439] Wang, X.; Long, R. Oxidation Notably Accelerates Nonradiative Electron–Hole Recombination in MoS2 by Different Mechanisms: Time-Domain Ab Initio Analysis. *The Journal of Physical Chemistry Letters* **2020**, *11* (10), 4086-4092. DOI: 10.1021/acs.jpclett.0c01056.

[440] Chen, K.; Roy, A.; Rai, A.; Valsaraj, A.; Meng, X.; He, F.; Xu, X.; Register, L. F.; Banerjee, S.; Wang, Y. Carrier Trapping by Oxygen Impurities in Molybdenum Diselenide. *ACS Applied Materials & Interfaces* **2018**, *10* (1), 1125-1131. DOI: 10.1021/acsami.7b15478.

[441] Schätz, J.; Nayi, N.; Weber, J.; Metzke, C.; Lukas, S.; Walter, J.; Schaffus, T.; Streb, F.; Reato, E.; Piacentini, A.; et al. Button shear testing for adhesion measurements of 2D materials. *Nature Communications* **2024**, *15* (1), 2430. DOI: 10.1038/s41467-024-46136-8.

[442] Wang, S.; Li, W.; Xue, J.; Ge, J.; He, J.; Hou, J.; Xie, Y.; Li, Y.; Zhang, H.; Sofer, Z.; et al. A library of 2D electronic material inks synthesized by liquid-metal-assisted intercalation of crystal powders. *Nature Communications* **2024**, *15* (1), 6388. DOI: 10.1038/s41467-024-50697-z.

[443] Calabrese, G.; Pimpolari, L.; Conti, S.; Mavier, F.; Majee, S.; Worsley, R.; Wang, Z.; Pieri, F.; Basso, G.; Pennelli, G.; et al. Inkjet-printed graphene Hall mobility measurements and low-frequency noise characterization. *Nanoscale* **2020**, *12* (12), 6708-6716, 10.1039/C9NR09289G. DOI: 10.1039/C9NR09289G.

[444] Majee, S.; Liu, C.; Wu, B.; Zhang, S. L.; Zhang, Z. B. Ink-jet printed highly conductive pristine graphene patterns achieved with water-based ink and aqueous doping processing. *Carbon* **2017**, *114*, 77-83. DOI: 10.1016/j.carbon.2016.12.003.

[445] Fuchs, K. The conductivity of thin metallic films according to the electron theory of metals. *Mathematical Proceedings of the Cambridge Philosophical Society* **1938**, *34* (1), 100-108. DOI: 10.1017/S0305004100019952 From Cambridge University Press Cambridge Core.

[446] Zhou, T.; Zheng, P.; Pandey, S. C.; Sundararaman, R.; Gall, D. The electrical resistivity of rough thin films: A model based on electron reflection at discrete step edges. *Journal of Applied Physics* **2018**, *123* (15), 155107. DOI: 10.1063/1.5020577.